Technische Universität München

Fakultät für Elektrotechnik und Informationstechnik

Lehrstuhl für Elektrische Energiespeichertechnik

Current distribution in parallel-connected battery cells

Markus H. Hofmann

Vollständiger Abdruck der von der Fakultät für Elektrotechnik und Informationstechnik der Technischen Universität München zur Erlangung des akademischen Grades eines

Doktor-Ingenieurs (Dr.-Ing.)

genehmigten Dissertation.

Vorsitzender:		Prof. Dr.-Ing. Ulrich Wagner
Prüfer der Dissertation:	1.	Prof. Dr.-Ing. Andreas Jossen
	2.	Prof. Dr.-Ing. Kai Peter Birke

Die Dissertation wurde am 09.03.2020 bei der Technischen Universität München eingereicht und durch die Fakultät für Elektrotechnik und Informationstechnik am 29.06.2020 angenommen.

Vorwort und Danksagung

An erster Stelle möchte ich mich bei Herrn Professor Dr.-Ing. Andreas Jossen für die Möglichkeit der Promotion bedanken. Sie haben meine Arbeit stets begleitet und hatten zu jeder Zeit ein offenes Ohr für fachliche Diskussionen. Weiterer Dank geht auch an Herrn Professor Dr.-Ing. Kai Peter Birke für die Übernahme des Koreferats und Herrn Professor Dr.-Ing. Ulrich Wagner für die Leitung der mündlichen Prüfung.

Meine Arbeit war begleitet von einer guten Zusammenarbeit mit den Kollegen am Lehrstuhl für Elektrische Energiespeichertechnik. Hervorheben möchte ich das Team Batteriesystemtechnik. Von Philipp Berg, Elisabeth Gillich, Marco Steinhardt und Philipp Jocher erhielt ich in zahlreichen Diskussionen meiner Ideen konstruktive und interessante Anmerkungen. Daneben war für mich die technische Unterstützung von Korbinian Schmitt und Jens Dietrich sehr hilfreich. Der Austausch von Daten und Geräten sowie anregende Diskussionen mit Peter Keil war ebenso gewinnbringend. Ein herzliches Dankeschön an alle.

Besonderer Dank gilt Martin Brand, durch den ich an den Lehrstuhl gekommen bin. Auf die gemeinsame Arbeit zu Beginn meiner Promotion konnte ich aufbauen und das Thema meiner Forschung finden.

Weiterhin danke ich allen Studenten, die von mir betreut wurden und die mit Ihrer Arbeit einen wichtigen Teil zum Gelingen dieser Promotion beigetragen haben.

Abschließend möchte ich meinen Eltern Sonja und Walter, meinem Bruder Thomas und vor allem meiner Frau Julia für ihre Unterstützung in allen Situationen danken.

München, 2020 Markus H. Hofmann

Kurzfassung

Fortschritte in der Lithium-Ionen-Batterietechnik erschließen neue Anwendungsfelder. Heute liefern sie die Energie für Autos, Schiffe, Züge und dienen dem Energieversorgungsnetz als Pufferspeicher. Für diese Anwendungen sind hunderte bis tausende Zellen nötig, die parallel und seriell verschaltet sind. Der Strom in den Parallelschaltungen teilt sich in Abhängigkeit der System- und Zellparameter auf. Diese Aufteilung ist nur homogen, wenn alle Parameter exakt gleich sind, was in der Realität nie der Fall ist. Die folglich in der Praxis asymmetrische Stromaufteilung kann zu einer asymmetrischen Alterung oder zu einer sicherheitskritischen Überlastung einzelner Zellen führen.

Diese Studie analysiert die Stromaufteilung in Parallelschaltungen aufgrund zellinterner Einflussfaktoren simulativ und messtechnisch. Ein Zustandsraummodell, basierend auf einem Ersatzschaltbild berechnet die Stromaufteilung. Das Modell ist mit Parametern von fünf verschiedenen Typen von kommerziell erhältlichen Rundzellen unterschiedlicher Zellchemie bedatet. Es simuliert Zellspannungen und berechnet daraus die Stromaufteilung. Beides ist anhand von Messdaten validiert. Zusätzlich liefert ein Messaufbau Zellstrommesswerte von zwei parallel verschalteten und einzeln temperierten Batteriezellen. Der Aufbau minimiert Einflüsse der Messtechnik auf die Stromverteilung. Anhand von weiteren Messungen der Stromaufteilung an einem Batteriespeicher mit 1440 Zellen konnte gezeigt werden, dass eine Skalierung der Messergebenisse von Zell- auf Systemebene möglich ist.

Eine asymmetrische Stromaufteilung wird durch Spannungsunterschiede in den Zellen erzeugt. Für die Zellspannung ist die Gleichgewichtsspannung und der Spannungsabfall an der Impedanz der Zelle verantwortlich. Zudem nehmen die Hysterese der Gleichgewichtsspannung und die Entropie Einfluss auf die Klemmenspannung der Zelle. Es zeigt sich, dass Temperaturdifferenzen zwischen den Zellen und damit verursachte Impedanzunterschiede zu den wichtigsten Einflussfaktoren auf die Stromverteilung gehören. Die Temperaturabhängigkeit der Zellimpedanz ist somit eine entscheidende Größe, die über die Stromaufteilung entscheidet. An Zellen mit flacher Ruhespannungskennlinie können Hysterese und Entropie zu Ladezustandsunterschieden im zweistelligen Prozentbereich führen.

Eine messtechnische Analyse mit einem realitätsnahen Lastprofil identifiziert kritische Betriebszustände. Vor allem bei Stromsprüngen kommt es zu einer stark asymmetrischen Stromaufteilung. Auch der absolute Ladungsumsatz steigt durch Ausgleichsströme abhängig vom Lastprofil bis zu 14 %. Weiterhin beeinflusst die Nichtlinearität der Ruhespannung die Stromaufteilung. Beim Ladevorgang zweier parallel geschalteter Zellen mit flacher Ruhespannungskennlinie, die unterschiedlich temperiert sind, übernimmt die kältere Zelle am Ende des Ladevorgangs den größten Anteil des Gesamtstroms. Ein Alterungsexperiment beweist, dass diese Stromüberhöhung zu beschleunigter Alterung durch Lithium Plating führt. Um negative Auswirkungen durch die asymmetrische Stromaufteilung zu verhindern, kann auf der Zell und Systemebene auf Homogenität der Parameter geachtet werden. Kritische Situationen, wie

die Effekte einer nichtlinearen Ruhespannungskennlinie, können mittels Steuerung des Lastprofils abgefangen werden. Die Ergebnisse dieser Arbeit dienen der Entwicklung von intelligenten und zellschonenden Schnellladestrategien.

Abstract

Progress in lithium-ion technology has opened new fields for its application. Today, lithium-ion battery cells power cars, ships, and trains as well as support the grid as buffer storage. For these applications, hundreds to thousands of cells in parallel and series connection are necessary. The load in parallel connections is split depending on the parameters of the system and cells. A symmetric distribution only occurs when all values are identical, which is never the case in reality. Asymmetry can lead to inhomogeneous ageing or generate safety issues caused by cell overload.

This study investigated the current distribution in parallel connections caused by internal cell parameters by means of simulation and measurement. A state-space model based on an electrical equivalent circuit was used to calculate the current distribution. The model was parametrised with data from five types of commercial cells of different cell chemistry. The model simulated the cell voltages and calculated the current distribution; both results were validated with measured data individually. Furthermore, a measuring setup was used to acquire the cell currents of a parallel connection of two individually tempered cells. The design of the test bench minimised the influences of the shunts on the distribution and prevented back couplings. Additional measurements of a large storage of 1440 cells confirmed the scalability of the results in terms of current distribution.

Asymmetric current comes from voltage differences in the cells. Cell voltage consists of the equilibrium voltage and the voltage drop at the internal impedance. Furthermore, the hysteresis of the equilibrium voltage and entropy influence the potential. Temperature differences—and with them impedance differences—are some of the most crucial drivers of asymmetric current distribution. The temperature dependence of the impedance of cells plays a vital role in the current distribution. In cells with flat open-circuit voltage, hysteresis and entropy can lead to differences in the state of charge in a double-digit percentage range.

Finally, measurements were made to analyse critical states using a realistic load profile. Strong asymmetry appeared especially at steps of the total current. Furthermore, the total charge throughput increased. A simple constant current discharge followed by a relaxation phase led to a 14 % increase because of equalisation currents after the load phase. Moreover, the nonlinearity of the open-circuit voltage influenced the current distribution. At the end of the charging process of two parallel-connected cells with a temperature difference, the cold cell took the major part of the current. This led to accelerated ageing caused by lithium plating. An ageing experiment was used to confirm this hypothesis. To prevent asymmetric current distribution, it is a good idea to consider homogeneity in the system and cell design. Critical effects such as those of nonlinear open-circuit voltages can be eliminated by controlling the load profile. Therefore, the results of this work can help to develop intelligent and gentle fast charging strategies for lithium-ion batteries.

List of publications

Selection of conference contributions

M. H. Hofmann, B. Einhauser, M. Steffan, A. Jossen: Asymmetric current distribution within parallel-connected battery cells and its influencing factors. AABC 2019 (Poster)

A. Jossen F. B. Spingler, **M. H. Hofmann**, J. Wilhelm, I. Zilberman, Y. Wu: The Influence of the Entropic Effect on Battery Performance. AABC Europe, 2019 (Oral Presentation)

M. H. Hofmann, M. Steinhardt, M. Y. Kuhn, A. Jossen: Current distribution in hybrid battery systems loaded with a dynamic drive cycle, MSE Colloquium 2017, 2017 (Poster)

M. H. Hofmann, M. Winkler, M. J. Brand, S. Behne, A. Jossen: pAgeing - Ageing of Lithium-Ion Batteries in Parallel Connection, Advanced Battery Power 2017, 2017 (Oral Presentation)

M. Steinhardt, D. Jöst, G. M. Reuther, R. Pufall, **M. H. Hofmann**, T. Zimmermann, M. F. Horsche, D. U. Sauer, A. Jossen: Benchmark of Battery Storage Topologies in Cost, Efficiency and Safety, Advanced Battery Power 2017, 2017 (Poster)

M. Steinhardt, **M. H. Hofmann**, T. Zimmermann, M. F. Horsche, A. Jossen: Efficiency Analysis of a Lithium Ion Battery Systems, Batterieforum Deutschland 2017, 2017 (Poster)

M. H. Hofmann, M. Steinhardt, M. J. Brand, S. F. Schuster, A. Jossen: Effects of compensating Current in the parallel Connection of Battery Cells, EVS29 - The 29th International Electric Vehicle Symposium, 2016, 2016 (Oral Presentation)

M. H. Hofmann, M. J. Brand, M. Steinhardt, S. F. Schuster, A. Jossen: Measurement and simulation of the current distribution within parallel connected battery cells, Advanced Battery Power 2016, 2016 (Oral Presentation)

M. H. Hofmann, M. J. Brand, M. Steinhardt, M. F. Horsche, T. Zimmermann, A. Jossen: DriveBattery2015 - Untersuchungen an vielzelligen und modularen Batteriesystemen, Batterieforum Deutschland 2016, 2016 (Poster)

M. F. Horsche, **M. H. Hofmann**, T. Zimmermann, A. Jossen: DriveBattery2015 - Intelligente Steuerungs- und Verschaltungskonzepte für modulare Elektrofahrzeuge-Batteriesysteme, Batterieforum Deutschland 2015, 2015 (Poster)

Scientific reports

T. Zimmermann, **M. H. Hofmann**, M. Steinhardt, G. Rahn-Koltermann, A. Jossen: Intelligente Steuerungs- und Verschaltungskonzepte für modulare Elektrofahrzeug-Batteriesysteme zur Steigerung der Effizienz und Sicherheit sowie zur Senkung der Systemkosten – Abschlussbericht des Verbundvorhabens: DriveBattery2015 Phase 2, 2017

M. H. Hofmann, M. F. Horsche, T. Zimmermann, A. Jossen: Intelligente Steuerungs- und Verschaltungskonzepte für modulare Elektrofahrzeug-Batteriesysteme zur Steigerung der Effizienz und Sicherheit sowie zur Senkung der Systemkosten – Abschlussbericht des Verbundvorhabens: DriveBattery2015 Phase 1, 2015

Journal contributions

M. Steinhardt, M. J. Brand, **M. H. Hofmann**, S. F. Schuster, A. Jossen: Den Füllstand genau bestimmen. Stommessung einzelner Batteriezellen., E&E - Faszination Elektronik, 2017

M. Steinhardt, M. J. Brand, **M. H. Hofmann**, S. F. Schuster, A. Jossen: Hochpräzise Strommessung in parallel verschalteten Batteriezellen unter dynamischer Belastung, in: R. Jamal (Ed.), R. Heinze (Hrsg.), Virtuelle Instrumente in der Praxis 2016, VDE Verlag, Berlin, Germany, 2016, ISBN 978-3-8007-4208-0

M. H. Hofmann, M. Steinhardt, M. J. Brand, S. F. Schuster, A. Jossen: Effects of compensating Current in the parallel Connection of Battery Cells, World Electric Vehicle Journal Volume 8 - The 29th International Electric Vehicle Symposium 2016

M. J. Brand, P. Keil, **M. H. Hofmann**, A. Jossen: Hochdynamische Messung des Innenwiderstands von Batteriezellen. Virtuelle Instrumente in der Praxis, in: R. Jamal (Ed.), Virtuelle Instrumente in der Praxis 2014, VDE Verlag, Berlin, Germany, 2014, ISBN 978-3-8007-3572-3

Peer-reviewed journal contributions [1]

M. J. Brand, **M. H. Hofmann**, M. Steinhardt, S. F. Schuster, A. Jossen: Current distribution within parallel-connected battery cells., Journal of Power Sources (334), 2016, 202-212

T. Zimmermann, P. Keil, **M. H. Hofmann**, M. F. Horsche, S. Pichlmaier, A. Jossen: Review of system topologies for hybrid electrical energy storage systems., Journal of Energy Storage 8, 2016

M. H. Hofmann, K. Czyrka, M. J. Brand, M. Steinhardt, A. Noel, F. B. Spingler, A. Jossen: Dynamics of current distribution within battery cells connected in parallel., Journal of Energy Storage (20), 2018, 120-133

M. J. Brand, **M. H. Hofmann**, S. F. Schuster, P. Keil, A. Jossen: The Influence of Current Ripples on the Lifetime of Lithium-Ion Batteries., IEEE Transactions on Vehicular Technology Volume: 67 Issue: 11, 2018

---

[1] Self-produced sections of publications are partially contained in this doctoral thesis without any further reference in the text.

Content

Abbreviations

ADC	analogue-to-digital converter
BEV	battery electric vehicle
BMS	battery management system
CC	constant current
CPE	constant phase element
CT	charge transfer
CTS	BaSyTec Cell Test System
CV	constant voltage
DAQ	data acquisition
DLC	double-layer capacitor
DoD	depth of discharge
DVA	differential voltage analyses
EDLC	electric double layer capacitances
EEBatt	part of the cell naming
EEC	equivalent electrical circuit
EFC	equivalent full cycles
EIS	electrochemical impedance spectroscopy
EV	electric vehicle
HE	high energy
HEV	hybrid electric vehicle
HP	high power
LAM$_{NE}$	loss of active material at the negative electrode (anode)
LAM$_{PE}$	loss of active material at the positive electrode (cathode)
LCO	lithium cobalt oxide
LFP	lithium iron phosphate
LG_HB2	battery cell type: ICR18650 HB2 from LG Chem Ltd.
LG_MJ1	battery cell type: INR18650 MJ1 from LG Chem Ltd.
Li-S	lithium–sulphur
LLI	loss of lithium inventory
LMO	lithium manganese oxide
LNO	lithium nickel oxide
MHH	part of the cell naming
NCA	lithium nickel cobalt aluminium oxide
NiMH	nickel–metal hydride
NiZn	nickel–zinc
NMC	lithium nickel cobalt manganese oxide
OCV	open-circuit voltage
OEM	original equipment manufacturer
Pan_PF	battery cell type: NCR18650 PF from Panasonic Corporation
PCM	physicochemical model

PHEV	plug-in hybrid electric vehicle
PI	proportional-integral controller
PV	photovoltaic
RC	resistor-capacitor
RL	resistor-inductor
RMS	root mean square
RQ	research question
Sam_25R	battery cell type: INR18650-25R from Samsung SDI Co., Ltd.
SEI	solid electrolyte interface
SoC	state of charge
SoH	state of health
Sony_FT	battery cell type: US26650 FT from Sony Corporation
WB	Warburg element
XsYp	connection of X cells in series and Y cells in parallel
ZARC	Z-Arch, impedance and arch element

Nomenclature

Symbols

a	state of charge step at the analysis of the open-circuit voltage nonlinearity using a hyperbolic tangent function in %
A <conductivity>	area in m²
A <optimisation>	matrix of the MATLAB 'fmincon' optimisation, unitless
A <state space model>	system matrix of the state space model in s^{-1}
Aeq	matrix of the MATLAB 'fmincon' optimisation, unitless
B	input matrix of the state space model in F^{-1}
b <open-circuit voltage nonlinearity>	slope of the open-circuit voltage nonlinearity at the analysis of the open-circuit voltage nonlinearity using a hyperbolic tangent function, unitless
b <optimisation>	vector of the MATLAB 'fmincon' optimisation, unitless
beq	vector of the MATLAB 'fmincon' optimisation, unitless
C <capacitance>	capacitance of a capacitor in F
C <cell capacity>	cell capacity in Ah
c <Fick's law>	concentration in mol·m^{-3}
c <open-circuit nonlinearity>	voltage step at the analysis of the open-circuit voltage nonlinearity using a hyperbolic tangent function in V
c <optimisation>	function of the MATLAB 'fmincon' optimisation, unitless
c <state space model>	output vector of the state space model, unitless
D	diffusion coefficient in m²·s^{-1}
d <Preisach model>	state of charge difference since the last change of state of charge direction at the hysteresis calculation with the Preisach model, unitless
d <state space model>	feedforward vector of the state space model in Ω
DoD	depth of discharge in %
e	error of measurement respectively simulation in V
E <energy>	energy in Ws
E <state space model>	resistor matrix of the state space model
f	frequency in s^{-1}
F	resistor matrix of the state space model
G	Gibbs free energy in J
h	number of simulation steps, unitless
H	enthalpy in J

I, i	electric current in A
J	diffusion flux in $mol \cdot m^{-2} \cdot s^{-1}$
l	length in m
L	inductance of an inductor in H
lb	lower bound of the MATLAB 'fmincon' optimisation, unitless
m	slope of the open-circuit voltage over the state of charge in V
nb	number of data points, unitless
OVC	open-circuit voltage in V
Ox	chemical activity of the oxidised form in the Nernst equation, unitless
p	parallel, unitless
Q	charge in C
R	ohmic resistance in Ω
Red	chemical activity of the reduced form in the Nernst equation, unitless
S	entropy in $J \cdot K^{-1}$
s \<battery system configuration\>	serial, unitless
s \<Laplace transform\>	Laplace operator
SoC	state of charge in %
SoH	state of health in %
t	time in s
T \<cycle duration\>	cycle duration in s
T \<state space model\>	unit vector of the state space model, unitless
T \<temperature\>	temperature in °C
u \<state space model\>	input of the system state space model in A
U, u	voltage in V
ub	upper bound of the MATLAB 'fmincon' optimisation, unitless
w	weighing factor of the hysteresis depending on the state of charge, unitless
x \<Fick's law\>	position in m
x \<optimisation\>	input of the MATLAB 'fmincon' optimisation, unitless
x \<state space model\>	state vector of the state space model in V
x \<stoichiometry\>	stoichiometry of the negative electrode, unitless
y \<Preisach model\>	hysteresis output of the Preisach model in V
y \<state space model\>	open-circuit voltage vector of the state space model in V
y \<stoichiometry\>	stoichiometry of the positive electrode, unitless
$\underline{Z}$	impedance in Ω
α	threshold of the hysteresis calculation with the Preisach model, unitless
β	threshold of the hysteresis calculation with the Preisach model, unitless

γ <analysis of parameter variation>	relative parameter differences at the analysis of parameter variation in %
γ <Preisach model>	hysterons at the hysteresis calculation with the Preisach model, unitless
ε	normalised resistance variation in %·K^{-1}
μ <mean value>	mean value
μ <Preisach model>	Preisach density of the hysteresis calculation with the Preisach model, unitless
ξ	parameter of a constant phase or a Z-Arch element that defines the downward shift of the half-circle, unitless
ρ	electrical conductivity in S·m^{-1}
σ	standard deviation, unitless
τ	time constant in s
ω	angular frequency in s^{-1}

Indices

0	at starting conditions
1..K	number of the cell in a parallel connection of cells
1..N	number of resistor-capacitor element in a series connection of resistor-capacitor elements
10 °C	at a temperature of 10 °C
25 °C	at a temperature of 25 °C
act	actual
Ah	regarding capacity
Anode	anode
c	cut-off
C	of a capacitance
C/100	at a c-rate of C/100
Cathode	cathode
CC	constant current
cell(s)	regarding cells
coeff	coefficient of the state space model
connection	of a connection
CPE	of a constant phase element
CT	charge transfer
CV	constant voltage
Diffusion	diffusion
EDLC	electric double layer capacitance
end	at ending conditions
entropy	entropy
FullCell	full cell
HE	high energy

HP	high power
hysteresis	hysteresis
i	control variable
Im{$\underline{Z}$(fc)}(B1)	regarding the imaginary part of the impedance at cut-off frequency of the charge B1 in the paper of Rumpf et al.
junction	of a junction
k	index resistor-capacitor elements of a cell connected in series
L	of an inductance
LFP	regarding lithium iron phosphate cathode material
lin	linear
log	logarithmic
loss	losses
m	measured
max	maximum
min	minimum
n	index parallel connection
NCA	regarding nickel cobalt aluminium oxide cathode material
neg	regarding the anode
NMC	regarding nickel manganese cobalt oxide cathode material
OC	open-circuit
OC_S	open-circuit at standard conditions
OCV	open-circuit voltage
OV	overvoltage
p	(index) parallel
phase	regarding a certain phase of the measurement
pos	regarding the cathode
pulse	pulse
R	of a resistor
R_AC_1000Hz(B1)	regarding alternating current resistance at 1000 Hz of the charge B1 in the paper of Rumpf et al.
RC	of a resistor-capacitor
Re{$\underline{Z}$(fc)}(B1)	regarding the real part of the impedance at cut-off frequency of the charge B1 in the paper of Rumpf et al.
rel	relative
RL	of a resistor inductor
RMS	root mean square
s	series connection
sim	simulated
sine	sinus
skin	skin effect
step	step

T	temperature
Term	at the terminals
tot	total
W	ionic impedance parameter
WB	of a Warburg element
wire	of a wire
z	number of electrons transferred in the Nernst equation
Z	regarding impedance
ZARC	of a Z-Arch element
Ω	ohmic

Constants

e	Euler's number, unitless
F	Faraday constant in $C \cdot mol^{-1}$
j	complex symbol note
R	universal gas constant in $kg \cdot m^2 \cdot s^{-2} \cdot mol^{-1} \cdot K^{-1}$

1 Introduction

Lithium-ion technology had its breakthrough in consumer electronic devices and information technology [1]. The first commercial application of lithium-ion battery cells was the Sony CCD-TR1 8 mm camcorder in 1991 [1]. The developer used a series connection of two cells with a capacity of 1.2 Ah each [2]. To date, most smartphones and consumer electronic devices employ a single-digit number of cells for power. Power tools have a higher power and energy requirement [3]; therefore, more battery cells are connected. Normally these devices require a single- to double-digit number of cells to power them.

With the transformation toward a low-carbon future, the demand for large energy storage systems grows [4, 5]. In the automotive sector, hybrid electric vehicles (HEVs), plug-in HEVs (PHEVs), and battery electric vehicles (BEVs) powered with lithium-ion batteries have up to several thousands of cells [6]. In other applications such as buses, trucks, and ferries, the energy and power demands are even higher.

In the field of stationary storage systems, a new market has grown within the last years. Lithium-ion storage systems appear in different sizes. Home energy storage systems collect energy from photovoltaic (PV) panels during the day and power homes at night. Community storage systems such as Energy Neighbor can buffer the power peak of the power grid [7]. This battery storage system consists of almost 20,000 cylindrical lithium-ion cells [7]. Storage plants such as the 129 MWh battery storage system built by Tesla Inc. in Australia are even larger. Supposing they use 60 Ah cells with a nominal voltage of 3.65 V, then more than 0.5 million cells would be necessary to reach the storage capacity [8].

1.1 Motivation

The abovementioned examples demonstrate that the number of cells in lithium-ion battery storage systems is increasing. Figure 1.1 illustrates this increase with the help of different applications over time.

In addition, the size of cells has grown. The first commercial Sony cells in the CCD-TR1 8 mm camcorder from 1991 had a capacity of 1.2 Ah [2]. In 2018, several cell producers offer cells with a capacity larger than 50 Ah. Today, it is unclear whether it is better to use small or big cells to build large storage systems [13]. Tesla, for example, employs small cylindrical cells in 18650 or 21700 formats [14]. Most other automotive original equipment manufacturers (OEMs) use pouch or prismatic cells with capacities exceeding 20 Ah. Regardless, the number of cells in battery systems has grown much more than the capacity of single cells. This is why the

connection of battery cells is essential for providing power for applications such as cars and grid storage systems.
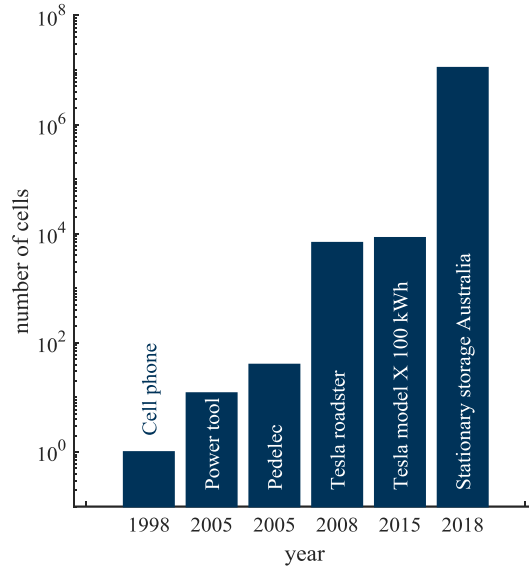
Figure 1.1: *Number of cells in different applications on a logarithmic scale (data from [1, 8–12])*

To fulfil the needs of energy and power, battery cells can be connected in series, in parallel, or in a combination of series and parallel connections. It is common to use an acronym for series and parallel connections. For example, $5s3p$ describes a battery system with five cells connected in series and three cells connected in parallel. This system consists of $5 \cdot 3 = 15$ cells. A purely series connection of five cells is denoted by $5s$ and a purely parallel connection of three cells is denoted by $3p$. Series connections increase the voltage of a system. The total voltage U_{tot} of s cells connected in series can be calculated by the sum of all cell voltages U_i. When the cell capacities are similar $C_1 = C_2 = \cdots = C_s$, the total capacity C_{tot} remains unchanged and is similar to the cell capacities $C_1, C_2 \ldots C_s$. All cells have similar currents of the total current I_{tot} and the cell currents $I_1, I_2 \ldots I_s$:

$$U_{tot} = \sum_{i=1}^{s} U_i \tag{1.1}$$

$$I_{tot} = I_1 = I_2 = \cdots = I_s \tag{1.2}$$

$$C_{tot} = C_1 = C_2 = \cdots = C_s \tag{1.3}$$

A higher system voltage leads to a higher power at a constant current. A series connection of battery cells keeps the current low but increases the voltage.

By contrast, a parallel connection of battery cells is used to increase the total capacity C_{tot} in case of similar cell parameters. The following equations apply to parallel connections:

$$U_{tot} = U_1 = U_2 = \cdots = U_p \tag{1.4}$$

$$I_{tot} = \sum_{i=1}^{p} I_i \tag{1.5}$$

$$C_{tot} = \sum_{i=1}^{p} C_i \quad \text{(at symmetric usage)} \tag{1.6}$$

Power electronics are limited at certain voltage limits [15]. A higher voltage means higher costs of the power electronics and a larger effort on isolation [16]. This is a particularly strong limitation in automotive and consumer products. In automotive applications, higher voltages also increase the need for electrical isolation in the electric machines. This reduces the efficiency of such machines because the space for the isolation material reduces the slot fill factor in the motor [17]. Because of this limitation, parallel connections are often combined with series connections.

The 2017 BMW i3 model uses no parallel connections at all. Its battery system consists of 96 cells connected in series, each with a capacity of 94 Ah [18]. Nissan's Leaf features two parallel cells [19]. In the automotive field, Tesla uses the largest number of cells connected in parallel; its Model S uses up to 86 parallel cells. In the field of stationary storage, many manufacturers build systems with a large number of small cells connected in parallel.

A parallel connection of battery cells is related to a current divider. The impedance in the branches influences the current distribution. During the design phase of a battery system, the current distribution in a parallel connection can be estimated homogenously as a first approximation, because normally the cells are of the same type and age. In this ideal case, all cells charge and discharge with similar currents. To reach such a homogeneous current distribution, not only must the impedances of all parallel-connected cells be the same but also all impedances of the electrical wiring and junctions. This is not the case in real-world battery systems. Rumpf et al. analysed the cell-to-cell variation of brand-new lithium-ion battery cells and measured coefficients of variation of approximately 0.3 % in capacity and 1.3 % in impedance [20]. Furthermore, it is obvious that different cable lengths with similar wire cross-sections that connect cells have different resistances.

In the field of batteries, degradation associated with worsening cell parameters is a critical problem [21]. This means that the ageing of batteries will also influence current distribution. Baumhöfer et al. showed that the spread of cell parameters becomes larger with the service life of batteries [22]. This allows the assumption that inhomogeneity in terms of current distribution will worsen during the lifetime of a battery. However, the impedance parameters of battery cells do not only depend on ageing but also on temperature and the state of charge (SoC) [23].

Furthermore, comparing a parallel connection of batteries with a current divider is not entirely convenient. A battery includes a voltage source, which also depends on other parameters such as SoC and temperature [23]. Its voltage is also influenced by the history of usage. Researchers such as Dreyer et al. have analysed the hysteresis behaviour of lithium-ion battery cells [24].

According to this number of influencing factors, a homogenous current distribution in parallel-connected battery cells is unlikely. In relevant literature, studies have shown asymmetric current distributions, such as Brand et al. [25] and Bruen et al. [19]. A systematic investigation of the drivers of current distribution is still missing. Because charge throughput, current

height, and temperature can increase ageing [26] or lead to unsafe situations [27], the harmful impact of asymmetric current distribution and its countermeasures are also critical.

1.2 Research questions and limitations

The aim of this thesis is to analyse current distribution, including its drivers and impacts. The following research questions (RQs)) are answered:

+ RQ 1: What are the influencing factors of current distribution in parallel-connected lithium-ion battery cells?
+ RQ 2: What are the impacts of asymmetric current distribution and how do they lead to unsafe situations or accelerated ageing?
+ RQ 3: Which countermeasures can prevent these effects?

The measurements and simulations for this thesis were performed on commercial cylindrical lithium-ion battery cells in the 18650 and 26650 formats. The cells differed in their cathode material: two cells had lithium nickel cobalt manganese oxide (NMC, $LiNiCoMnO_2$), two had lithium nickel cobalt aluminium oxide (NCA, $LiNiCoAlO_2$), and one had lithium iron phosphate (LFP, $LiFeO_4$) cathode materials. Two were designed as high power (HP), one as high energy (HE), and two as an intermediate type. This work focused on the influencing factors coming from the cell and not on those coming from the system design. The results can help to build better battery systems consisting of cells connected in parallel. The cells were only used within their specifications from the datasheets.

1.3 Structure of this thesis

This work addresses effects that have not yet been analysed. It shows the effects of parameter differences on linear and time-dependent impedances. The parameter variations were based on real-world effects. Parameter differences came from cell to cell variations of new cells analysed by Rumpf et al. [20]. Furthermore, other influences on the impedance such as the state of health (SoH), SoC, and temperature were investigated. Furthermore, the effects of open-circuit voltage (OCV) nonlinearities are not well known today. Simulations with defined changes in the OCV slope based on a hyperbolic Tangent function were performed and are discussed in this work. Because the OCV slope affects the current distribution, a simulation with a nonlinear OCV was performed. Another focus were the effects of hysteresis and entropy on current distribution. A variation of HP and HE cell dimensioning with a certain parameter difference was analysed. The rate of equalisation depends on the cell parameters of impedance and capacity [25]. This means that HP and HE cells are influenced differently by parameter variations [28].

The study conducted for this thesis analysed and compared the influencing factors of current distribution in parallel battery cells theoretically and through measurements. Figure 1.2 presents the structure of this thesis. Chapter 1 provides an introduction and clarifies the motivation behind the analyses. Chapter 2 presents the fundamentals, starting with the basics of lith-

ium-ion cells before continuing to discuss the modelling of batteries and the parameters necessary for the simulations. Furthermore, the chapter presents a discussion of literature that has focused on the calculation or measurement of current distribution in parallel-connected batteries, particularly those in battery cells. In the last part of the chapter, the analytical calculation approach is detailed.
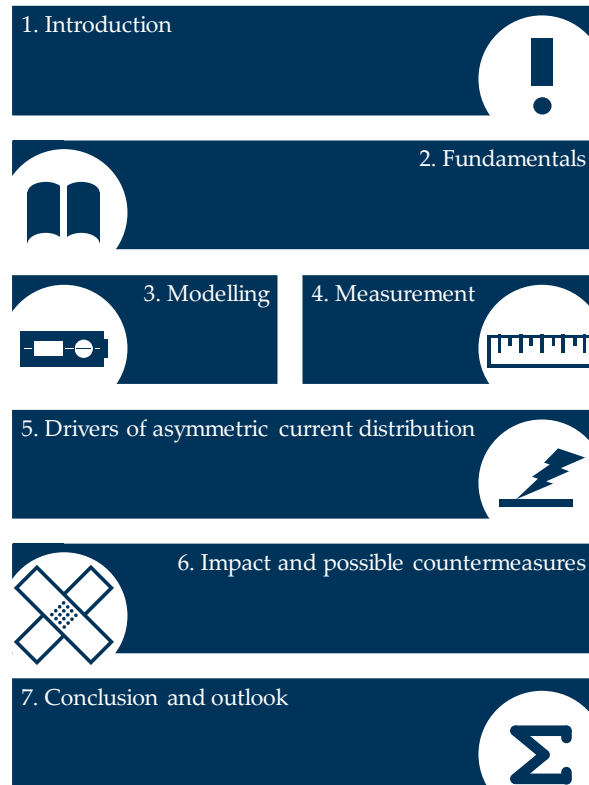
Figure 1.2:   Structure of this thesis

Chapters 3 and 4 are concerned with the methods used to analyse an asymmetric current distribution. Chapter 3 focuses on modelling, including the structure of the model. Furthermore, the chapter presents and discusses the methods used to generate the model parameters. At the end of Chapter 3, the results of the simulations are verified with measured data. Chapter 4 explains the required measurement technique that acquires the cell current without influencing the current distribution. Furthermore, it describes an ageing experiment that analysed the risk of lithium plating in parallel connections.

In Chapter 5, these instruments are used to perform a detailed analysis of the drivers of asymmetric current distribution. An overview of the possible influence gives access to variation options. Subsequently, overvoltage, entropy, hysteresis, and SoC are discussed separately.

Chapter 6 focuses on the impact of asymmetric current distribution, which can harm batteries or lead to unsafe situations. Therefore, measured data that represent the typical operation of battery systems are analysed. A temperature difference of 15 °C gives the necessary asym-

metry. Moreover, discrepancies between different electrode chemistries are analysed. The results of the ageing experiment confirm the risk of accelerated ageing in parallel connections. Finally, countermeasures are given to prevent plating and other risks through system design or operation strategy. Chapter 7 concludes with all the results and presents an outlook on the application relevance and further research requirements.

2 Fundamentals of the current distribution

This chapter gives an overview of the state of the art in lithium-ion battery cells as well as their modelling. These are the basics for the analysis of current distribution. Furthermore, ageing influences and is influenced by current asymmetry. Therefore, ageing fundamentals are explained in this chapter. The statements focus on the knowledge on current distribution in the relevant literature.

2.1 Structure of lithium-ion battery cells

Battery systems are used to supply electrical power to electric devices, vehicles, or the national grid. The supplied power can also be negative, and energy can be stored. The devices connected to batteries are electrical sources, sinks, or in most cases both. Figure 2.1 illustrates the processes in a lithium-ion cell schematically. It consists of two electrodes—an anode and a cathode. The purpose of the separator is to divide the electrodes. All parts of the cell except the current collectors are soaked with electrolytes. The separator is permeable and wetted with electrolyte. The electrolyte allows the flow of lithium ions. Because the electrodes are connected to electrically conductive current collectors made of copper and aluminium, an attached sink can discharge, or an attached source can charge a battery cell.
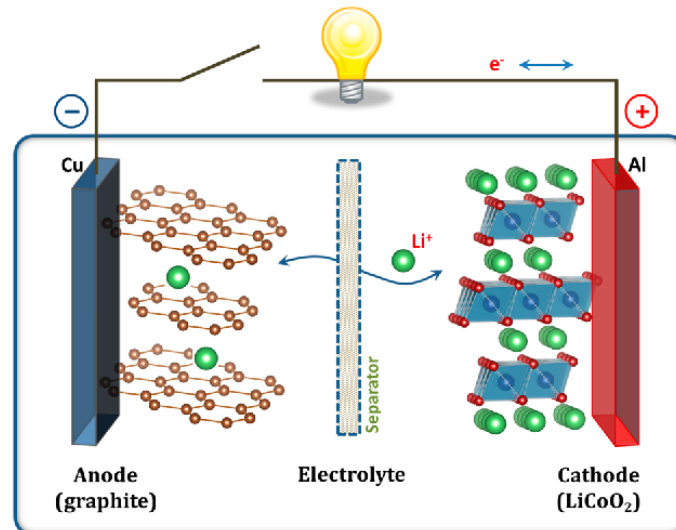
Figure 2.1:   *Schematic representation of a lithium-ion battery cell [29]*

At the anode, oxidation occurs in the case of discharge. The use of porous carbon materials as the negative electrode (anode) is common [3]. These materials are cheap and have a low potential of approximately 0.1 V versus Li/Li+ of $Li_{0.5}C_6$ [3]. Carbon can store and retrieve lithium atoms with an effect on its geometric size below 7 % [30].

Alternatively, using a lithium metal anode is possible. This would provide a higher specific capacity of 3.86 Ah/g compared with graphite (0.372 Ah/g) and lower potential of 0 V versus Li/Li+ [3]. Because lithium metal anodes show a short lifetime and forms dendrites, which can break through the separator and short the cell, lithium metal anodes are rarely used in lithium-ion cells [31].

At the graphite anode, the following electrochemical reaction occurs:

$$C_6 + x Li^+ + x e^- \rightleftharpoons Li_x C_6 \qquad (2.1)$$

At the metal oxide cathode, the following chemical reaction occurs (where M stands for metal):

$$Li_M O_2 \text{-} x Li^+ \text{-} x e^- \rightleftharpoons Li_{1-x} MO_2 \qquad (2.2)$$

The simplified overall electrochemical reaction results in

$$LiC_6 + MO_2 \rightleftharpoons C_6 + LiMO_2 \qquad (2.3)$$

The cathode usually consists of lithiated metal oxide. During discharge, the positive electrode (cathode) is reduced. Common cathode materials are lithium cobalt oxide (LCO, $LiCoO_2$), lithium nickel oxide (LNO, $LiNiO_2$), lithium manganese oxide (LMO, $LiMnO_2$), lithium nickel cobalt manganese oxide (NMC, $LiNiCoMnO_2$), lithium nickel cobalt aluminium oxide (NCA, $LiNiCoAlO_2$), and lithium iron phosphate (LFP, $LiFeO_4$). Figure 2.2 details the certain advantages and disadvantages in energy density, power density, safety, stability, and cost per ampere-hour. NMC or NCA cathodes are used in BEV or PHEV applications because of their stability and energy density. LFP systems are often used in stationary storage systems because they are cheap, and the energy density requirements are low. LCO cells are costly because of the high percentage of cobalt, whereas LMO systems are not stable for long-term use. [32]

material	energy density	power density	safety	stability	costs per Ah
LCO $LiCoO_2$					
NCA $LiNi_{0.80}Co_{0.15}Al_{0.05}O_2$					
NMC $LiNi_{0.33}Mn_{0.33}Co_{0.33}O_2$					
LMO $LiMn_2O_4$					
LFP $LiFePO_4$					

very good ▢ ▨ ▧ ▦ very bad

Figure 2.2: *Comparison of cathode materials regarding energy density, power density, safety stability, and costs per ampere-hour (according to Wohlfahrt-Mehrens [32])*

The separator, electrolyte, and the two current collectors do not participate in the electrochemical reactions in regular operation. The current collectors are thin metal foils. The negative

electrode is usually on copper foil because copper is stable at the potential range of the anode, whereas the positive electrode is on aluminium foil because it is stable in the potential window of the cathode. [33, 34].

The separator isolates the cathode and anode from each other. For safety reasons, the separator must be able to do this in every situation in the operating conditions of the battery. Furthermore, the separator must be permeable to lithium ions and do not impair the ionic flow. [3, 33, 35, 36]

The electrolyte in a lithium-ion battery is usually an organic fluid that allows ionic conduction. Polymer or ceramic solid-state electrolytes are under development [3, 33]. Today, hardly any applications use lithium-ion batteries with a solid electrolyte.

2.2 Characteristics and modelling of lithium-ion battery cells

2.2.1 Open-circuit voltage and capacity

The influence of OCV on the behaviour of lithium-ion battery cells is high because it defines the major part of the cell voltage. For example, in a 1 Ah NMC | graphite cell at a nominal voltage of 3.7 V with an internal impedance of 0.05 Ω, the OCV takes 99 % of the voltage at a discharge of 1 A. The terminal voltage of the battery cell U_{Term} is the sum of the U_{OC} and overvoltage U_{OV}:

$$U_{Term} = U_{OC} + U_{OV} \tag{2.4}$$

$$U_{OV} = U_{\Omega} + U_L + U_{Skin} + U_{CT,EDLC} + U_{Diffusion} \tag{2.5}$$

The overvoltage consists of an ohmic part U_{Ω}, an inductive part U_L, a voltage drop caused by the skin effect U_{Skin}, a voltage drop caused by charge transfer (CT) resistance and electric double layer capacitance (EDLC) $U_{CT,EDLC}$, and the diffusion overvoltage $U_{Diffusion}$. [37]

Figure 2.3 depicts the OCV of cathode and anode materials plotted against their stoichiometry x. The data are from the COMSOL Multiphysics software package [38]. The half-cell OCV of LFP is rather flat compared with the slopes of other OCVs. Through combining two half-cells, the full cell OCV is the voltage difference between the cathode and the anode:

$$U_{OC,FullCell} = U_{OC,Cathode} - U_{OC,Anode} \tag{2.6}$$

Therefore, the stoichiometry and the balancing of the two electrodes define the OCV of the full cell [3]. In a battery, high stoichiometry values at the cathode mean low values at the anode. When a battery is discharged, the OCV of the anode rises and that of the cathode drops [3]. The steep slope of the anode forms the lower SoC limit of the full cell. At high SoCs, the charging process is limited by the cathode and electrolyte. The electrolyte is not stable at upper voltage levels: $U_{OC} > 4.3$ V [39–41].

The capacity of a battery cell C is necessary to calculate the $SoC(t)$ of the battery. Equation (2.7) shows the integration of the cell current i over time t. This charge is divided by the capacity C and added to the SoC at $t = 0$, SoC_0. In this work, all positive currents are charge currents and all negative currents are discharge currents.

$$SoC(t) = SoC_0 + \frac{1}{C} \int i \, dt \qquad (2.7)$$
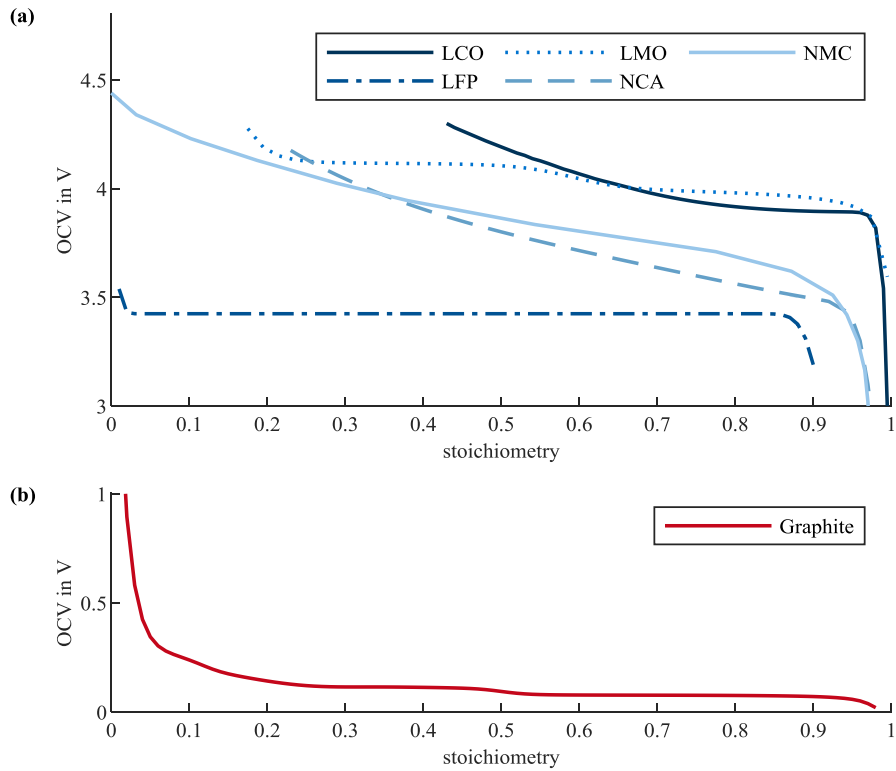
Figure 2.3:   *Half-cell OCV profiles (a) cathode materials, and (b) anode material graphite [38]*

The cell capacity C can be measured by a complete charge (from $SoC = 0$ to $SoC = 1$) or discharge (from $SoC = 1$ to $SoC = 0$) of the cell. Therefore, respecting the voltage limits of the cell is necessary. Because overvoltage exists in the internal resistance, a phase of constant current (CC) is followed by a phase of constant voltage (CV) until the current reaches a certain value. Further parameters can be varied. The norm IEC 62660-1, for example, provides different temperatures and currents to measure the cell capacity [42].

2.2.2   Internal impedance

Batteries are not ideal voltage sources. A battery behaves like a real-world voltage source with internal resistance. This resistance is not solely ohmic; it consists of inductive, ohmic, and capacitive parts [43, 44]. It is an appropriate solution for describing the impedance of lithium-ion battery cells using equivalent electrical circuits (EECs) [23]. Explanations are provided in this subsection and Figure 2.4. Therefore, using an EEC to simulate cell behaviour is suggested. Because high dynamic effects with time constants $\tau < 10^{-4}$ s are not the focus of this work, external inductances and the skin effect are not modelled.

EEC modelling is a common method of calculating the behaviour of batteries. These models must represent the factors that influence the cell voltage. In most cases, the aim is to calculate the voltage at the battery tabs depending on the cell current. Therefore, the models consist of

cell impedance and OCV. The EEC parameters depend on numerous influencing factors; for instance, Nikolian et al. presented a temperature, SoC, and cell chemistry-dependent model [23].

The second part, which creates the cell voltage, is the sum of the overvoltages (compare Equations (2.4) and (2.5)). The effects of different overvoltages and their appearance at different dynamics are explained as follows.

Internal processes occur in the charge and discharge processes of all lithium-ion cells. The upper chart in Figure 2.4 shows these processes and their time constants. The time scale is logarithmic and starts at microseconds and ends at weeks. The internal ohmic resistance has no time constant. It appears instantaneously after a charge or discharge event. The ohmic resistance appears because of the electrical characteristics of the copper and aluminium current collectors and whose geometry, the electrical impedance in the electrodes, electrical contact impedance, and resistance in the liquid phase is where ionic conductivity occurs [45].

Electrical effects cause low time constants. Inductive behaviour results from a pure electrophysical effect caused by the geometry of the current path of a battery cell. Current-carrying conductors are surrounded by a magnetic field. In a lithium-ion battery, the electrons move from one terminal via the current collectors to the first electrode. Between the electrodes, an ionic flow exists through the electrolyte and separator. From the second electrode to the terminal, it is an electron current again; this path is given by the geometry of the cell. The change in current flow di/dt results in an overvoltage u_L. Equation (2.8) shows this correlation together with the inductivity L. An inductor can model the behaviour of the battery cell. [37]

$$u_L = L \cdot \frac{di}{dt}$$

(2.8)

According to the skin effect, the current density of a conductor carrying a high, frequently alternating current is not homogeneous. This behaviour can be observed in lithium-ion cells and was demonstrated by Martin Brand [37]. A resistor-inductor (RL) circuit can represent the skin effect in batteries [37]. Series inductance and the skin effect are no longer relevant in the range of milliseconds; therefore, they were not a focus of this work.

At medium time constants, the solid electrolyte interface (SEI) impacts the current flow. The SEI is a passivating layer, which is formed in the first cycles of battery life on the anode [64]. Lithium ions can pass this layer [33, 64, 65]. Lithium ions diffusing through the SEI passivation layer cause overvoltage. In the Nyquist plot of an electrochemical impedance spectroscopy (EIS) measurement, the SEI creates a half-circle, which means that it behaves like a resistor-capacitor (RC) circuit.

Similar to the SEI, CT resistance and the EDLC form a half-circle in the Nyquist plot of an EIS measurement, which appears between the electrode and electrolyte. In the literature, three explanations are provided to understand the double-layer phenomena: the Helmholtz model [66] published in 1853, the Gouy and Chapman model [67] from 1910, and the model of Stern [68] from 1924. The three models differ in the formation of overvoltage and the variation in

voltage drop from the electrode and electrolyte. The time-dependent behaviour can be modelled using an RC circuit. Some lithium-ion cells produce a Nyquist graph that looks like a compressed half-circle with a larger radius in the real than in the imaginary direction. To improve the simulation in such cases, elements other than an RC circuit are used. Buller described how to use a Z-Arch element (ZARC) to model the charge transfer and EDLC, as well as demonstrated how to approach the ZARC element using a row of five RC elements. [44]
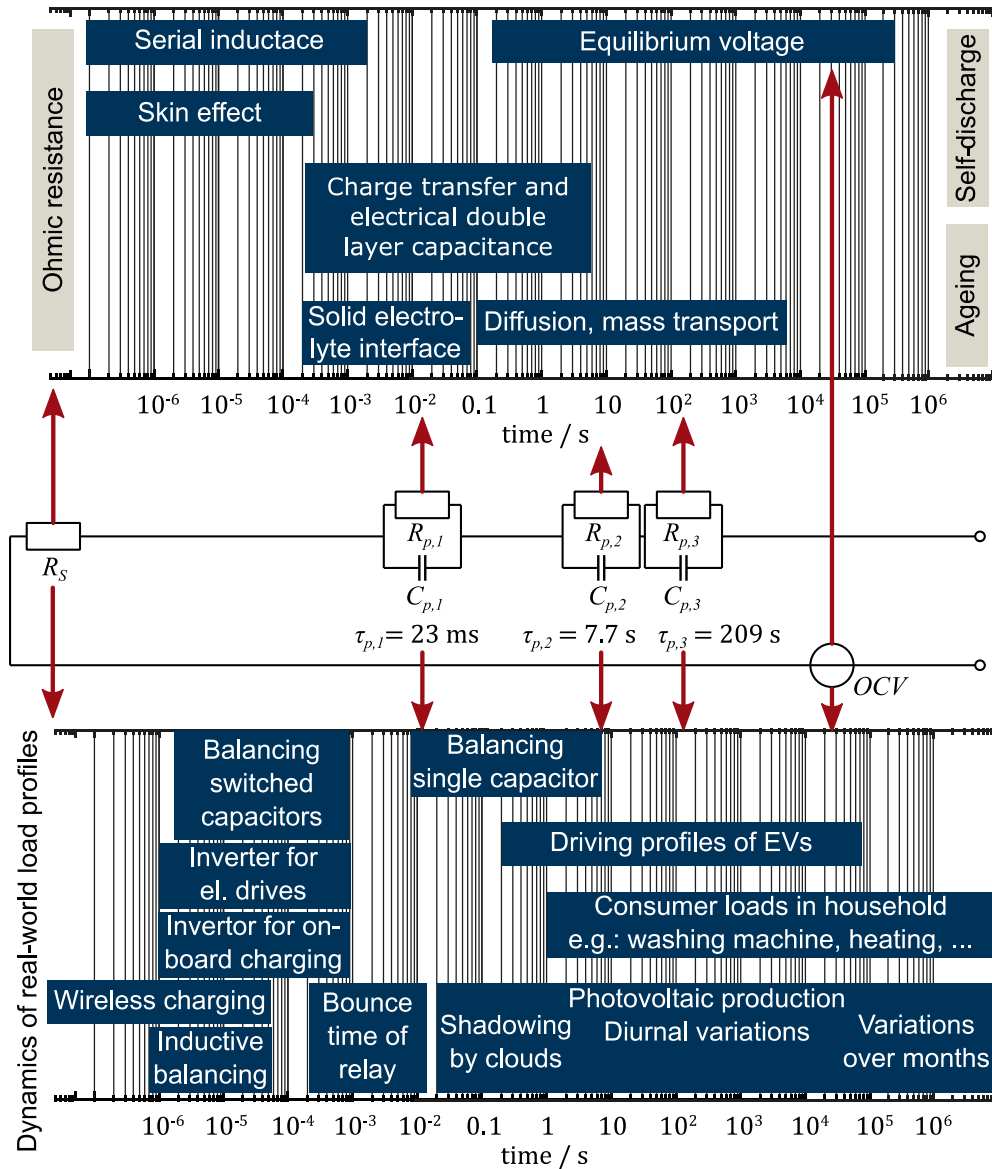
Figure 2.4: *Dynamic processes and time constants for a simulation model (according to Jossen [46]) and the dynamics of real-world load profiles [47–63]*

Usually, the time constant of the EDLC parallel the CT resistance (EDLC/CT) is higher than that of the SEI. The time constant of the two phenomena overlap at most lithium-ion batteries, and thus it is not possible to see the half cycles of the EDLC/CT and SEI separately.

Diffusion processes appear at different locations in the cell. Solid-phase diffusion occurs in the electrodes and liquid phase diffusion occurs in the electrolyte. These phenomena can be described using Fick's law of diffusion [69, 70] from 1855, which describes the diffusion process in liquids; diffusion in solids was not considered in the work of Fick. Today, it is also used in solids as well as gases [71]. Equations (2.9) and (2.10) show Fick's first and second law, where J represents the diffusion flux, D is the diffusion coefficient, c is the concentration, x is the position, and t is the time.

$$J = -D \cdot \frac{dc}{dx} \tag{2.9}$$

$$\frac{\partial c}{\partial t} = D \cdot \frac{\partial^2 c}{\partial x^2} \tag{2.10}$$

The time constants of diffusion processes are in the range of seconds to hours. Furthermore, the time constants in the cathodes' solid phase on the electrodes are more than a factor of 10^9 higher than they are in the liquid phase [72]. In the Nyquist plot, the effects of semi-infinite diffusion appear as a 45° slope. Therefore, a Warburg element (WB) is appropriate for modelling this behaviour. Buller showed how a series connection of RC elements can approach the WB element [44].

In 2002, Linden quantified the self-discharge rate of lithium-ion batteries in his "Handbook of Batteries" from 2 to 10 %/month [3]. The self-discharge rate is dependent on temperature. Furthermore, the rule of thumb states that a temperature increase of 10 °C causes the self-discharge rate to double [33]. More recent publications have shown clearly lower rates. Schmidt et al. calculated the self-discharge resistance in a 2 Ah blended LCO and NCA cell to be 40 kΩ at 70 % of the SoC. This means that the self-discharge current was 105 µA. No self-discharge could be observed at SoC values between 10 and 65 % [73]. Self-discharge is not the focus of the present work and is not discussed further as its impact on capacity is in the range of 1 %/month [74].

In real-world applications, the dynamics of load profiles are orders of magnitude apart (see Figure 2.4). For example, the charge profile of a PV storage battery on a sunny day has time constants in the range of hours; clouds causing shade over PV panels leads to changes within seconds; and switching a consumer load changes the load profile in milliseconds. [28]

Battery EEC modelling starts with simple structures. In the easiest case, battery storage is represented by its capacity, but this model does not represent the internal resistances. The OCV corresponds to the charge and discharge characteristics of a capacitance, which is a linear curve depending on the SoC of the capacitor [75, 76]. Real lithium-ion battery cells do not have a linear OCV. Therefore a nonlinear look-up table usually simulates the OCV [75, 76].

Although a battery is not an ideal form of storage, it is real storage, and thus internal resistance is necessary to simulate the voltage under load. Figure 2.5 shows the impedance of a battery cell out of an EIS measurement. In the easiest case, an ohmic resistor represents the overvoltage of the internal resistance. To model more precisely, the time range of modelling is crucial. As

discussed in Section 2.2, the different impedance effects range over decades of time constants. Table 2.1 presents impedance elements for the modelling of a battery's internal impedance and its equations.
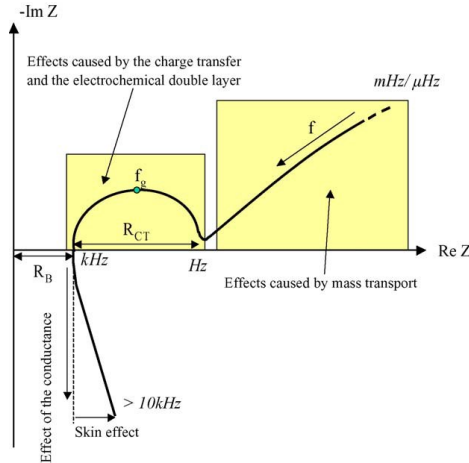
Figure 2.5:   *Nyquist plot and a representation of the physical effects in a battery cell [46]. R_B represents the ohmic resistance, R_{CT} is the resistance of the charge transfer, f is the frequency, and f_g is the cut-off frequency.*
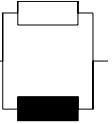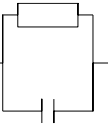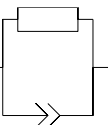
To obtain better results in the time range of milliseconds to seconds, the SEI, EDLC/CT, and CT must be simulated (compare Figure 2.4). These parts of the impedance generate a half circle in the Nyquist impedance plot, whereas an RC element creates an exact half-circle. Some batteries exhibit curves that have a radius in the real direction larger than that in the imaginary direction. A ZARC element can model this characteristic; its shape in the Nyquist plot is a downward-shifted circle, and it consists of a parallel connection of a resistor and constant phase element (CPE).

A WB element, one or more RC elements in a series connection, can simulate the slow effects such as diffusion. Buller demonstrated how to convert a WB element in a row of RC circuits connected in series [44]. To improve this approximation, the number of RC elements can be increased.

The calculation of ageing effects and self-discharge would only be necessary for simulations of several days, which is not in the scope of the present work.

In addition, approaches exist that use EEC modelling to simulate local potentials within battery cells [80–82]. Because this work focuses on the current distribution between battery cells, inner cell potential distribution is not in its scope. However, the influences of the system components must be modelled [83–85]. Battery cells are connected through wires or bus bars of different sizes depending on the current they are required to carry. These elements exhibit mainly ohmic and inductive behaviour [25]. Brand et al. studied the connection of battery cells and wires or bus bars [83–85]. They found ohmic resistances of different junction techniques in the range of several hundred microhms.

Table 2.1:   *Impedance elements of an EEC*

Electric symbol	Formula	Equation	Explanation
	Inductance $\underline{Z}_L = \text{j} \cdot \omega \cdot L$	(2.11)	L: inductance
	RL circuit $\underline{Z}_{RL}(\omega) = \frac{\text{j}\omega L_{RL}}{R_{RL} + \text{j}\omega L_{RL}}$	(2.12)	L_{RL}: inductance of the RL circuit R_{RL}: resistance of the RL circuit
	Ohmic resistance $\underline{Z}_R = R$	(2.13)	R: resistance
	Capacitance $\underline{Z}_C = \frac{1}{\text{j} \cdot \omega \cdot C}$	(2.14)	C: capacitance
	RC circuit $\underline{Z}_{RC}(\omega) = \frac{R_{RC}}{1 + \text{j}\omega R_{RC} C_{RC}}$	(2.15)	R_{RC}: resistance of the RC circuit C_{RC}: capacitance of the RC circuit
	CPE element $\underline{Z}_{CPE}(\omega) = A \cdot (\text{j}\omega)^{-\xi_{CPE}}$ [44]	(2.16)	A: generalized capacitance of the CPE element ξ_{CPE}: CPE parameter that defines the downward shift of the half-circle
	ZARC element $\underline{Z}_{ZARC}(\omega) = \frac{R_{ZARC}}{1 + (\text{j}\omega\tau_{ZARC})^{\xi_{ZARC}}}$ [44, 77, 78]	(2.17)	R_{ZARC}: resistance of the ZARC element τ_{ZARC}: time constant of the ZARC element ξ_{ZARC}: ZARC parameter that defines the downward shift of the half-circle Note: The ZARC element can be approximated by a row of five RC circuits connected in series [44].
	WB element (reflecting boundary conditions) $\underline{Z}_{WB}(\omega) = \sqrt{\frac{R_{WB}}{\text{j}\omega C_{WB}}} \cdot \coth\left(\sqrt{R_{WB} \cdot \text{j}\omega C_{WB}}\right)$ [44, 79]	(2.18)	R_{WB}: resistance of the WB element C_{WB}: capacitance of the WB element Note: The WB element can be approximated by a row of RC circuits connected in series. More RC circuits improve the approximation. [44]

The impedance of a connection $R_{connection}$ consists of the sum of the junction resistances $R_{junction}$ and the impedance of the wire or bus bar R_{wire}. R_{wire} is calculated using the material-dependent parameter of electrical conductivity ρ and the geometry of the connection, which consists of the length l and cross-sectional area A:

$$R_{connection} = \sum R_{junction} + R_{wire} \tag{2.19}$$

$$R_{wire} = \frac{l}{\rho \cdot A}$$ (2.20)

Because the high-frequency area is not in the scope of this work, the cell connection can be simulated using an ohmic resistance.

### 2.2.3 Ageing of lithium-ion cells

In addition to self-discharge, which is a reversible capacity fade, nonreversible capacity fade occurs in lithium-ion batteries. Nonreversible capacity fade is one of two ageing phenomena, the other being the growth of internal resistance.

Capacity loss defines the SoH_{Ah} by calculating the ratio between the actual capacity C_{act} and nominal capacity C_n (compare Equation (2.21)). The ratio between the actual resistance R_{act} and nominal resistance R_n results in the ageing of the impedance SoH_Z (compare Equation (2.22)).

$$SoH_{Ah} = \frac{C_{act}}{C_n}$$ (2.21)

$$SoH_Z = \frac{R_{act}}{R_n}$$ (2.22)

In the automotive field, it is common to define the end of life of batteries at $SoH_{Ah} < 0.8$ or $SoH_Z > 2$ [3, 33, 86]. Many reasons exist for degradation. In Figure 2.6, Birkl et al. showed the causal connections from an event or cause until its effect.
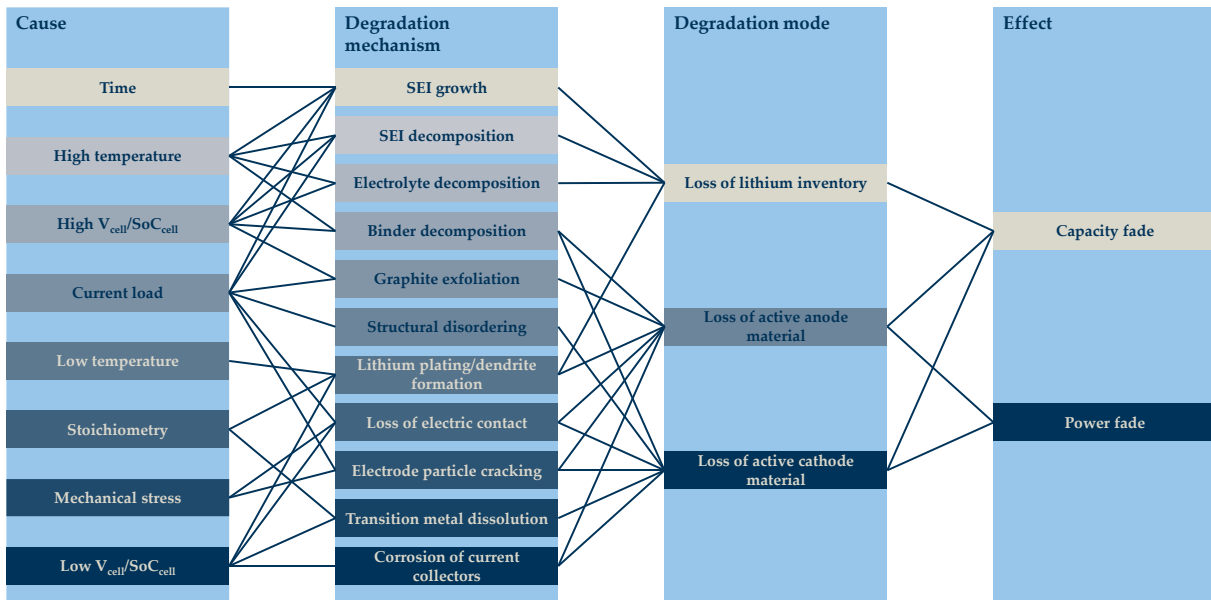
Figure 2.6:   *Cause and effect of degradation mechanisms and associated degradation modes (according to Birkl et al. [26])*

Capacity fade is driven by the loss of lithium inventory (LLI), active material at the negative electrode (anode) (LAM_NE), or active material at the positive electrode (cathode) (LAM_PE).

Power fade, which means an increase in the internal impedance of a cell, is driven by the loss of active material on one of the electrodes. [26]

Battery cells age with time. The SEI layer grows through side reactions, which are supported by high temperatures, high SoCs, and current load. Furthermore, SEI decomposition and electrolyte decomposition lead to LLI. These reactions are caused by high temperatures. [87]

LAMNE and LAMPE reduce the capacity and power of cells. The amount and the balancing of cathode and anode material define the OCV of a cell. Losses at one of the electrodes lead to a shift or a compression versus the other electrode. Therefore, the nonlinearities of half-cell OCVs can be used to detect LAMNE and LAMPE. To observe this, the OCV is differentiated and the position of the peaks is observed. This method is called differential voltage analyses (DVA) and was described by Bloom et al. [88] in 2005. Additionally, Smith et al. [89–91], Dahn et al. [92], Keil et al. [21, 93, 94], and Lewerenz et al. [95] used the method to characterize ageing phenomena.

Low temperatures reduce chemical reactions. This means that side reactions are lowered, which is positive for ageing. On the other hand, low temperatures engender the risk of lithium plating at the anode when the cells are charged. The degradation mechanism of lithium plating implies the deposition of metallic lithium on the surface of the anode. The deposed lithium is lost for further cycling. This effect appears when the lithium atoms cannot intercalate into the lattice structure of the active material, which occurs when the anode potential drops below 0 V. [96–100]

The potential of a graphite anode is low when the SoCs of a battery cell are high (see Figure 2.3). A high charge current leads to high overvoltage because of internal resistances that grow with lower temperatures. Overall, lithium plating is driven by low temperatures, high currents, and high SoCs. Further comprehensive ageing studies on lithium-ion cells were conducted by Ecker et al. [101–104] and Keil et al. [21, 63, 93, 94, 105].

2.2.4 Entropy and hysteresis

The OCV depends on the SoC. Its potential comes from the potential difference of the cathode and anode, as explained in Subsection 2.2.1. However, the OCV is not only dependent on the SoC—two other factors also influence it. Entropy leads to the OCV being temperature dependent [106, 107]. The simulations in the present work did not allow changes in the temperature during a test. No thermal model has been included up to now; however, the model is prepared to subjoin a temperature calculation with temperature-dependent impedance and OCV parameters. For this work, all sets of parameters were determined at certain temperatures and did not change with the temperature during the simulations.

The second influence on OCV is hysteresis. Dreyer et al. [24, 108] gave a thermodynamic explanation of the phenomena of OCV dependence on the SoC history of lithium-ion batteries. They stated that a single particle model cannot predict hysteresis. Thus, it is necessary to observe a multi-particle model. The authors assumed that a scenario in which the particles in a

cell were charged one after each other instead of all particles in parallel would generate the effect of hysteresis and could explain its voltage impact. [24, 108]

Figure 2.7 shows the measured voltage hysteresis of an LFP | graphite cell over the SoC. The upper and lower limit differ up to 35.4 mV at 40 % of SoC.
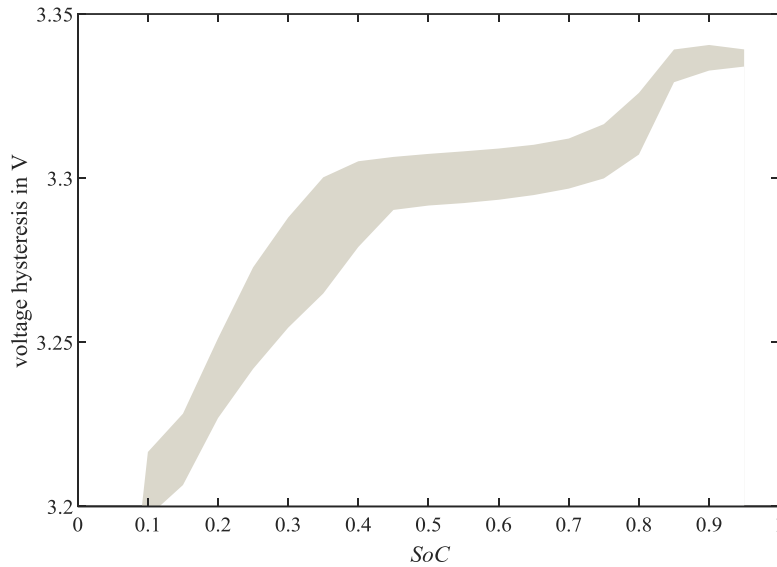
Figure 2.7:   *Measured upper and lower limit of the voltage hysteresis of an LFP | graphite cell over the SoC*

Zhu et al. [109] and Baronti et al. [110] described measurements of the voltage difference, and they demonstrated a way to model hysteresis using the discrete Preisach model. This method counts the sum of activated hysterons in a triangle. The relationship between activated and nonactivated hysterons is a measure of hysteresis. In Figure 2.8, activated hysterons in the triangle are shown by grey stars and nonactivated ones by blue stars. The model of this work uses the cell's SoC as the input for the discrete Preisach model. When the SoC is rising, the dashed red line in Figure 2.8 will move up and activate the hysterons. This is the case in steps 1 and 3. The deactivating line is the vertical-chain dotted red line. In steps 2 and 4, this line moves from right to left and deactivates the hysterons. Activated hysterons hold a value of $\gamma[d(t)] = 1$ and deactivated ones hold a value of $\gamma[d(t)] = -1$:

$$\gamma[d(t)] = \begin{cases} 1 & d(t) > \alpha \\ -1 & d(t) < \beta \\ \text{remain unchanged,} & \beta \leq d(t) \leq \alpha \end{cases} \qquad (2.23)$$

where γ is the value of the hysteron, $d(t)$ is the SoC difference since the last change of SoC direction, and α, β are the threshold of the hysteresis.

The Preisach model suggests equation (2.24), where μ corrensponds to the Preisach density, which is a type of weighting of the hysterons, and $y(t)$ is the output of the model at time t. In the case of battery hysteresis, this is how the OCV is shifted.

$$y(t) = \iint_{\alpha \geq \beta} \mu(\alpha, \beta) \gamma[d(t)] \, d\alpha d\beta \qquad \textit{(2.24)}$$

In Figure 2.8, the range of α and β are from 0 to 1. This would mean that it takes 100 % of the SoC to go from the maximum hysteresis value to the minimal value and vice versa. In reality, this occurs much faster. The measured and fitted range of the parameters α and β lie between 0.08 and 0.20. Details on the parametrisation are described in Subsection 3.3.4 and the specific cell and temperature values are summarised in Table 3.4.
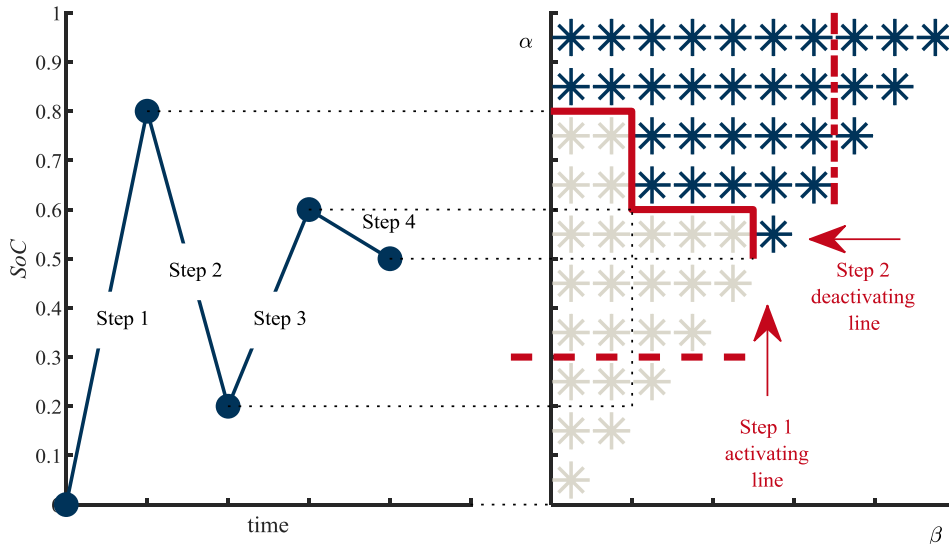
Figure 2.8: *Discrete Preisach modelling according to Zhu et al. and Baronti et al. [109, 110]. The red solid line shows the state after step 4.*

A MATLAB implementation of the discrete Preisach model was provided by the GitHub user jhart12 [111]. The model can calculate the hysteresis at a configurable number of hysterons. Furthermore, the delta of the SoC required to get from maximal to minimal OCV values can be adapted. The result of the discrete Preisach calculation is a voltage that is added to the OCV. Not all of the calculations in the present work use the hysteresis calculation; the use of this submodel is indicated in the descriptions on the simulations.

2.2.5 Parameter variation

The capacity is dependent on temperature, measuring methods and conditions, and the SoH_{Ah}. Rumpf et al. [20], Brand et al. [25], Schuster et al. [112, 113], and Baumhöfer et al. [22] revealed the variation in the capacity of commercial lithium-ion battery cells. This variation differs from a standard deviation divided by the mean capacity in new Sony LFP cells of Rumpf et al. [20] of 0.3 % to a spread in cell capacity of 56 % of strong aged cells at $SoH_{Ah} = 0.43$ [22].

2.3 Determination of the current distribution of battery cells

Research has been conducted into the effects of cell parameter variations on current distribution in parallel-connected cells. Furthermore, numerous analyses of asymmetric current dis-

tribution have been performed [19, 25, 28, 45, 114–192]. Figure 2.9 structures this body of research into different groups: current distribution in a single cell and in that in parallel-connected cells. Each group has measurement and simulation studies.
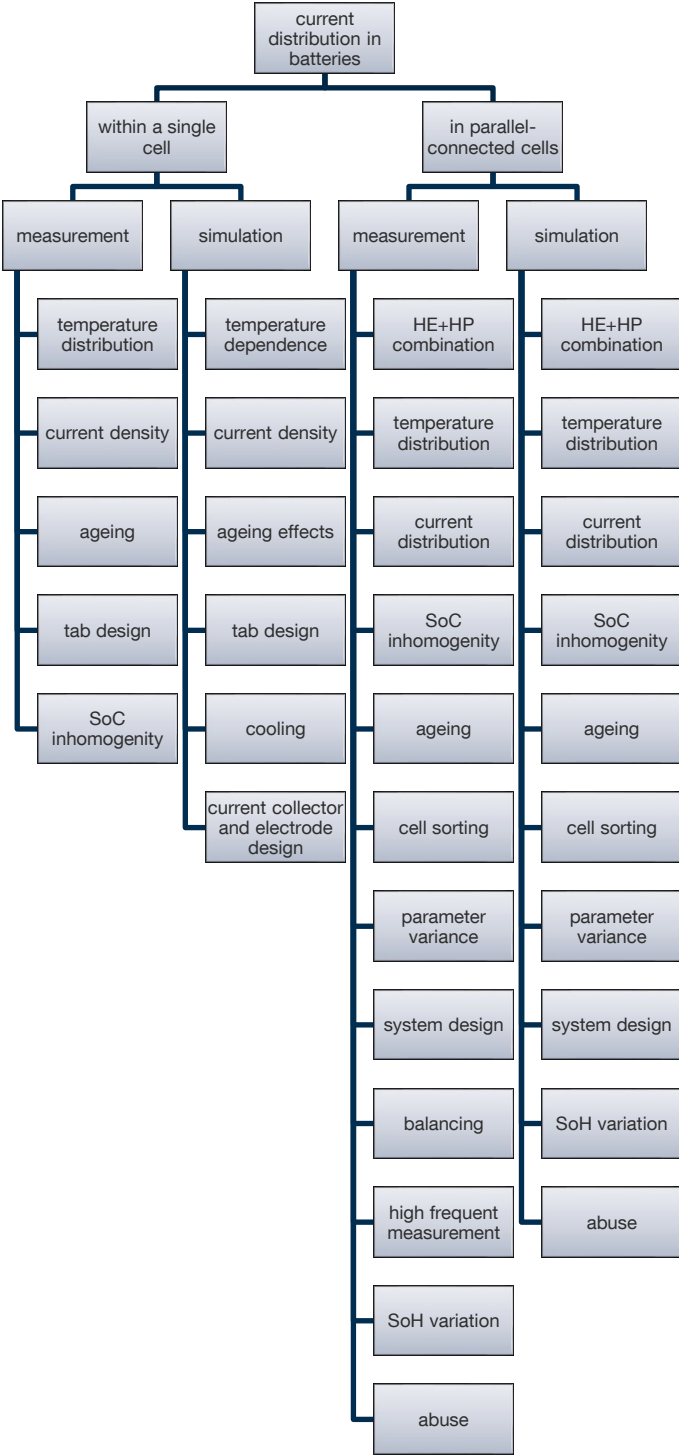
Figure 2.9: *Current distribution in batteries. This hierarchical diagram structures the relevant studies. It distinguishes between cell and system level, measurement or simulation, as well as the focus of the investigation. The corresponding references are listed in Table 2.2–Table 2.8.*

Some of the goals at the cell and system level are similar to the analysis of ageing, whereas others are specific in one part such as the tab design at the cell level or the combination of HP and HE cells at the system level. Moreover, some focus on how to make the SoC measurable or visible [114–124]. This represents an implicit measuring technique for asymmetric current distribution in battery cells.

2.3.1   Analyses in different cell types

Analyses on current distribution were made with lead-acid batteries before the invention of lithium-ion batteries. Euler et al. and Meissner et al. calculated the current density distribution in the porous electrodes of lead-acid batteries [114, 125, 126]. Their focus was to improve the geometry of the electrodes and the tab design. They did not look at the parallel connection of cells; they analysed the current density within the electrode. Euler and Nonnenmacher showed that the modelling of the inner cell distribution is close to the modelling of a parallel connection of cells [125]. Therefore, these two topics are closely related to each other.

Kim et al. analysed lithium-ion pouch cells with an NCA cathode [127]. Three different adaptions of the cell design were studied. From a nominal design, the tabs were narrowed, the cell was made wider and thinner, and the tabs were oriented on both sides of the cell instead of one side (counter tab design). The authors found that the counter tab design leads to the most homogeneous current distribution. A longer cell exhibited the worst results regarding these criteria [127]. This result was confirmed by later publications using LFP and NMC cells [128, 185, 186].

A very different idea in the field of parallel-connected battery cells came from Schmid et al. They proposed using nickel-based cells connected in parallel to lithium-ion cells to prevent overcharging, an idea based on the ability of nickel-based cells to bear moderate overcharging without damage [138]. This method is called electrochemical balancing. Table 2.2 provides an overview of the publications of current distribution in batteries with different cell chemistries.

Table 2.2:   *Review of publications on current distribution in lithium-ion cells and in parallel connections of lithium-ion cells (Part I: Cell chemistry)*

Cell chemistry	
Lead-acid	[114, 125, 126, 132, 133, 136, 158, 187]
Nickel–metal hydride (NiMH)	[132, 133, 138]
Nickel–zinc (NiZn)	[138]
EDLC	[131, 132, 134–137, 187, 192]
Vanadium oxide	[147]
LFP	[116, 117, 119–121, 124, 128–130, 140, 142, 144, 145, 148, 152, 154, 166, 169, 173, 176–178, 181, 185, 188]
LCO	[115, 118, 137, 143, 151, 157, 159, 161, 165, 170, 174, 177, 178, 191]
LMO	[134, 138]
NCA	[28, 127, 135, 139, 143, 146, 149, 155, 164, 171, 180, 182, 189]
NMC	[25, 28, 45, 121–123, 145, 153, 172, 183, 184, 186, 190]
NMC-LMO blend	[150, 168, 179]
Lithium-ion (no more specific indication)	[19, 131, 132, 141, 158, 160, 162, 163, 167, 192]
Lithium–sulphur (Li-S)	[156]

2.3.2   Analyses at the cell and system level

Between 2002 and 2014, several scientists attempted to improve the power and energy performance of battery systems by combining a high energy system with a high power storage system through connecting them in parallel [131–137, 187]. The idea behind this was that high power storage requires short-time power peaks and protect the high energy storage system from overload.

Several studies have focused on similar cells and concentrated on the variation of battery cells coming from the production or ageing process. For example, An et al. analysed cell sorting before the parallel connection. They proposed using an ohmic resistance in series with the OCV as the internal resistance, and for the sorting, it was necessary to consider ageing [139].

Studies that work at the cell level, for example, have attempted to find the optimal tab design [114, 125–130, 185, 186, 190]. These researchers have used lead-acid batteries as well as lithium-ion cells with different cathode materials. Meissner et al. found that reducing the grid impedance of a lead-acid battery's electrode grid—and therefore the voltage drop on the grid structure—caused higher discharge voltage, less heat evolution, higher capacity, and a more homogeneous current distribution over the electrode [126]. A more uniform active material utilisation would improve the cycle life of lead-acid batteries [126]. Table 2.3 categorises the publications on the number of parallel-connected cells; that is, one, two, or more cells in parallel.

Table 2.3:   *Review of publications on current distribution in lithium-ion cells and in parallel connections of lithium-ion cells (Part II: Scope)*

Scope	
Inner cell (1p)	[114–122, 124–130, 147–156, 185, 186, 190]
Inter cell (2p)	[25, 28, 123, 138–140, 142–144, 155, 189]
Inter cell (>2p)	[19, 45, 131–137, 141, 145, 146, 155, 157–174, 176–184, 187–189, 191, 192]

2.3.3   Modelling approaches

Brand et al. showed that differences in the impedance of cells lead to short-term effects, whereas differences in cell capacity lead to long-term effects. The rule of thumb is that the current at the beginning of a current step can be calculated according to the current divider equation in an impedance difference scenario, whereas currents divide proportionately to battery cell capacities (in long-term behaviour) in a capacity-difference scenario. These results come from a very simple EEC model consisting of a linear OCV and ohmic resistance per cell. [25]

Other approaches have used physicochemical models (PCMs). Only Gogoana et al. used an ageing model to calculate the degradation of parallel-connected batteries [140]. Table 2.4 divides the publications by the used model type.

Table 2.4:   *Review of publications on current distribution in lithium-ion cells and in parallel connections of lithium-ion cells (Part III: Model)*

Model	
EEC	[25, 28, 45, 114, 124–126, 130, 133–137, 139, 143, 148, 150, 155, 157, 159–164, 167–170, 173, 174, 176–179, 181–184, 187, 188, 191, 192]
PCM	[122, 127, 128, 142, 144, 147–149, 151–154, 161, 165, 171, 185, 190]
Ageing model (PCM)	[140]
No model	[115, 118, 119, 123, 129, 131, 132, 138, 145, 146, 156, 172, 180, 189]

The OCV is a critical battery parameter because it generally defines the major part of the voltage of a battery. No study has concentrated specifically on OCV. Yang et al., Pastor-Fernández et al., and Shi et al. [142, 145, 146, 188] discovered effects related to the OCV but performed no detailed analyses. Klein et al. measured different SoCs but provided no simulations of the OCV nonlinearity [145]. In models, the OCV is implemented differently; sometimes it is linearised over the total SoC range, some studies have used nonlinear functions, and others have used look-up tables (see Table 2.5).

Table 2.5:   *Review of publications on current distribution in lithium-ion cells and in parallel connections of lithium-ion cells (Part IV: OCV)*

OCV	
Linear function	[25, 114, 125, 126, 133, 134, 176, 187]
Nonlinear function	[127, 128, 137, 144, 148, 149, 151–154, 161, 162, 164, 165, 168, 185]
Look-up table	[19, 25, 28, 45, 122, 124, 130, 135, 139, 141, 142, 147, 150, 155, 157, 159, 160, 163, 167, 177–179, 181–183, 186, 190–192]
Not specified	[136, 169–171, 173, 174, 184, 188]

Dynamic effects appear in a broad range of frequencies as shown in Figure 2.4 and a paper of Jossen [46]. Hence, the dynamic of the load profile will influence the overvoltage, and therefore the current distribution. Table 2.6 provides the load profiles that are used to analyse current distribution. It classifies CC, pulse load, load profiles of applications, and sine load.

Some studies have demonstrated the interaction of parameter changes through ageing and current distribution [140–142, 188]. Osswald et al. performed EIS measurements [119] and analysed the inner cell current distribution. Most studies have used CC to analyse the asymmetric current distribution. Only Bruen et al. used an electric vehicle (EV) load profile with a time step of $\Delta t = 1$ s [19, 141].

Table 2.6:   *Review of publications on current distribution in lithium-ion cells and in parallel connections of lithium-ion cells (Part V: Dynamic of the load profile)*

Dynamic of the load profile	
Constant current	[19, 45, 115–118, 120–122, 125–128, 130, 132, 136, 138–157, 159, 160, 162, 164–167, 169–171, 173, 174, 176, 177, 180, 181, 185, 186, 188–190]
Pulse load	[25, 28, 45, 114, 124, 129, 131, 132, 134, 135, 137, 145, 153, 155, 160, 162, 165, 168, 172, 177, 179, 183, 187]
Load profile of an application	[19, 133, 135, 136, 141, 163, 165, 178, 182, 191]
EIS / sine load	[28, 119, 123, 165]

2.3.4   Parameter variations and results

Some studies have focused on the variation of cell parameters such as temperature, ageing, cell-to-cell variations, or the mechanical design of cell tabs and electrodes. Others have analysed the system configuration in terms of the number of parallel-connected cells or the topology, or they have used a combination of HP and HE cells. The operation parameters in terms of current height and dynamic are further categorised in Table 2.7.

Table 2.7:   *Review of publications on current distribution in lithium-ion cells and in parallel connections of lithium-ion cells (Part VI: Parameter variation)*

Parameter variation	
Temperature	[118, 119, 122, 124, 129, 142, 143, 145, 148, 152, 153, 155–157, 165, 172, 185]
Ageing	[19, 45, 130, 139, 141, 142, 146, 156, 166, 169–172, 179, 180, 182, 188]
Cell-to-cell variation	[25, 123, 139, 140, 144, 155, 157, 163, 167, 168, 181, 189, 191]
Tab and electrode design	[114, 125–130, 185, 186, 190]
Number of parallel cells	[162, 164, 165, 167, 173]
Topology	[137, 138, 144, 159, 161, 164, 168, 169, 173, 177, 178, 183, 184, 189, 192]
HP HE combination	[119, 131–137, 187]
Current	[28, 118, 122, 127, 128, 144, 145, 153, 154, 159, 165, 169, 170, 176, 185, 186, 190]
Dynamic	[28, 119, 123, 129, 137, 174, 187]

Most of the studies on hybrid storage systems have not had promising results, or the advantages were limited to a small number of applications. Holland et al. found that in the evaluation of hybrid systems on a mass basis, there is no benefit because the battery/capacitor hybrid yielded only one-third of the available specific energy and power compared with the battery alone [131]. Shin et al. concluded that a large double-layer capacitor (DLC) drastically degraded the overall available energy density [137]. Cericola et al. reached an ambivalent result; their hybrid system was extremely sensitive to the load, and the available performance significantly increased under a pulsed load [135]. Since 2015 to the present day (2019), there have been no more publications on this topic. Table 2.8 summarises the publications on current distribution sorted by the focus on their results.

Table 2.8:   *Review of publications on current distribution in lithium-ion cells and in parallel connections of lithium-ion cells (Part VII: Result)*

Result	
HP HE combination	[119, 131–137, 187]
Asymmetric current	[19, 25, 28, 45, 114, 116, 117, 119, 122–131, 133–148, 150–174, 176–190, 192]
Asymmetric ageing	[118, 130, 139, 140, 142, 146, 151, 153, 156, 168–172, 178, 180, 182, 183, 188–190]
Temperature dependence	[118, 119, 124, 128, 129, 142, 145, 147, 148, 152, 153, 156, 162, 165]
SoC differences	[19, 25, 28, 45, 115, 118, 120, 121, 124, 128–130, 141, 144–146, 153–155, 160, 163, 169, 173, 177, 181, 189, 190]

Almost all of the studies in Table 2.8 detected a current asymmetry. Some of them were direct and others indirect in terms of the manner of SoC differences. In terms of ageing, the asymmetric current is supposed to cause asymmetric ageing. Impedance differences, which are a driver of asymmetry [25], may occur on account of the unequal ageing of cells. Wohlfahrt-Mehrens et al. [193], Vetter et al. [87], and Barré et al. [194] described the mechanism that leads

to power fade (impedance growth) and capacity fade (capacity loss). Cells within a battery system often do not have similar temperatures, which causes impedance differences.

Furthermore, diffusion, and especially solid-state diffusion, depends on the SoC [195]. The dependency is strong, and impedance is high mainly at low SoCs. Unfinished relaxation processes also influence the impedance behaviour [195], and hence the current distribution in parallel connections. The surface and design of electrodes also influence the complex impedance of the double layer, charge throughput, and diffusion [44]. The reasons for this are passivating layers such as the solid electrolyte interface or the porosity of the anode and cathode. Capacity fade is often expedited by the loss of lithium, loss of active material, loss of mechanical stability, and loss of electrolyte [87]. All of these ageing effects are dependent on parameters such as the SoC, temperature, and current rate, which are not distributed equally over the cells in a battery pack. This means that the inequality of cell parameters can change right up to the end of a cell's service life.

Furthermore, temperature influences the current distribution because of the temperature dependence of the impedance of battery cells. Table 2.8 presents a list of publications that analyse this effect. Because current causes losses that heat the cells, an asymmetric current distribution causes asymmetric heating, and therefore some type of back coupling.

In addition, no studies have discussed the reasons for asymmetric current distribution in detail, including internal cell effects such as hysteresis and entropy. Therefore, the present work focuses on this objective.

3 Modelling of the current distribution

A model allows for the systematic analysis of the influencing factors of current distribution. Furthermore, it allows for the examination of a single effect without mutual interaction with other processes in a cell. In simulations, it is possible to switch effects on or off.

The battery cell models used in this work consisted of an OCV and impedance in a series connection. Depending on the aim of the simulation, different variations of this basic model were utilised. The identifier of the model types was as follows:

$$OCV_{<characteristic>}(< dependencies >) + \underline{Z}_{<characteristic>}(< dependencies >)$$

Table 3.1 summarises the acronyms and meanings of the model types' characteristic and impedance parameters. The different methods of determining the OCV are explained in Subsection 3.3.3; Subsection 3.3.4 shows how hysteresis was measured; and Subsection 3.3.5 focuses on the temperature dependence of the OCV (entropy).

Table 3.1:   *Characteristics and dependencies of the EEC model types used in this work*

	OCV		Impedance	
	Acronym	Meaning	Acronym	Meaning
Characteristics	lin	Linearised OCV	R	Ohmic resistance
	mea_step	Nonlinear and stepwise measured OCV	nRC	n RC elements
	mea_nC	Nonlinear and continuous measured OCV with a CC current of n C		
	tanh	Combination of a linear OCV with a hyperbolic tangent		
Dependencies	SoC	SoC dependence	SoC	SoC dependence
	T	Temperature dependence (entropy)	T	Temperature dependence
	hyst	Dependence on the history of usage (hysteresis)		

For example, a model named "$OCV_{mea\_1C}(SoC, T, hyst) + \underline{Z}_R$" uses a nonlinear OCV measured with a c-rate of 1 C continuous current, which depends on the SoC, temperature, and history of usage (hysteresis). The internal resistance of that model consists of an ohmic resistance without any dependencies.

3.1 Analytical calculation of the current distribution

Calculating the current distribution in parallel-connected battery cells is more intricate than the simulation of a single cell. Figure 3.1 shows the differences between two black box views. The parallel-connected cells are mathematically linked by Kirchhoff's circuit laws.
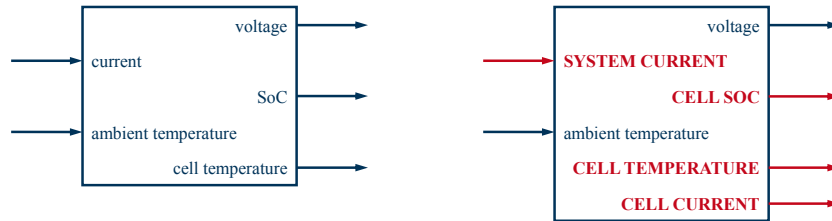
Figure 3.1: *Modelling of a single battery cell (left, according to Buller [44]) compared with that of a parallel connection of battery cells (right)*

A simple analytical calculation illustrates the method of calculating the current distribution. Figure 3.2 defines the basic setting. Two battery cells are connected in parallel, and then a load current i_{tot} is applied to the system. The EEC of each cell consists of one OCV and one ohmic resistance, and the OCV is a linear function of the SoC. There is no temperature dependence and the resistance of the junctions is neglected. The Kirchhoff's circuit point rule states that the sum of currents flowing into a node is equal to the sum of currents flowing out of that node:

$$i_1(t) = i_{tot}(t) - i_2(t) \tag{3.1}$$

Furthermore, the Kirchhoff's mesh rule states that the directed sum of potential differences (voltages) around any closed loop is zero:

$$U_1(t) = U_2(t) \tag{3.2}$$
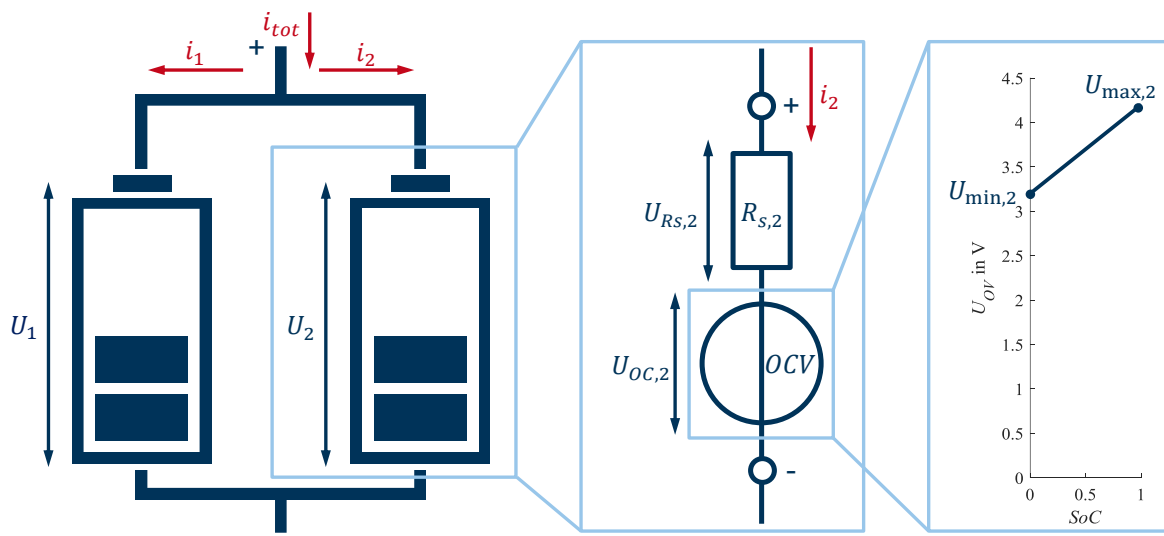
Figure 3.2: *EEC of the simple model for analytical calculations. Each cell consists of a linear OCV and a series ohmic resistance (model type: $OCV_{lin}(SoC) + \underline{Z}_R$)*

The voltages of the two cells U_1 and U_2 consist of the OCV voltages $U_{OC,1}$ and $U_{OC,2}$ plus the overvoltage at the ohmic resistances $R_{s,1}$ and $R_{s,2}$, which depend on the cell currents i_1 and i_2. This is the model type $OCV_{lin}(SoC) + \underline{Z}_R$. The OCV voltages and the cell currents are a function of the time t:

$$U_1(t) = U_{OC,1}(t) + R_{s,1} \cdot i_1(t) \tag{3.3}$$

$$U_2(t) = U_{OC,2}(t) + R_{s,2} \cdot i_2(t) \tag{3.4}$$

The cells' SoC comes from integrating the cell current and the relationship of this value with the cell capacities C_1 and C_2:

$$SoC_1(t) = \frac{1}{C_1} \cdot \int_{t_0}^{tend} i_1(t)dt \tag{3.5}$$

$$SoC_2(t) = \frac{1}{C_2} \cdot \int_{t_0}^{tend} i_2(t)dt \tag{3.6}$$

The OCV voltage characteristic of the cells is a linear function of the SoC: $f(x) = ax + b$. In this example, the slope $a = U_{\max} - U_{\min}$ and the coefficient $b = U_{\min}$. Accordingly, the OCV voltage is calculated using the following equations:

$$U_{OC,1}(t) = \left(U_{\max,1} - U_{\min,1}\right) \cdot SoC_1(t) + U_{\min,1} \qquad \text{(linearised OCV)} \tag{3.7}$$

$$U_{OC,2}(t) = \left(U_{\max,2} - U_{\min,2}\right) \cdot SoC_2(t) + U_{\min,2} \qquad \text{(linearised OCV)} \tag{3.8}$$

Equations (3.5) and (3.6) can be inserted into equations (3.7) and (3.8). Together with equations (3.3) and (3.4), the cell voltages result in the following terms:

$$U_1(t) = \frac{U_{\max,1} - U_{\min,1}}{C_1} \cdot \int_{t_0}^{tend} i_1(t)dt + U_{\min,1} + R_{s,1} \cdot i_1(t) \tag{3.9}$$

$$U_2(t) = \frac{U_{\max,2} - U_{\min,2}}{C_2} \cdot \int_{t_0}^{tend} i_2(t)dt + U_{\min,2} + R_{s,2} \cdot i_2(t) \tag{3.10}$$

Because Kirchhoff's mesh rule states that the voltages must be equal, equations (3.9) can (3.10) be equalised:

$$\frac{U_{\max,1} - U_{\min,1}}{C_1} \cdot \int_{t_0}^{t_{end}} i_1(t)dt + U_{\min,1} + R_{s,1} \cdot i_1(t) \tag{3.11}$$

$$= \frac{U_{\max,2} - U_{\min,2}}{C_2} \cdot \int_{t_0}^{t_{end}} i_2(t)dt + U_{\min,2} + R_{s,2} \cdot i_2(t)$$

Hence, the cell voltages vanish. The total current of the system i_{tot} is usually known. Using Kirchhoff's circuit point rule in equation (3.1), i_2 can be replaced. The deviation with respect to time eliminates the integration on both sides:

$$\frac{U_{\max,1} - U_{\min,1}}{C_1} \cdot \int_{t_0}^{t_{end}} i_1(t)\mathrm{d}t + U_{\min,1} + R_{s,1} \cdot i_1(t)$$

$$= \frac{U_{\max,2} - U_{\min,2}}{C_2} \cdot \int_{t_0}^{t_{end}} \big(i_{tot}(t) - i_1(t)\big)\mathrm{d}t + U_{\min,2} + R_{s,2}$$

$$\cdot \big(i_{tot}(t) - i_1(t)\big)$$

(3.12)

$$\frac{U_{\max,1} - U_{\min,1}}{C_1} \cdot i_1(t) + R_{s,1} \cdot i'_1(t)$$

$$= \frac{U_{\max,2} - U_{\min,2}}{C_2} \cdot \big(i_{tot}(t) - i_1(t)\big) + R_{s,2} \cdot i'_{tot}(t) - R_{s,2} \cdot i'_1(t)$$

(3.13)

To simplify the equation, the following substitutions were made:

$$m_1 = \frac{U_{\max,1} - U_{\min,1}}{C_1} \text{ and } m_2 = \frac{U_{\max,2} - U_{\min,2}}{C_2}$$

(3.14)

By inserting m_1 and m_2 into equation (3.13) and sorting the terms, a differential equation is generated:

$$m_1 \cdot i_1(t) + \big(R_{s,1} + R_{s,2}\big) \cdot i'_1(t) - m_2 \cdot i_{tot}(t) + m_2 \cdot i_1(t) - R_{s,2} \cdot i'_{tot}(t) = 0$$

(3.15)

$$i'_1(t) = \frac{R_{s,2} \cdot i'_{tot}(t) + m_2 \cdot i_{tot}(t) - m_1 \cdot i_1(t) - m_2 \cdot i_1(t)}{R_{s,1} + R_{s,2}}$$

(3.16)

$$i'_1(t) = \frac{R_{s,2}}{R_{s,1}+R_{s,2}} \cdot i'_{tot}(t) + \frac{m_2}{R_{s,1}+R_{s,2}} \cdot i_{tot}(t) - \frac{m_1+m_2}{R_{s,1}+R_{s,2}} \cdot i_1(t)$$

(3.17)

$$i'_1(t) + \frac{m_1+m_2}{R_{s,1}+R_{s,2}} \cdot i_1(t) = \frac{R_{s,2}}{R_{s,1}+R_{s,2}} \cdot i'_{tot}(t) + \frac{m_2}{R_{s,1}+R_{s,2}} \cdot i_{tot}(t)$$

(3.18)

This is an ordinary differential equation of the first order with the following form:

$$x'(t) + g(t) \cdot x(t) = h(t) \text{ with } x(t_v) = v \text{ (v is the value at $t = t_v$)}$$

(3.19)

The uniqueness quantification is defined in equation (3.20):

$$x(t) = e^{-\int_{t_v}^{t} g(s)\mathrm{d}s} \cdot \left\{ v + \int_{t_v}^{t} h(s) e^{\int_{t_v}^{s} g(\psi)\mathrm{d}\psi} \mathrm{d}s \right\}$$

(3.20)

i_{step} defines a unit step function of i_{tot}. With this, the response and the current distribution between the two cells can be calculated:

$$v = i_{step} \cdot \frac{R_{s,2}}{R_{s,1}+R_{s,2}} \text{ and}$$

(3.21)

$$t_v = t_0 = 0 \text{ and}$$

(3.22)

$$g(s) = \frac{m_1+m_2}{R_{s,1}+R_{s,2}} = A \text{ and}$$

(3.23)

$$h(t) = \frac{R_{s,2}}{R_{s,1}+R_{s,2}} \cdot i'_{tot}(t) + \frac{m_2}{R_{s,1}+R_{s,2}} \cdot i_{tot}(t)$$

(3.24)

With these relationships, the equation can be transformed to calculate the current $i_1(t)$ as follows:

$$i_1(t) = \mathrm{e}^{-\int_{t_v}^{t} A \, \mathrm{d}s} \cdot \left\{ i_{step} \cdot \frac{R_{s,2}}{R_{s,1} + R_{s,2}} \right. \tag{3.25}$$
$$\left. + \int_{t_v}^{t} \left(\frac{R_{s,2}}{R_{s,1} + R_{s,2}} \cdot i'_{tot}(t) + \frac{m_2}{R_{s,1} + R_{s,2}} \cdot i_{tot}(t) \right) \cdot \mathrm{e}^{\int_{t_v}^{s} A \, \mathrm{d}\sigma} \mathrm{d}s \right\}$$

$$i_1(t) = \mathrm{e}^{-A \cdot (t - t_v)} \cdot \left\{ i_{step} \cdot \frac{R_{s,2}}{R_{s,1} + R_{s,2}} + \int_{t_0}^{t} \frac{m_2}{R_{s,1} + R_{s,2}} \cdot i_{step} \cdot \mathrm{e}^{A \cdot (s - t_v)} \mathrm{d}s \right\} \tag{3.26}$$

$$i_1(t) = \mathrm{e}^{-A \cdot (t - t_0)} \cdot \left\{ i_{step} \cdot \frac{R_{s,2}}{R_{s,1} + R_{s,2}} + \frac{m_2}{R_{s,1} + R_{s,2}} \cdot i_{step} \cdot \mathrm{e}^{-A \cdot t_0} \cdot \frac{1}{A} \cdot (\mathrm{e}^{A \cdot t} - \mathrm{e}^{A \cdot t_0}) \right\} \tag{3.27}$$

With the start condition (equation (3.22)) of $t_0 = 0$ simplifies the equation (3.27):

$$i_1(t) = \mathrm{e}^{-A \cdot t} \cdot \left\{ i_{step} \cdot \frac{R_{s,2}}{R_{s,1} + R_{s,2}} + \frac{m_2}{R_{s,1} + R_{s,2}} \cdot i_{step} \cdot \frac{1}{A} \cdot (\mathrm{e}^{A \cdot t} - 1) \right\} \tag{3.28}$$

The term $\frac{1}{A}$ can be eliminated by equation (3.23):

$$i_1(t) = \mathrm{e}^{-A \cdot t} \cdot \left\{ i_{step} \cdot \frac{R_{s,2}}{R_{s,1} + R_{s,2}} + \frac{m_2}{m_1 + m_2} \cdot i_{step} \cdot (\mathrm{e}^{A \cdot t} - 1) \right\} \tag{3.29}$$

$$i_1(t) = \mathrm{e}^{-A \cdot t} \cdot i_{step} \cdot \frac{R_{s,2}}{R_{s,1} + R_{s,2}} + \mathrm{e}^{-A \cdot t + A \cdot t} \cdot i_{step} \cdot \frac{m_2}{m_1 + m_2} - \mathrm{e}^{-A \cdot t} \cdot i_{step} \cdot \frac{m_2}{m_1 + m_2} \tag{3.30}$$

$$i_1(t) = \mathrm{e}^{-A \cdot t} \cdot i_{step} \cdot \left(\frac{R_{s,2}}{R_{s,1} + R_{s,2}} - \frac{m_2}{m_1 + m_2} \right) + i_{step} \cdot \frac{m_2}{m_1 + m_2} \tag{3.31}$$

The cell current $i_1(t)$ is only dependent on the OCV, the resistance parameter of the two cells, and the current supplied to the system. The current of the second cell $i_2(t)$ is the total current $i_{tot}(t)$ minus the current of cell one, which concerns equation (3.1).

The first term of equation (3.31) is an exponential function. The time constant τ of an exponential function is defined as $y(t) = \mathrm{e}^{-t/\tau}$. Hence, the time constant $\tau = A^{-1}$ and can be expressed with the internal resistances of the two cells and parameters of the OCV using the following equation:

$$\tau = \frac{1}{A} = \frac{1}{\frac{m_1 + m_2}{R_{s,1} + R_{s,2}}} = \frac{R_{s,1} + R_{s,2}}{m_1 + m_2} = \frac{R_{s,1} + R_{s,2}}{\frac{U_{max,1} - U_{min,1}}{C_1} + \frac{U_{max,2} - U_{min,2}}{C_2}} \tag{3.32}$$

The time constant is independent of the applied current step i_{step}.

The following example calculates the time constant τ_p in case of a difference in the internal resistance ΔR and capacity ΔC between two cells connected in parallel. Therefore, the following values were assumed: $R_{s,1} = 0.02 \, \Omega$, $R_{s,2} = R_{s,1} \cdot 1.0183 = 0.020366 \, \Omega$, $C_1 = 2.5$ Ah, and $C_2 = C_1 \cdot 1.0072 = 2.518$ Ah. These differences refer to the standard deviation of R and C measured in a lot of 172 new lithium-ion battery cells by Brand et al. [25]. The limits of the OCV were kept similar: $U_{min,1} = U_{min,2} = 3.2$ V and $U_{max,1} = U_{max,2} = 4.2$ V.

$$\tau_p = \frac{R_{s,1} + R_{s,2}}{m_1 + m_2} = \frac{0.02 \, \Omega + 0.020366 \, \Omega}{\frac{4.2 \, \text{V} - 3.2 \, \text{V}}{2.5 \, \text{Ah}} + \frac{4.2 \, \text{V} - 3.2 \, \text{V}}{2.518 \, \text{Ah}}} = \frac{0.040366 \, \Omega}{0.7971 \, \text{V/Ah}} \tag{3.33}$$

$$\tau_p = 0.05064\,\text{h} = 182.3\,\text{s}$$

The simulation in Figure 3.3 shows the current distribution of this example. The applied total current is a discharge step at $t = t_0 = 0$ s of $i_{step} = -1$ A.
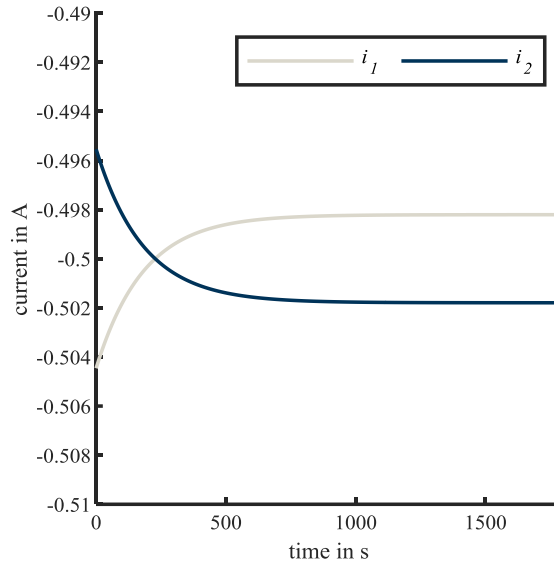
Figure 3.3: *Current distribution calculation results of a 2p connection of cells with different capacities (2.5 and 2.518 Ah) and internal resistances (0.02 and 0.020366 Ω)*

Producers of commercial lithium-ion battery cells usually provide the cell parameters, internal resistance, and capacity in datasheets. In Table 3.2, the standard deviation of R and C taken from [25] is applied to several types of commercial batteries. The parameters of cell 1, $R_{S,1}$, and C_1 come from the datasheet and the parameter of cell two were calculated using the variations of [25].

The cell capacities and impedances have a large influence on the behaviour of current distribution in cells connected in parallel. This is why cells with a variable ratio between capacity and impedance have been analysed. Different cell dimensions can be compared with the resistance coefficient λ [208, 209]:

$$\lambda = C_n \cdot R_s \tag{3.34}$$

Table 3.2:   *Datasheet parameters of several lithium-ion battery cells with NCA, NMC, and LFP cathode material and different cell dimensioning (HP, intermediate, and HE). The data in this table come from the cells' datasheets [196–207] (^{d}) and the researcher's own measurements (^{m}).*

Cell type	Dimensioning	Electrode chemistry (cathode | anode)	OCV (U_{min} | U_{max})	Internal resistance ($R_{s,1}$ | $R_{s,2}$)	Capacity (C_1 | C_2)
E-One Moli Energy IHR18650A	HE	NMC | graphite	3.2 V | 4.2 V	80 mΩ | 81.5 mΩ ^{m}	1.95 Ah | 1.96 Ah ^{d}
LG Chem ICR18650HB2	HP	NMC | graphite	3.2 V | 4.2 V	11 mΩ | 11.2 mΩ ^{m}	1.5 Ah | 1.51 Ah ^{d}
A123 ANR26650M1	HP	LFP | graphite	3.18 V | 3.34 V	8 mΩ | 8.1 mΩ ^{d}	2.3 Ah | 2.32 Ah ^{d}
A123 APR18650M1A	HP	LFP | graphite	3.18 V | 3.34 V	18 mΩ | 18.3 mΩ ^{m}	1.1 Ah | 1.11 Ah ^{d}
Sony US26650FT	intermediate	LFP | graphite	3.18 V | 3.34 V	18 mΩ | 18.3 mΩ ^{d}	3.0 Ah | 3.02 Ah ^{d}
Panasonic NCR18650PF	intermediate	NCA | graphite	3.2 V | 4.2 V	21 mΩ | 21.4 mΩ ^{m}	2.85 Ah | 2.87 Ah ^{d}
Panasonic NCR18650B	HE	NCA | graphite	3.2 V | 4.2 V	55 mΩ | 56.0 mΩ ^{m}	3.4 Ah | 3.42 Ah ^{d}
Samsung NCR18650-25R	HP	NMC | graphite	3.2 V | 4.2 V	13 mΩ | 13.2 mΩ ^{m}	2.5 Ah | 2.52 Ah ^{d}
O'cel IFR26650EC	HE	LFP | graphite	3.18 V | 3.34 V	50 mΩ | 50.9 mΩ ^{d}	3.3 Ah | 3.32 Ah ^{d}
GreatPower 26650/3400mAh	HE	LFP | graphite	3.18 V | 3.34 V	25 mΩ | 25.5 mΩ ^{d}	3.3 Ah | 3.32 Ah ^{m}
OptimumNano OPT26650F	intermediate	LFP | graphite	3.18 V | 3.34 V	15 mΩ | 15.3 mΩ ^{d}	3.0 Ah | 3.02 Ah ^{d}
LG Chem INR18650MJ1	HE	NMC | graphite	3.2 V | 4.2 V	40 mΩ | 40.7 mΩ ^{d}	3.5 Ah | 3.53 Ah ^{d}

Cell dimensioning is rather unspecific. The resistance coefficient can quantify this parameter. HP cells offer a lower impedance and a low capacity, which lead to a low resistance coefficient. In the case of HE cells, the impedance and capacity are high, and therefore the resistance coefficient is also high. In Figure 3.4, the resistance coefficient is plotted against the time constant τ_P. The resistance coefficient is calculated with $R_{s,1}$ and C_1. The flat OCV characteristic of LFP cells leads to higher time constants. Furthermore, a parallel connection of HE cells take longer to reach a steady-state than HP cells. This makes it necessary to observe the current distribution at different time scales, and differentiating between HP and HE cells makes sense. A further analysis using the analytical model on hybrid battery systems is provided in the Appendix.
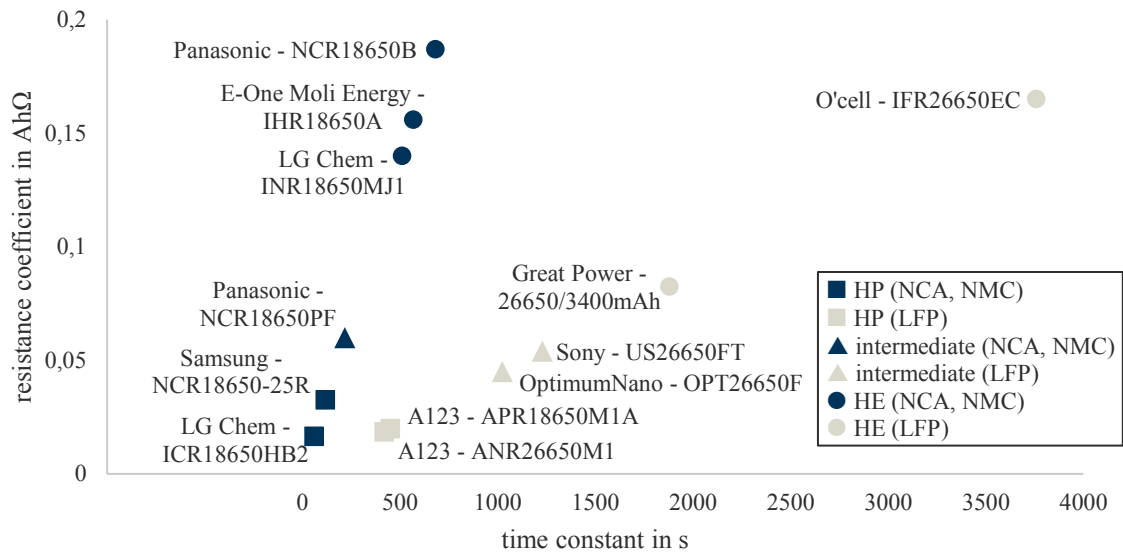
Figure 3.4: *Time constants τ_p considering the variation of different commercial lithium-ion cylindrical cells in 18650 and 26650 formats. The diagram differentiates between cathode materials with steep (NCA and NMC) and flat (LFP) OCV characteristic as well as HP, intermediate, and HE cells*

3.2 State-space model

Current distribution can be simulated with an EEC. Self-produced sections of [28] are partially contained in this chapter without any further reference.

In the present work, the inductive behaviour of battery cells is not the focus, and inductance L and RL elements are not considered in the model. The EEC only uses the OCV, one ohmic resistance, and RC elements. ZARC or Warburg elements are represented by RC elements (compare Figure 3.5) using Buller's transformation [44].
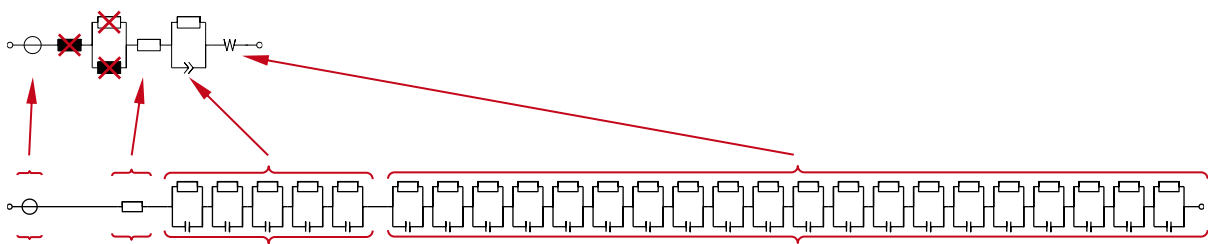
Figure 3.5: *EEC model consisting of the OCV, one ohmic resistance and RC elements. RC elements represent a ZARC and a Warburg element*

A state-space model is a common way to implement time-dependent processes. A matrix-based realisation utilises the strength of MATLAB [210], thereby providing an efficient computation time for the model.

The electrical voltage U_n of a lithium-ion cell n is composed of the sum of $U_{OC,n}$, resistive $U_{Rs,n}$, and dynamic voltage drops $U_{p,n}$ (3.35). Figure 3.6 shows the structure of the EEC model for N parallel-connected cells. The dynamic voltage drop for a cell can comprise the sum of K single

voltages of each RC-member k. Each dynamic voltage drop $U_{p,k,n}$ can be described in terms of the parameters $R_{p,k,n}$ and $C_{p,k,n}$, as well as the current i_n of cell n via a common differential equation of the first order (3.36). If N cells are connected in parallel, a total current i_{tot} results from the sum of all phase currents i_n (3.37).

$$U_n = U_{OC,n} + U_{Rs,n} + U_{p,n} \text{ with } U_{p,n} = \sum_{k=1}^{K} U_{p,k,n} \tag{3.35}$$

$$\frac{dU_{p,k,n}(t)}{dt} = -\frac{U_{p,k,n}(t)}{R_{p,k,n} \cdot C_{p,k,n}} + \frac{i_n}{C_{p,k,n}} \tag{3.36}$$

$$\sum_{n=1}^{N} i_n = i_{tot} \tag{3.37}$$
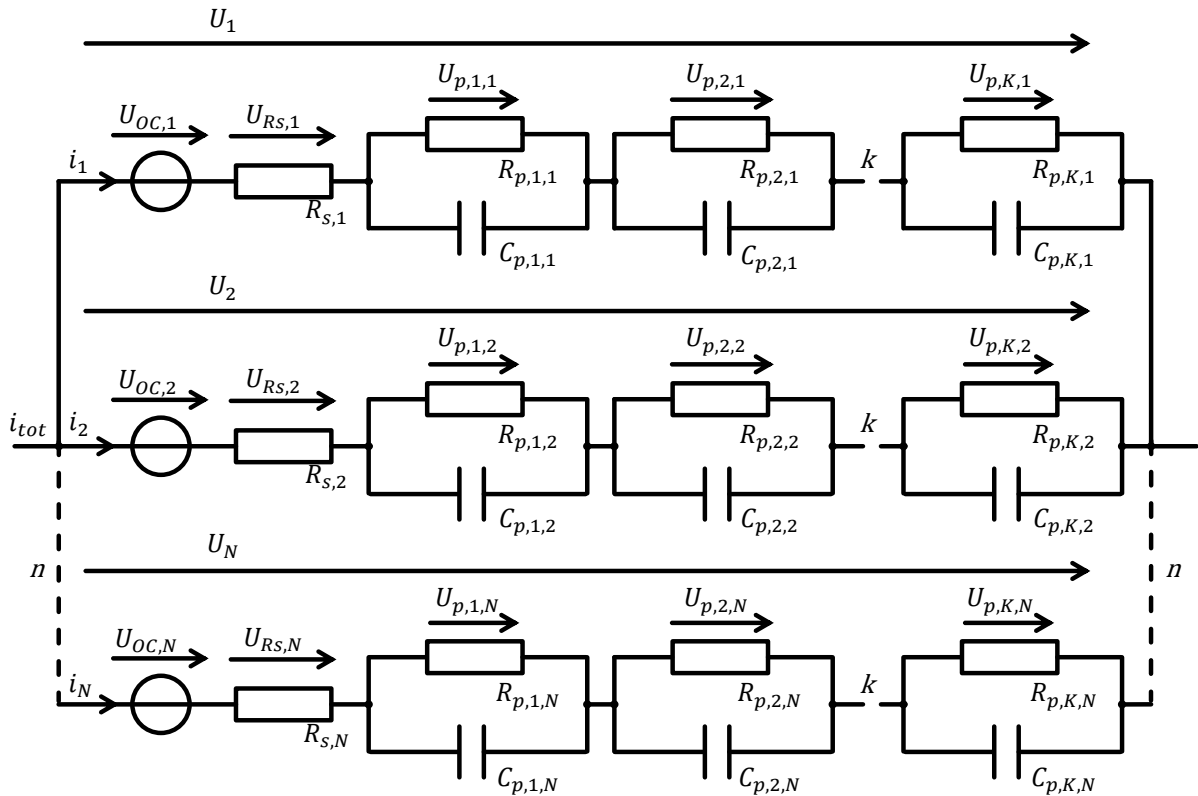
Figure 3.6: *Model structure with N parallel cells, each with an OCV, a series ohmic resistance R_S, and K RC elements*

The aim is to transfer the system equations (3.35) to (3.37) to the matrix-based state-space of the control standard forms (3.38) and (3.39), which are based on the system matrix A, input matrix B, output vector c, and feedforward vector d. Furthermore, an OCV vector y_{OCV} in combination with the corresponding unit vector T_{OCV} is implemented in the output equation (3.39). The state vector x contains every dynamic voltage $U_{p,k,n}$ of the total cell count N, in which each cell n has a total of K dynamic single voltages. In addition, the size of each matrix can be adjusted dynamically depending on the circuit to be simulated. The input u of the system is represented by all phase currents i_n. Therefore, this type of algorithm provides the user with more flexibility by changing the number of parallel-connected cells or the count of RC elements to represent the dynamic voltage drop without losing calculation time. As shown in

Subsection 2.2.2 (Table 2.1), it also allows the representation of ZARC and WB elements by multiple RC elements while maintaining good performance and valid results.

$$\dot{x}(t) = Ax(t) + Bu(t), \qquad x = \left[\overbrace{U_{p,1,1} \quad \cdots \quad U_{p,K,1}}^{1 \times K \cdot N} \; U_{p,1,2} \quad \cdots \quad U_{p,K,N} \right]^{\mathrm{T}} \tag{3.38}$$

$$y(t) = T_{OCV} \cdot y_{OCV} + cx(t) + du(t) \tag{3.39}$$

Because MATLAB is designed to calculate matrices, a variable state-space offers the ideal prerequisites for an efficient and general description of a parallel circuit and the analysis of current distributions, which are presented in the following sections. The investigations of Bruen et al. [19] and Shi et al. [188] were based on system equations in current distribution simulations. Using their modelling approaches, an algorithm is presented in which the OCV is linearised or the state-space model reduced to a linear equation system. To achieve enhanced cell behaviour and consequently an accurate current distribution of parallel-connected cells, neither the OCV nor the state-space model are linearised. To enable the analysis of the impact of different OCV curves, the nonlinear OCV is not part of the state vector, which contains all voltages of the electrical circuits.

Instead, the OCV is considered separately in combination with a unit vector T_{OCV}. Because only one parallel string is required for the output scale $y(t) = U$ (3.40), only the first position of the unit, output c, and pass vector d is occupied (3.43) by transforming the linear differential equation (3.36) into the control standard forms (3.38). Whereas the pass vector d has the length N to combine every phase current of vector u, the output vector c deals with the state vector x. It combines all K dynamic voltage drops of the cell in the first phase, and thus every following dynamic voltage is multiplied by zero. Therefore, the output vector c has the dimension $1 \times (K + N)$.

The input matrix B and system matrix A are composed of the system parameters $C_{p,k}$ (3.44), which are the time constant $\tau_{k,n}$ (3.45) of cell n, and RC-member k, respectively. The time constant $\tau_{k,n}$ can be calculated by multiplying the corresponding RC-parameters $R_{p,k,n}$ and $C_{p,k,n}$ (3.41). For a comprehensible description, the input matrix B offers the subcomponent B_n in its diagonal, which in equation (3.38) combines all capacities of cell n with the corresponding phase current i_n. The system matrix A has the time constant of each cell in its diagonal and contains every corresponding dynamic voltage drop of the circuit.

$$y = U \tag{3.40}$$

$$\tau_{k,n} = C_{p,k,n} \cdot R_{p,k,n} \tag{3.41}$$

$$u = [i_1 \quad \cdots \quad i_N]^{\mathrm{T}} \text{ and } y_{OCV} = [U_{OC,1} \quad \cdots \quad U_{OC,N}]^{\mathrm{T}} \tag{3.42}$$

$$T_{OCV} = \overbrace{[1 \; 0 \quad \cdots \quad 0]}^{1 \times N}, \; c = \left[\overbrace{1 \quad \cdots \quad 1}^{1 \times K} \; \overbrace{0 \quad \cdots \quad 0}^{1 \times N} \right] \text{ and } d = \overbrace{\left[R_{s,1} \; 0 \quad \cdots \quad 0 \right]}^{1 \times N} \tag{3.43}$$

$$B = \begin{bmatrix} B_1 & \cdots & 0 \\ \vdots & \ddots & \vdots \\ 0 & \cdots & B_N \end{bmatrix}, \; B_n = \left[\frac{1}{C_{p1,n}} \quad \cdots \quad \frac{1}{C_{pK,n}} \right]^{\mathrm{T}} \tag{3.44}$$

$$
A = \begin{bmatrix}
-\dfrac{1}{\tau_{1,1}} & \cdots & & & & & 0 \\
\vdots & \ddots & & & & & \\
& & -\dfrac{1}{\tau_{K,1}} & 0 & & & \\
& & 0 & -\dfrac{1}{\tau_{1,2}} & & & \\
& & & & \ddots & & \vdots \\
0 & & & & \cdots & & -\dfrac{1}{\tau_{K,N}}
\end{bmatrix} \overbrace{\qquad\qquad\qquad}^{K\cdot N \times K\cdot N}
$$

(3.45)

The aim of further transformations is to transfer the nonlinear ratio y_{OCV} of the state-space representation (3.39) together with the total current I_{tot} into a new input u', and simultaneously convert the vector of all phase currents i_n into a new output y' of the differential (3.38) and output equation (3.39). This is done by linking the matrix form of both Kirchhoff's laws (3.36) and (3.37), in which the dynamic voltage drops $U_{p,k}$ are still regarded as state x. This results in a matrix-based calculation rule for phase currents (3.46). The new input u' offers handling nonlinear OCV curves very easily without computationally intensive linearisation methods that have been used in the literature thus far, except for [28].

$$
u = \begin{bmatrix} i_1 \\ \vdots \\ i_N \end{bmatrix} = R_{coeff} \cdot (Ex + Fu'), \quad u' = \begin{bmatrix} I_{tot} \\ y_{OCV} \end{bmatrix}
$$

(3.46)

The resistance coefficient R_{coeff} (3.47) is composed of the ohmic internal resistance $R_{s,n}$ of every parallel-connected cell n in the parallel circuit, whereas the resistor matrices F (3.48) and E (3.49) both couple the state vector x and newly generated input u' into the vector-based phase current calculation. The two resistor matrices are results of the linking of Kirchhoff's laws (3.36) and (3.37) under the aforementioned assumption.

$$
R_{coeff} = \left(\sum_{k=1}^{N} \prod_{\substack{i=1 \\ i \neq k}}^{N} R_{s,n} \right)^{-1}, \quad F_{n,x} = \prod_{\substack{i=1 \\ i \neq n, i \neq x}}^{N} R_{s,n}
$$

(3.47)

$$
F = \begin{bmatrix}
\prod_{\substack{i=1 \\ i \neq n}}^{N} R_{s,n} & -\sum_{\substack{x=1 \\ x \neq n}}^{N} F_{1,x} & F_{1,2} & \cdots & F_{1,x} \\
\vdots & & F_{2,1} & \ddots & \cdots & F_{2,x} \\
\vdots & & \vdots & \vdots & \ddots & \vdots \\
\prod_{\substack{i=1 \\ i \neq n}}^{N} R_{s,N} & F_{N,1} & F_{N,2} & \cdots & -\sum_{\substack{x=1 \\ x \neq n}}^{N} F_{N,x}
\end{bmatrix}
$$

(3.48)

$$
E = \underbrace{\begin{bmatrix}
-\sum_{\substack{z=1 \\ z \neq n}}^{N} F_{1,z} & F_{1,2} & \cdots & F_{1,z} \\
F_{2,1} & \ddots & \cdots & F_{2,z} \\
\vdots & \vdots & \ddots & \vdots \\
\underbrace{F_{N,1}}_{N \times K} & \underbrace{F_{N,2}}_{N \times K} & \cdots & \underbrace{-\sum_{\substack{z=1 \\ z \neq n}}^{N} F_{N,z}}_{N \times K}
\end{bmatrix}}_{N \times N \cdot K}
$$

(3.49)

Using this calculation rule in the initial and differential equations (3.38) and (3.39) produces a state-space model that requires no knowledge of current distributions (3.50)–(3.58). The currents of each string can be determined according to the matrix-based calculation rule by solving the differential equation and a consequent calculation of state x (3.46). This new algorithm enables easy modifications depending on the interconnection thanks to short computing times. The number of dynamic voltage drops can be varied for each cell to improve the voltage behaviour and number of parallel cells, with no appreciable loss of calculation performance. Even with several cells in series, each phrase can be easily simulated. This is particularly true for large battery systems, such as the Tesla Model S, where up to 86 cells are used in parallel. This newly developed calculation method achieves good validation results, as shown in Section 3.4, and represents an efficient and flexible method for dimensioning the system as well as for on-board computing. In summery the equations are:

$$\dot{x} = Ax + B\big[R_{coeff} \cdot (Ex + Fu')\big] \tag{3.50}$$

$$y' = T_{OCV} \cdot y_{OCV} + cx + d\big[R_{coeff}(Ex + Fu')\big] \tag{3.51}$$

$$\Rightarrow \dot{x} = A'x + B'u' \quad \text{and} \quad y = T_{OCV} \cdot y_{OCV} + c'x + d'u' \tag{3.52}$$

$$\text{with} \quad A' = A + BER_{coeff} \quad \text{and} \quad B' = BFR_{coeff} \tag{3.53}$$

$$u' = \begin{bmatrix} I_{tot} \\ y_{OCV} \end{bmatrix} \tag{3.54}$$

$$x = [U_{p,1,1} \quad \cdots \quad U_{p,K,1} \quad U_{p,1,2} \quad \cdots \quad U_{p,K,N}]^{\mathrm{T}} \tag{3.55}$$

$$c' = c + dER_{coeff} \quad \text{and} \quad d' = dFR_{coeff} \tag{3.56}$$

3.3 Model parameterisation

In this work, the battery cell parameters of different cells were determined. Table 3.3 shows the basic information of the cells. All cells were parametrised in terms of capacity, OCV, and internal resistance measurements. For further measurements of current distribution, parameter sets of two temperatures were necessary. Therefore, the measurements took place in temperature chambers at 10 and 25 °C. Capacity, pulse impedance, OCV, hysteresis, and validation measurements were performed with a BaSyTec Cell Test System (CTS). Additional EIS measurements were performed with a Bio-Logic VMP3 potentiostat. These parametrisations are precise, extensive, and time-consuming. Therefore, only two to seven cells were treated this way. All cell types have a short name shown in Table 3.3, which is used for further identification in this work.

Table 3.3:   *Basic parameters of the lithium-ion battery cells used in this work [198–200, 202, 204]*

Producer	LG Chem Ltd.	Panasonic Corporation	Samsung SDI Co., Ltd.	Sony Corporation	LG Chem Ltd.
Type	ICR18650 HB2	NCR18650 PF	INR18650-25R	US26650 FT	INR18650 MJ1
Short name	LG_HB2	Pan_PF	Sam_25R	Sony_FT	LG_MJ1
Capacity	$C_n = 1.5$ Ah	$C_n = 2.7$ Ah	$C_n = 2.5$ Ah	$C_n = 3.0$ Ah	$C_n = 3.5$ Ah
Current limits (charge ǀ discharge)	4 A ǀ 30 A	1.44 A ǀ 10 A	4 A ǀ 20 A	3 A ǀ 20 A	3.5 A ǀ 10 A
Voltage limits (charge ǀ discharge)	4.2 V ǀ 2.0 V	4.2 V ǀ 2.5 V	4.2 V ǀ 2.5 V	3.6 V ǀ 2.0 V	4.2 V ǀ 2.5 V
Dimensioning	HP	intermediate	HP	intermediate	HE
Year of market launch	2011	2012	2014	2013	2016
Electrode chemistry (cathode ǀ anode)	NMC ǀ graphite	NCA ǀ graphite	NCA ǀ graphite	LFP ǀ graphite	NMC ǀ graphite and silicon [190]

3.3.1   Capacity determination

The capacity determination was similar to the norm ICE 62660-1 [42]. First, it was necessary to equalize the cell temperature in the temperature chamber. Then, the measurement procedure followed the steps in Figure 3.7:
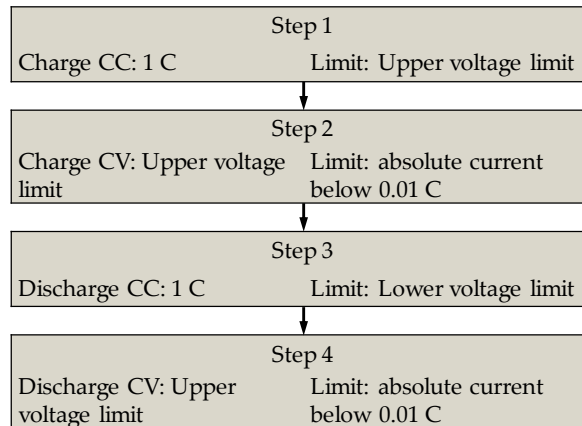
Figure 3.7:   *Flow chart of the capacity determination measurements*

The cell capacity calculation followed equations (3.57) to (3.59). The capacity is the current integral of the discharge in Steps 3 and 4.

$$C_{m,CC} = \int_{start\ Step\ 3}^{end\ Step\ 3} i \, \mathrm{d}t \qquad (3.57)$$

$$C_{m,CV} = \int_{start\ Step\ 4}^{end\ Step\ 4} i \, \mathrm{d}t \qquad (3.58)$$

$$C_{m,CCCV} = C_m = C_{m,CC} + C_{m,CV} \tag{3.59}$$

To eliminate random errors, measurement steps 1 to 4 were repeated three times. C_m is the arithmetic mean of all valid values without outliers. The boxplot of Figure 3.8 shows the measured CCCV cell capacities at two different temperatures T: 10 and 25 °C. Three cells of each type were analysed. The cell numbering starts with MHH or EEBatt. The left axis indicates the Ah values and the right axis indicates the normalised capacities. A normalised capacity of one is the mean value of all measurements of this cell type.
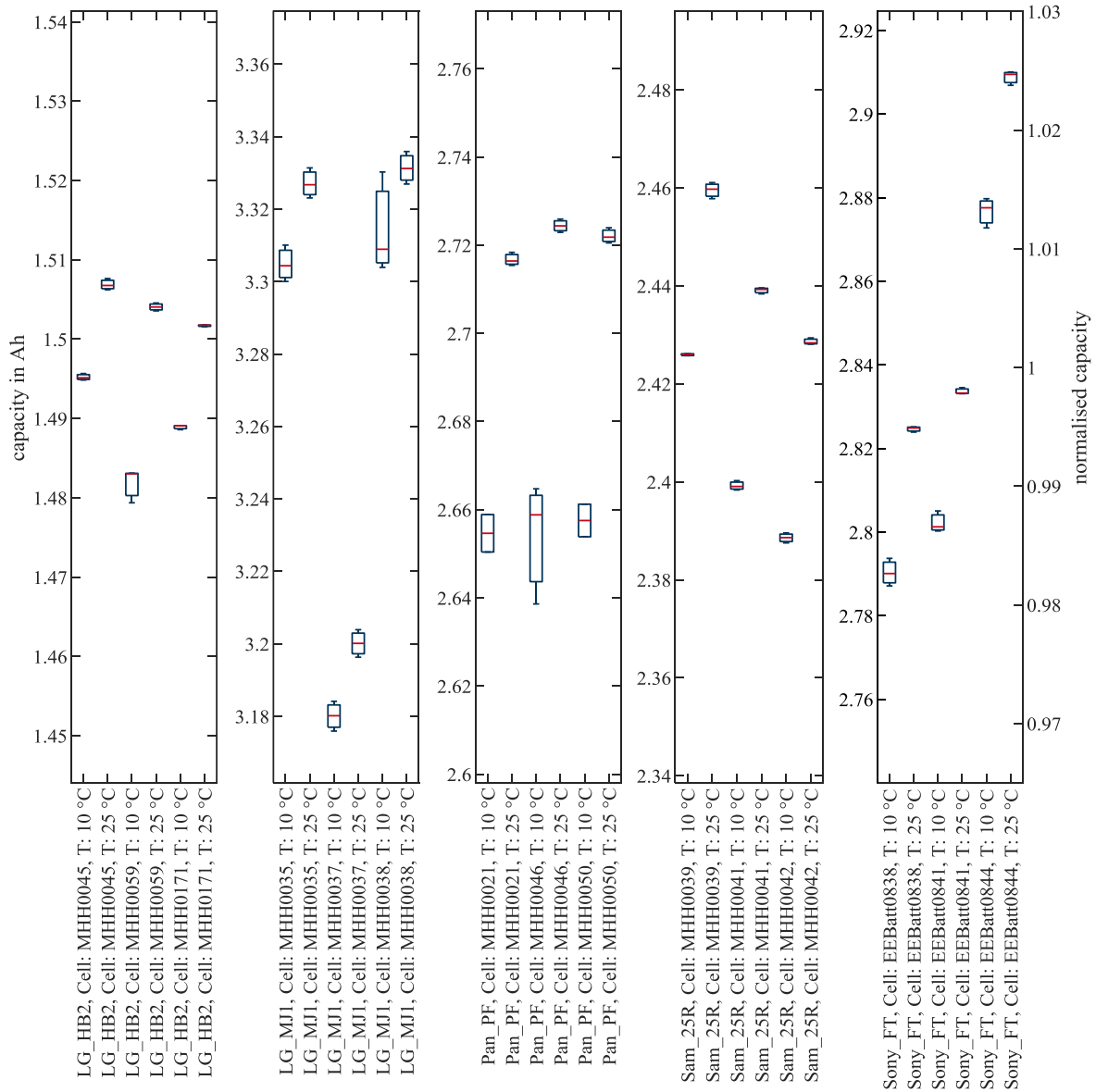
Figure 3.8:   *Box plot of capacity measurements at 10 and 25 °C of three cells of LG_HB2, LG_MJ1, Pan_PF, Sam_25R, and Sony_FT (the second y-axis at the right side refers to all subplots)*

The deviation between the three measurements was below 1 %. In all cells, the capacity of the 25 °C measurement was higher than the 10 °C measurement. The differences rank from the lowest in the LG_MJ1 cell (0.5 %) to the highest in the Pan_PF cell (2.6 %).

3.3.2   Internal impedance parameter determination

Impedance parameters of lithium-ion cells depend on several influencing factors such as temperature, SoC, current direction, and current rate [23]. Furthermore, the parameters of one cell type vary because of variations in the production process, and the cells change their parameters while ageing. A more detailed explanation was provided in Subsection 2.2.2.

For current distribution analysis, a precise cell voltage calculation is required in all situations. The equalisation processes of current distribution take time in the range of minutes or hours, as shown in Figure 3.3 in Section 3.1. Therefore, long-term voltage calculations must be ensured. The current dependence of the parameters is small in the operational area of cells [211]. Hence, the influence of current was not considered. The model parameters were averaged between the impedance at charge and discharge pulses.

Predicting parameter changes during ageing is difficult; it depends on the ageing mechanisms. Detailed explanations can be found in Subsection 0 and in Birkl et al. [26]. In this work, the impedance parameters of the simulations did not change while the cells were in use because of ageing. Instead, specific parameter sets were extrapolated from new cell parameters and literature dates, such as from Ecker et al. [102].

The impedance parameters were estimated with pulse measurements. The model consisted of the OCV, ohmic resistance R_S, and a row of RC elements connected in series. An analytic calculation gives the initial value of the ohmic resistance R_S by the division of the voltage step ΔU_{Step} using the absolute value of the current pulse $|I_{Pulse}|$ between the last measured data point before and the first after the current pulse. The Basytec CTS instrument uses a sample rate of 1 MS:

$$R_S = \frac{\Delta U_{Step}}{|I_{pulse}|} \tag{3.60}$$

Therefore, the voltage difference between the last sample point when current flows and the first sample point after the current pulse was calculated. With that, the ohmic law allows a resistance to be calculated, which can be assumed as the ohmic resistance of the cell. This method provides good results at a simulation step size in the range of seconds. Section 3.4 provides a validation with the dynamic load profile of Campestrini et al. [212] which includes a variation of the dynamic.

Figure 3.9 illustrates the procedure of these tests. A pulse of $\Delta SoC = 5$ % with a current rate of 1 C excites the cell, which occurs at every 5 % of the SoC in the discharge direction, as illustrated in Figure 3.9, as well as in the charge direction. When the pulse hits the lower voltage limit minus 0.1 V or the upper voltage limit plus 0.1 V, the current is reduced. All measurements were conducted in temperature chambers once at 10 and once at 25 °C.

Step 1
Charge CC: 1 C | Limit: Upper voltage limit

Step 2
Charge CV: Upper voltage limit | Limit: absolute current below 0.1 C

Step 3
Discharge CC: 1 C | Limit: ΔSoC > 5 % or 19 iterations

Voltage limit

Step 4
Relaxation | Limit: 2 h

no

yes

Step 5: End
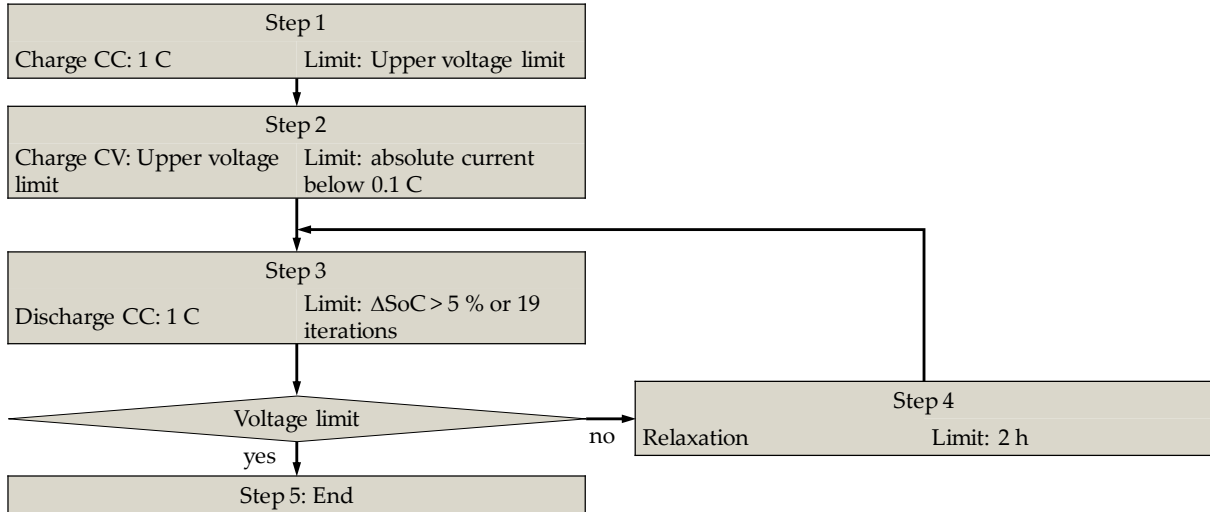
Figure 3.9: *Test plan of the measurements for impedance calculation. The flow chart shows the process of using negative pulses from 100 to 0 % of the SoC. The test with positive pulses discharges the cell at steps 1 and 2. In step 3, the cell is charged in 5 % steps*

Figure 3.10 (a) illustrates the data that go into the fitting process to fit the impedance parameters. The data consist of the overvoltage values in the time as well as the current pulse and overvoltage values in the same length of the relaxation phase. The overvoltage is fitted with an EEC consisting of one OCV, one ohmic resistance, and several RC elements. It is assumed that the voltage at the end of 2 hours of relaxation is the OCV. From that point, the overvoltage can be calculated as the difference between this voltage and the measured cell voltage.

The model in Section 3.2 can handle a variable number of RC elements K per cell. In addition, the fitting can calculate the parameters of a variable number of RC elements. For the choice of starting parameter of the fitting process, the time constants of the RC elements are spread equally from zero to the length of the measured data. It is possible to do so on a linear $\tau_{k,lin}$ or logarithmic scale $\tau_{k,log}$, which is the user's choice. The smallest time constant τ_1 correspondends to twice the step size of the simulation. The initial parameter of R_k comes from equation (3.63), where the overvoltage at time τ_k is multiplied by the absolute value of the high of the current pulse I_{pulse}.

$$\tau_{k,lin} = \tau_1 + (k-1) \cdot \frac{\tau_K - \tau_1}{K-1} \text{ and } k \in [1..K] \tag{3.61}$$

$$\tau_{k,log} = 10^{\log_{10}\tau_1 + (k-1) \cdot \frac{\log_{10}\tau_K - \log_{10}\tau_1}{\max(k-1)}} \text{ and } k \in [1..K] \tag{3.62}$$

$$R_k = \frac{U_{OV,\tau_k}}{|I_{pulse}|} \tag{3.63}$$

$$C_k = \frac{\tau_k}{R_k} \tag{3.64}$$

The fitting process uses the MATLAB function "fmincon" from the Optimization Toolbox. This nonlinear programming solver finds the minimum of a problem specified by

$$\min_x f(x) \text{ such that } \begin{cases} c(x) \leq 0 \\ ceq(x) = 0 \\ A \cdot x \leq b \\ Aeq \cdot x = beq \\ lb \leq x \leq ub \end{cases} \tag{3.65}$$

where b and beq are vectors, A and Aeq are matrices, $c(x)$ and $ceq(x)$ are functions that return vectors, and $f(x)$ is a function that returns a scalar. Furthermore, $f(x)$, $c(x)$, and $ceq(x)$ can be nonlinear functions, and x, lb, and ub can be passed as vectors or matrices. [213]

The fitting results show that five RC elements are a good compromise between accuracy and calculation efforts. Because the OVC at the fitting is measured at 0.05 C CC current and the fittings take place at different SoCs and temperatures, this model is of the type $OCV_{mea\_0.05C}(SoC) + \underline{Z}_{R.5RC}(SoC, T)$. Figure 3.10 shows the simulated and measured overvoltages of the pulses and the absolute simulation error at different SoCs. The fitting includes the pulse and the subsequent relaxation phase of the same length as the pulse.
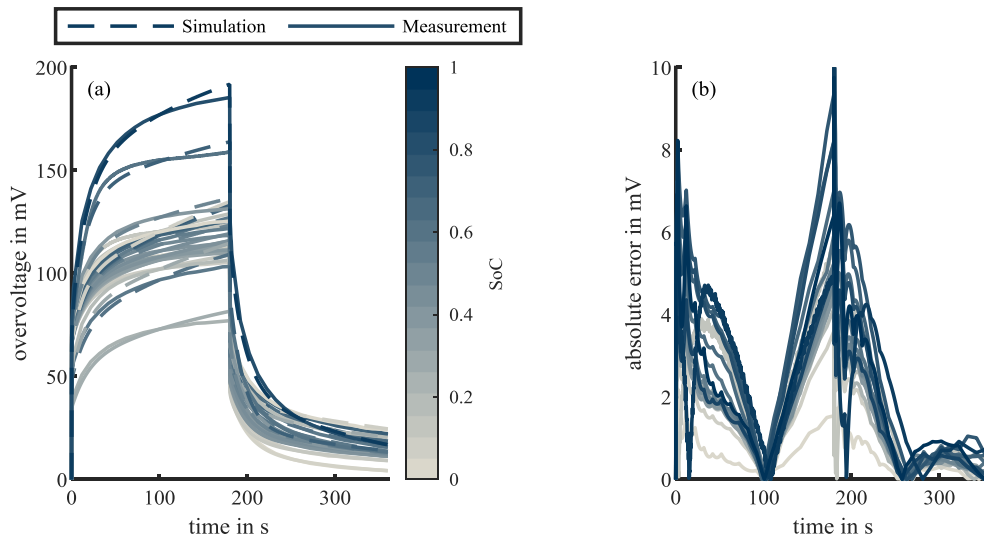
Figure 3.10:   *Simulated and measured overvoltages (a) and the absolute simulation error (b) at different SoCs. The simulation used an EEC with five RC elements in the Sony_FT cell at 25 °C (model type: $OCV_{mea\_0.05C}(SoC) + \underline{Z}_{R,5RC}(SoC, T)$)*

Because the pulse measurements were performed at two temperatures (10 and 25 °C) and in positive and negative pulse directions, the fitting resulted in four parameter sets per cell. The results at different pulse directions were averaged as the differences were small. Figure 3.11 illustrates all parameters of one Sony_FT cell depending on the SoC and temperature. Cold cells at 10 °C exhibit larger overvoltages than cells at 25 °C. Especially at low temperatures, the real part of the impedance at a low SoC is higher than for other SoCs. The capacities C_P do not show a trend with the SoC. The basic behaviour of the other cells used in this work is similar to that in Figure 3.10 and Figure 3.11. These results are in accordance with other publications, such as Waag et al. [211].
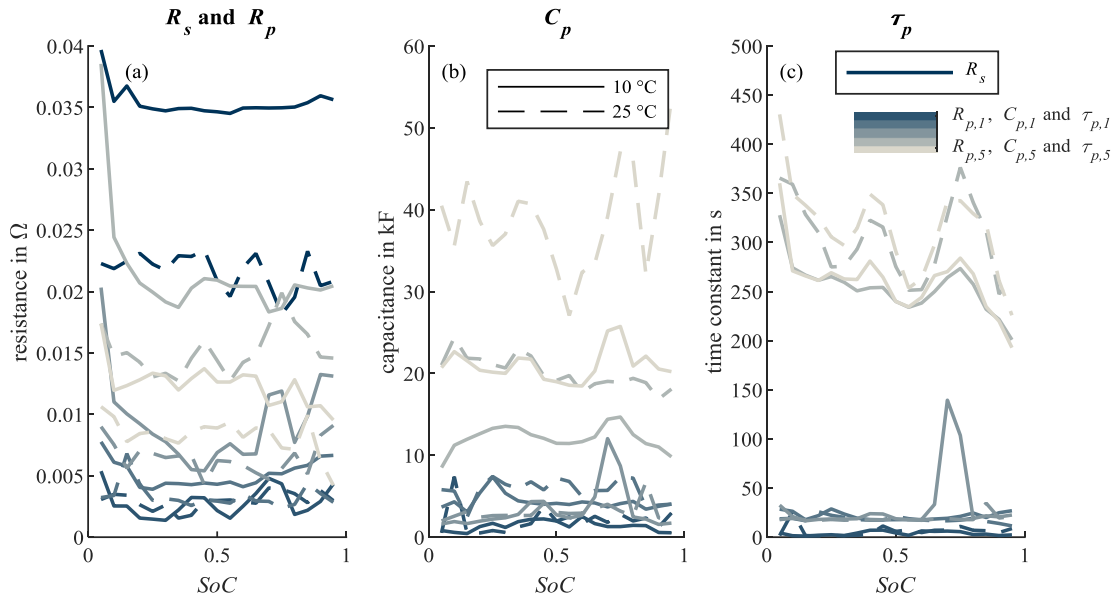
Figure 3.11: *Impedance parameter of one Sony_FT cell depending on the SoC and tempera-*
ture, (a) resistance, (b) capacitance, and (c) time constant (impedance parame-
ters R_S, $R_{p,1...5}$, $C_{p,1...5}$ and $\tau_{p,1...5}$ from dark blue to grey)

3.3.3 Open-circuit voltage determination

As shown in Section 3.1 the slope of the OCV has a significant influence on the current distri-
bution. Therefore, the method used for OCV determination is crucial. Two methods are com-
mon:

+ Constant current discharge and charge at low current
+ Stepwise relaxation at different SoCs

The first method uses a small current to discharge and charge the cell between 100 and 0 % of
the SoC. The OCV is the average between the discharge and charge voltage. The process is
simple and provides a high resolution in terms of SoC supporting points. Because of this res-
olution, it is possible to calculate the differential voltage and incremental capacity spectra. Fig-
ure 3.12 shows the OCV curves of five lithium-ion battery cells used in this work. The c-rate
of these measurements was 0.05 C and the temperature was 25 °C.

The second option for determining the OCV is to perform the measurements in a stepwise
manner. Figure 3.13 shows the SoC steps in the diagram (a). Each step includes a CC current
to go to the next SoC and a relaxation phase of 3 hours to relax to the OCV. Figure 3.13 (b)
shows the cell voltage and current of one step. This procedure is a part of the hysteresis meas-
urements described by Zhu et al. [109]. The OCV voltage U_{OC} is shown in Figure 3.13 (b) with
a red cross. These values are affected by the voltage hysteresis. To eliminate this effect, the
mean value between the maximal OCV values $U_{OC,max}$ and minimal values $U_{OC,min}$ over the
SoC is calculated:

$$U_{OC,\text{min}} = \begin{pmatrix} \min_{SoC=0} U_{OC} \\ \min_{SoC=0.05} U_{OC} \\ \vdots \\ \min_{SoC=1} U_{OC} \end{pmatrix} \quad \text{and} \quad U_{OC,\text{max}} = \begin{pmatrix} \max_{SoC=0} U_{OC} \\ \max_{SoC=0.05} U_{OC} \\ \vdots \\ \max_{SoC=1} U_{OC} \end{pmatrix} \tag{3.66}$$

$$U_{OC} = \frac{U_{OC,\text{min}} + U_{OC,\text{max}}}{2} \tag{3.67}$$
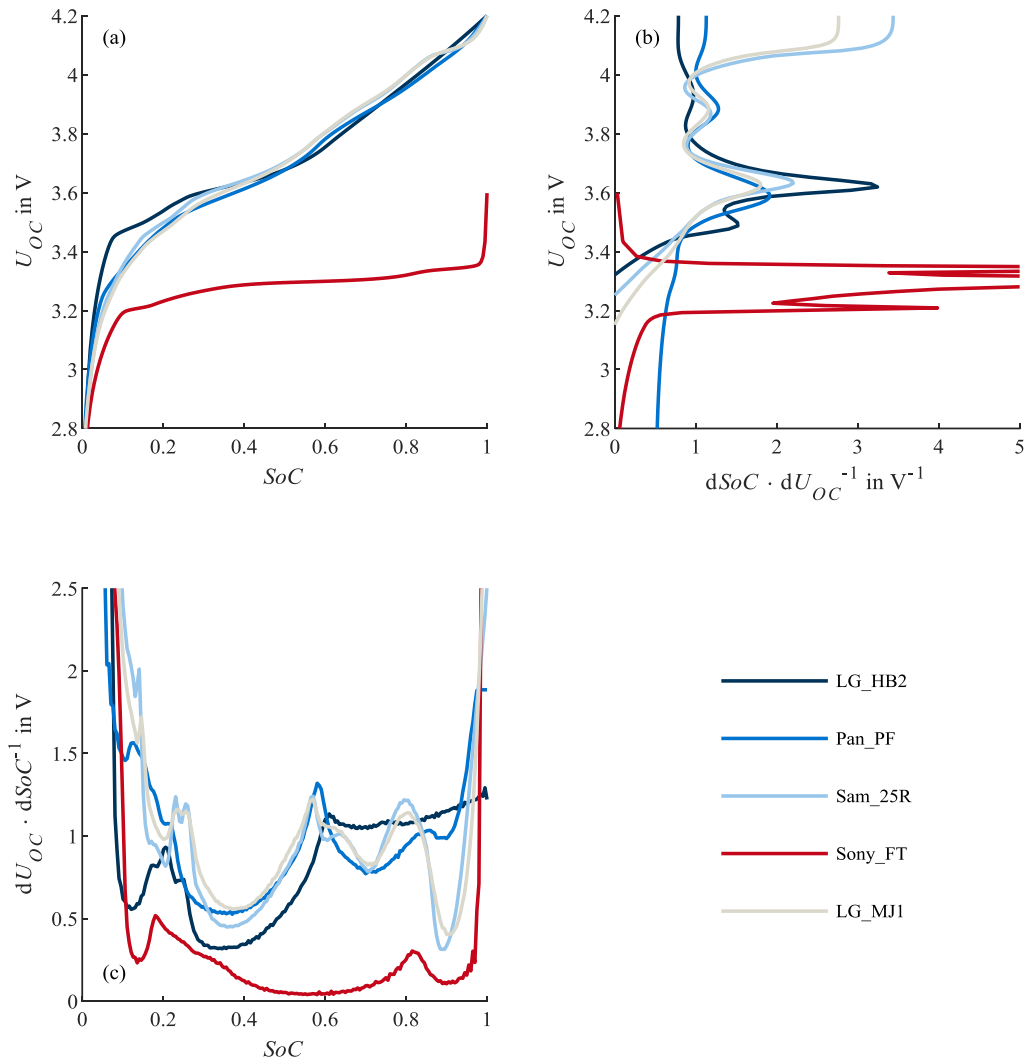
Figure 3.12: *OCV curves of the five battery cells at 25 °C: (a) OCV over SoC, (b) differential voltage spectrum OCV over $dSoC/dOCV$, and (c) incremental capacity spectrum $dOCV/dSoC$ over the SoC*

Figure 3.14 compares OCVs determined in four different ways. The solid lines in the diagrams (a) to (e) were calculated CC measurements at the c-rates of 1 C, C/10, and C/100. The dashed line comes from the stepwise measurement. The ambient temperature for all of these tests was 25 °C. In the second row of diagrams, (f) to (j) indicate the different slopes of the measurements

with CC. A high current leads to filtering of the OCV slope, and the peaks in the DVA shrink. Results of current distribution in battery cells in the literature allow the assumption that this is caused by an asymmetric current and SoC distribution in the cell [127, 130, 154]. The OCV coming from stepwise measurements has too few sampling points to calculate the DVA. Subsection 5.4.2 goes into detail about the variation of the slope of the OCV on the current distribution between parallel-connected cells.
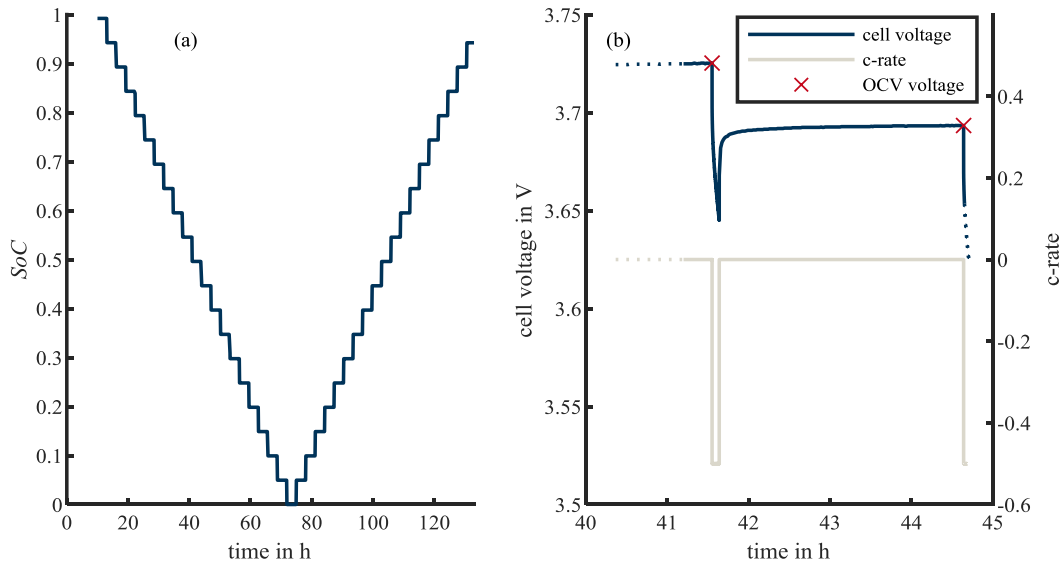
Figure 3.13:   *Procedure of the stepwise OCV calculation from hysteresis measurement described by Zhu et al. in [109]*

At a c-rate of 1 C and an SoC close to 1, a horizontal line can be seen in the diagrams (g), (h), and (j). Because the maximum cell voltage is limited, it is not possible to obtain the OCV until an SoC of 1 using a current of 1 C because of high overvoltages. Hence, an extrapolation of the OCV at high SoC is necessary, which leads to a horizontal line in the DVA. The last row of diagrams, (k) to (o), shows the voltage difference between the OCV measurement at a c-rate of C/100 and all other OCVs.
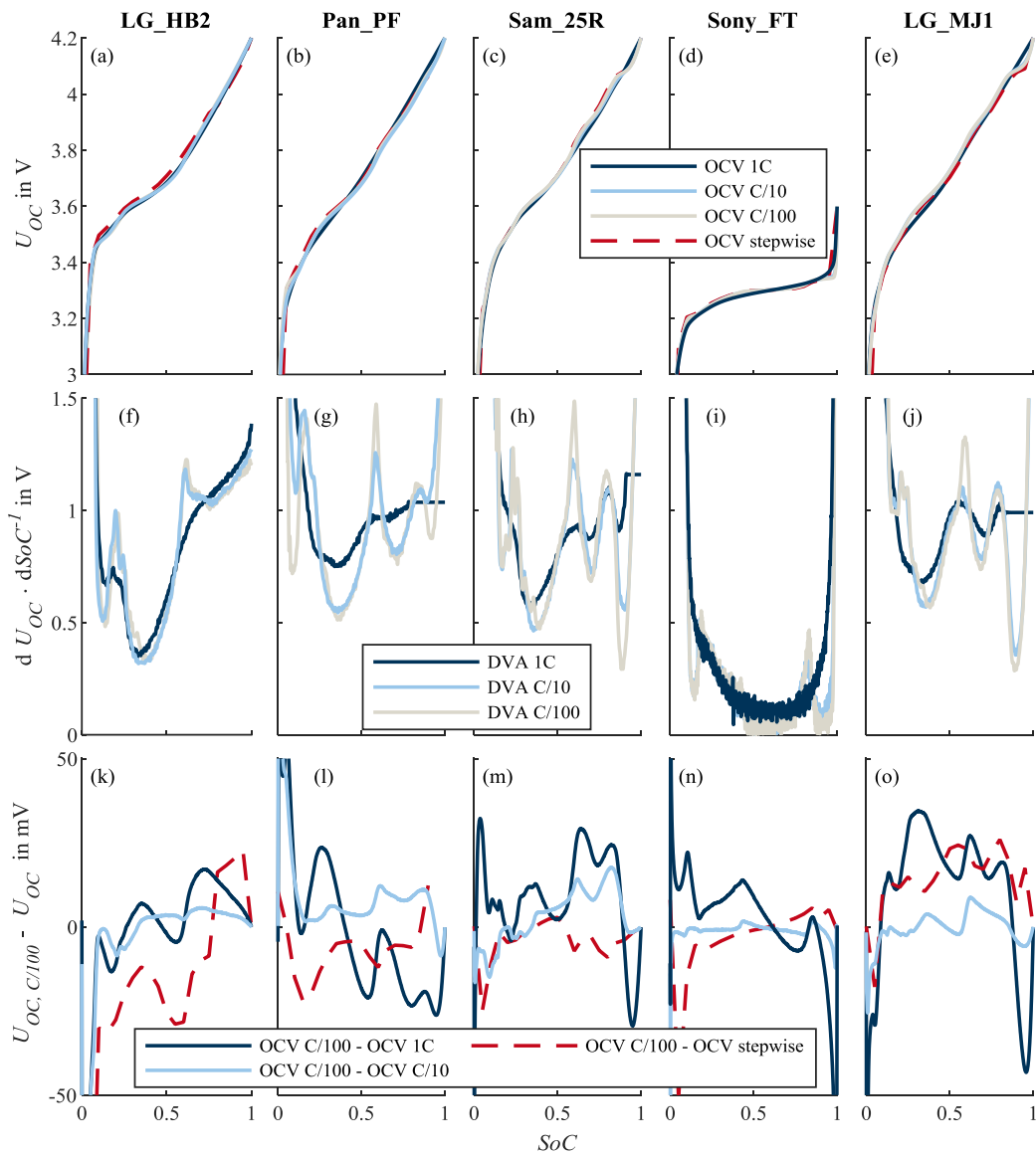
Figure 3.14: *OCV curves of the five battery cells. Diagrams (a) to (e) show the OCV over the SoC. Each consists of four different measurements. The solid lines are from CC measurements with c-rates of 1 C, C/10, and C/100, whereas the dashed lines are from stepwise measurements. In the second row of diagrams, (f) to (j) show the DVA of the OCVs in the first row. The stepwise measurement has too few sampling points to calculate the DVA. In the last row of diagrams (k) to (o), the difference of the OCV measured with the lowest current and all other OCVs is illustrated.*

3.3.4 Hysteresis

To accurately model the cell voltage, a hysteresis calculation is also necessary. Several papers have shown an SoC-dependent effect of some 10 mV in lithium-ion cells [110, 214, 215] with different cathode materials. Zhu et al. described a procedure for measuring hysteresis, which has already been discussed in the previous subsection.

The measurement consists of a stepwise approach of SoCs in a step size of 5 %. At every change of the SoC's direction, the number of steps is reduced by one step (compare Figure 3.13 (a)). Furthermore, there are three minor loops performing the same procedure as in SoC ranges from 10 to 50, 30 to 70, and 50 to 90 %. Each approach of the SoCs is performed with a current of 0.5 C and followed by a relaxation phase of 3 hours. At the end of the relaxation phase, the OCV including hysteresis is reached. These points are marked with a red cross at an exemplary step in Figure 3.13 (b).

These data allow the hysteresis limits of each SoC to be calculated. Figure 3.15 (a) shows the absolute difference between the minimal and maximal OCV curve of all cells and the temperatures 10 and 25 °C. Notably, a voltage difference of only < 5 mV exists between the two temperatures in most cases. The range of hysteresis of different cell chemistries is in the same magnitude. With the maximum and minimum OCV values, it is possible to determine the mean OCV, which is a stepwise calculated OCV. A detailed description of this can be found in Subsection 3.3.3. Figure 3.15 (b) shows the difference between the stepwise calculated OCV and an OCV measured with a CC current of C/20.

In this work, a simplified hysteresis calculation was used. The sum of all hysteron states $\gamma[u(t)]$ divided by the number of hysterons N gives a normalized factor. The data in Figure 3.15 (a) shows the maximum absolute hysteresis. The output of the model is unitless and multiplied with the SoC-dependent maximum of absolute hysteresis data divided by two, $w(SoC)$:

$$y(t) = \frac{w(SoC)}{N} \sum \gamma[u(t)] \tag{3.68}$$

The limits of α and β are necessary for the Preisach calculation; see Figure 2.8 on page 19. The assumption applies that $\alpha_{max} = \beta_{max}$. With the measurements of Figure 3.13, a maximum, minimum, and mean OCV can be calculated. When the SoC progression changes its direction, the hysteresis changes from increasing to decreasing or vice versa. The difference between the turning point and crossing of the OCV, including the hysteresis and the mean OCV without hysteresis, corresponds to $\alpha_{max}/(1 + \sqrt{2})$ because of the quadratic relation coming from the Preisach model. The SoC difference between the maximum and minimum curve can be determined only when one of these curves is reached at the turning point. From the paper of Baronti et al., a range of α and β of approximately 10–20 % can be expected [110]. Hence, only turning points were used for this type of calculation with a history of SoC changes larger than 20 %. Table 3.4 summarises all α and β parameter at 10 and 25 °C. The values were averaged from all calculations at the usable turning points.
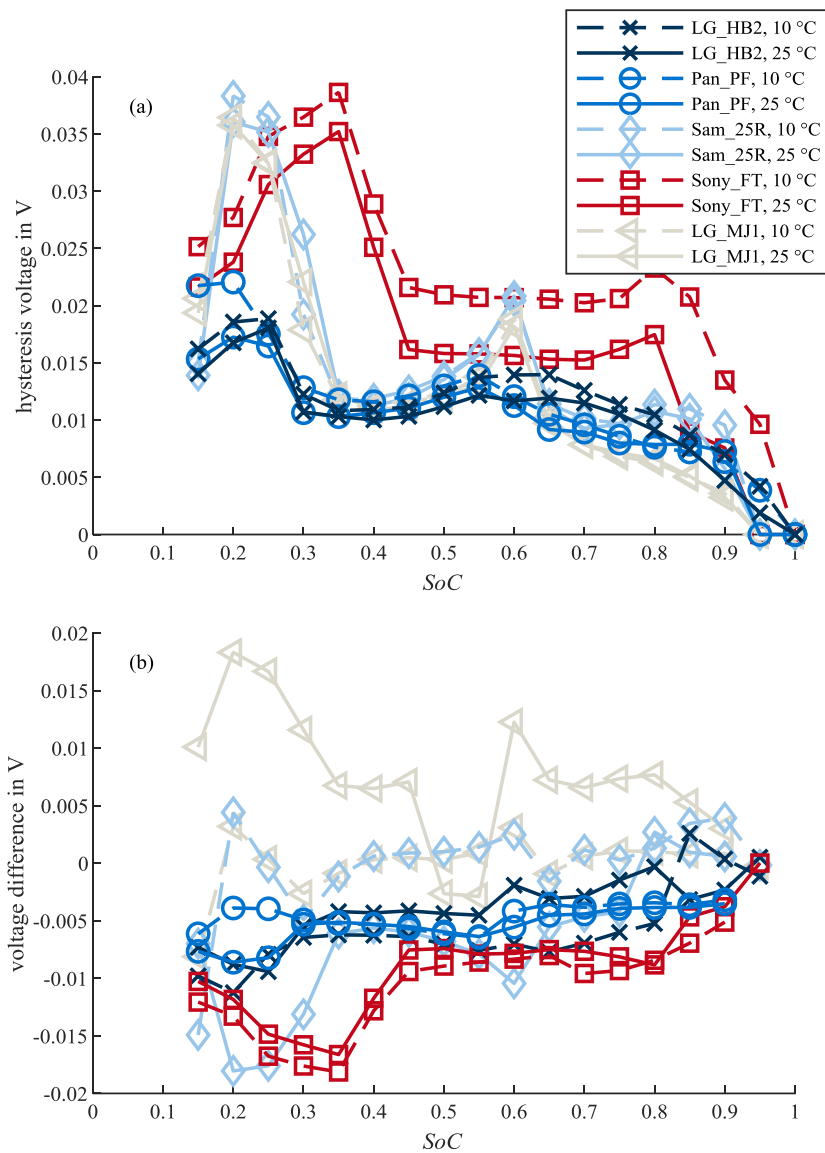
Figure 3.15: *Voltage range of the hysteresis of all cells. Diagram (a) shows the absolute voltage difference between charge and discharge. Diagram (b) shows the difference between the OCV measured with C/20 CC and the mean OCV out of the hysteresis measurements.*

Table 3.4: *Range of α and β from the maximum to minimum hysteresis and vice versa*

Cell	LG_HB2	Pan_PF	Sam_25R	Sony_FT	LG_MJ1
α_{max} and β_{max} at 10 °C	0.11	0.13	0.18	0.10	0.16
α_{max} and β_{max} at 25 °C	0.16	0.17	0.20	0.08	0.20

3.3.5   Entropy

The change of entropy of lithium-ion battery cells ΔS results in the thermodynamic potential. This can be calculated from the change of reaction enthalpy ΔH, which is the chemical energy stored in a chemical compound minus the free reaction enthalpy ΔG, which is the maximum energy that can be transformed into electrical energy divided by the temperature T:

$$\Delta S = \frac{\Delta H - \Delta G}{T} \tag{3.69}$$

The equilibrium potential at standard conditions (one molar concentration) U_{OC_S} is followed by dividing the free reaction enthalpy by the number of exchanged electrons z and the Faraday constant F:

$$U_{OC\_S} = -\frac{\Delta G}{z \cdot F} \tag{3.70}$$

The Nernst equation (3.71) allows for calculating the equilibrium potential at temperature T. In this calculation, Red and Ox stand for the chemical activity of the reduced and oxidised forms of the reactants:

$$U_{OC} = U_{OC\_S} + \frac{R \cdot T}{z \cdot F} \cdot \ln \frac{[Red]}{[Ox]} \tag{3.71}$$

From (3.70) and (3.71) we get the relation between the temperature coefficient (entropic coefficient) of the OCV and the reaction enthalpy:

$$\frac{\mathrm{d}U_{OC}}{\mathrm{d}T} = -\frac{\Delta S}{z \cdot F} \tag{3.72}$$

Figure 3.16 shows the entropic coefficients of NMC, NCA [216], and LFP | graphite [144, 217, 218] full cells. This means that parallel-connected battery cells with different temperatures have different OCVs at similar SoCs.
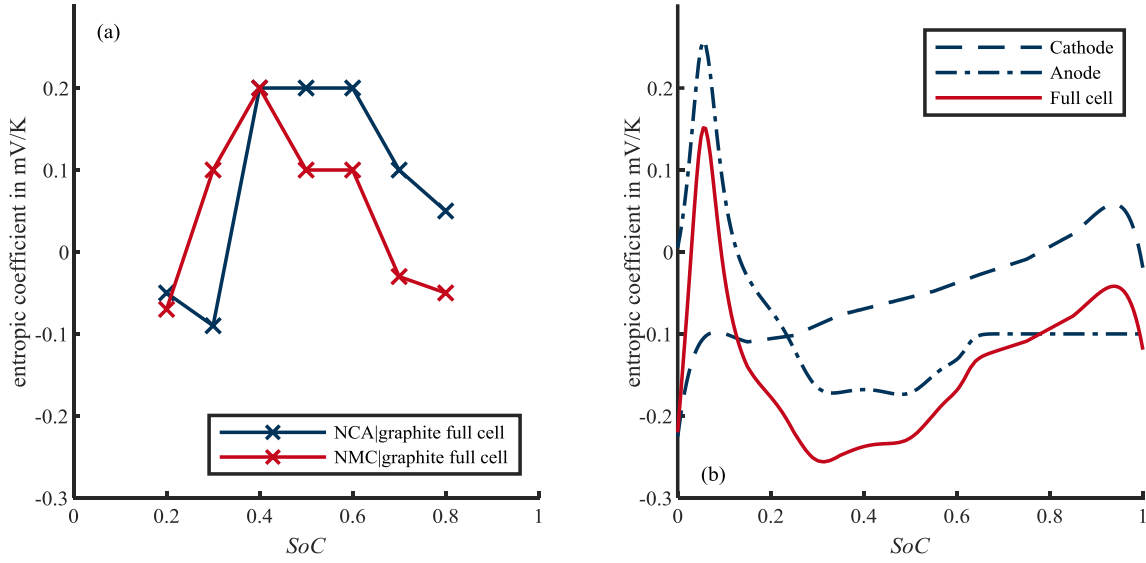
Figure 3.16: *Entropic coefficients (a) of NCA and NMC | graphite full cells and (b) of cathode, anode, and full cell LFP | graphite cells. The data in diagram (a) are from Eddahech et al. [216] and those in diagram (b) are from Li et al. [217], Guo et al. [218], and Rumpf et al. [144].*

3.4 Model validation

The model validation consisted of two steps. First, the cell voltage simulation of a single cell had to be valid. In the second step, the simulation of the current distribution at different dynamic load profiles was checked. Self-produced sections of [28] are partially contained in this chapter without any further reference.

3.4.1 Cell voltage simulation

Campestrini et al. described a validation profile used to validate the cell voltage calculation of the EEC model [212]. It includes positive and negative pulses with varying lengths at 10, 50, and 90 % of the SoC. Figure 3.17 presents the results of the validation of the cell's overvoltage exemplarily of a Sony_FT cell at 10 % of SoC with the model type $OCV_{mea\_0.05C}(SoC) + \underline{Z}_{R,5RC}(SoC, T)$. The root mean square (RMS) error e_{RMS} is calculated with the following equations using all simulated and measured data points nb. The validation at 50 and 90 % of SoC both result in an RMS error of $e_{RMS} = 0.0033$ V.

$$e_{RMS} = \sqrt{\frac{1}{nb} \cdot \sum_{1}^{nb} |i_{sim} - i_m|^2} \tag{3.73}$$
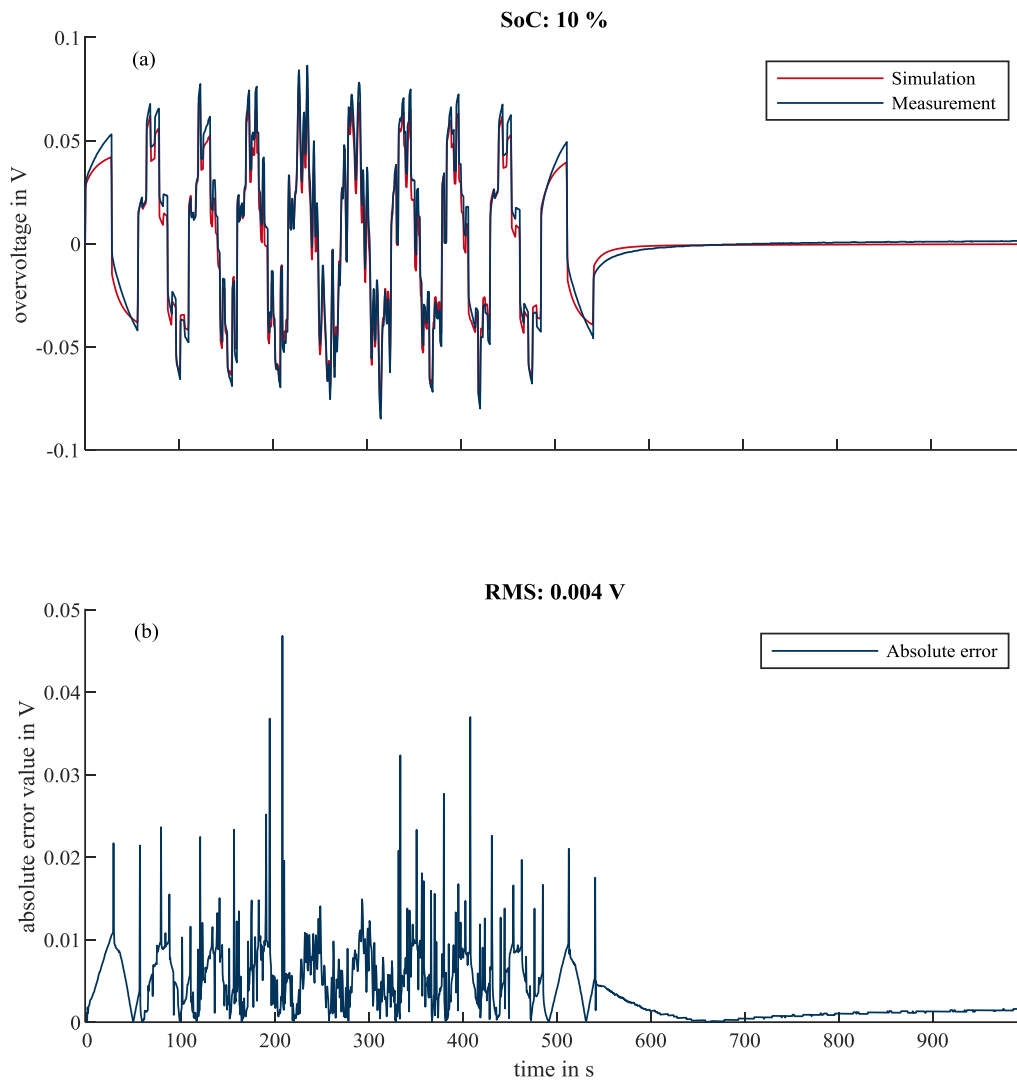
Figure 3.17: *Validation of the overvoltage simulation of a Sony_FT cell at 25 °C and the SoC of 10 %. This simulation does not include hysteresis effects. The load profile comes from Campestrini et al. [212] and includes various dynamics. The error in (b) is the absolute voltage difference between measurement and simulation.*

The hysteresis model is validated in Figure 3.18. The diagram presents measured and simulated hysteresis data of a Sony_FT cell at 25 °C. Because of the flat OCV of the LFP cathode material, the hysteresis is more relevant than in cells with steeper OCVs. The Preisach model, described in Subsection 2.2.4, provides the results of the simulation. In Section 3.3, the parametrisation is explained. In the diagram, the "x" markers stand for the voltage after a relaxation phase of 3 hours. Simulations and measurements showed good correlation, especially at SoCs larger than 10 %.
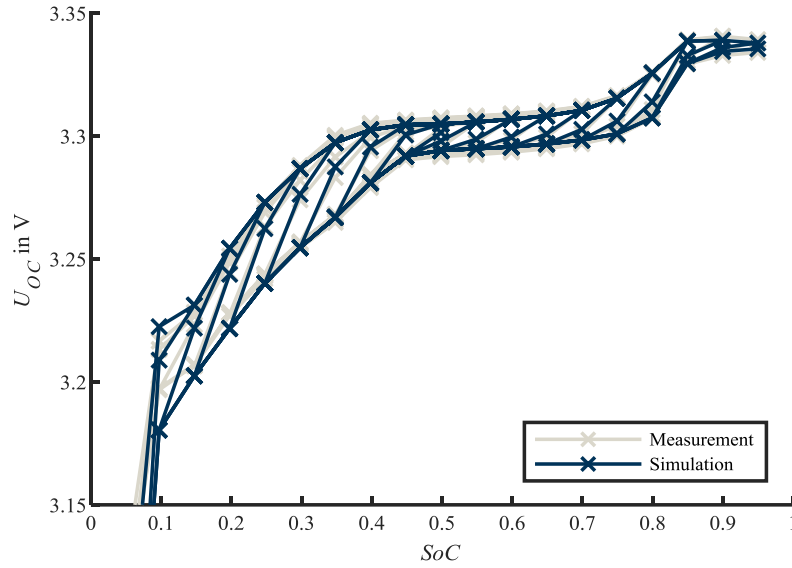
Figure 3.18: *Validation of the hysteresis simulation. The diagram shows the measured and simulated hysteresis of the Sony_FT cell at 25 °C*

3.4.2 Current distribution calculation

An EEC model with different parameter sets was used to show different influences. To validate the EEC, an HP cell from LG (LG_HB2) and an HE cell from Panasonic (Pan_PF) were connected in parallel. This constellation can represent an impedance difference on the one hand and a capacity difference on the other. Further parameter studies were conducted using a virtual cell with a capacity of 1.00 Ah. Whereas the ohmic resistance and RC circuit models of the real cells displayed a good correlation, the virtual cell model consisted of one ohmic resistance, one ZARC element, and one WB element. This model is flexible and could be described with only a few parameters. These nonlinear elements were approximated with five RC circuits for the ZARC and 15 for the WB element, as suggested by Moss et al. [79] with the ionic impedance parameters R_W and C_W and the time constant τ_W:

$$k_1 = \frac{\tau_W}{C_W} = R_W \tag{3.74}$$

$$k_2 = \frac{\sqrt{\tau_W}}{C_W} = \sqrt{\frac{R_W}{C_W}} \tag{3.75}$$

$$C_{WB,n} = \frac{k_1}{2k_2^2} \tag{3.76}$$

$$R_{WB,n} = \frac{8k_1}{(2n-1)^2 \cdot \pi^2} \tag{3.77}$$

An analytical transformation of the ZARC into RC circuits is not known. Buller presented an empirical approach to modelling a ZARC element using five RC circuits, which was used in the present work [44]. All equations that can be used to calculate the impedance of different elements are presented in Table 2.1.

Therefore, varying a few parameters can influence the current behaviour in a certain frequency range. To obtain valid results, a measured OCV characteristic was used in the EEC of the real

cells. In the case of the virtual cell, a linear OCV was assumed. This helped to separate influences on the parameter variations. Table 3.5 provides an overview of the models and parameters used for the validation of the current distribution and dynamic analysis.

Table 3.5:   *Parameters of the HP, HE, and virtual cells. The HP and HE cells validated the model, and the virtual cell was systematically varied to investigate the effects of dynamic load profiles in chapters 5.1 and 5.4*

	HP cell for validation	HE cell for validation	Virtual cell for further parameter studies
Type	LG ICR18650HB2	Panasonic NCR18650PF	virtual
Model	$OVC_{mea\_0.05C}(SoC) + \underline{Z}_{R,3RC}(SoC)$	$OVC_{mea\_0.05C}(SoC) + \underline{Z}_{R,3RC}(SoC)$	$OVC_{lin}(SoC) + \underline{Z}_{R,20RC}$
Capacity	$C_m = 1.52$ Ah	$C_m = 2.90$ Ah	$C_n = 1.00$ Ah
OCV	measured	measured	virtual

Measurements and simulations of the combination of one HE and one HP cell were performed to validate the model. A CC discharge with a depth of discharge (DoD) of more than 80 % represents long-term effects; see Figure 3.19 (a). Sine half-waves with a varying cycle duration ($T = 0.001 \dots 1000$ s) were used to test the validity of the dynamic behaviour of the model; see Figure 3.19 (a).

A BaSyTec GSM and a BioLogic SP-300 (in case of $T = 0.001$ s or $T = 0.1$ s) instrument were used to provide up to -10 A at 25 °C during the short sine half-waves of up to 10 s starting at 100 % SoC. The test setup further consisted of a clamping construction that allowed 18650 or 26650 battery cells to be connected to soldering tags in parallel. In the test bench, a shunt of 1 mΩ created a voltage drop in each battery string. This voltage drop was measured at 25 °C with a self-developed measurement board, which provided a resolution of 24 bit, or a Pico-Scope 5243B (in case of $T = 0.001$ s or $T = 0.1$ s), which provided a resolution of 15 bit. A more detailed description follows in Chapter 4.

To compare the current distribution without taking the warming of cells into account, the current had to be lowered by a factor of approximately 10 for long cycle durations ($T = 1000$ s) and for the CC discharge measurement.

In the first ca. 9 % of DoD in Figure 3.19 (a), the HP cell delivers the larger part of the current. This is because of its lower ohmic resistance. Because the capacity of the HP cell was less than the HE cell, the OCV of the HP cell decreased faster than that of the HE cell. Thus, the SoCs diverge, and hence the OCVs do too. Later, the difference in OCV overcompensated for the difference of overpotential at the inner resistance. Up to 35 % of DoD, the results of Brand et al. [25] regarding short- and long-term behaviour were confirmed. Simulations with a linearised OCV would show a constant difference until the cut-off voltage. The simulations that are shown in Figure 3.19 (a) used nonlinear OCVs. Measurements and simulations showed the effect of these nonlinearities.
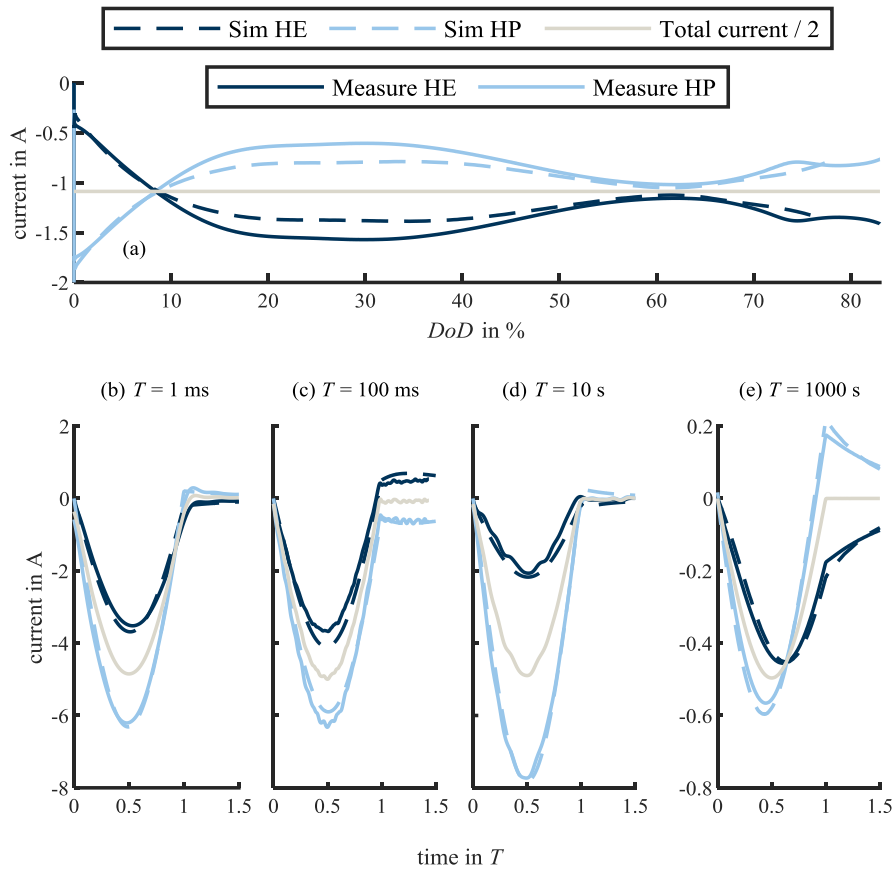
Figure 3.19: *Validation of the simulation of current distribution with a CC and different dynamic load profiles (dark blue: HE cell current; light blue: HP cell current; continuous line: measured results; dashed line: simulation results; grey: half current of the applied load profile). The model type is $OCV_{mea\_0.05C}(SoC) + \underline{Z}_{R,3RC}(SoC)$.*

In Figure 3.19 (b), a sine half-wave with a width of $T = 1$ ms is used as a load profile. In this short time, the impedance effects are dominant. At the sine half-wave with a width of $T = 1000$ s, the curves intersect at approximately 630 s. At this point in time, long-term effects such as OCV differences gain influence. The measurements and simulations using a sine half-wave with a width of $T = 100$ ms and $T = 10$ s were difficult to interpret. The effects of SEI, double layer, charge transfer, diffusion and mass transport overlapped (compare Figure 2.4). The maximum simulation errors were below 0.5 A at the sine half-waves with 10 A, below 0.1 A at the sine wave with 1 A, and below 0.2 A in the CC test.

Unlike the analytical calculation in Section 3.1 and its results in Figure 3.3, the CC measurements in Figure 3.19 (a) do not reach a constant relationship between cells. As the analyses in the Subsections 5.4.2 and 6.1.5 show later, the nonlinearity of the OCV is responsible for this effect.

Therefore, the difference between the simulated current i_{sim} and measured current i_m was used. To calculate the relative error, the maximum total current of the load profile $i_{tot,max}$ formed the reference.

Table 3.6 shows the RMS and relative error at CC and the four different values of T. The RMS error e_{RMS} and relative error e_{rel} were used to quantify the error of the measurement, and e_{rel} was calculated using the following equation:

$$e_{rel} = \frac{e_{RMS}}{i_{tot,max}} \cdot 100\ \%$$ (3.78)

With relative error e_{rel} up to 5 % at CC and up to 2.9 % at the sine half-wave load profile, Table 3.6 shows good accordance between measurements and simulations.

Table 3.6: *RMS and relative error between simulated and experimental data*

	CC	$T = 1$ ms	$T = 100$ ms	$T = 10$ s	$T = 1000$ s
$e_{RMS,HP}$	0.11 A	0.19 A	0.23 A	0.20 A	0.24 A
$e_{RMS,HE}$	0.11 A	0.17 A	0.29 A	0.23 A	0.23 A
$e_{rel,HP}$	5 %	1.9 %	2.3 %	2.0 %	2.4 %
$e_{rel,HE}$	5 %	1.7 %	2.9 %	2.3 %	2.3 %

4 Measurement of current distribution and ageing

Measurements bring reference to the real world. It is crucial that the measuring tools do not influence the measurement results, and the measured current distribution should reproduce the situations in battery systems. An ageing experiment is used to study the harmful effect of asymmetric current distribution.

4.1 Measurements at the cell level

To measure the current distribution at two different tempered parallel-connected lithium-ion cells, a test bench was constructed. Figure 4.1 illustrates the measuring setup. Preventing the influence of measuring tools on the current distribution was crucial. Section 3.1 showed that the current distribution depends on resistances in the cells. The shunts in Figure 4.1 are connected in series with the cell resistance, and therefore they also influence the current distribution.
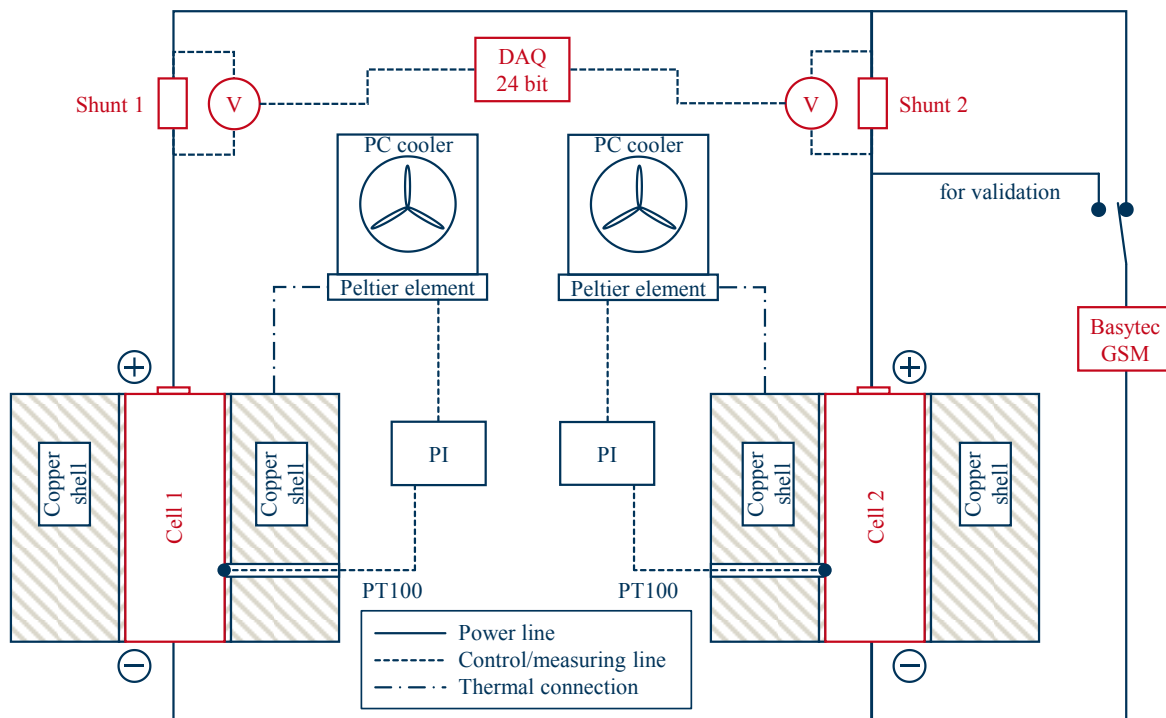
Figure 4.1: *Measuring setup of the 2p connection of cells. This setup can temper each cell individually and acquire the single-cell current without having a significant influence on the current distribution*

Selecting the optimal current sensing technology is a complex task, and some type of compromise is necessary. Hall- or fluxgate sensors are common tools for measuring the current of a conductor [219]. These sensors measure the magnetic field around a conductor and calculate the current. This measuring principle would not lead to any growth in resistance. Because of the effects of hysteresis and drift, the accuracy of the hall- and fluxgate sensors are not sufficient for simultaneously measuring the cell current and current differences in a range of less than 1 % of the cell current (compare Figure 3.3 on page 32) [220].

Therefore, a shunt-based measuring technique is more suitable; however, the shunts must have low resistance. The setup used a precision shunt type PBV-R001-F1-0.5 (Isabellenhütte Heusler GmbH & Co. KG, Dillenburg, Germany) with a resistance value of 1.0 mΩ on each cell to measure the cell current. To show the influence of the current distribution, the fictitious example from Section 3.1 is used. The results without measuring shunts are presented in Figure 3.3. The impedances of both cells are increased by the shunt resistance of 1 mΩ. The graphs in Figure 4.2 (a) illustrate the current distribution with and without shunts; almost no difference is visible. Figure 4.2 (a) shows the current difference caused by the shunt.
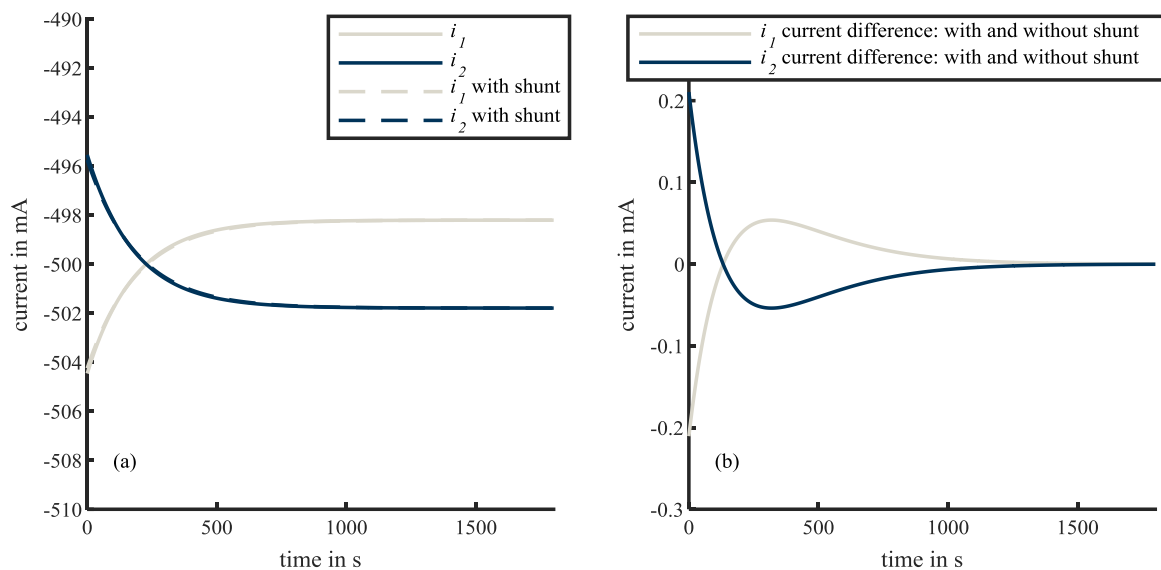
Figure 4.2: *Influence of a 1 mΩ shunt on the current distribution shown in the example from Section 3.1. The graphs in diagram (a) correspond to the total currents. Diagram (b) shows the current difference caused by shunts.*

Furthermore, the resistance of the shunt depends on the temperature. Shunts with high resistance values generate more heat, which warms the shunt. The selected shunt generates 10 mW of head at the maximum current of 10 A. By mounting the shunt on the bracket, this head can be conducted, and the temperature remains constant.

In addition, the joining technique must not influence the current distribution. Resistance measurements performed with a precision resistance meter (Hioki BT3562) yielded an additional resistance of the joining technique of 0.3 mΩ and a difference in the strings of 9 μΩ. This was

below the measurement uncertainty of the Hioki BT3562 resistance meter of ± 15 μΩ and equates to 0.013 % of the mean measured cell impedance of the Sony_FT cells at 1 kHz of 17.427 mΩ [20]. An analogue-to-digital converter (ADC) was used to measure the voltage drop at the shunt with a resolution of 24 bit. After the calibration with a Keysight 34470A multimeter and a Burster 1240-0.2 precision shunt, the cell current measurement reached a reliability of ± 0.1 mA at a controlled temperature of 25 °C. At temperatures between 20 and 60 °C, the PBV shunt changed resistance at 30 ppm/K. [20]

To analyse the effects of temperature differences, the cells had to be tempered continuously with a good thermal connection. To achieve this, copper shells were placed around the cells. The connection between the cells and the copper shells was improved using heat conductive foil. A proportional-integral (PI) controller set the temperature, the reference of which was a PT100 sensor placed in a drill hole of the copper shells, which measured the surface temperature of the cells. Two Peltier elements combined with common computer cooler units generated the heat flow. The PI controller controlled the Peltier element and the fan of the computer cooler. Figure 4.3 presents a labelled photograph of the test bench. The total load of the 2p connection was provided by a BaSyTec GSM battery tester, which reached up to ± 10 A with a resolution of 16 bit and current measurement uncertainty of 0.05 %.
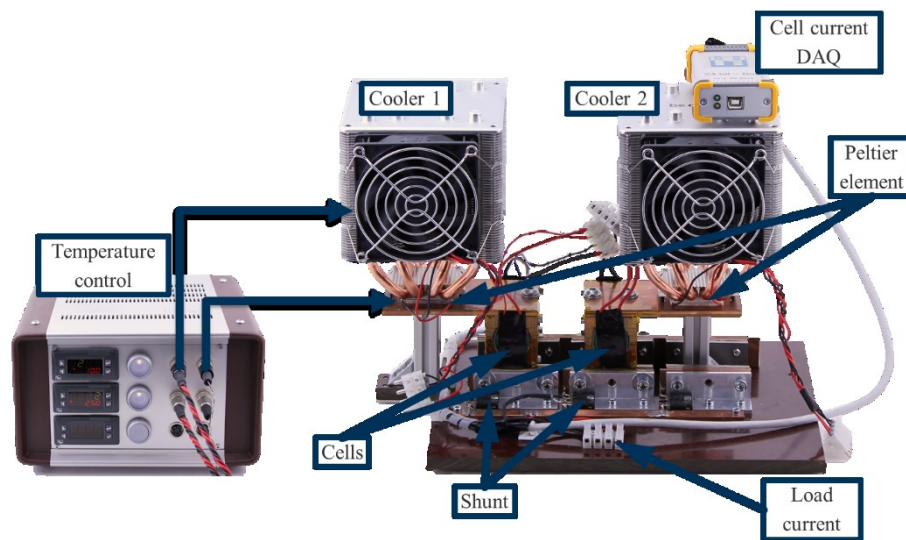
Figure 4.3:   *Photograph of the test setup including the temperature controller and cell current data acquisition (DAQ) system. The DAQ is not placed on the cooler in measuring position to prevent temperature influence.*

To validate the cell current measurement, the BaSyTec GSM tester powered the 2p connection in a second manner. Figure 4.1 illustrates the validation switch at the right side of the schematic diagram. In this option, both shunts measure the current of cell 1 but with the opposite sign. This allows the charge throughput of the two sensors in operation to be calculated. The load profile consisted of CCCV full cycles and smaller cycles of 20 % DoD. With this setup, a charge throughput of approximately 50 Ah was generated over approximately 30 h. In this test, an RMS error 1.8 mA and a difference in charge throughput of 0.13 % were determined. Because

the current applied to the two cells was in the range of amperes and the charge throughput was in the range of several ampere-hours, the test accuracy of the test setup was sufficient.

To analyse the influences of the OCV, impedance, hysteresis, and entropy, cells with different characteristics were chosen. Two Sony_FT cells with a similar SoH were used for the measurements. The anode material is graphite and the cathode consists of LFP. This means the OCV was steep at high and low SoCs and exhibited a flat area between 10 and 95 % of the SoC. Further measurements were performed with the other cells in this thesis—LG_HB2, Pan_PF, Sam_25R, and LG_MJ1—each in a 2p connection with similar SoHs. An analysis of the cell parameters can be found in Section 3.3. The OCV of these cells was steeper at medium SoCs because of the cathode material NMC or NCA. The slope between 10 and 100 % of SoC was approximately 8 mV/%. At SoCs below 10 %, the OCV was also more steep.

To define the worst-case situation, thermoelectric simulations on a module of 648 cylindrical 18650 cells were performed in a preliminary investigation which is not explained in detail here. The results showed a temperature spread of up to 15 °C. Hence, this difference builds the basis for the worst-case analysis of the asymmetric current and ageing experiments in the present study. One of the cells was maintained at 10 °C and the other at 25 °C.

The load profile consists of five phases, representing the charging, standby, and utilisation of a storage system. The procedure represents different phases of the usage of a lithium battery. It consists of charge and discharge current in CV and CC characteristics. An example is provided in Figure 4.4.
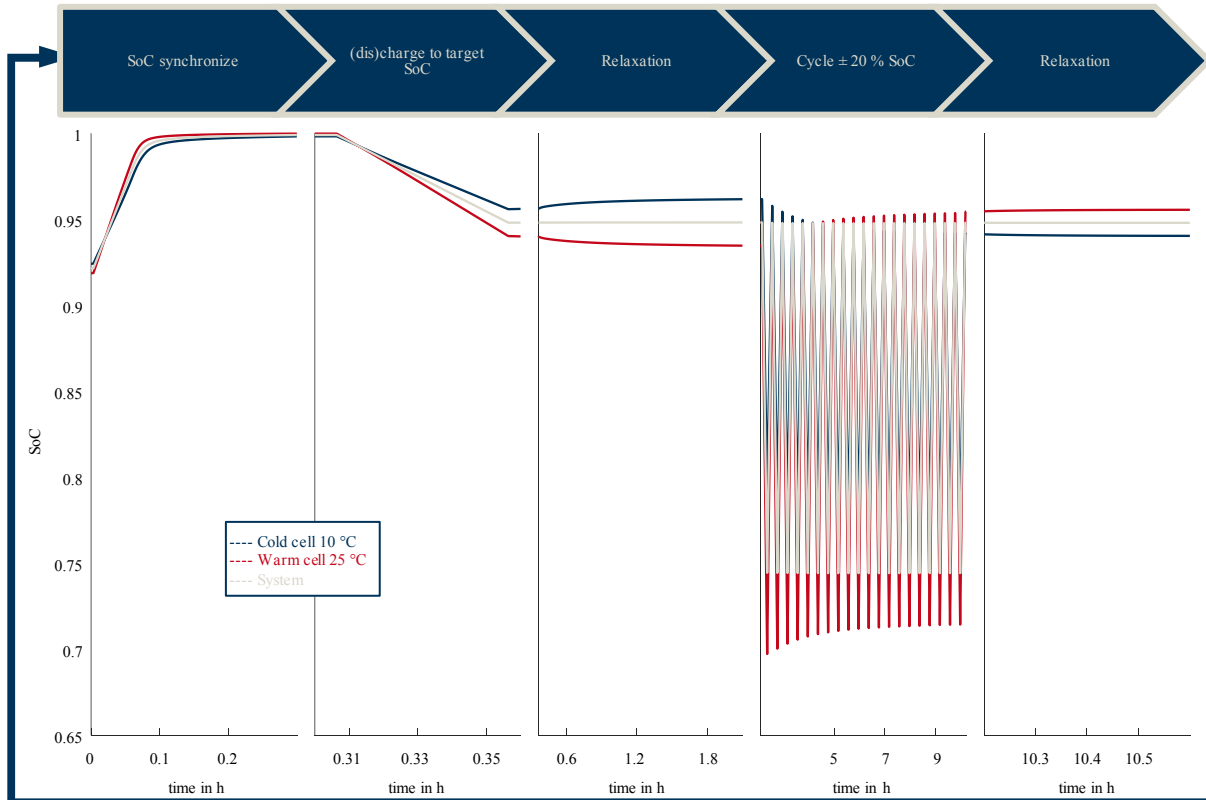
Figure 4.4:   *Measurement procedure including the CV phase, CC phase, relaxation, cycling, and relaxation of two cells connected in parallel; one cell is at 10 and the second cell is at 25 °C.*

4.2   Measurements in larger storage systems

As shown in Section 1.1, battery storage systems for automotive or stationary systems often consist of hundreds of cells connected in series and parallel. However, whether it is possible to scale up measured results at the cell level for larger storage systems remains to be answered. In the research project DriveBattery2015, a demonstrator was built that consisted of one HP and one HE string. Each string consisted of 96 cells in a series connection. For the HP string, the LG_HB2 cell entered into operation in a 5p connection, whereas the Pan_PF cells were used for the HE string in a 10p connection. Hence, the storage system consisted of $96 \cdot 5 + 96 \cdot 10 = 1440$ cells. The system measures the currents of the two cell strings with two 300 A shunts (PMBE-300A; Sensor-Technik Wiedemann GmbH, Kaufbeuren, Germany) with 1 % accuracy. [175]

The numbers of parallel connection can be scaled by a factor of 1/5. This means that one HP cell is connected in parallel to two HE cells. Figure 4.5 shows the measurement at the cell level on the left side. The cell tempering is not installed because no tempering occurs at the pack level. The battery system is constructed inside a switch cabinet (Figure 4.5 right side).
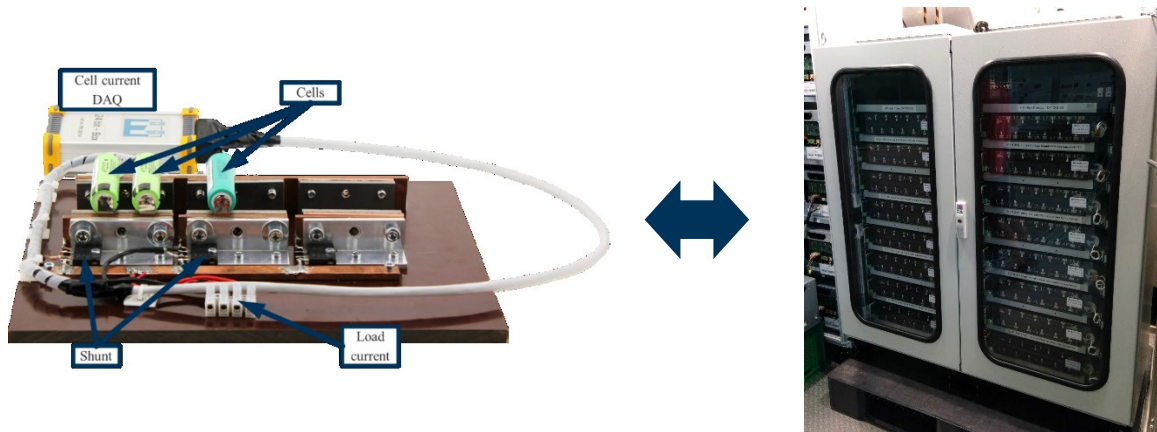
Figure 4.5: *Comparison between the current distribution at the cell and pack levels. On the left, two Pan_PF cells are connected in parallel to one LG_HB2 cell on the cell test bench without tempering. The right side shows a storage system consisting of 96s5p LG_HB2 in parallel to 96s10p Pan_PF cells*

With this setup, a comparison of the current distribution between cell and system was possible. To observe the effects in a dynamic load profile, the two systems were loaded by an EV drive cycle recorded in Stuttgart. Figure 4.6 demonstrates good agreement between the measurements at the cell and system levels. The results in Figure 4.6 allowed all further measurements at the cell level. Furthermore, the good agreement between the two measurements allowed the findings to be scaled up from the cell to system level.
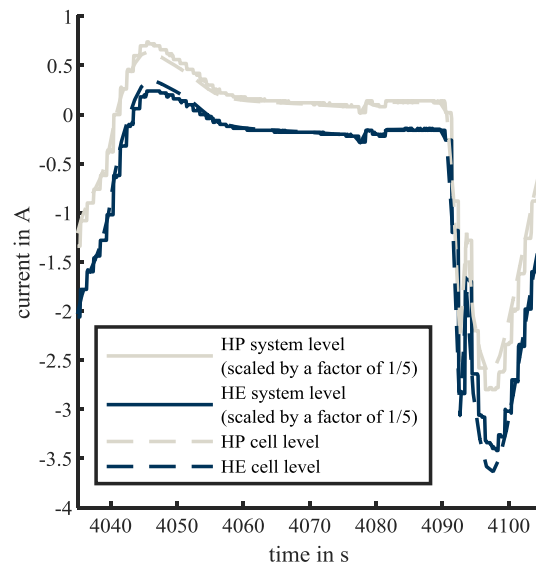
Figure 4.6: *Measured current distribution at the cell and system level. The diagram shows an extract of an EV drive cycle containing a braking, stopping, and accelerating phase. The current at the system level is scaled by a factor of 1/5.*

4.3   Ageing

Because ageing depends on charge throughput [21, 26, 101], the asymmetric current distribution is supposed to have an influence on ageing. An ageing experiment was performed to analyse the influences, for which CCCV cycling of two cells connected in parallel with different temperatures was supposed.

The effect of ageing should be shown in a worst-case scenario for the example of a 2p connection of cells. Cells with LFP cathode material have exhibited the most sensitive behaviour in terms of current distribution. Section 3.1 confirmed this assumption using a simple calculation. Therefore, the Sony_FT cells were used for the ageing experiment, and the basic parameters of this cell type are listed in Table 3.3.

Accelerated ageing should not be generated by using cells outside of their specifications. All of the cells in Table 3.3 have a smaller current limit in the charge than in the discharge direction. This was because of the ageing mechanism of lithium plating, which is the most harmful ageing effect when charging cells at temperatures below 25 °C [96]. For many applications, charging the battery at temperatures below 25 °C is common. Therefore, the ageing experiment addressed this operation, and lithium plating was the most sensitive ageing effect. At the 2p level, this means a limit of 6 A in the charge direction for the connection of the cells.

An asymmetric current distribution should cause asymmetric ageing of cells. Different scenarios can cause an uneven load distribution. To find the most harmful temperatures at a temperature difference of 15 °C, three cases were tested, beginning at 0–15 °C and ending at 10–25 °C with an increase of + 5 °C at each step. These measurements were performed with the test bench described in Section 4.1. When the tempering system reaches the target temperature, the cells were discharged to 0 % of SoC. Figure 4.7 shows the current distribution at the following charge phase.

The worst plating tendency is supposed to be at the lowest temperatures. Nevertheless, at the temperature combination of 0 and 15 °C, the current of the cold cell (cell 1) remained below 3 A. At the temperature combination of 10 and 25 °C, cell 1 reached a maximum current of more than 3.6 A at an SoC of the 2p system of 91 %. This is a critical state because the maximum charge current of 3.0 A is exceeded and the plating risk is high because of a high SoC, low temperature, and high current, as described in [96, 100, 221].
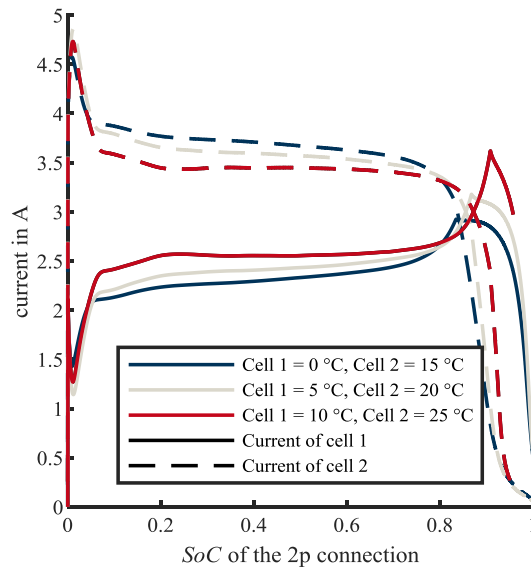
Figure 4.7: *Current distribution measurement with Sony_FT cells at various temperature differences using a CCCV current and a current of 1 C*

After this definition of the critical load profile, the ageing experiment uses the cells in a 1p connection. The study used 12 cells in total. Each cell was cycled in its own channel of a BaSyTec CTS. The cells were split into four groups. The first two groups were the reference cells. The load profile of these cells was a simple CCCV charge and discharge profile with a CC phase of 1 C and a CV phase that ended at a total current below 0.1 C. Group 1 operated at 10 and group 2 at 25 °C, as ensured by a temperature chamber. Group 3 was cold cells in a 2p connection, and their charge current was the load profile shown Figure 4.7 (red solid line) at a temperature of 10 °C. Group 4 represents the warm cells in a 2p connection, and therefore, they were charged with the current of the red dashed line in Figure 4.7 at a temperature of 25 °C. Because lithium plating did not occur in the discharge phase, groups 3 and 4 were discharged as the reference cells. Table 4.1 summarises the four groups in the test.

Table 4.1: *Four groups from the ageing experiment and their operation conditions*

	Group 1	Group 2	Group 3	Group 4
Matter	Reference cold	Reference warm	Cold	Warm
Number of cells	3	3	3	3
Temperature	10 °C	25 °C	10 °C	25 °C
Charge	CCCV at 1 C	CCCV at 1 C	Load profile 10 °C, see Figure 4.7	Load profile 25 °C, see Figure 4.7
Discharge	CCCV at 1 C	CCCV at 1 C	CCCV at 1 C	CCCV at 1 C

The SoH_{Ah} and SoH_Z were measured consistently every 50 cycles in a check-up procedure with the ageing of the cells. This is necessary once to track the ageing as well as to control the charge current. The check-up began with a capacity determination in a CCCV discharge at 1 C until

the current dropped below 0.1 C. When the cell degraded and lost capacity, the phase with an almost constant current from 20 to 80 % of SoC was shortened by the value of the capacity loss. In a further check-up process, pulses at 10, 50, and 90 % of the SoC were applied to the cells. In each stage, one positive and one negative 60 s 1 C pulse were followed by 1 hour of relaxation. Figure 4.8 shows the test procedure, which was repeated until the end of the study. For a proper comparison between cold- and warm-cycled cells, capacity and impedance determinations of all cells were made at 25 °C.
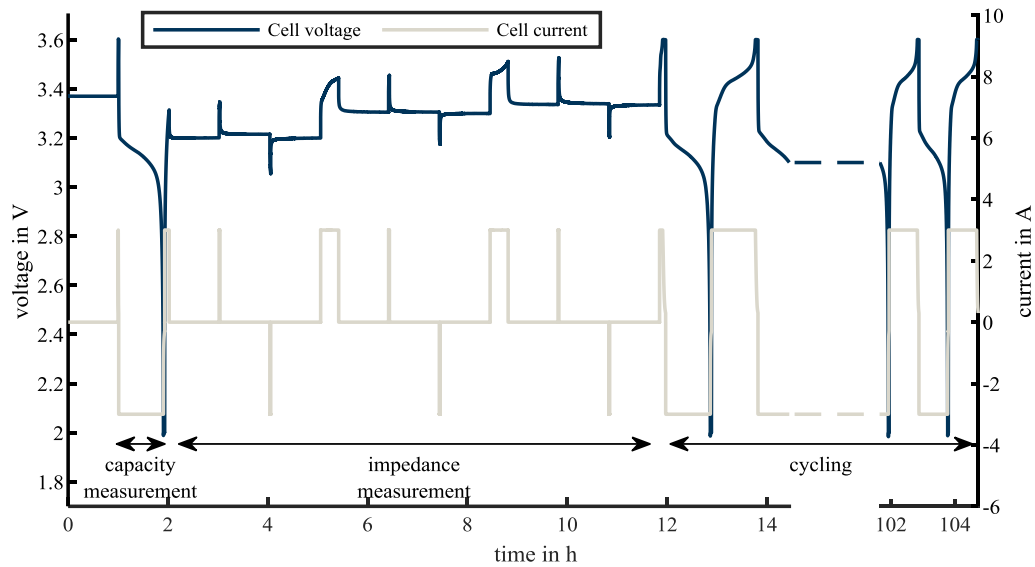
Figure 4.8:   *Test procedure of the ageing experiment. The routine began with a capacity determination followed by six pulses at three SoCs. Subsequently, 50 iterations of cycling began. The cycling current differed depending on the group of the cell. This figure shows the cycling current of the cells of reference groups 1 and 2. Next, the procedure began again with the capacity determination.*

5 Drivers of asymmetric current distribution

For a systematic evaluation of the drivers of asymmetric current distribution, this chapter provides a detailed analysis of the occurring factors. The simple analytical calculation from Section 3.1 gave a first impression but neglected important influencing factors. Self-produced sections of [28] are partially contained in this chapter without any further reference.

Figure 5.1 brings the dependencies into a hierarchical structure. The asymmetry in current ΔI is at the top of the chart. A voltage difference coming from the cells ΔU_{cells} or from the system is necessary to create ΔI. System effects such as impedance differences caused by different cable lengths or differences in the conductivity of junctions were analysed by Rumpf et al. [144] and are not a focus of the present work.
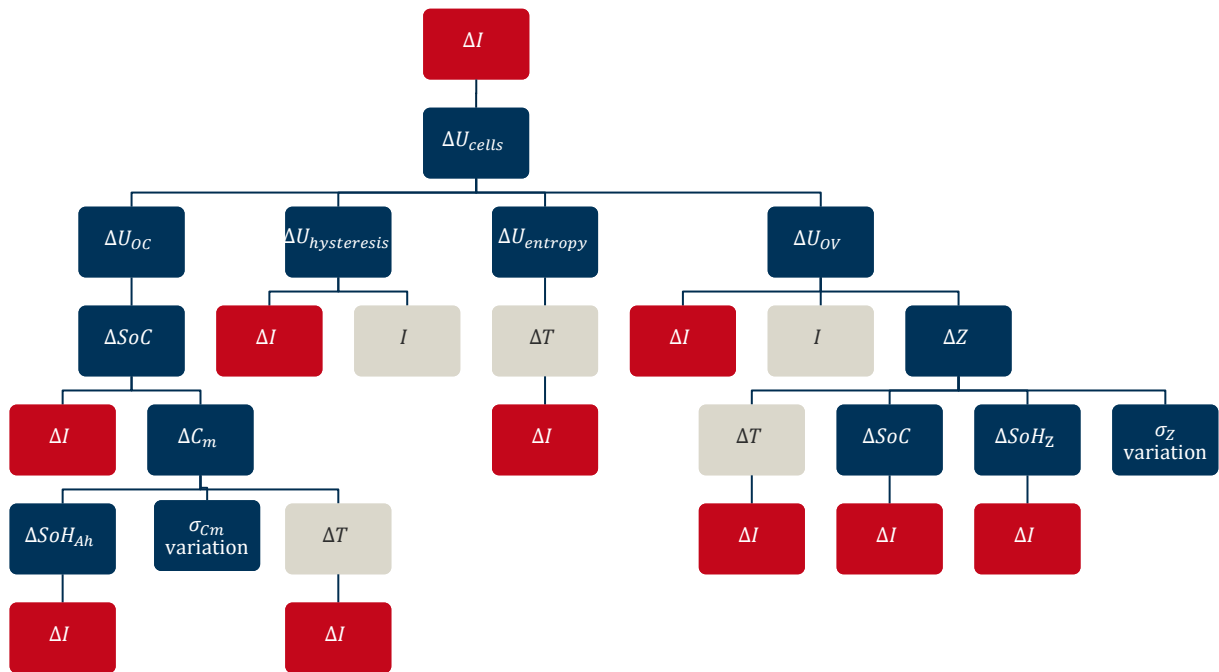
Figure 5.1:   *Relation between the effects that lead to asymmetric current distribution in parallel connections of batteries. To accentuate the back couplings of the current distribution, the ΔI-fields, which represent asymmetric current distribution, are marked in red, whereas grey is used to represent the factors controlled by the test bench, the total load current I and the temperature difference ΔT.*

From EEC modelling, it is obvious that the cell voltage consists of the OCV U_{OC} and cell overvoltage U_{OV}. In Figure 5.1, there are two more influencing factors of ΔU_{cells}: the entropy $U_{entropy}$ and hysteresis $U_{hysteresis}$. They can be handled as part of the OCV, but for separating the drivers of asymmetric current distribution it is clearer to list them separately.

In the hierarchical level below, the reasons for ΔU_{OC}, $\Delta U_{hysteresis}$, $\Delta U_{entropy}$, and ΔU_{OV} are collected. The OCV voltage depends on the SoC having a nonlinear relationship. The height of the charge current—and therefore the asymmetry in current distribution ΔI together with the actual capacity C_m—define the cells' OCV. At this point, the first back-coupling of the current distribution occurs on the effects of asymmetric current distribution. For emphasis, all ΔI in Figure 5.1 have a red background colour. Furthermore, the results of Figure 4.6 allowed all further measurements to be conducted at the cell level. Furthermore, the good agreement of the two measurements allowed the findings from the measurements to be scaled up from the cell to system level.

Back-couplings occur on the path of capacity difference ΔC_m. The ageing of the capacity depends on the charge throughput of the cells, and therefore also on the current distribution. Parameter variations from the production process σ_{Cm} can influence the capacity as well as the temperature. Because the test bench described in Section 4.1 can control the temperature and system current I, these values are marked in grey colour in Figure 5.1. Through the operation of battery cells, losses warm the cells, which means another back-coupling occurs in the current distribution.

Hysteresis effects on battery voltage mean that there is a difference in OCV between reaching a certain SoC from a higher SoC than from a lower SoC. Dreyer et al. explained this effect in LFP batteries through different stable arrangements between lithium-rich and -poor particles [24]. This means that the hysteresis voltage depends on the total current I together with the cell currents coming from ΔI. Hysteresis effects are strong in LFP cells and less relevant in cells with a steeper OCV curve.

In addition, entropy has an effect on cell voltage because of the temperature; therefore, the current and current difference influence the height of $\Delta U_{entropy}$. The voltage difference is low compared with hysteresis and overvoltage effects. Schmidt et al. found an SoC-dependent entropy from −0.50 to 0.08 mV/K in NCA/LCO cells and from −0.45 to 0.15 mV/K in LFP cells [106].

The effect of differences in the overvoltage of cells ΔU_{OV} is caused by numerous factors. It is obvious that current influences the overvoltage, and therefore the current distribution does too. Another factor is the impedance Z, which depends on the temperature, SoC, and ageing. All these factors have a back-coupling with the current distribution. Furthermore, parameter variations σ_Z from the production can lead to impedance differences ΔZ.

The manifold interconnections and back couplings make it clear that the total separation of single effects is not possible in real-world measurements. The following work analyses the effects of current distribution in individual sections on overvoltage, hysteresis entropy, and SoC. Table 5.1 gives an overview of the simulative analyses that are described in detail in the following sections. To ensure the maximum degree of freedom, Subsections 5.1.1, 5.4.1, and 5.4.2 used virtual cell parameters instead of real ones. In all the other simulations described in

Chapter 5, measured parameters from real cells were utilised. Some effects required the additional asymmetry of another parameter. For the simulations on the SoC dependence of impedance and hysteresis effects, a temperature difference of 15 °C was used to provide such asymmetry. Without this additional parameter difference, no asymmetric current distribution would appear.

Table 5.1: *Overview of the simulative analyses of the drivers of the asymmetric current distribution*

Effect	Chapter	Variation parameter	Model type	Conditions
Overvoltage, Parameter variation	5.1.1	$R_s, R_{ZARC}, \xi,$ R_{WB}, C_{WB}	$OCV_{lin}(SoC) + \underline{Z}_{R,20RC}$	Virtual cell parameter, $\Delta T = 0\,°C$
Overvoltage, SoH	5.1.2	SoH	$OCV_{lin}(SoC) + \underline{Z}_{R,5RC}$	Real cell parameter, $\Delta T = 0\,°C$
Overvoltage, SoC	5.1.3	SoC dependence of $\underline{Z}$	$OCV_{lin}(SoC) + \underline{Z}_{R,5RC}(SoC,T)$ and $OCV_{lin}(SoC) + \underline{Z}_{R,5RC}(T)$	Real cell parameter, $\Delta T = 15\,°C$
Overvoltage, Temperature	5.1.4	Temperature	$OCV_{lin}(SoC) + \underline{Z}_{R,5RC}$	Real cell parameter, $\Delta T = 5..15\,°C$
Hysteresis	5.2	Hysteresis	$OCV_{mea\_0.05C}(SoC) +$ $\underline{Z}_{R,5RC}(T)$	Real cell parameter, $\Delta T = 15\,°C$
Entropy	5.3	Entropy	$OCV_{mea\_0.05C}(SoC,T) + \underline{Z}_{R,5RC}$	Real cell parameter, $\Delta T = 5..15\,°C$ (without effect on $\underline{Z}$)
SoC, Parameter variation, capacity	5.4.1	C_n	$OCV_{lin}(SoC) + \underline{Z}_{R,20RC}$	Virtual cell parameter, $\Delta T = 0\,°C$
SoC, OCV	5.4.2	SoC nonlinearity	$OCV_{tanh}(SoC) + \underline{Z}_{R,20RC}$	Virtual cell parameter, $\Delta T = 0\,°C$

5.1 Overvoltage

First, the observations relate to the connection of two battery cells in parallel. The effects demonstrated by Brand et al. [25] occur when a linear OCV and no SoC dependencies of the impedance parameters are assumed. In the present work, the time-dependent impedance was also analysed at different frequencies of the total current. The EEC contained the OCV, an ohmic resistance, a ZARC, and a Warburg element.

5.1.1 Parameter variation

This subsection discusses the simulation results of current distributions caused by impedance parameter variations originating from the production process. The parameter differences were chosen to be realistic in terms of real-world applications. Figure 5.2 shows the EIS measurements (a) and four histograms. Histogram (b) illustrates the real part of the ZARC Re$\{\underline{Z}_{ZARC}\}$. It represents the length in the horizontal direction between the zero crossing of the EIS curve and the local maxima of the imaginary part at about 24 mΩ in diagram (a). Im$\{\underline{Z}(f_c)\}$ histogram

(c) is the imaginary part of the impedance at the local minimum at approximately 20 m Ω in diagram (a), and f_c is the cut-off frequency. Re$\{\underline{Z}(10\text{ mHz})\}$ (d) and Im$\{\underline{Z}(10\text{ mHz})\}$ (e) are the real and imaginary parts of the impedance at 10 mHz, respectively. All these parameters were used to calculate the parameter variations. To separate the influence of the OCV on the asymmetric current distribution, a linear dependence of the OCV on the SoC was assumed.
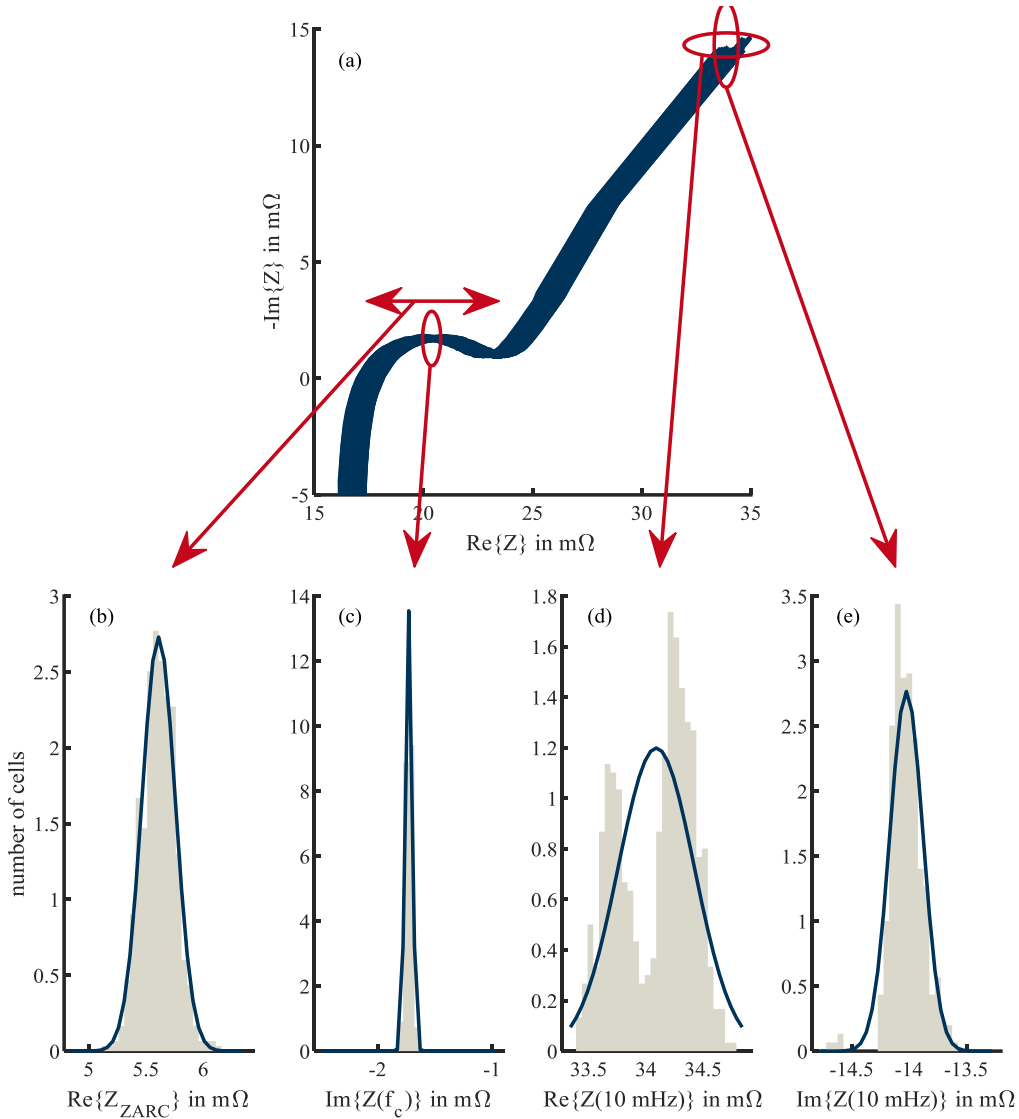
Figure 5.2:   *Nyquist plot of Sony_FT cell measurements of group B1 of the dataset of Rumpf et al. [20] in diagram (a) and histograms of Re$\{\underline{Z}_{ZARC}\}$ (b), Im$\{\underline{Z}(f_c)\}$ (c), Re$\{\underline{Z}(10\text{ mHz})\}$ (d), and Im$\{\underline{Z}(10\text{ mHz})\}$ (e)*

This study focused on the parameters at the beginning of the cells' life. Rumpf et al. [20], Baumhöfer et al. [22], and Schuster et al. [112] have analysed the statistical spread of cell parameters. Rumpf et al. [20] measured the parameter of series produced LFP ǀ graphite cells in the 26650 format. These Sony_FT cells were described in Table 3.3 on page 39. The results of group (B1) in [20] define the relative parameter differences (γ) shown in Table 5.2, which were used in

this analysis of current distribution. The parameter differences chosen for this part are plus/minus twice the standard deviation σ. The parameter difference γ of R_S was calculated using equation (5.1) using the standard deviation σ and mean value μ of R_S:

$$\gamma_{R_S} = \frac{|-2 \cdot \sigma_{R\_AC\_1000Hz(B1)}| + |2 \cdot \sigma_{R\_AC\_1000Hz(B1)}|}{\mu_{R\_AC\_1000Hz(B1)}} = \frac{4 \cdot 0.310 \text{ m}\Omega}{17.4 \text{ m}\Omega} = 7.6 \text{ \%} \tag{5.1}$$

R_{ZARC} and C_n are calculated by equal measurements using the parameters $\mu_{R\_AC\_min\,(B1)}$, $\sigma_{R\_AC\_min\,(B1)}$ $\mu_{C\_DCH\_CCCV\,(B1)}$, and $\sigma_{C\_DCH\_CCCV\,(B1)}$. The Warburg parameters R_{WB} and C_{WB} can be evaluated from the raw data provided in [20]. The standard deviation and the mean value of the real and imaginary part of the impedance of the lowest measured frequency are used. Rumpf et al. [20] chose a minimum frequency of 10 mHz. The relative parameter differences $\gamma_{R_{WB}}$ and $\gamma_{C_{WB}}$ are calculated using the variance of the real $\text{Re}\{\underline{Z}(10 \text{ mHz})\}$ and imaginary $\text{Im}\{\underline{Z}(10 \text{ mHz})\}$ part of the impedance at 10 mHz:

$$\gamma_{R_{WB}} = \frac{4 \cdot \sigma_{Re\{\underline{Z}(10\,mHz)\}(B1)}}{\mu_{Re\{\underline{Z}(10\,mHz)\}(B1)}} = \frac{4 \cdot 0.333 \text{ m}\Omega}{10.9 \text{ m}\Omega} = 12 \text{ \%} \tag{5.2}$$

$$\gamma_{C_{WB}} = \frac{4 \cdot \sigma_{Im\{\underline{Z}(10\,mHz)\}(B1)}}{\mu_{Im\{\underline{Z}(10\,mHz)\}(B1)}} = \frac{4 \cdot 0.144 \text{ m}\Omega}{14.0 \text{ m}\Omega} = 4 \text{ \%} \tag{5.3}$$

The parameter ξ of the ZARC element depends on the imaginary part of the semi-circle of the Nyquist plot. A statistical calculation for the imaginary part of the highest point of the semi-circle in the Nyquist plot produced $\sigma_{Im\{\underline{Z}(f_c)\}(B1)} = 0.042 \text{ m}\Omega$ and $\mu_{Im\{\underline{Z}(f_c)\}(B1)} = 1.70 \text{ m}\Omega$. The highest point of the semi-circle appeared at the cut-off frequency f_c [46].

$$\text{Im}\{\underline{Z}(f_c)\}_{\max} = 2 \cdot \sigma_{Im\{\underline{Z}(f_c)\}(B1)} + \mu_{Im\{\underline{Z}(f_c)\}(B1)} = 1.79 \text{ m}\Omega \rightarrow \xi_{\max} \approx 0.56 \tag{5.4}$$

$$\text{Im}\{\underline{Z}(f_c)\}_{\min} = 2 \cdot \sigma_{Im\{\underline{Z}(f_c)\}(B1)} - \mu_{Im\{\underline{Z}(f_c)\}(B1)} = 1.62 \text{ m}\Omega \rightarrow \xi_{\min} \approx 0.46 \tag{5.5}$$

$$\gamma_{\xi} = 2 \cdot \frac{\xi_{\min} - \xi_{\max}}{\xi_{\min} + \xi_{\max}} = -20 \text{ \%} \tag{5.6}$$

Apart from the parameters analysed by Rumpf et al. [20], the impedance parameters of the ZARC and Warburg elements were used to calculate the current distribution. Analysis of the raw data showed that these parameters were also normally distributed and did not exhibit any correlations.

Table 5.2 shows the initial value of the EEC that corresponded to the parameter set of cell 1 and the variation that results in the parameter set of cell 2. The initial values of this virtual cell (see Table 3.5 on page 54) are derived from measurements of several 18650 and 26650 cell types. The variation values come from the analyses of the data of Rumpf et al. [20] on Sony 26650 LPF cells.

A linear OCV was assumed in the simulation experiments to rule out any effects of the OCV's nonlinearities on the current distribution. All simulations started at 100 % SoC. Because the OCV was linear and the impedance parameters were assumed to not be dependent on the SoC, the current distribution was not influenced by the change of the OCV slope and varying im-

pedance parameters when the SoC changed. Variations in OCV linearity are discussed in Subsection 5.4.2. Ageing effects, temperature, and joining technology can lead to further parameter variations between the cells.

Table 5.2:   Parameter differences for the sensitivity analysis

	R_S	R_{ZARC}	ξ	R_{WB}	C_{WB}	C_n	OCV
Initial value	0.02 Ω	0.023 Ω	0.4	0.100 Ω	3000 F	1.00 Ah	$\dfrac{\mathrm{d}OCV}{\mathrm{d}SoC} = 0.52$ V
Variation value (γ)	+7.6 %	+10 %	-20 %	+12 %	+4 %	-1 %	no variation

The simulations described next used two load shapes to compare situations with different dynamics in terms of current distribution. A sine half-wave represented current rising slopes of differing steepness. A pulse load indicated the current distribution in a constant current case. Both load profiles had different lengths and were followed by a phase of no current flow except for compensating current between the cells. The time for the current flow T varied between $T = 1$ ms and $T = 1000$ s with logarithmic steps.

A focus here was to show the influence of the dynamics of the load profile on the current distribution of two cells connected in parallel when certain parameters are varied. A pulse load is a commonly used case and comprises infinite frequencies, as is known from Fourier transformation. A sine load only has one certain frequency. Furthermore, real-world load profiles are often more similar to the current rise of a sine half-wave. In the following simulations, a discharge pulse and sine half-wave are applied to a parallel connection of two cells.

The cells are virtual cells with a linear OCV and a capacity of 1.00 Ah; moreover, the impedance of the EEC consists of one ohmic resistance, one ZARC, and one Warburg element (Table 3.5 and Table 5.2). Because the impedance of a ZARC element is equal to an RC element at $\xi = 1$, the chosen model displayed a flexible structure. The simulation transformed the ZARC and the Warburg elements into a string of RC elements with similar impedance.

Figure 5.3 and Figure 5.4 show the simulation results. The model was run 16 times with a sine and 16 times with a pulse load at a constant difference in the ohmic resistance R_S to observe current differences in 16 steps. The time for the current flow T was 1 ms during the first and 1000 s during the 16th run, with a maximum total discharge current of -2 A. T_h is the time of the current flow of the m run. T_h grows logarithmically as seen in the following equation:

$$T_h = 10^{\log_{10} 0.001 + h \cdot \frac{\log_{10} 1000 - \log_{10} 0.001}{\max(h)}} \text{ s} \quad \text{and} \quad h \in [0..15] \tag{5.7}$$

Diagrams (a) and (d) show the cell current; (b) and (e) the current difference Δi between cell 1 and cell 2; and (c) and (f) the SoC difference ΔSOC between the two cells connected in parallel over the time that has been normalised by T. The total current is a sine half-wave in (a)–(c) and a square pulse in (d)–(f).

$\Delta i(T)$ and $\Delta SoC(T)$ were calculated as follows:

$$\Delta i(T) = i_1(T) - i_2(T) \tag{5.8}$$

$$\Delta SoC(T) = SoC_1(T) - SoC_2(T) = \tag{5.9}$$

$$SoC_{0,1} + \frac{100\,\%}{C_{n,1}} \int_0^{3\cdot T} i_1(t)\,\mathrm{d}t - SoC_{0,2} + \frac{100\,\%}{C_{n,2}} \int_0^{3\cdot T} i_2(t)\,\mathrm{d}t$$

Index 1 refers to cell 1, whereas 2 refers to cell 2. $SoC_{0,1}$ and $SoC_{0,2}$ are the SoCs at $T = 0$.
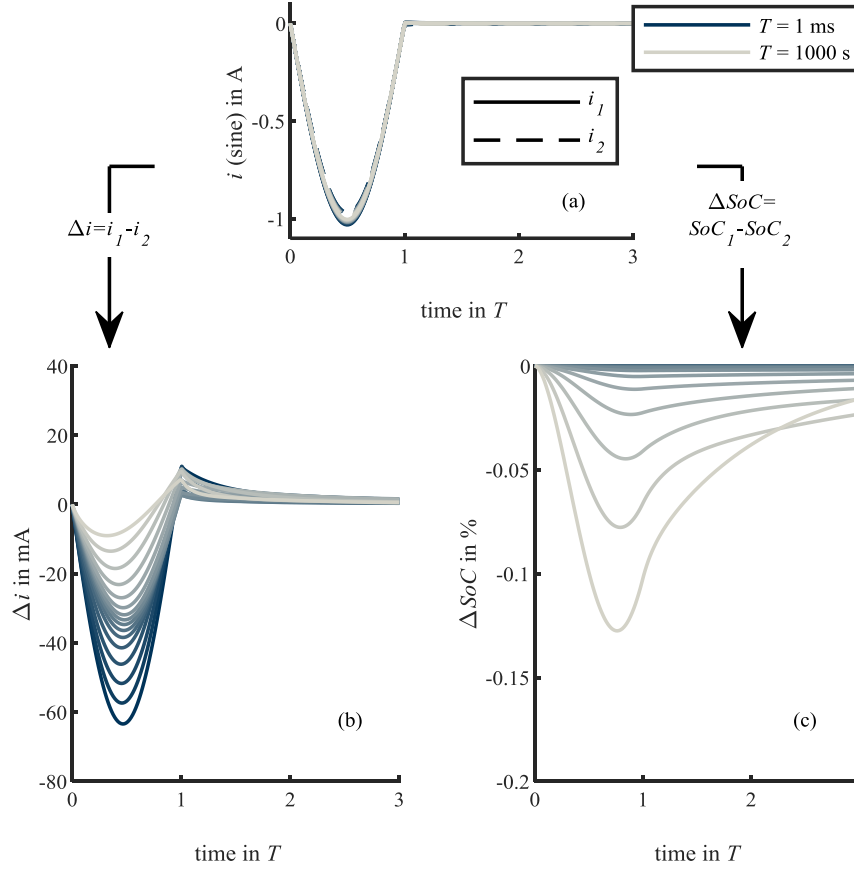
Figure 5.3: *Simulation of the current distribution of a 2p connection with an impedance difference of $\Delta R_s = 7.6\,\%$. It shows a sine half-wave load profile. The colour change from blue to grey stands for a pulse duration of T from 1 ms to 1000 s. Both cells have a capacity of 1 Ah. (model type: $OCV_{lin}(SoC) + \underline{Z}_{R,20RC}$)*

If a difference existed in ohmic resistance, a variation of the current distribution would be observed in the sine and pulse loads. The assumed difference in resistance of $\Delta R_S = 7.6\,\%$ leads to a maximum current difference of $\Delta i_{sine} = 0.063$ A and $\Delta i_{pulse} = 0.076$ A and a maximum SoC difference of $\Delta SoC_{sine} = 0.128\,\%$ and $\Delta SoC_{pulse} = 0.187\,\%$. The differences in current and SoC in the pulse load are higher than the differences in the sine load.

As explained in the validation tests in Subsection 3.3.5, the current difference leads to a difference in SoC. A detailed description of the characteristics of SoC, OCV, and cell currents was provided by Brand et al. [25]. In case of an ideal square pulse, the slope of the current rise is infinite. This means that no ΔSoC exists and the current difference is only dependent on the inner resistances of the cells. In the case of the sine half-wave load, there is a period $T/2$ until the maximum current is reached. During this period, a ΔSoC is formed and this counteracts

the asymmetric current distribution caused by the impedance difference. That is why the maximum current difference with sine half-wave load is lower than with square pulses as well as decreases with increasing values of T.
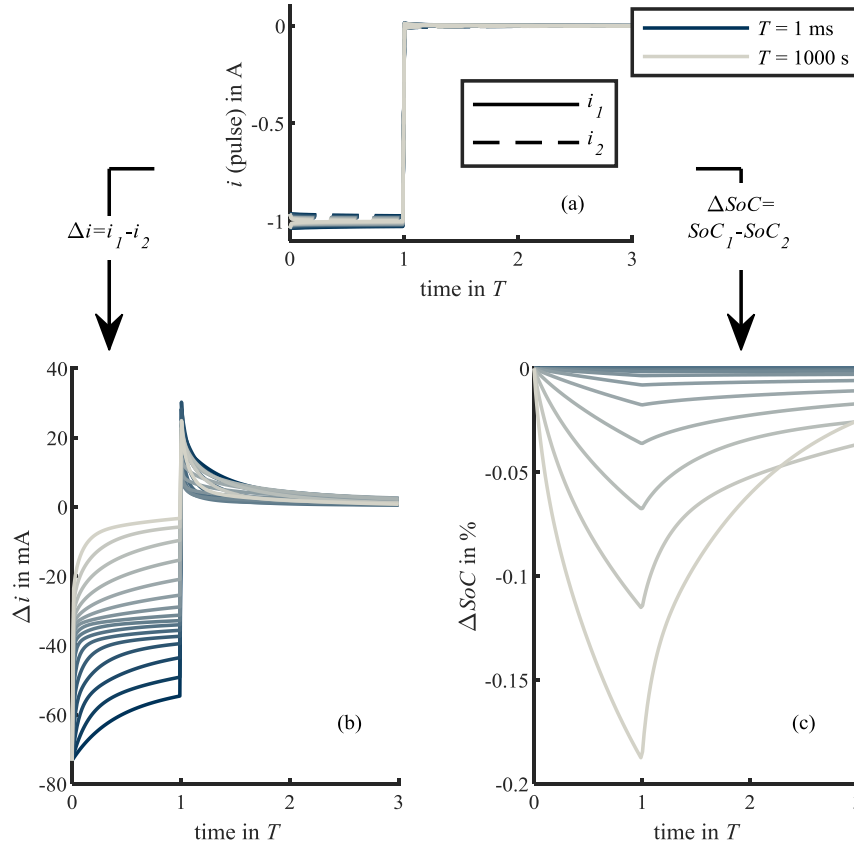
Figure 5.4: *Simulation of the current distribution of a 2p connection with an impedance difference of $\Delta R_S = 7.6$ %. It shows a pulse load profile. The colour change from blue to grey stands for a pulse duration of T from 1 ms to 1000 s. Both cells have a capacity of 1 Ah. (model type: $OCV_{lin}(SoC) + \underline{Z}_{R,20RC}$)*

When T is high, the mean current difference is small. The short-term current difference in the ΔR_S scenario could also be observed qualitatively in the first 9 % of DoD in the CC validation measurements; see Figure 3.19 (a). When T increases, the influence of the short-term effects decreases. This is in accordance with the results of Brand et al. [25]. In the case of the pulse load, a higher maximum ΔSoC can be observed. This is caused by the higher charge throughput of the pulse load at similar peak currents.

Furthermore, the difference in current between the two load profiles was compared with the parameter differences described in Table 5.2. The curves shown in Figure 5.5 are the result of simulations with sine and pulse profiles. The diagrams (a) and (f) in Figure 5.5 are analogous to the diagrams (b) in Figure 5.3 and Figure 5.4.

In case of resistance differences, ΔR_S and ΔR_{ZARC} or ZARC coefficients $\Delta \xi$, short pulses predominantly led to current asymmetry. Varying the Warburg coefficients ΔR_{WB} and ΔC_{WB} only affected the current distribution at high values of T. Of the chosen parameters, the difference

in C_{WB} had the least impact on the current distribution. All impedance variations led to a change in the sign of Δi.
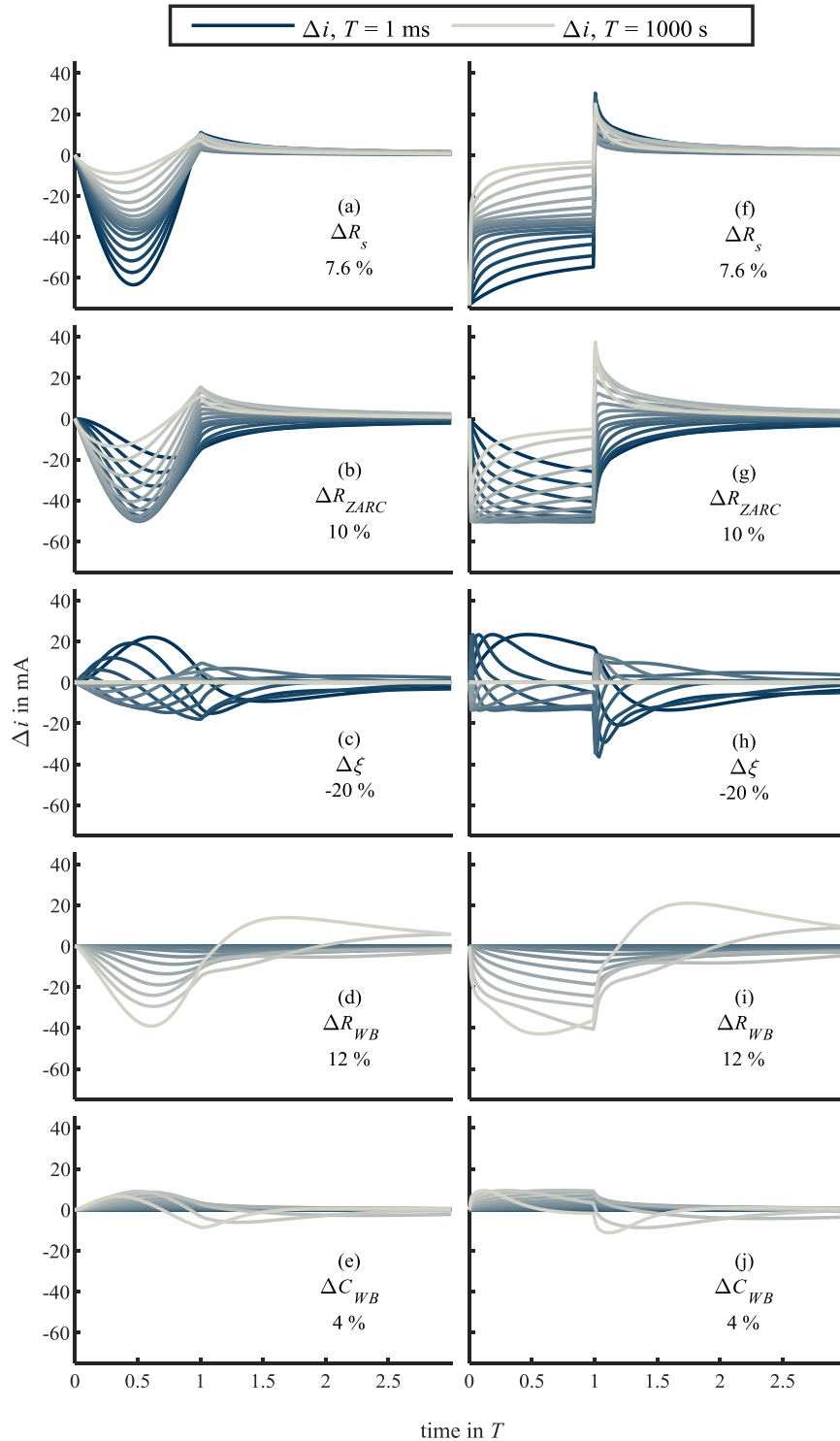
Figure 5.5: *Differences in current Δi between cell 1 and cell 2 simulated with the parameter differences described in Table 5.2. Both cells have a capacity of 1 Ah. (left column: sine input; right column: pulse input; model type: $OCV_{lin}(SoC) + \underline{Z}_{R,20RC}$)*

The current differences in the diagram (g) seem to change the sign of their slope as a function of T. A closer look indicates that it takes approximately $T = 0.25$ s to reach a minimum current difference. All simulations using a pulse length less than this time period showed a rising absolute current difference until the end of the pulse. At pulse durations longer than $T = 0.25$ s, the current difference reached this minimum and the absolute current difference decreased afterwards. The minimum value of $\Delta i \approx -50$ mA appears because of the complex (and therefore time-dependent) character of the ZARC element. At the beginning of the current pulse, the voltage drop at the ZARC element was zero. This means that the relationship of the ohmic resistances R_S defines the current difference. Because the values of both R_S are equal, no current difference existed at the beginning. Then, the current difference rose because of different R_{ZARC}. The period of decreasing current difference, determined in the ΔR_S scenario, was only reached when the pulse length was longer than 0.25 s. Furthermore, the variation of R_{WB} showed a minimum value of Δi at approximately −43 mA. This value was only reached when $T = 1000$ s.

There is no external current flow after $T = 1$. The voltage difference between cells 1 and 2 at this time created a gap in SoCs, which was associated with a voltage gap; see Figure 5.3 (c) and Figure 5.4 (c). In most cases, the relaxation lasted longer than $2 \cdot T$. Variations in the Warburg parameter in particular resulted in a long-term equalisation current between cells 1 and 2. After 2000 s of relaxation, the current between the cells Δi was larger than 9 mA (compare diagram (d) and (i) in Figure 5.5). This influenced the further operation of the cells. Furthermore, the load on the connection of cells started with a difference in SoC. This could increase the effects of asymmetric current distribution.

To analyse the effects of the parameter differences at various T, Figure 5.6 shows the maximum current discrepancy Δi_{max} and normalised charge discrepancy ΔQ at $T = 0.001 \ldots 1000$ s at a logarithmic scale and sine/pulse load. To prevent spikes, Figure 5.6 consists of ten times more simulation runs than the previous diagrams. T consists of values given by equation (5.7) with $h \in [0..159]$. The calculations were as follows:

$$\Delta i_{\mathrm{max}} = \max_{T \in 0.001 \ldots 1000 \text{ s}} |i_{cell\,2} - i_{cell\,1}| \tag{5.10}$$

$$\Delta Q = \max_{T \in 0.001 \ldots 1000 \text{ s}} \left(\int_{t=0}^{t=3\cdot T} |i_{cell\,2}| \mathrm{d}t - \int_{t=0}^{t=3\cdot T} |i_{cell\,1}| \mathrm{d}t \right) \tag{5.11}$$

The absolute values of the differences in current and charge throughput with a pulse load are always higher than with a sine load. Figure 5.6 shows a strong dependence on the time of current flow, and therefore on the dynamics of the load profile.

The ΔQ graphs at parameter differences ΔR_S and ΔR_{ZARC} in (f) and (g) show maximum values at $T \approx 0.5$ s. The reason can be found in the Nyquist plot of cell impedance. The local maximum of the imaginary part of the cell impedance between the ZARC and Warburg impedance is close to 2 Hz. In this area, the impedance change $\mathrm{d}\underline{Z}/\mathrm{d}\big(\log(f)\big)$ is small. The normalisation of the charge throughput with T leads to the maximum ΔQ.

The SoCs of the two cells moved apart slowly and this process was not finished at T; see Figure 5.3 and Figure 5.4. The impact correlated with the time of the current flow T in terms of maximum current discrepancy $\Delta i_{\max}$ as well as normalised charge throughput.
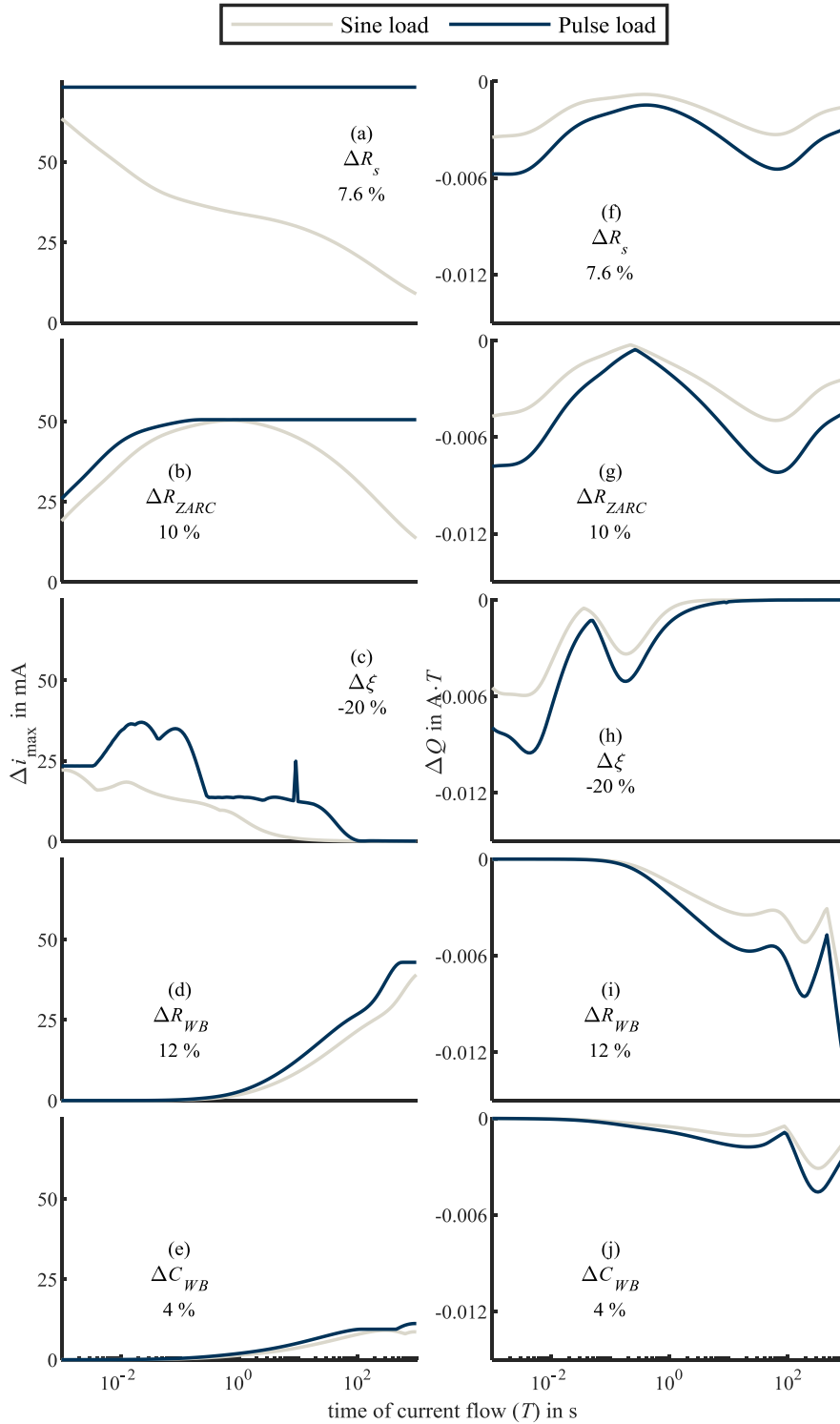
Figure 5.6:   *Analysis of the maximum current difference Δi_{max} and normalised charge throughput difference ΔQ at $T = 0.001 \ldots 1000\ s$. Both cells have a capacity of 1 Ah. (model type: $OCV_{lin}(SoC) + \underline{Z}_{R,20RC}$)*

In terms of the maximum current difference, the values at pulse load were higher than the values of sine load in any case. Hence, a pulse load represents the worst-case scenario in terms of maximum asymmetric current distribution.

Figure 5.3 and Figure 5.4 show an aggregation of lines at medium values of T in both Δi diagrams (b). This cannot be explained without taking into account time-dependent parts of the inner resistance modelled as ZARC and Warburg elements. The diagrams on the left side show the maximum current difference and those on the right show the difference in charge throughput ΔQ_n. The x-axis of all diagrams is the time of current flow T in a logarithmic scale. In diagrams (f) and (g) of Figure 5.6, a small difference in charge throughput ΔQ_n at these T can be observed. The time constant of the Warburg element $\tau_W = R_W \cdot C_W = 0.1\,\Omega \cdot 3000\,\text{F}=300\,\text{s}$ seems to influence the charge throughput behaviour in case of R_S and R_{ZARC} difference. Diagrams (i) and (j) in Figure 5.6 show a minimum at $T = 300$ s. The limits of a minimum Δi at the differences in R_{ZARC} and R_{WB} at pulse load are also visible in diagrams (b) and (d) in Figure 5.6. In terms of sine load, diagram (b) shows that the maximum Δi is only reached at a certain time when current flow $T \approx 0.7$ s. In diagram (c), a spike appears in the pulse graph at about $T = 10$ s. This is caused by numerical instabilities of the simulation.

5.1.2 State of health-dependent impedance parameters

Not only parameter variations from the production process lead to impedance differences in battery systems but also ageing yields to rising cell impedance. Three constellations of cells with different impedance caused by ageing are feasible. First, battery cells do not age similarly even when the same load profile is applied at similar boundary conditions [22]. In reality, cells age differently because of dissimilar loads, temperatures, SoCs, and self-heating. This is the second option. Lastly, in the third possibility, it can be imagined that a part of a battery system must be replaced by new cells. This would represent broadly uneven aged battery cells in a battery system.

In real battery systems, it is not possible to separate ageing effects that concern the impedance from those that concern the capacity; neither is it possible to inhibit self-heating effects that influence the impedance because losses always appear in reality. Simulations help to observe the effect of impedance ageing in a separate manner. To ensure the present study employed a realistic case, impedance growth while ageing was used according to the analyses of Ecker et al. [102]. In their study, an increase of impedance of approximately 40 % was observed while the capacity decreased by up to 20 %. The authors also observed the impedance increase at different time constants. They calculated the impedance at 2, 10, and 17 s after a pulse load. The impedance growth after about 360 days at 30 % of SoC measured 2 s after the pulse was about 140 %, 10 s after the pulse about 142 %, and 17 s after the pulse about 146 %. Hence, the simulations of current distribution in this work assumed a similar growth of R_S, $R_{p,1}$, $R_{p,2}$, $R_{p,3}$, $R_{p,4}$, and $R_{p,5}$. The ohmic resistances of cell 2 were increased in three steps from 0 to 60 %. In this experiment, no SoC dependence of the impedance parameters was included. The simulation used an average value of all R and C in an SoC range from 50 to 100 % because the cells in

the simulations are in this area. The capacities of the EEC represent the geometry of the electrodes inside the cells [46]. It was assumed that this does not change with ageing, and therefore, $C_{p,1}$, $C_{p,2}$, $C_{p,3}$, $C_{p,4}$, and $C_{p,5}$ remained unchanged. With this, the impedance parameters did not vary with the SoC. The values remained constant and the dependence of the impedance on the SoC was switched off.

At the beginning of this chapter, it was mentioned that the OCV and SoC dependence of the impedance parameters influence the current distribution; these effects are analysed separately in Subsections 5.1.3 and 5.4.2, respectively. Therefore, these influencing factors were excluded in the simulations presented in Figure 5.7. Two different linearised OCVs were used. $U_{OC,NMC,NCA}(SoC) = 0.9\,\text{V} \cdot SoC + 3.3\,\text{V}$ represents the OCV curve of all NMC and NCA cells. For the Sony_FT cell, which has an LFP cathode, the OCV equates to $U_{OC,LFP}(SoC) = 0.15\,\text{V} \cdot SoC + 3.2\,\text{V}$.
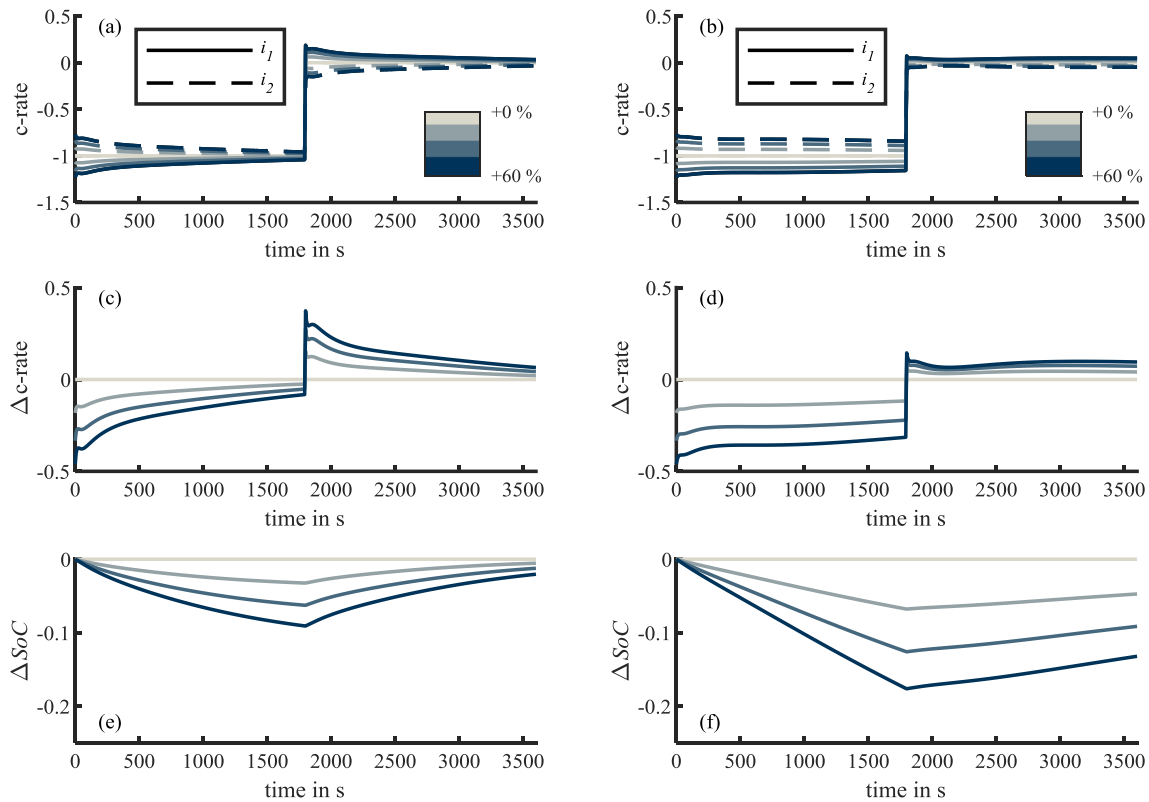
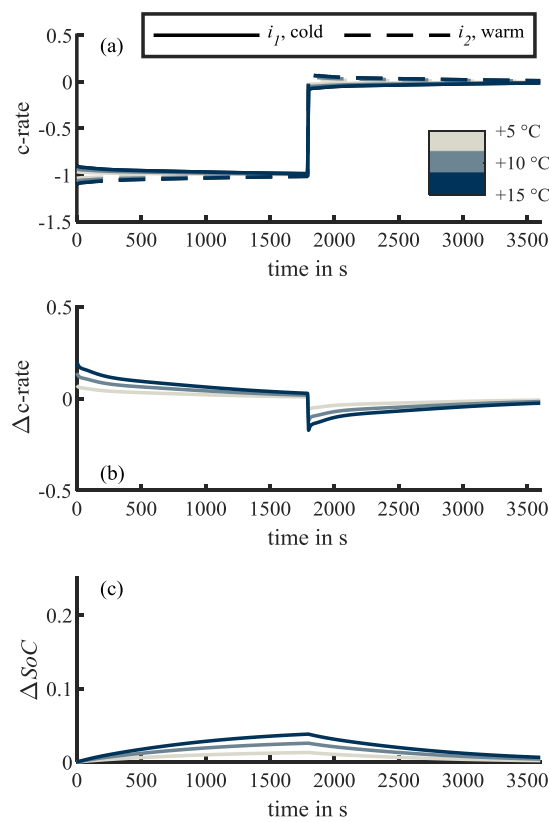

Figure 5.7: *Current distribution of two batteries connected in parallel with a pulse load of 1 C from 100 to 50 % SoC. The ohmic resistance of cell 2 was increased in three steps from 0 to 60 %. The left diagrams show simulation results of the LG_HB2 and the right ones come from the Sony_FT cell at 25 °C (model type: $OCV_{lin}(SoC) + \underline{Z}_{R,5RC}$).*

The flat OCV curve of the Sony_FT cell led to the slow convergence of the two cell currents. Diagrams (a) and (b) show converging cell currents i_1 and i_2 until 1800 s. At the beginning of

the simulation, there was no SoC, and therefore no OCV difference between the cells. Because unequal impedance causes an unequal current when the capacity is similar, the OCV of cell 1 decreases faster than that of cell 2. This difference is unequal because of unequal slopes of the OCV curves. The OCV difference counteracts the current difference. Hence, cells with flat OCV curves reach higher SoC differences in this experiment. This can be seen in Figure 5.7 in diagrams (e) and (f).

After the current pulse, the OCV difference led to an equalisation current that balances the SoC. Because of the flat OCV characteristic, this process took a long time and was not finished after another 30 min. In reality, the hysteresis phenomenon is responsible for not reaching the equilibrium of the full cell at all. In the simulations presented in Figure 5.7, the hysteresis is neglected. Section 5.2 analyses the effects of hysteresis in detail.

Another approach to the adaption of impedance parameters is to increases all R values and decrease the C values in a manner that the time constants τ remain unchanged. This does not change the basic findings, it just smooths the results in the current difference in the first 100 s after the current changes. Other cells with NMC or NCA cathode materials exhibit similar behaviours to LG_HB2 cells.

5.1.3 State of charge-dependent impedance parameters

Numerous publications show that impedance parameters of lithium-ion battery cells depend on the SoC [23, 37, 222]. In this work, the modelling parameters were determined at various SoCs. Figure 3.11 in Subsection 3.3.2 shows the parameters of the Sony_FT cell. The impact of the SoC is stronger at lower temperatures, which can be seen in Figure 5.8.
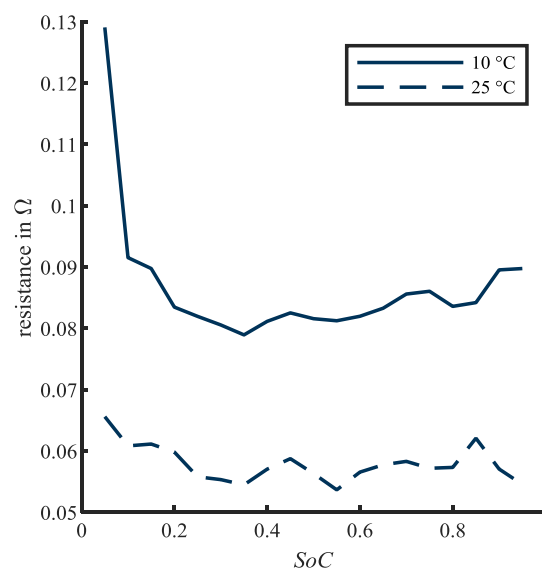
Figure 5.8: *SoC-dependent impedance parameters of the Sony_FT cell at two temperatures. The curves show the sum of the ohmic resistances of the EEC (R_S + $R_{p,1}$ + $R_{p,2}$ + $R_{p,3}$ + $R_{p,4}$ + $R_{p,5}$). The separate impedance values are shown in Figure 3.11.*

The diagram shows parameters of the Sony_FT cell, where the lines correspond to the sum of all resistances of the EEC R_{tot} at 10 and 25 °C.

$$R_{tot} = R_S + R_{p,1} + R_{p,2} + R_{p,3} + R_{p,4} + R_{p,5}$$ (5.12)

Next, a simulation experiment was conducted to compare three different sets of impedance parameters. First, all parameters depended on the SoC. Supporting points existed every 5 % of the SoC and between the values were interpolated. The results of this simulation are plotted in grey in Figure 5.9. Diagrams (a), (c), and (e) refer to LG_HB2 cells and diagrams (b), (d), and (f) refer to Sony_FT cells. To obtain the parameter difference, cell 1 used the parameters measured at 10 and cell 2 used the parameter measured at 25 °C. All experiments used a linearised OCV so as to not influence the effect of SoC-dependent impedance parameters. The load profile was similar to that is Subsection 5.1.2. A −1 C pulse discharged the parallel connection of two cells from 100 to 50 % of the SoC.
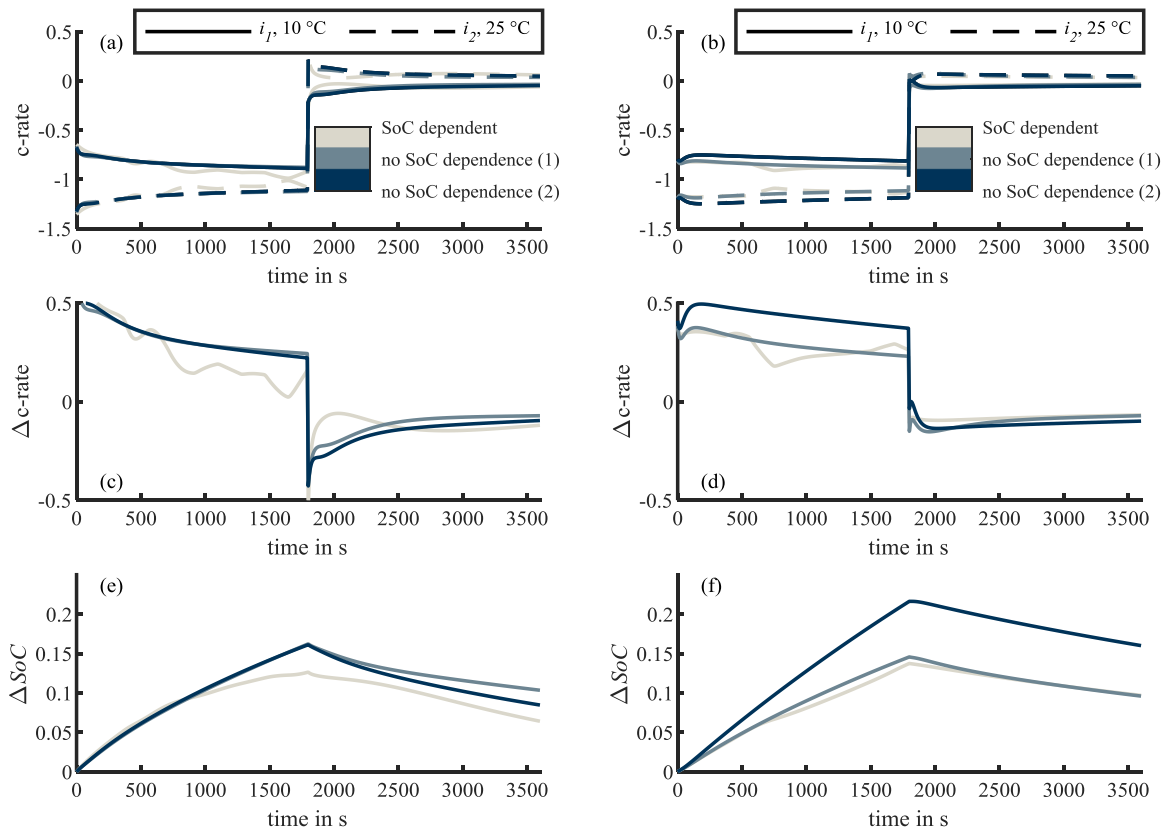
Figure 5.9: *Current distribution of two batteries connected in parallel with a pulse load of 1 C from 100 to 50 % SoC. This figure analyses the influence of SoC-dependent impedance parameters. It uses the model type $OCV_{lin}(SoC) + \underline{Z}_{R,5RC}(SoC,T)$ for SoC dependent parameters and model type $OCV_{lin}(SoC) + \underline{Z}_{R,5RC}(T)$ for the other simulations. Diagrams (a), (c), and (e) are based on LG_HB2, whereas diagrams (b), (d), and (f) are based on Sony_FT parameters; "no SoC dependence (1)" uses averaged parameters in the range of 50 to 100 % of SoC, whereas "no SoC dependence (2)" uses averaged parameters in the range of 0 to 100 % of SoC.*

The second type of simulation used averaged parameters that did not depend on the SoC. In this step, the whole SoC range from 0 to 100 % was not averaged, but the relevant area between 100 and 50 % of the SoC was. This meant that the parameters had a constant value from 0 to 100 % of the SoC, which correlated to the mean values between 100 and 50 % of the SoC. The results of this simulation are plotted in dark grey and marked with "no SoC dependence (1)". The last type of simulation is named "no SoC dependence (2)". The parameters were also SoC-independent, but in this case, the parameters were averaged over the whole SoC range from 0 to 100 %. Figure 5.9 presents the results of the third method in dark blue.

The current distributions in diagrams (a) and (b) exhibit fundamentally similar behaviour. At the beginning of the current pulse, the current of cell 1 (10 °C) is considerably lower than that of cell 2 (25 °C). This difference shrinks until the end of the pulse independently of the SoC, as opposed to the dependency of the cell parameters. This is the result of the decreasing OCV.

Diagrams (c) and (d) illustrate the current difference, where the influence of SoC-dependent impedance parameters is obvious. The curse of the grey curve, which refers to the simulation results with SoC dependency, has a more dynamic course than the two other curves with SoC-independent parameters. In the case of the LG_HB2 cell, the two alternately averaged parameter sets appear quite similar, which is not the case for the Sony_FT results. Here, the current difference is calculated using averaged parameters in a SoC range from 0 to 100 %. The current difference during the current pulse is up to 0.15 C higher than when the parameters are averaged in the range of 50 to 100 % of SoC. This is because of the rapidly increasing impedance at low SoCs; see Figure 5.8. The values below 20 % of SoC are only included in "no SoC dependence (2)" and not in "no SoC dependence (1)". The result is the current difference as well as the higher ΔSoC plotted in diagram (f).

Hence, an SoC dependence in the modelling of current distribution in parallel-connected batteries makes sense. To ensure supporting points, a closed mesh is only necessary when short-time current distribution must be analysed. In particular, the strong increase of impedance at low SoCs as well as at high SoC in some cells influences the calculation of current distribution.

5.1.4 Temperature-dependent impedance parameters

Temperature is one of the most important parameters in the field of batteries. It influences long-term processes such as ageing [93] and self-discharge [223], as well as the present internal impedance of battery cells. This chapter subsection on the impedance variation caused by temperature and its effect on current distribution.

The total ohmic impedance of a battery cell R_{tot} equals the sum of R_S and all $R_{p,k}$ following equation (5.12). This can be calculated for all cell types, temperatures, and SoC supporting points. With this, the normalised impedance growth R_{rel} can be calculated:

$$R_{rel} = \frac{R_{tot,10°C}}{R_{tot,25°C}} \qquad\qquad (5.13)$$

Figure 5.10 illustrates the results of this calculation. The impedance growth is not homogeneous for various SoC and cell types. The Sony_FT cells show quite a stable shift of + 50 % overall SoCs.
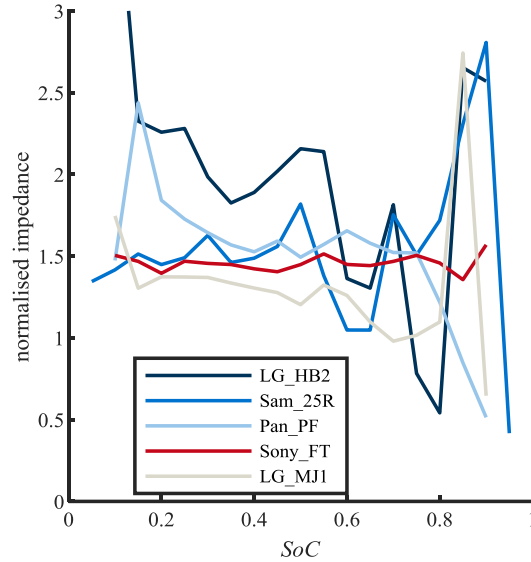
Figure 5.10:   *Normalised growth of total ohmic resistances of the EEC ($R_S + R_{p,1} + R_{p,2} + R_{p,3} + R_{p,4} + R_{p,5}$) at temperatures decreasing from 25 to 10 °C. The diagram shows the change of the fitted parameter from the pulse measurements described in Subsection 3.3.2.*

The curves of Figure 5.10 are not smooth. Therefore, Table 5.3 uses mean values over all SoCs to give an overview of the impedance change with the temperature. It shows the averaged impedance values for the overall SoC at 10 and 25 °C. The results do not correlate to the cells' basic data in Table 3.3. In the end, an increase in resistance of 1.5 to 4.3 % by a decrease of 1 °C was determined. Referring to the impedance growth with ageing of 40 % [102], this means a temperature decrease of 27 °C in the LG_MJ1 or of 9 °C in the LG_HB2 cell is equivalent in resistance growth.

Table 5.3:   *Average of the total resistance at 10 and 25 °C, overall SoCs, and normalised growth at temperatures decreasing from 25 to 10 °C*

Cell	LG_HB2	Pan_PF	Sam_25R	Sony_FT	LG_MJ1
Mean of the total resistance at 10 °C in Ω	0.159	0.116	0.178	0.090	0.095
Mean of the total resistance at 25 °C in Ω	0.097	0.076	0.133	0.058	0.078
Normalised resistance growth (resistance at 10 °C / resistance at 25 °C)	1.64	1.53	1.33	1.55	1.22
Normalised resistance variation ε_T referred to temperature increase in %/K (linearised)	4.3	3.5	2.2	3.7	1.5

Using the results of Table 5.3, a simulation experiment was set up. Three different temperature variations based on the parameters of 25 °C were simulated. A relative increase in impedance $\Delta \underline{Z}_{rel}$ in percent resulted from the normalised resistance variation ε_T referring to temperature increases:

$$\Delta \underline{Z}_{rel} = \Delta T \cdot \varepsilon_T \qquad (5.14)$$

Boundary conditions such as cell parameters, load profile, OCV linearity, and slope were similar to the experiments in Subsections 5.1.2 and 5.1.3. Figure 5.11 presents the simulation results at an impedance growth of ΔT of 5, 10, and 15 °C.
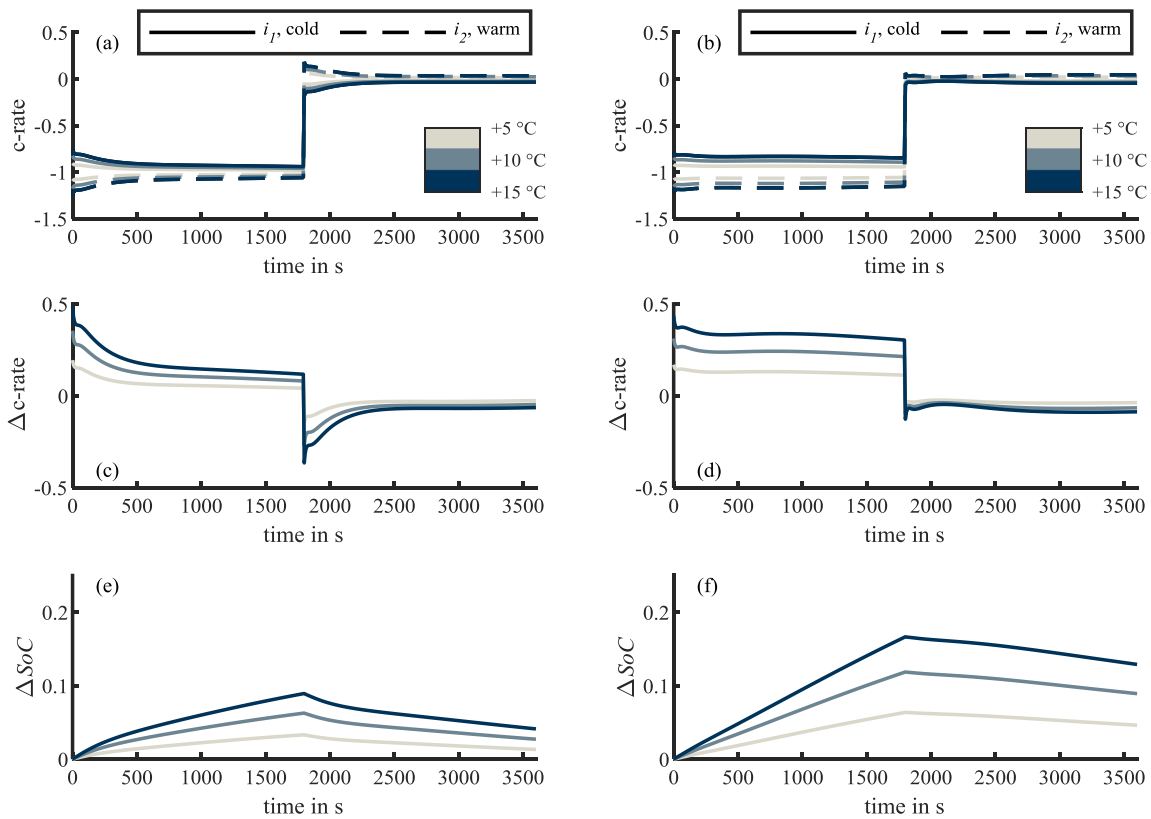

Figure 5.11:   *Current distribution of two batteries connected in parallel with a pulse load of 1 C from 100 to 50 % SoC. The figure analyses the influence of the temperature. The diagrams (a), (c), and (e) are based on LG_HB2; diagrams (b), (d), and (f) are based on Sony_FT parameters; and the increase with temperature refers to Table 5.3 (model type: $OCV_{lin}(SoC) + \underline{Z}_{R,5RC}$).*

LG_MJ1 cells showed the lowest increase of impedance with decreasing temperatures. Table 5.3 lists a gradient of 1.5 %/K. To compare the temperature effects at different ε_T, Figure 5.12 analyses the current distribution results of two LG_MJ1 cells connected in parallel.

All current distributions in Figure 5.11 and Figure 5.12 exhibit similar behaviour. At the beginning of the pulse, the current distribution is higher than that in the end. The temperature

dependence of the impedance parameters defines the height of the SoC difference at the end of the pulse. Because the OCV of cells with LFP cathode material is flat, the current difference decreases more slowly with the current flow of the pulse. Therefore, larger SoC differences are reached. Regarding Table 5.3, temperature differences of 10 and 25 °C mean an increase in resistance of 22 to 64 %. Ecker et al. measured an impedance increase of approximately 40 % while the capacity decreased to 80 % [102], which is a usual definition of the end of life. This means that the influence on the current distribution of $\Delta T = 15$ °C with respect to impedance is in the same range as one cell at the beginning of its life connected with another cell at the end of its life in parallel referring to the results of Ecker et al. [102]. In case of aged cells, the influence of the capacity would be added.

Figure 5.12: *Current distribution of two LG_MJ1 batteries connected in parallel with a pulse load of 1 C from 100 to 50 % SoC. The figure analyses the influence of the temperature. The increase in temperature refers to Table 5.3 (model type:* $OCV_{lin}(SoC) + \underline{Z}_{R,5RC}$*).*

5.2 Hysteresis

Hysteresis influences the OCV depending on the previous current, and therefore the SoC's history. Because voltage differences in parallel-connected batteries drive inhomogeneous current distribution, hysteresis contributes to this effect. Furthermore, because the current distribution in parallel-connected cells is not homogeneous, the hysteresis voltage also differs.

In LFP lithium-ion battery cells, hysteresis is particularly relevant because of its flat OCV curve. Figure 3.15 (a) illustrates how the hysteresis of LFP and other cathode materials are in the same range. At certain SoCs, the width of LFP hysteresis is more distinctive, whereas at other SoCs, NMC or NCA cathode materials exhibit higher hysteresis voltages. However, the effect on current distribution is quite different. Figure 5.13 indicates the upper and lower limits of hysteresis of an LG_MJ1 (NMC | graphite) and a Sony_FT (LFP | graphite) cell at 25 °C. The data include the cell terminal voltage after 3 hours of relaxation for every 5 % of SoC from the measurements described in Subsection 3.3.4.
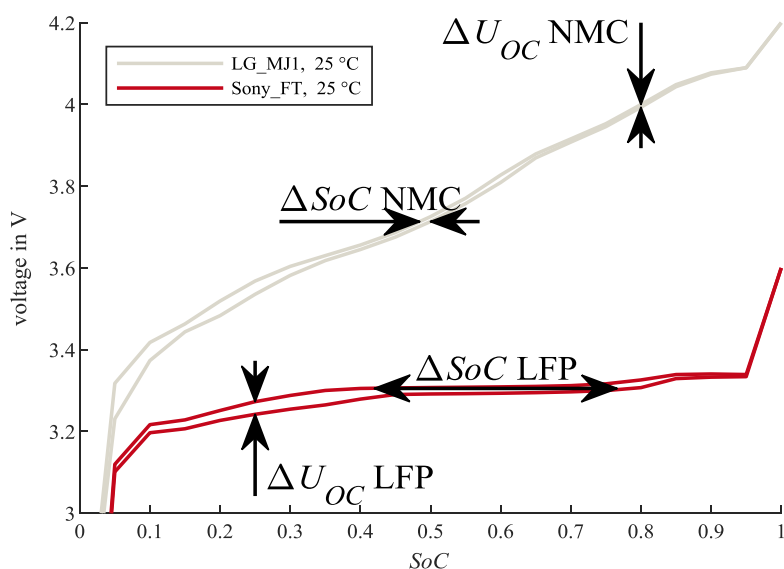
Figure 5.13:   *Upper and lower limits of the hysteresis-afflicted OCV of an LG_MJ1 (NMC | graphite) and a Sony_FT (LFP | graphite) cell at 25 °C*

LG_MJ1 cells are exemplary of all NMC and NCA cells having a steep OCV characteristic. In fact, the ΔU_{OC} of these cells' electrode materials is in the same range, but this does not apply to the difference in SoC. The arrows in a vertical direction indicate exemplary the maximum difference of OCV values of a certain SoC, whereas the arrows in a horizontal direction indicate the maximum difference of SoC values of a certain OCV.

For example, an LFP cell that is discharged to 43 % of its SoC starting in a fully charged state ends up on the upper curve. Another cell that is charged to 76 % of its SoC starting from a fully discharged state ends up on the lower curve. Both cells will have the same voltage after relaxation. This means there is no equalisation force that brings these cells to the same SoC when they are connected in parallel—both would keep their SoC.

This is clearly illustrated in Figure 5.13. Figure 5.14 presents a calculation of the maximum ΔSoC depending on the SoC. The datapoints are mapped to the mean of upper and lower U_{OC} of SoC on the x-axis. In summary, LFP cells can be connected in parallel with the same voltage but an ΔSoC of more than 30 %. In NMC or NCA cells, this value does not exceed 4 % of the

SoC. Measurements at 10 °C exhibit a larger ΔSoC in LFP cells. Other electrode materials do not show this dependency.
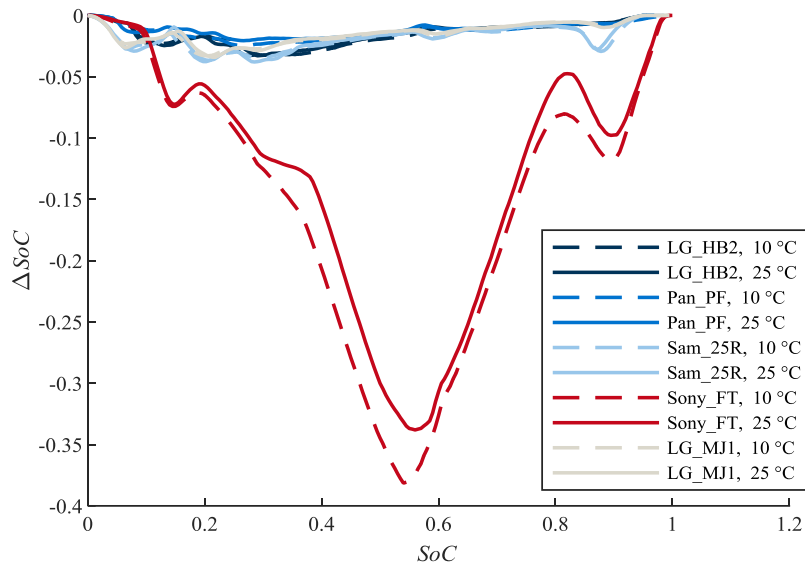
Figure 5.14:   *Possible SoC differences of two cells of various types connected in parallel at the upper and lower limits of hysteresis at 10 and 25 °C*

The hysteresis effect on current distribution within parallel-connected cells is analysed in Figure 5.15. Again, a discharge pulse load of 1 C is provided for a parallel connection of two cells, which lasts for 0.5 h and starts from a fully charged system. All simulations used measured nonlinear OCV curves. A linearised OCV would not have a flat area at approximately 55 % of SoC, which leads to an ΔSoC of more than 30 %, as illustrated in Figure 5.14.

In these simulations, the impedance parameters do not have an SoC dependence. However, they are temperature-dependent, otherwise there would be no difference in current, and thus in hysteresis. The upper and lower limits of hysteresis at 25 °C come from the measurements in Subsection 3.3.4, as shown in Figure 3.15 and validated in Figure 3.18.

In Figure 5.15, the ΔSoC relaxation ends after 0.5 h of relaxation in an unfinished state. A longer simulation with similar parameters sets analyses for the proceeding ΔSoC over 10 h of simulation. The results with and without hysteresis for LG_HB2 and Sony_FT cells are presented in Figure 5.16. At the beginning, the ΔSoC rises for 0.5 h while the pulse discharges the cells. Afterwards, the equalisation is illustrated over 9.5 h. This process is driven by the voltage differences in OCV, as well as by overvoltages and hysteresis.
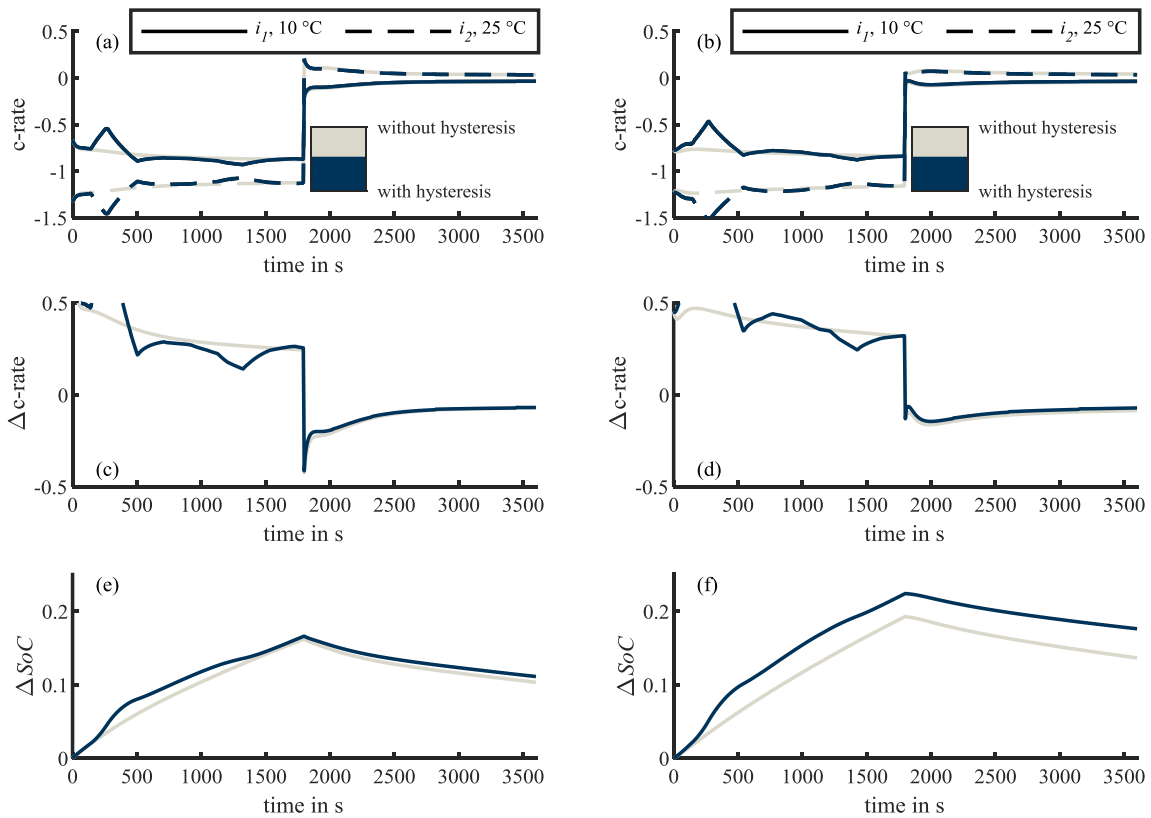
Figure 5.15: *Current distribution of two batteries connected in parallel with a pulse load of 1 C from 100 to 50 % SoC. This figure analyses the influence of hysteresis. Cell 1 is at 10 and cell 2 is at 25 °C. Diagrams (a), (c), and (e) are based on LG_HB2, whereas diagrams (b), (d), and (f) are based on Sony_FT parameters (model types:* $OCV_{mea\_0.05C}(SoC) + \underline{Z}_{R,5RC}(T)$ *and* $OCV_{mea\_0.05C}(SoC, hyst) + \underline{Z}_{R,5RC}(T))$

In this case, cell 1 has a higher SoC because of higher impedance, which is caused by lower temperature. The current direction of cell 2 changes from discharge to charge. Hence, the hysteresis moves from the lower hysteresis curve toward the upper curve while cell 1 discharges further and remains on the lower hysteresis curve. This is only the case when the hysteresis is calculated; Figure 5.16 shows the discrepancy. While the solid lines without hysteresis calculation end up at $\Delta SoC = 0$, in the chain dotted lines, an ΔSoC remains after 9.5 h of equalisation. At the maximum ΔSoC, the SoC-dependent ΔSoC values in Figure 5.14 are possible.

The relaxation behaviour is quite similar to a PT1 element. To calculate the time constant, this study assumed that the final ΔSoC was reached at the end of the simulation. Hence, the time constant could be taken when 63.2 % of the total decrease was reached. The mean time constant of the Sony_FT cell resulted in 1.5 h and that of the LG_HB2 cell in 1.3 h. These time constants had similar values with or without hysteresis calculation.
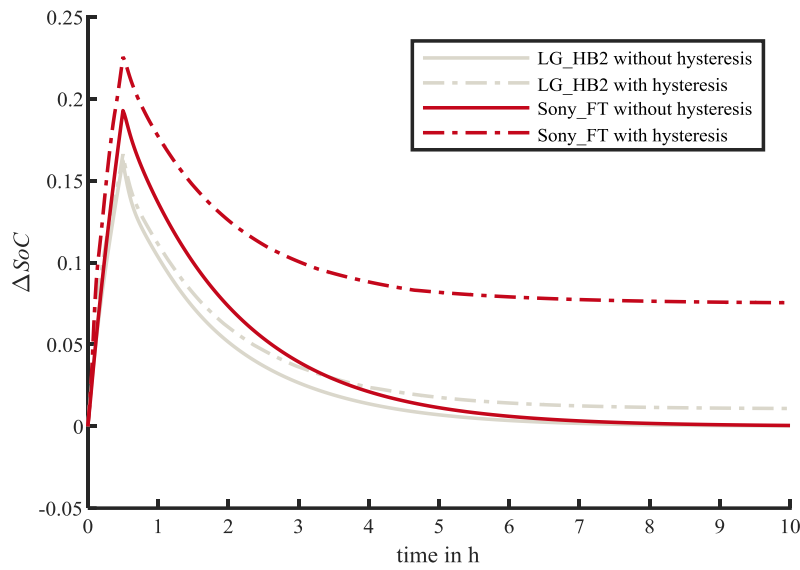
Figure 5.16: *Simulated ΔSoC progression with a 0.5-h current pulse and relaxation phase afterwards with and without considering hysteresis for LG_HB2 and Sony_FT cells (model types: $OCV_{mea\_0.05C}(SoC) + \underline{Z}_{R,5RC}(T)$ and $OCV_{mea\_0.05C}(SoC, hyst) + \underline{Z}_{R,5RC}(T)$)*

5.3 Entropy

Similar to hysteresis, entropy also changes the OCV of cells with the same SoC, and different temperature and voltage differences affect the current distribution in parallel connections of batteries. The value of voltage influence is defined by the entropic coefficient shown in Figure 3.16. These data come from the literature [144, 216–218] and depend on the SoC. Figure 3.16 (b) shows the entropic coefficient divided into the cathode, anode, and full cell of the Sony_FT cell. This voltage difference is driven by the temperature, and therefore, the current distribution also influences $\Delta U_{entropy}$.

First, the maximum impact on ΔSoC is analysed in Figure 5.17 in a similar manner to Figure 5.14. Diagram (a) shows four curves of four temperature differences $\Delta T = [1; 5; 10; 15]$ °C. The results indicate SoC differences of the LG_HB2 cell less than 1 % at $\Delta T = 15$ °C. Other cells with NMC or NCA cathode materials provide comparable results. This is because of the steep slope of the OCV. As shown in the case of hysteresis in Figure 5.13, a small voltage difference leads to a small SoC difference at a steep OCV. This is not the case at a flat OCV in LFP cells. Moreover, in cases of entropy, the voltage difference has a higher influence on the ΔSoC in the Sony_FT cell (compare Figure 5.17 (b)). An ΔSoC up to 5.5 % is reached at a temperature difference of 15 °C. This extremum is at the same SoC as that of ΔSoC in case of hysteresis, which is because of the flat slope of the OCV in this area. Also notable is that the maximum influence on ΔSoC of hysteresis at Sony_FT cells is by a factor 6.5 times larger than the influence of entropy at $\Delta T = 15$ °C.
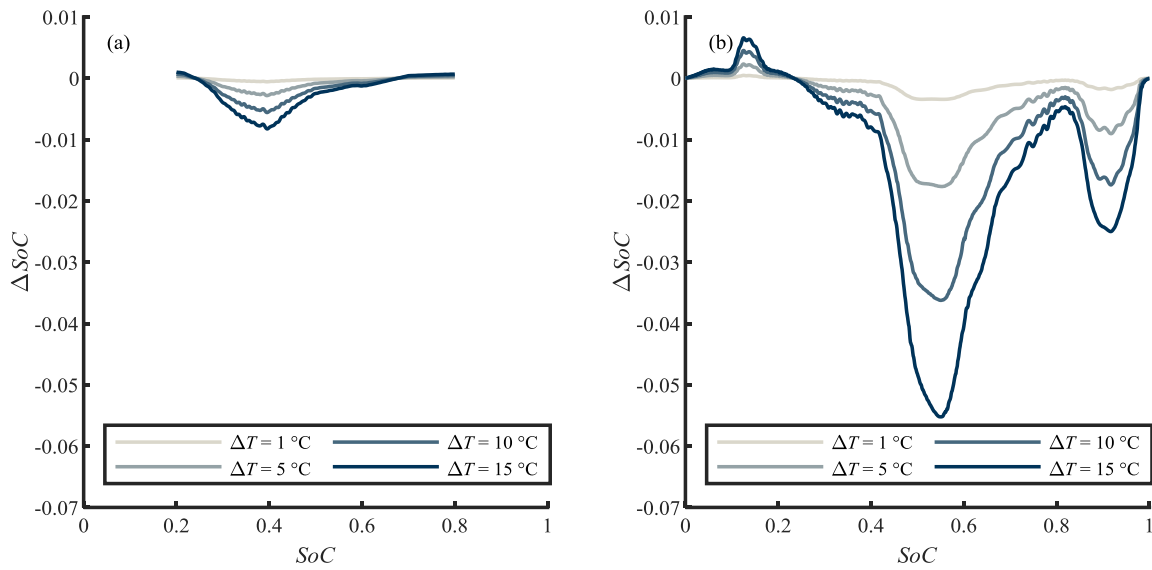
Figure 5.17: *Possible SoC differences of two cells of various cell types connected in parallel at different temperatures, and therefore at different levels of entropy. Diagram (a) refers to LG_HB2 and (b) to Sony_FT cells.*

To analyse the influence in a parallel connection, simulations were performed using a 1 C discharge pulse that lasted 0.5 h. The OCV was not linearised in these experiments but the impedance parameters were averaged in the range from 100 to 50 % of SoC, and therefore they were not SoC-dependent. Because the entropic coefficient of NMC and NCA cells started at 20 and ended at 80 % of the SoC (see Figure 3.16 (a)), the LG_HB2 cell was discharged from 80 to 30 % instead of from 100 to 50 %. Figure 5.18 shows the simulation results for the LG_HB2 cells on the left side and for the Sony_FT cells on the right. Three steps of temperature difference $\Delta T = [-5; -10; -15]\,°C$ were calculated. The fourth step did not use entropic data from the literature but cells' individual OCV curves measured at 25 and 10 °C.
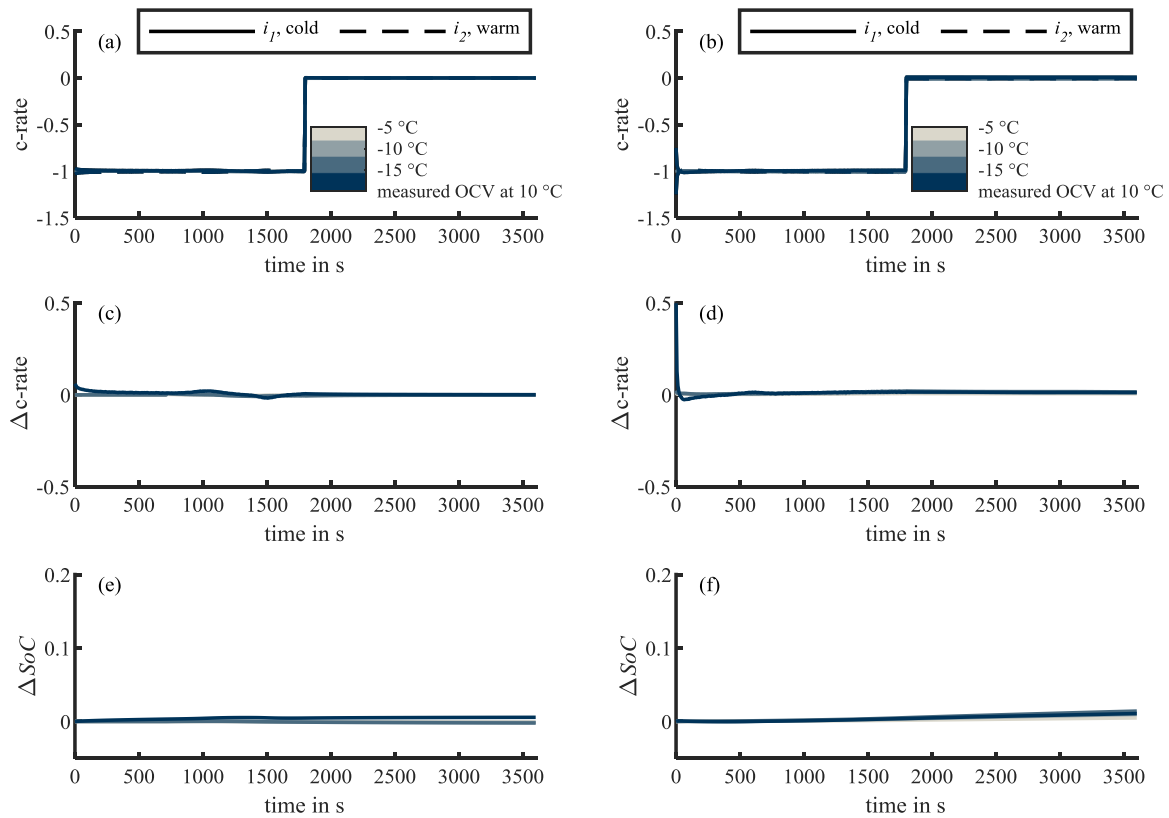
Figure 5.18:   *Current distribution of two batteries connected in parallel with a pulse load of 1 C from 100 to 50 % SoC. This figure analyses the influence of entropy. The impedance parameters are similar in both cells. Diagrams (a), (c), and (e) are based on LG_HB2, whereas diagrams (a), (c), and (e) are based on Sony_FT parameters. Because no data above 80 % of SoC were available on LG_HB2 cells, the starting SoC was set to that value (model type:* $OCV_{mea\_0.05C}(SoC,T) + \underline{Z}_{R,5RC}$*).*

Differences in current and SoC were hardly visible, which is because no SoC dependence of the impedance parameters was simulated. Both cells used the SoC-independent impedance parameters of a 25 °C warm cell. Simulations without temperature dependent impedance parameters help to observe the effect of entropy more clearly. This method cannot be used for hysteresis analysis, because in that case, no current difference would appear.

During the relaxation phase after the current pulse, a change in ΔSoC was noticeable. To analyse the further proceedings, simulation cases $\Delta T = -15\,°C$ were repeated using a relaxation phase of 9.5 h. The results of this experiment are shown in Figure 5.19. The ΔSoC of the LG_HB2 cell at the end of relaxation was below 0.3 % and for the Sony_FT cell about 6 %. Entropy led to a difference in SoC that was independent of the current history. This behaviour differs from hysteresis. The impact depends on the slope of the OCV, and therefore on the SoC. Figure 5.17 indicates critical SoCs.
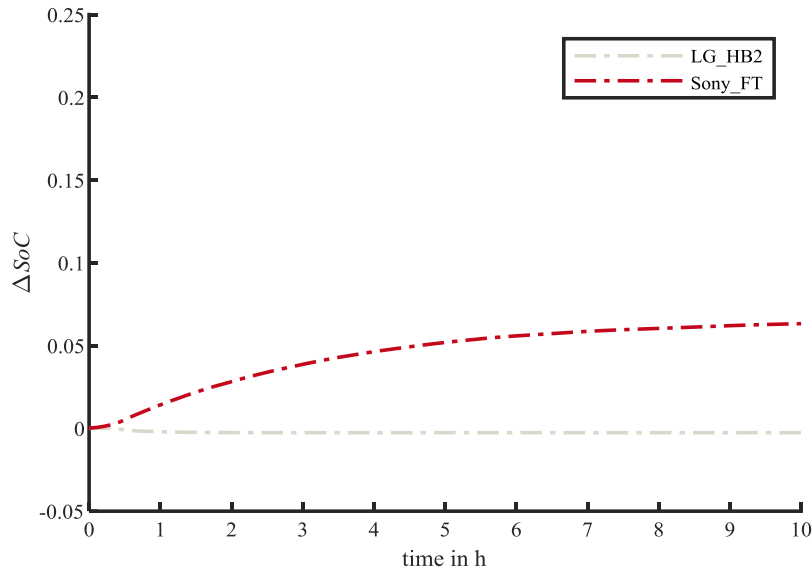
Figure 5.19: *Simulated ΔSoC progression during the 0.5 h current pulse and relaxation phase afterwards at $\Delta T = -15\,°C$. The proceeding ΔSoC is a result of different entropy and the slopes of the cells' OCVs (model type: $OCV_{mea\_0.05C}(SoC, T) + \underline{Z}_{R,5RC}$).*

5.4 State of charge

It is obvious that not only the impedance but also the capacity of battery cells differs because of production, ageing, or other influencing factors. Brand et al. showed that capacity differences affect current distribution in parallel connections [25]. The terminal voltage of ideal parallel-connected cells is similar as per their definition. This means that they were discharged until the cut-off voltage in a similar time; hence, the current must differ at an unequal capacity.

5.4.1 Capacity

In this subsection, the influence of capacity differences ΔC_n are analysed in a parallel connection of two cells. The analyses use the same conditions as those in Subsection 5.1.1. Figure 5.20 and Figure 5.21 are similar to Figure 5.5 and Figure 5.6.
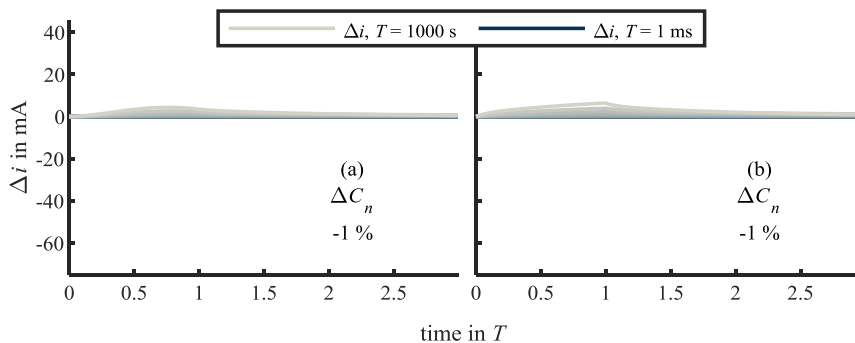
Figure 5.20: *Differences in current Δi between cell 1 and cell 2 simulated with the parameter differences described in Table 5.2: (a) sine input, (b) pulse input. Cell 1 has a capacity of 1 Ah and cell 2 a capacity of 0.99 Ah. (model type: $OCV_{lin}(SoC) + \underline{Z}_{R,20RC}$)*

The difference in capacity has less of an impact on the current distribution than the impedance variations in Figure 5.5. In contrast to changing the sign of Δi in Figure 5.5, at ΔC_n in Figure 5.20 there are only positive values. In this case, the cell with lower capacity takes a lower current, which results in less overpotential. At the end of the load, the SoC of the cell with higher capacity is higher. In contrast to the ΔSoC results in Figure 5.3 (c) and Figure 5.4 (c), the ΔSoC at ΔC_n gives positive values; therefore, Δi does not change the sign after the load.

Figure 5.21 proves that capacity differences are only relevant to long-term current loads. This is valid regarding the maximum current difference and charge throughput difference in sine and pulse loads. The effects of capacity differences at $T = 1000$ s are less than the simulated effects of impedance differences in Figure 5.6. The capacity, as well as the impedance simulations, refer to the parameter variations of Rumpf et al. [20], summarised in Table 5.2.
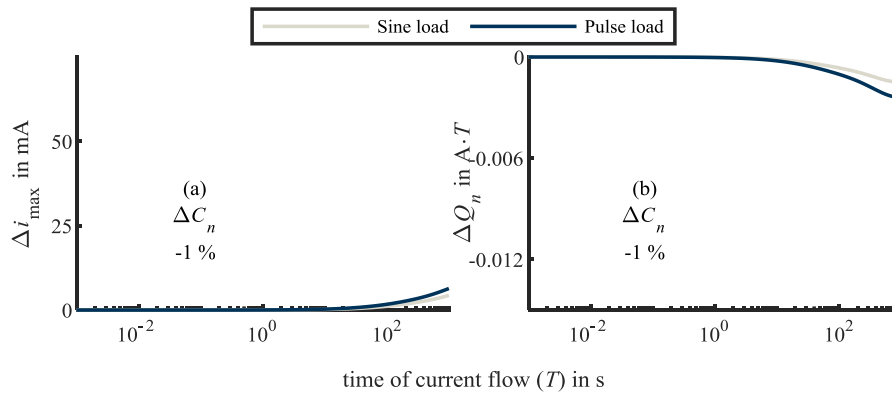
Figure 5.21: *Analysis of the maximum current difference Δi_{max} and normalised charge throughput difference ΔQ at $T = 0.001 \ldots 1000$ s (model type: $OCV_{lin}(SoC) + \underline{Z}_{R,20RC}$)*

To summarise, in the analysed scenario, the influence of a capacity variation on current difference and charge discrepancy was low compared with the influence of the impedance. One major reason for this observation was the unequal parameter differences shown in Figure 5.3 and Figure 5.4. An additional analysis where all parameter differences were set to + 10 % gave the largest current differences in the ΔR_S scenario, followed by in the ΔC_n scenario. Especially at long pulse durations T, the current difference at ΔC_n was high, which fits well with the results of Brand et al. [25].

As has already been shown, cell capacities and impedances have a large influence on the dynamic behaviour of current distribution in cells connected in parallel. This is why cells with a variable ratio between capacity and impedance were analysed. Different cell dimensions can be compared with the resistance coefficient λ; see equation (3.34) on page 32. [208, 209]

HP cells offer a lower impedance $\underline{Z}$ and a low capacity C_n, which led to a low resistance coefficient λ. In the case of HE cells, the impedance $\underline{Z}$ and capacity C_n are high, and therefore the resistance coefficient λ is high.

The resistance coefficient of the HP cell LG_HB2 is $\lambda = 1.5$ Ah $\cdot$ 0.010 Ω = 0.015 AhΩ. A widely used HE cell is the LG_MJ1, the resistance coefficient of which is calculated with $\lambda = 3.5$ Ah $\cdot$ 0.040 Ω = 0.140 AhΩ. These values are based on the datasheet parameters for the cells. This study adapted the ohmic resistance R_s and cell capacity C_n for the following simulations. Therefore, the analysis in Figure 5.22 was performed beyond these values at $\lambda = 0.005 \ldots 0.165$ AhΩ; λ was varied linearly in 16 steps. The ZARC and Warburg model parameters, as well as the variation of the ohmic resistance ΔR_s and cell capacity ΔC_n, remained unchanged from the initial values in Table 5.2 and a linear OCV. The load profile was scaled for the size of the cells. The simulations were performed with a c-rate of 1 C relative to the total capacity of the 2p connection. The current flow of the discharge sine half-wave and the discharge pulse lasted 1000 s.
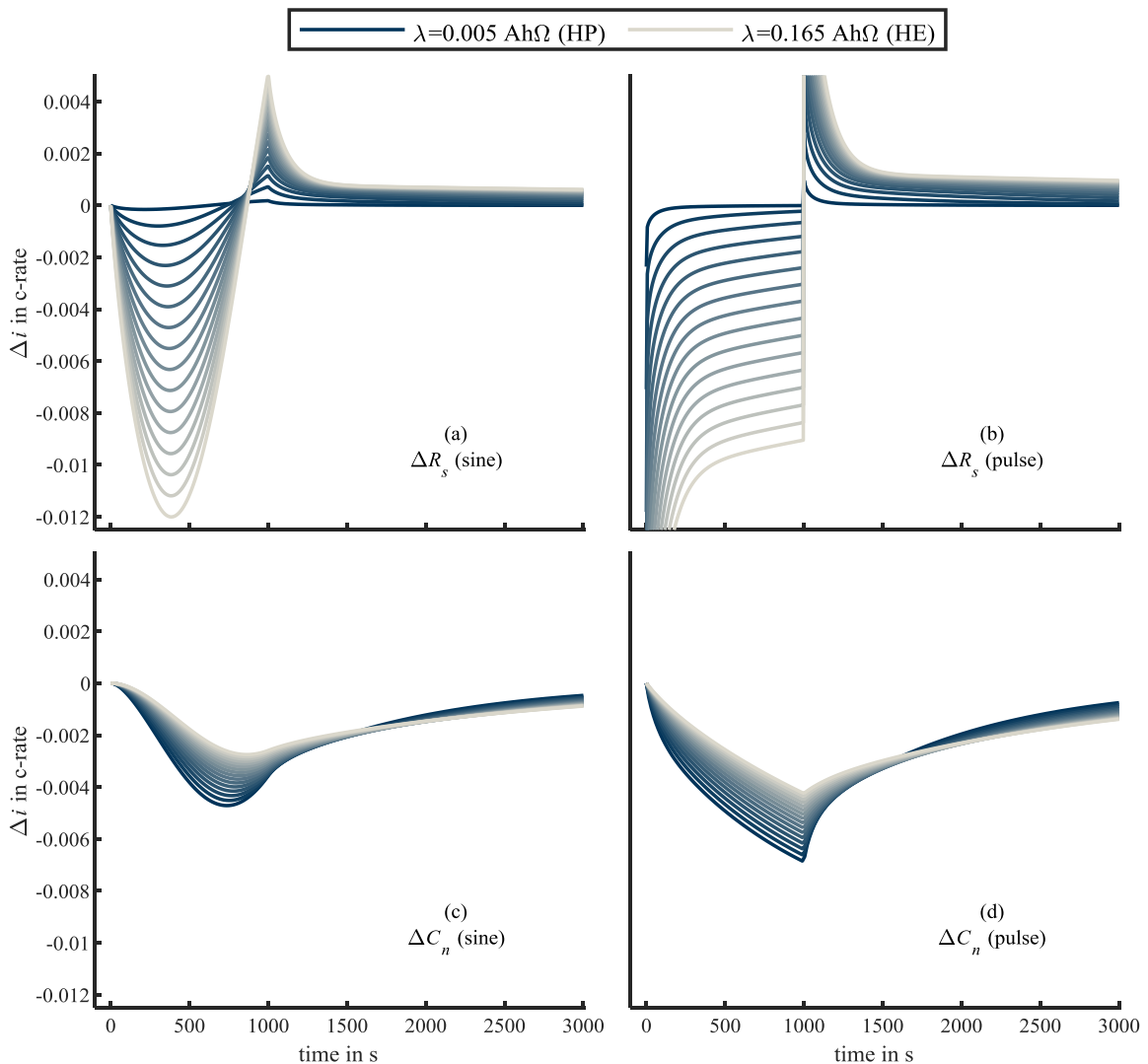
Figure 5.22:   *Resistance coefficient variation ($\lambda = \mathbf{0.005 \ldots 0.165}$ AhΩ) and its influence on the current distribution at capacity ($\Delta C_n = -\mathbf{1}$ %) and impedance ($\Delta R_s = \mathbf{7.6}$ %) differences with a sine (left diagrams) and pulse load (right diagrams) (model type: $OCV_{lin}(SoC) + \underline{Z}_{R,20RC}$)*

To compare the cell sizes, the current difference Δi in Figure 5.22 is plotted as a c-rate. In the case of ΔR_s, the current difference Δi changes direction at the end of the external current flow after 1000 s. The SoC difference—and therefore the OCV difference in these two scenarios— has a different sign. This can also be observed in the simulation results of Brand et al. [25]. When the external current stops, this voltage difference drives the equalisation current with a different sign.

Furthermore, it is obvious that the influence of the ohmic resistance ΔR_s (as seen in Figure 5.22 diagrams (a) and (b)) is larger than the influence of the cell capacity ΔC_n. HE cells, shown as light grey lines, display a long-term influence, which occurs because of two influences. The first observation is the fact that the variation of R_s is higher than C_n. Second, ΔR_s has an impact on the short term while at ΔC_n, Δi grows with the time of the pulse. At the end of the simulation, $t = 3000$ s, a current difference remains in all four diagrams. Even if it is small, it disappears very slowly, and thus it can be assumed to last for hours. Furthermore, it is remarkable that the ohmic resistance difference ΔR_s has a larger influence on HE cells, whereas the cell capacity difference ΔC_n has a larger influence on HP cells.

An additional influence of reversible heat can be expected because different cell currents generate unequal heat and SoC. Both affect the entropy of the cells [208], which causes an interdependency. This is not considered in the simulation results of Figure 5.22. In sum, HP cells are more likely to be influenced by capacity differences and HE cells by impedance differences.

5.4.2 Open-circuit voltage

The OCV is the major part of a cell's voltage. Because the asymmetric current distribution is driven by voltage differences, the OVC is critical. Many simulations to date have used a linearised OCV curve (see Table 2.6). Simulations with real OCV curves display a significant impact on the current distribution of the OCV slope. Because a difference in OCV exists between the cells connected in parallel, a change in the OCV gradient leads to a rise or fall in OCV differences. For a linear OCV, the two cells form a constant ΔSoC as long as there is a constant total current flow. This constellation was described for the ΔC_n and ΔR_s scenario by Brand et al. [25]. A nonlinear OCV disturbs the formation process of a constant ΔSoC. In reality, OCV curves are nonlinear on account of graphite steps, for example, and change their shape during their lifetime [93]. Because the OCV is formed by a difference in voltage between the half-cell potential of cathode and anode materials, these materials and their balance lead to OCV variations. The following equation represents a linear OCV containing a single nonlinear area. Fuller et al. [224] and Doyle et al. [225] also used hyperbolic tangent functions to fit the open circuit potential. Furthermore, the shape can optionally be varied using the parameters m (slope of the linear area), b (slope of the nonlinear area), and c (height of the voltage step of the nonlinear area):

$$OCV(SoC) = m \cdot \frac{SoC}{100\,\%} + t + \frac{c}{2} \cdot \tanh\left[\left(\frac{SoC-a}{100\,\%}\right) \cdot b\right] \qquad (5.15)$$

$$SoC = 100\,\% - DoD \qquad (5.16)$$

Table 5.4 summarises the initial and variation values from equation (5.15). The parameters of the OCV's nonlinearity change over 16 simulation runs from the minimum to the maximum value. Both cells of the 2p connection use the same OCV. The cell parameters and the differences in capacity ΔC_n and ohmic impedance ΔR_S are taken from Table 5.2.

Table 5.4: *Parameter variation in the OCV nonlinearity analysis*

	m Slope OCV	SoC	t OCV at $SoC = 1$	a SoC step	b Slope nonlinearity	c Voltage step
Initial value	-1 V	100 %	4.2 V	90 %	-100	-0.02 V
Variation value	-0.2 … 1 V	No variation	No variation	No variation	210 … 50	-0.01 … 0.042 V

The load profile is a −2 A square discharge pulse that lasts 1000 s. The simulation starts at 100 % SoC and reaches the maximum OCV slope at 90 % SoC. Figure 5.23 illustrates the corresponding effects of parameter variations on the current difference Δi between cells 1 and 2, whereas the highlighted boxes display the OCV changes, respectively. Diagrams (a) to (f) show the simulation results of the current difference, comparable to Figure 5.4 (b). In the results in Figure 5.23, the time of the current flow is constant but the OCV is not linear.

Nonlinearities in the OCV curve have a significant effect on current distribution. The peaks of current discrepancy at 360 s are in the range of the current difference caused by the impedance or capacity difference. Higher voltage steps lead to increasing differences in current; see Figure 5.23 (c) and (f). The change in the OCV gradient in the nonlinear area has the largest effect on the current behaviour; see Figure 5.23 (b) and (e). In Figure 5.23 (a), it becomes clear that the equalisation current after 1000 s drops faster with steep OCV curves when $m = -1$ V, with a capacity difference of ΔC_n and a variation of the OCV slope. At this time, no external current flow is provided. The effects of OCV nonlinearities on current distribution can also be expected to appear within the cells along the electrodes [122].

In sum, changing the OCV slope has a significant influence on the current difference. The step height and overall slope of the OCV are less relevant.

The OCV is crucial for modelling the battery voltage because it represents the major part of the output voltage of the cell. First, the OCV depends on the SoC. Normally the OCV characteristic curve is plotted against the SoC. The voltage of the half-cell potentials of the cathode and anode can be calculated together with their stoichiometric relationship. Furthermore, it is possible to measure the anode's and cathode's potential separately and combine them with the cells' OCV. For example, Sturm et al. did this in their paper on the LG_MJ1 cell [190]. Furthermore, overvoltage, entropy, and hysteresis influence the cell voltage.

Figure 5.23 makes clear that the slope of the OCV has the largest influence on the current distribution. The measured OCVs are nonlinear but their slope changes depending on the SoC.

Because the OCV of a battery cell is composed of the OCVs of the cathode and anode, nonlinearity also comes from the electrode material properties. Figure 3.14 on page 47 depicts the measured OCVs of the various cells used in this work. The diagrams prove that the slope of the OCV depends on the current used to determine the curves. Together with the results in Figure 5.23 (b) and (e), this means that the method of measuring the OCV influences the result of simulated current distribution. Simulations of current distribution using an OCV measured with a current of C/100 are strongly affected by the nonlinear parts of the OCV, whereas a simulation using an OCV measured at a current of 1 C will be hardly influenced.
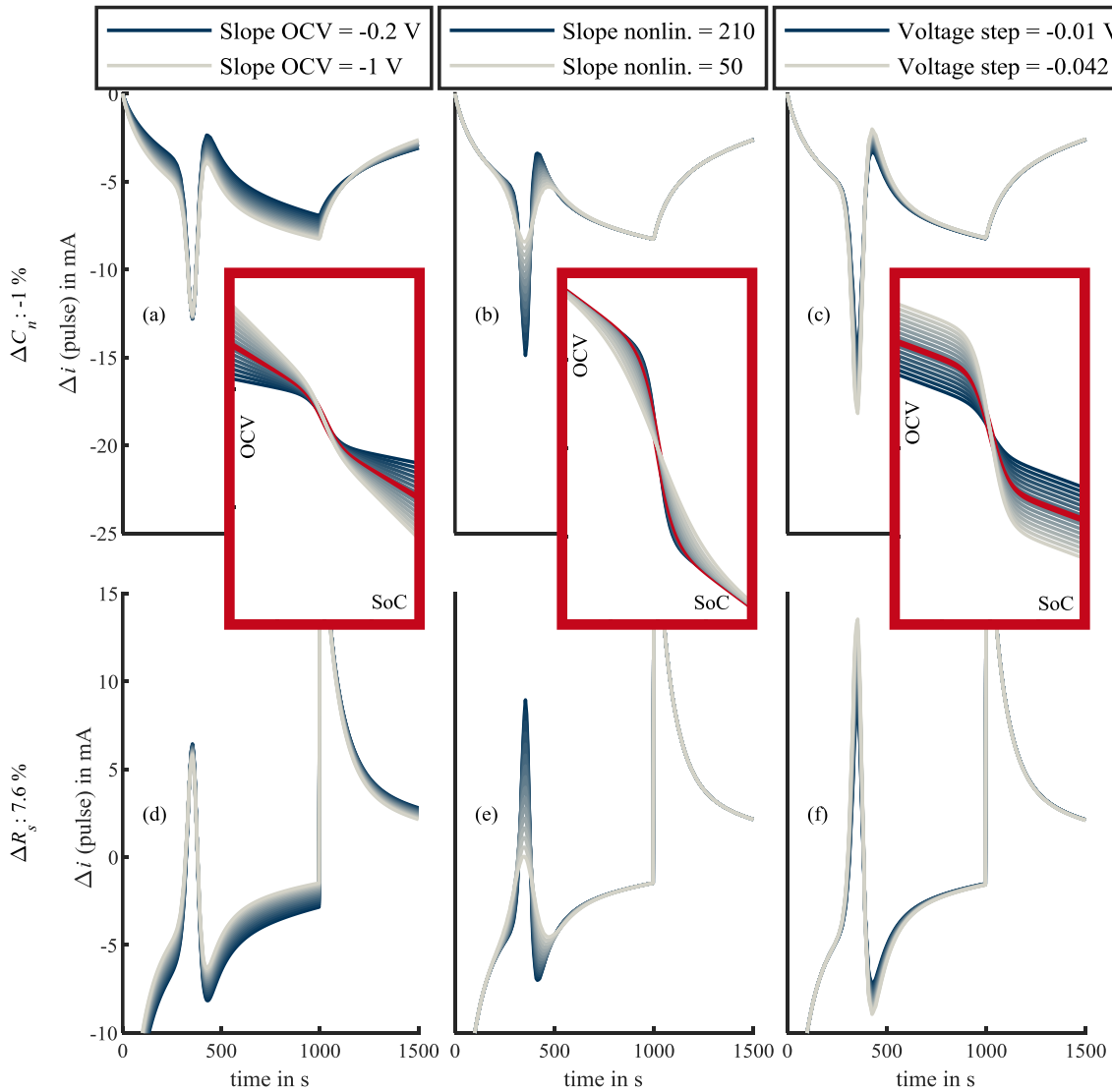
Figure 5.23: *Three variations of OCV nonlinearities ((a) and (d): slope of the OCV; (b) and (e): slope of a nonlinear area; (c) and (f): voltage height of a nonlinear area) and their effect on current distribution at capacity ($\Delta C_n = -1$ %) and impedance ($\Delta R_s = 7.6$ %) differences with a pulse load (model type: $OCV_{tanh}(SoC) + \underline{Z}_{R,20RC}$)*

Additionally, the current has an influence on the current distribution in real battery systems. Figure 5.24 and Figure 5.25 analyse this effect through CCCV measurements of two cells of the

same type. Figure 5.24 shows the results of measured and normalised current differences between cold cell 1 at 10 and a warm cell 2 at 25 °C under CCCV charge and discharge as well as a varying current. Diagram (a) shows the results of an LG_HB2 cell with a steep OCV and (b) the results of the Sony_FT cell with a flat OCV caused by the LFP cathode material.
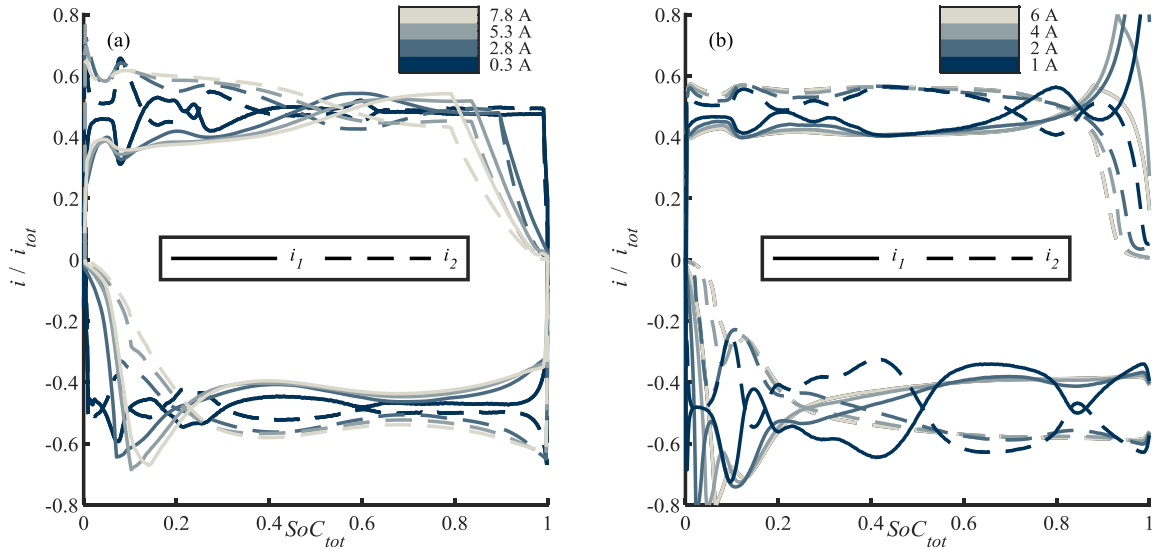
Figure 5.24: *Measured and normalised current differences between a cold cell 1 at 10 and a warm cell 2 at 25 °C under CCCV charge and discharge and a varying current. Diagram (a) shows the results of an LG_HB2 cell with a steep OCV and (b) the results of the Sony_FT cell with a flat OCV caused by the LFP cathode material.*

In every charge and discharge cycle, the current is varied. The values depend on the limits in the cell's datasheet. At higher currents, the dynamic of the current distribution sinks, and this influence seems to be nonlinear. For example, there is hardly a distinction between 7.8 and 5.3 A in diagram (a), but 2.8 and 0.3 A differ strongly. In diagram (b), there is an effect that does not appear in diagram (a). At high SoCs in the charge direction, the cold cell 2 takes almost all of the current. This super elevation is critical in terms of lithium plating and is analysed in the ageing experiment discussed in Section 6.2. The SoC is calculated using the integration of the cell current and difference in ΔSoC, which equals the SoC of cell 1 minus the SoC of cell 2:

$$\Delta SoC = SoC_2 - SoC_1 = SoC_{25°C} - SoC_{10°C} \tag{5.17}$$

First and most obviously, the SoC difference in Figure 5.25 reaches its highest rate at the highest currents. No important discrepancy exists between discharge (negative ΔSoC values) and charge (positive ΔSoC values) cases. In all diagrams in Figure 5.25, the DVA curve of the appropriate cell is plotted. At low currents, a correlation is observable between the peaks in ΔSoC and those in the DVA. This is not the case at higher c-rates.

Simultaneously, the changes in the OCV slope depend on the c-rate of its measurement. Numerous studies have analysed the current distribution—and therefore also the SoC distribution—within battery cells [114–122, 124–130, 147–156, 185, 186, 190]. Forouzan et al. and Lin et al. showed that current increases lead to increasing current inhomogeneity, and therefore to SoC inhomogeneity [153, 154]. In OCV measurements, this leads to some type of filtering of the OCV. The graphite steps are less steep with the results of a reduced peak in the DVA curve (compare Figure 3.14).
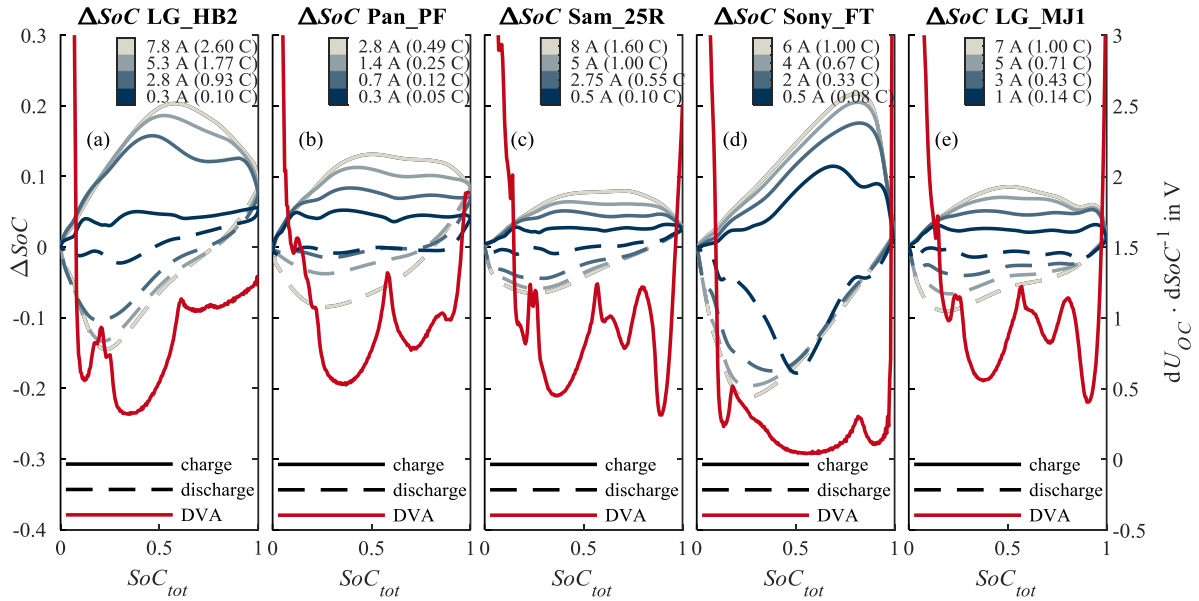
Figure 5.25: *SoC difference between a warm cell at 25 and a cold cell at 10 °C under CCCV charge and discharge ($\Delta SoC = SoC_{25\,°C} - SoC_{10\,°C}$). In the charge phase, the SoC differences are positive. The DVA curves of the cells, averaged between charge and discharge OCV curves, indicate a correlation with the ΔSoC results at low c-rates.*

To determine the current's influence on the OCV, Figure 5.26 examines literature-based data of LFP | graphite cells. Furthermore, it deals with the anode $U_{OC,neg}$ and cathode $U_{OC,pos}$ open-circuit potentials depending on the stoichiometry of the negative x and positive electrode y. The data come from Li et al. [217], Guo et al. [218], and Rumpf et al. [144], and the calculations follow equations (5.18) and (5.19):

$$U_{OC,neg}(x) = 0.6379 + 0.5416 \cdot e^{(-305.5309 \cdot x)}$$
$$+ 0.044 \cdot \tanh\left(-\frac{x - 0.1958}{-0.1088}\right)$$
$$- 0.1978 \cdot \tanh\left(\frac{x - 1.0571}{0.0854}\right) \tag{5.18}$$
$$- 0.6875 \cdot \tanh\left(\frac{x + 0.0117}{0.0529}\right)$$
$$- 0.0175 \cdot \tanh\left(\frac{x - 0.5692}{0.0875}\right)$$

$$U_{OC,pos}(y) = 3.4323$$
$$- 0.8428 \cdot e^{(-80.2493 \cdot (1-y)^{1.3198})} \tag{5.19}$$

$$-3.2474{\cdot}10^{-6}{\cdot}\mathrm{e}^{(20.2645{\cdot}(1-y)^{3.8003})}$$
$$+3.2482{\cdot}10^{-6}{\cdot}\mathrm{e}^{(20.2646{\cdot}(1-y)^{3.7995})}$$

Diagram (a) in Figure 5.26 shows the deviation with respect to the SoC of the cathode's and anode's open-circuit potential over the SoC. The cathode's potential increases, and therefore the DVA curve is positive and the anode decreases, which means that the DVA curve is negative. The two curves show that the LFP cathode is linear and flat in a wide range of SoC. Nonlinearities of the OCV come from the stage transitions of the graphite anode [226, 227].

To explain the effects on the current distribution of these stages, diagram (b) shows an idealised stage transition with a height of U_{step}. Again, an example is chosen of charging two cells connected in parallel with unequal temperatures. The blue marker ① is at the SoC and OCV of the colder cell 1 after a certain charge time. Due to the temperature difference—and therefore impedance difference—between the cells, the warmer cell 2 marked with a red ① is already charged more and its SoC is higher. Because the slope of the OCV is flat in this area, there is hardly any OCV difference and the SoC difference is broad. For the next step in time, diagram (b) considers two cases: low and high charge currents.

The cell voltage is the sum of the OCV and overvoltage U_{OV}, which is illustrated in the EEC of Figure 5.26. At low currents, the overvoltage is small because it depends directly on the current i, as shown in the equation in Figure 5.26 on the right side. In this case, cell 2 moves from the red mark ① to ② and its OCV rises moderately. Furthermore, cell 1 moves from blue ① to ②. Hence, the overvoltage decreases, and with that so does the current of cell 2, because the terminal voltages of the cells must be similar. With this shift in current, the SoC difference between the two cells decreases. The warmer cell seems to "wait" for the colder one.
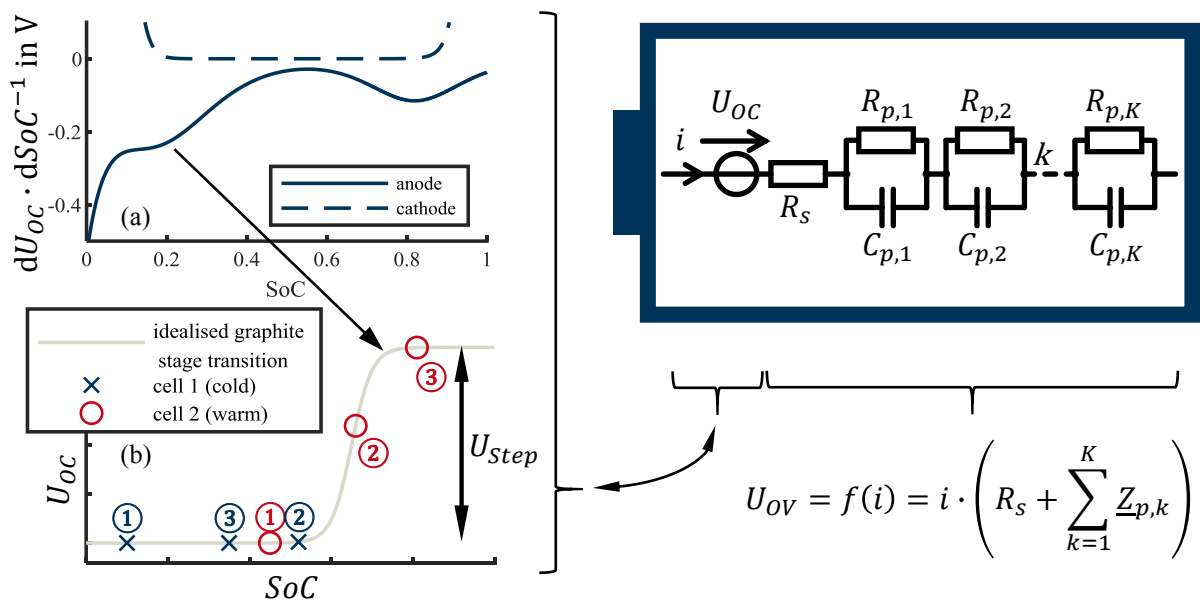
Figure 5.26: *Influence of low and high current on current distribution in parallel-connected cells in nonlinear parts of the OCV*

In the second case, a current i charges the cells, which generates an overvoltage U_{OV} that is much larger than U_{step}. In this scenario, cell 1 moves from blue ① to ③ and cell 2 moves from red ① to ③. Cell 2 can overcome the graphite stage transition and reaches a flat area of the OCV. Moreover, the SoC difference between the cells increases further but slower. This effect was found by Hust [155] and confirmed in the present work. It also provides an explanation for a change in voltage relaxation in the SoC of a graphite stage. At this SoC, less SoC relaxation occurs compared with other SoCs. This makes clear the strong influence on current distribution at low c-rates and less influence on high c-rates.

In addition, this effect is likely to occur within battery cells along the electrodes. Inhomogeneous SoC distributions in the cells have been shown by several studies [114–122, 124–130, 147–156, 185, 186, 190].

The slope of the OCV characteristic curve of LFP cells is flat between 10 and 95 % SoC compared with other cathode materials such as NMC or NCA; see Table 3.3 and Figure 3.12. This is important in matters of current distribution between parallel-connected battery cells. At a flat OCV, a certain voltage difference represents a higher SoC difference than in the case of a steep OCV characteristic.

5.5 Summary of the influencing factors

Chapter 5 analysed the interrelationships of the drivers of asymmetric current distribution in parallel-connected lithium-ion battery cells. System technology such as junctions and wiring were not the focus of this work, but preliminary studies by Rumpf et al. [20] resulted in the influence of the connection impedance that cannot be neglected. Its impact grows at low cell impedance and high connection impedance.

The present study examined the effects of an electrochemical cell, which was modelled with an OCV and series connection of a variable number of RC elements. The cells' impedance $\underline{Z}$ played a major role and its value depended on temperature, SoH, SoC, and parameter variations from the production process. Furthermore, the influence was time-dependent because the RC elements consist of certain time constants.

To compare these effects, values were chosen regarding a worst-case scenario in technical applications. Specifically, temperature differences up to 15 °C were assumed. A thermal simulation of a battery module with 420 cells showed a temperature difference between the hottest and coldest cell. The SoH influence on the impedance lay at ≤ 60 %, as shown by Ecker et al. [102]. SoC-dependent parameters were measured in five different cells every 5 % of the SoC. In the simulation of current distribution, the results of three different options of averaging were compared. These were averaged values over the total SoC, averaged values of the utilised SoC, and not averaged parameters. The paper of Rumpf et al. [20] provided the basis for the parameter variation. From those variation results, $\pm 2 \cdot \sigma$ was derived. In terms of dynamic load, pulse and sine half-wave loads with lengths of 1 ms to 1000 s provided the electrical

excitation. EEC simulations allowed certain influencing factors to be cut off. Table 5.5 compares the influencing factors that impact the impedance of cells—temperature and ageing are clearly important influences.

Measurements made clear that the temperature dependence of a cell's impedance differs strongly for various cell types. With this, the influence of the temperature on current distribution also differs. In terms of ageing, the way that cells age in parallel connection is still under discussion. Therefore, it is unclear how far the impedance and capacity differences in parallel connections can go. SoC dependence only occurs at low SoCs where the gradient of the impedance is highly relevant, and the parameter variations of new cells are either quite small or the effect only appears at high time constants.

Table 5.5:   *Comparison and weighting of influencing factors that impact the impedance of cells*

	Maximum parameter variation	Annotation	Rating
$\underline{Z}(\sigma)$	$\leq 12\ \%$ at R_{WB}	Calculated using data from [20]	12 % only at high time constants, and much lower at the R_S
$\underline{Z}(SoH_Z)$	$\leq 2\ \frac{\%}{\Delta SoH_{Ah}\ \%}$	Impedance growth of 40 % at a capacity decrease of 20 % [102]	A ΔSoH_{Ah} of 5 to 10 % in a battery pack is realistic [112]. This means 10 to 20 % of $\Delta\underline{Z}$.
$\underline{Z}(SoC)$	$\leq 8\ \frac{\%}{\Delta SoC\ \%}$	Compare Figure 5.8 from 10 to 5 % of SoC at 10°C	Relevant only at low SoCs where the gradient of $\underline{Z}$ is high.
$\underline{Z}(T)$	$\leq 4.3\ \frac{\%}{\mathrm{K}}$	Compare Table 5.3 LG_HB2 cell	Highly relevant because double-digit temperature differences in a battery pack are possible.

In sum, the most critical results of these analyses are listed as follows:

+ Parameter variations in new cells were only relevant at millihertz frequencies.
+ Impedance differences caused by ageing led to asymmetric current distribution.
+ SoC-dependent parameters influenced the current distribution in the range of minutes.
+ SoC-dependent parameters were most crucial at very low SoCs because the gradients of the SoC-dependent impedance there were higher than in the middle area of the SoC.
+ The temperature dependence of impedance differed strongly. The normalised resistance variation ε_T referring to temperature increases varied from 1.5 to 4.3 %/K between the used cell types.
+ The influence of temperature on current distribution was most significant in all cells compared with other factors.
+ The long-term influence increased in all types of impedance influence in flat OCV curves, such as that of an LFP | graphite cell.
+ A low dynamic load had a larger influence on current distribution than did a higher dynamic load.

Figure 5.27 compares the voltage influence of hysteresis and entropy with the overvoltage. Diagram (a) shows the OCVs of an LG_HB2 and a Sony_FT cell as solid lines. Furthermore, the charge voltage curves at 1 C and at cell temperatures of 10 and 25 °C are plotted in dashed lines. Immediately next to the OCV, the maximum and minimum hysteresis lines are plotted in dotted-chain lines and entropy +7.5 | −7.5 °C in dotted lines.
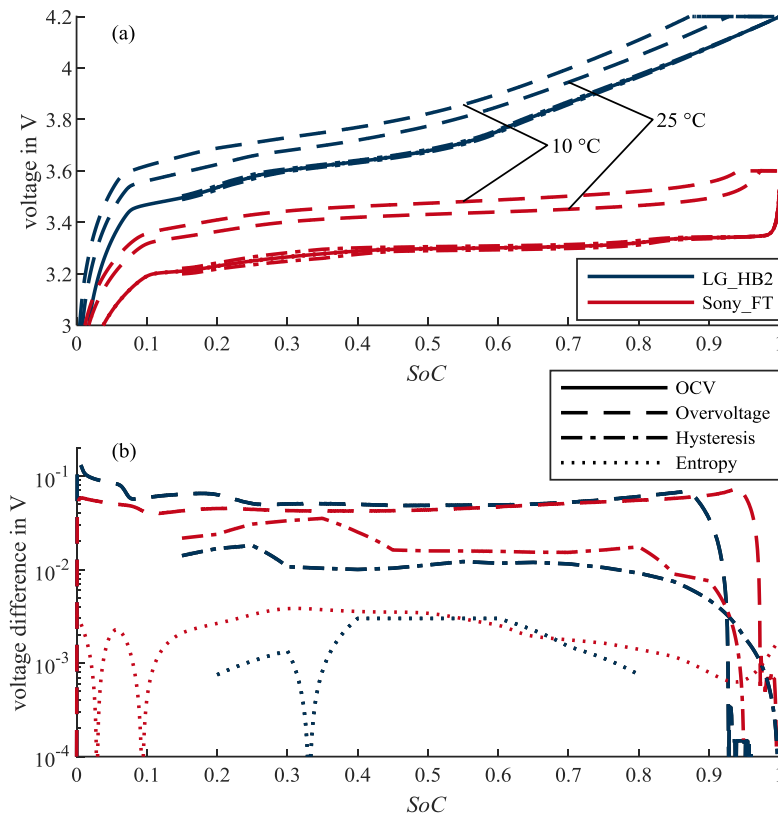
Figure 5.27:   *Diagram (a): OCV and charge voltage at 10 °C | 25 °C at 1 C, maximum | minimum hysteresis voltage and OCV plus entropy of +7.5 | -7.5 °C. Diagram (b): absolute difference between charge voltages at 10 and 25 °C, maximum and minimum hysteresis and entropy of 15 °C on a logarithmic scale. The data come from LG_HB2 and Sony_FT cells.*

These lines can hardly be separated from the OCV. Therefore, diagram (b) shows the absolute difference between the two charging, two hysteresis, and two entropic voltage lines. Plotting them on a logarithmic scale is necessary, otherwise entropy would just be a horizontal line at the bottom of the diagram. Diagram (b) makes it clear that in the case of current flow, the effect of overvoltage is dominant compared with those of hysteresis and entropy. Nevertheless, Figure 5.16 and Figure 5.19 show SoC differences caused by hysteresis up to 8 % and those caused by entropy up to 5.5 %. Therefore, these effects cannot be neglected. Hysteresis and entropy are active without current flow and can lead to significant SoC differences.

A crucial difference is that overvoltage does only appear in current flow. Hysteresis and entropy also have an effect in the nonoperating state. Figure 5.16 and Figure 5.19 illustrate long-lasting relaxation processes caused by hysteresis and entropy, respectively, which last as significant SoC differences that come to change starting positions for the next charge or discharge phase.

In an ideal case, differences in cell capacities lead to asymmetric current distributions in the ratio of capacity asymmetry [25]. In real-world batteries, other effects overlie this. Capacity differences caused by parameter variations have effects smaller than the impedance-based effects of SoH, SoC, temperature-dependent impedance, and impedance parameter variations. Furthermore, the cell dimensioning in terms of HP or HE design of battery cells influences the inclination on asymmetric current distribution. HP cells are more likely to be influenced by the effect of capacity difference, whereas HE cells are more likely to be influenced by impedance differences.

To analyse all of the aforementioned effects, it was necessary to use a linearised OCV curve. The nonlinearity of the OCV leads to a significant impact in the current distribution. Figure 5.23 shows that the change of the slope of OCV in particular affects the asymmetric current distribution by creating a variable OCV step using a hyperbolic tangent function. The OCV curves used in this work were averaged voltage curves from CC charge and discharge measurements. DVA analysis showed that the slope and change of the slope depend on the height of the CC current. The peaks in the DVA characteristic grow with decreasing current. This study supposed that the current distribution within batteries' electrodes leads to this effect. Together with the knowledge of the influence of the OCV slope on current distribution, the measuring current of the OCV can be said to directly influence the simulation result of asymmetric current distribution.

The simulation using the OCV measured with the lowest current did not generate the most realistic results. This became clear when the measured current distribution was examined at various CCCV currents, as shown in Figure 5.24. The EEC model did not reproduce any current dependency. Therefore, the simulation results at different currents led to similar normalised current distributions, which did not correspond to the measurements. This represents a disadvantage for this type of simulation.

In addition, the dependency of current distribution on the current proved an effect found by Hust [155]; that is, a high current leads to a high overvoltage. When the SoC of one cell in parallel-connected cells reaches a nonlinear area of the OCV—for instance, a graphite stage—this step will be overcome because of a high overvoltage. At a lower current, the cell cannot overcome the step and must "wait" for the other cell(s) in the parallel connection. This effect is explained in Figure 5.26.

In Figure 5.1, numerous back-couplings of temperature and current are illustrated. Because of the freedom of simulation, these effects were neglected at the best possible rate in the present study. For future studies, it would be interesting to analyse these back-couplings step by step.

6 Harmful impacts and countermeasures

With knowledge of the interrelationships that influence the asymmetric current distribution, this study identified harmful states and assessed countermeasures.

6.1 Identification of critical operations with a real-world procedure

A critical operation can be a safety issue or damage the battery over a long period in terms of ageing. Ruiz et al. distinguished between mechanical, electrical, environmental, and chemical safety concerns. [27]

External effects such as an external short circuit are not a specific effect. Overcharge and over-discharge can theoretically occur in parallel connections. Because of a parallel connection, the voltages of parallel strings are similar. The string voltage consists of an OCV, the overvoltage at the internal impedance, and the voltage drop at the junctions. An asymmetric current distribution, as well as impedance differences, can lead to differences in OCVs, and therefore in SoCs. However, if the battery management system (BMS) works well, the voltage limits of the cell will not be exceeded. In all the measurements described in Section 4.1, no negative cell current appeared in CV phases with a positive total current, and no positive cell current appeared in the CV phases with a negative total current.

Electrical internal short circuits can be caused by plating and dendrite growth. Because plating is a major ageing factor, this will be analysed together with other ageing phenomena. This is the same for self-heating through asymmetric current. Other environmental influences are not within the scope of this work.

In terms of ageing, the influencing states are time, SoC, temperature, charge throughput, current, and stoichiometric shifts; see Figure 2.6 in Subsection 0. Therefore, the following analyses calculate the situation at maximum cell current, maximum SoC difference, power dissipation, and charge throughput. Furthermore, special relevant settings such as a change in the current direction, lithium plating, dendrite growth, and the influence of nonlinear OCVs at different c-rates are analysed.

The following analyses use the measurement results of a 2p connection of cells described in Section 4.1. One cell is at 10 and the other is at 25 °C. This represents a worst-case scenario, for example, within a home storage system in a cellar with one side next to the house's heating system. The temperature difference leads to an impedance difference, as was explained in Subsection 5.1.4. Figure 4.4 on page 61 shows the load profile procedure in the form of the SoC variation of single cells and the system.

The cycle shown in Figure 4.4 in Section 4.1 for two Sony_FT cells starts with synchronising the cells' SoCs at 0 and 100 % of SoC, respectively, with a CV phase. The load profile consists of five phases. It represents the charging, standby, and utilisation of a storage system. With that, all typical operational states of a battery can be analysed. The five cell types from Table 3.3 are used in these measurements. Furthermore, the synchronised SoC (0 or 100 %), target SoC, current direction (charge or discharge) of the starting cycling, and current height are varied. The target SoC is the system's SoC, which is reached after the CC phase. Figure 6.1 exhibits exemplary results for the measurements of the Sony_FT cell synchronised at 100 % of the SoC with target SoCs from 10 to 90 % in 10 % increments. Some measurements do not include a cycling phase, which is the case when the voltage limits are hurt when cycling. The total procedure is illustrated and described in Figure 4.4 in Section 4.1.
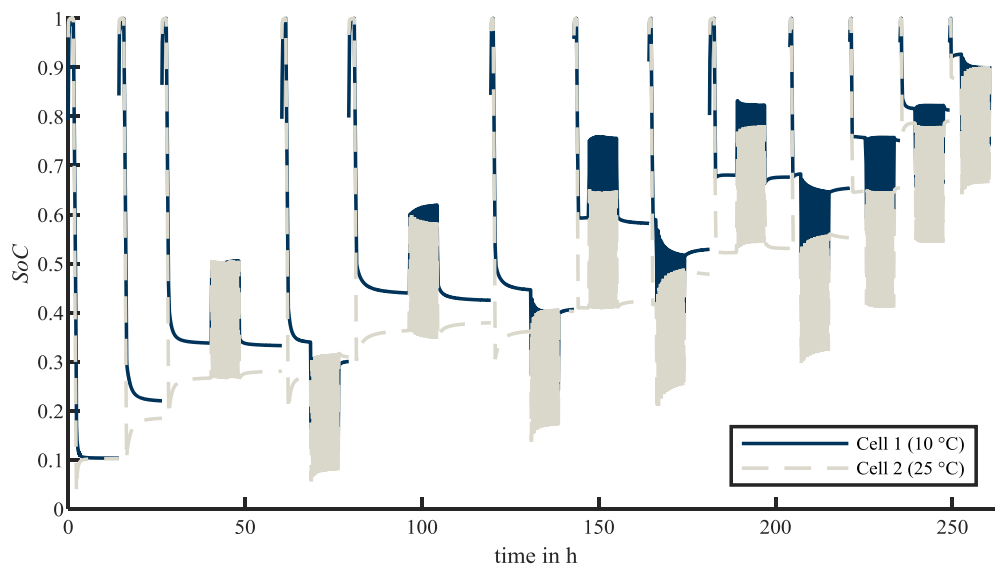
Figure 6.1:   Exemplary results of two Sony_FT cells at 10 and 25 °C. The data consist of 13 separately measured parts, which are set behind each other in this diagram.

6.1.1   Maximum cell current

Current load has the most versatile effects on degradation mechanisms [26]. It influences SEI growth, SEI decomposition, graphite exfoliation, structural disordering, loss of electrical contact, and electrode particle cracking [26]. Other authors have explained the effect of charge current on lithium plating [96–100]. The test procedure in Figure 4.4 in Section 4.1 analysed the different phases of a lithium battery's usage. It consists of charge and discharge current in CV and CC characteristics. Furthermore, relaxation phases, as well as cycling, are included. Figure 6.2 illustrates an exemplary current distribution result of these measurements on a Sam_25R cell. Diagram (a) includes the total time, and diagrams (b) and (c) detail the CC discharge and first part of the cycling phase, respectively. Two similar cells were connected in parallel; one was kept at 10 and the other at 25 °C. The test setup described in Section 4.1 measures the cell currents.
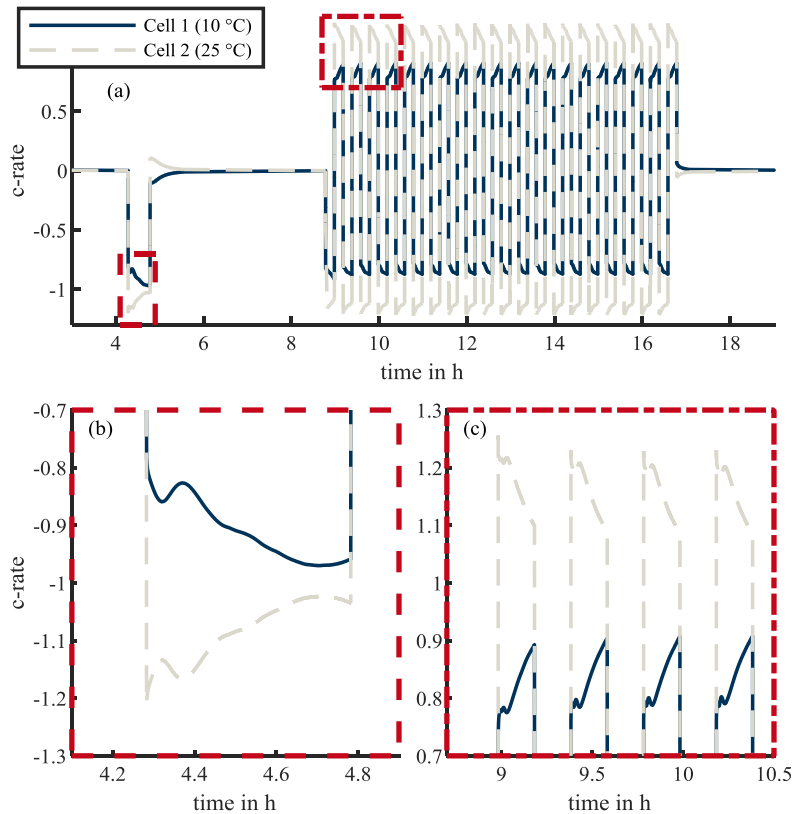
Figure 6.2: *The c-rates of a cold and warm Sam_25R cell connected in parallel. Diagram (a) shows the whole procedure consisting of a CV (before the CC pulse), CC, relaxation 1, cycling, and relaxation 2 phases; (b) and (c) detail the current distribution in CC and the first part of the cycling phase (compare Figure 4.4).*

A CV phase synchronised the cells' SoCs at 100 % until approximately 4.3 h. Afterwards, a CC discharge pulse discharged the combination of cells until a target SoC of 50 %. During a relaxation phase, the existing SoC difference between the cells was equalised except for the justified differences caused by hysteresis and entropy (compare Subsections 3.3.4 and 3.3.5). In the cycling phase, the cells were charged and discharged 20 times with a cycle depth of 20 % per cycle followed by a second relaxation phase. The CC, as well as the cycling phase, used a c-rate of ± 1 C.

With the knowledge from Chapter 5, the current distribution in Figure 6.2 (b) is large at the beginning of CC discharging because of the impedance difference of the cells with different temperatures. The current difference became smaller because it led to a difference in SoC, which offsets the asymmetric current distribution. Nonlinearities of the OCV and SoC dependent impedance parameters disrupted an exponential convergence of the cell currents. In the cycling phase in diagram (c), similar phenomena come to pass.

The most asymmetric current distribution occurred at the beginning of a current pulse. That was the case in the CC and cycling phases. Diagram (c) exhibits the highest current of the

warm cell at approximately 9 h. At this time the current changed from −1 to +1 C. In further cycles, the peak at this change in current direction was lower.

The subsequent analysis focused on the influence of the target SoC at the end of the CC phase, the synchronisation SoC of 0 %, and the cell chemistry. Figure 6.3 analyses all of these instances. It shows the maximum absolute c-rate in the CC and cycling phases. Four vertical lines divide the x-axis from the start to end of the CC phases and from the start to end of the cycling phase. The area between the start and end is relative to the length of the respective phase. In diagrams (a) and (b), the synchronisation of the cells occurs at 0 % of SoC. Afterwards, the parallel connection was charged until the target SoCs of 10, 30, 50, 70, or 90 %. In diagrams (c) and (d), the synchronisation occurs at 100 % of the SoC followed by a CC discharge until the target SoCs. Figure 6.3 separates the current maxima of the cold and warm cells of the parallel connection. The left-hand diagrams (a) and (c) show the maxima of the cold cell and the right-hand diagrams (b) and (d) refer to the warm cell. The shape of the marker differentiates between the target SoCs and the colour codes represent the cell types.
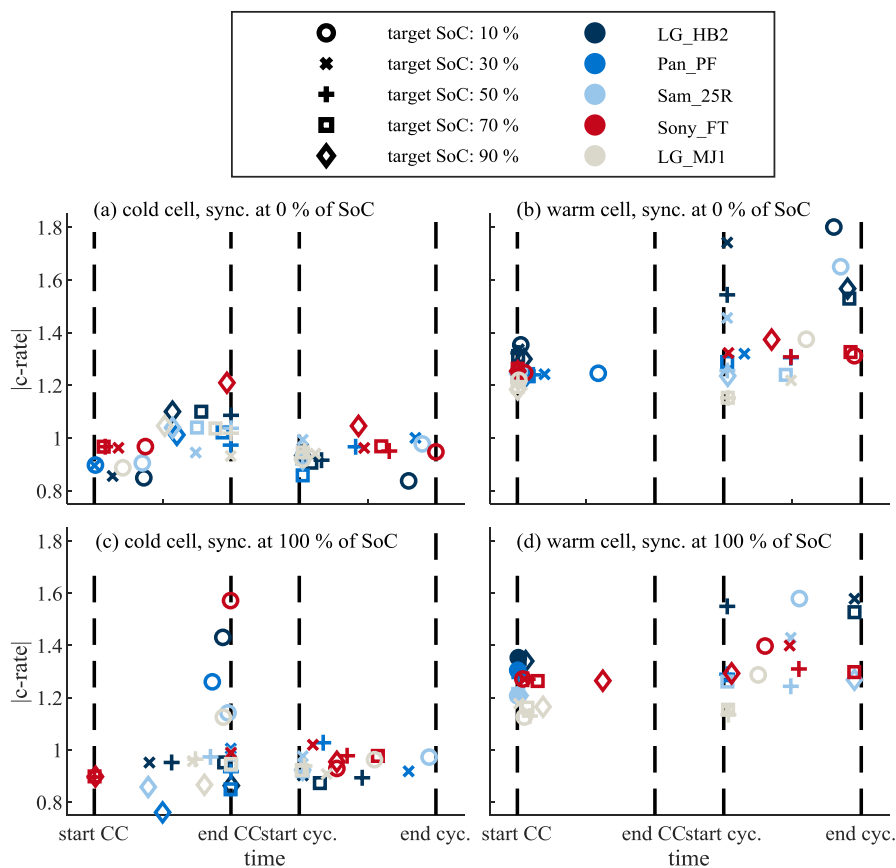
Figure 6.3: *Maximum absolute c-rate during the CC and cycling phases. In (a) and (c) the maximum absolute c-rate of the cold cell is shown. Diagram (b) and (d) refer to the maximum absolute c-rate of the warm cell. The results of the diagram (a) and (b) are synchronised at 0 %, whereas those of (c) and (d) are synchronised at 100 % of the SoC.*

During the CC phase, the cold cell exhibited the highest values at the end of the phase, as shown in diagrams (a) and (c). This agrees with the single measurement of Figure 6.2 diagram (b). Especially in the charging case, Figure 6.3 diagram (a) indicates the highest peaks for all measurements until a target SoC of 50 %, except for the Sony_FT measurement, at the end of the CC phase. At other target SoCs where the OCVs have nonlinear areas, the maxima appear at the beginning or in the middle of the CC phase.

In diagram (a), only the Sony_FT cells show a maximum c-rate of the cold cell larger than 1.1 C in the CC or cycling phase. The maximum of the Sony_FT cell is 1.21 C at a CC charge from 0 to 90 % SoC. Overall, the short-term current overload in the diagram (a) is low compared with the other cases.

Furthermore, diagram (c) shows c-rate maxima of the cold cell after 100 % synchronisation SoC. In the CC phase, it is conspicuous that for all measurements that are discharged from 100 to 10 % of SoC, the maxima of the cold cell take over the larger part of the current at the end of the CC phase. The red "o" marker in diagram (c) represents the highest current of the cold cells. It is at the end of a CC discharge phase from 100 to 10 % of SoC of two Sony_FT cells. In diagram (a), the highest current also appears after a long CC phase of a Sony_FT cell, in this case from 0 to 90 % of SoC. Other cell types also show this behaviour, but it is not that pronounced. The maximum in diagram (c) exclusive of the target SoC of 10 % is a c-rate of 1.05 C.

Diagrams (b) and (d) refer to the warm cell at 25 °C. As expected, the current maxima are higher than those of the cold cell. In the CC phase, almost all maxima appear at the beginning of the phase. Only at small DoDs (0 to 10 % in the diagram (b) or 100 to 90 % in the diagram (d)) is the maximum reached in the middle of the phase using the Pan_PF and Sony_FT cells, respectively. It is also remarkable that the order of the cells and their maxima in the CC phase correlate with the impedance dependence of the impedances shown in Table 5.3. The LG_MJ1 cell has the smallest and the LG_HB2 cell has the highest maximum c-rates and temperature dependence of the impedance.

During the cycling phase of the warm cell in diagrams (b) and (d), the maxima often appear at the beginning or end of the phase. However, this trend is not distinct. There are several exceptions where the maximum appears in the middle of the phase. It was assumed that the change of hysteresis leads to a growing or shrinking current difference during cycling.

Furthermore, the cycling at 10 or 90 % of SoC was not possible in some cases without passing over the end-of-charge or end-of-discharge voltage, respectively. In these cases, no data are available in Figure 6.3. Almost all cells with data of a target SoC of 10 % show the highest c-rates in diagrams (b) and (d) during the cycling phase. Only the Sony_FT cell in the diagram (b) is an exception. The explanation lays again in the strong nonlinearity of all OCVs at this SoC, which leads to a strong asymmetric current distribution. The LG_HB2 cell exhibits a c-rate up to 1.8 C, which means the warm cell takes 90 % of the total current at this time. Furthermore, during cycling, the highest values appear in the LG_HB2 cell, which has the strong-

est temperature dependence of the impedance. The cycling generates more asymmetric current peaks than the pure charge or discharge, which could be caused by the immediate change of the current direction from −1 C to 1 C and back.

The measured current peaks do not last longer than some minutes, sometimes less. These short overcurrents have rarely been analysed in the literature, nor have the effects of pauses during ageing. These are two crucial topics for further research in combination with current distribution.

6.1.2   SoC spread

Simulative analyses, as well as the CCCV measurements in Chapter 5, revealed double-digit percentages of SoC differences in parallel connections caused by the drivers of asymmetric current distribution. The 2p measurements based on real-world usage of batteries (load profile of Figure 4.4) confirmed these results. To compare the SoC spread, Figure 6.4 plots the SoC difference over the SoC of the 2p system. As a flat OCV curve compounds the spread, the figure shows data of the Sony_FT LFP cell.

Diagram (a) compares the cycling in positive and negative directions. The two measurements in the graph start at $SoC = 1$. During the CC discharge phase, the system's SoC drops to 0.38. The SoC difference at the end of the CC phase deviates because of the variation between the measurements. In the following relaxation phase, the system's SoC remains constant and an equalisation current between the cells reduces the SoC difference in both cases from approximately 20 to 8 %. At this point, the hysteresis influence sets an SoC difference that cannot be equivalised as described in Section 5.2. The relaxation phase takes 4 h, and during this time, the cell current of the warm cell drops from 0.28 A to less than 1 mA.

Figure 6.5 shows the SoCs of the two cells of this measurement over time. The synchronisation of the cells takes place in the fully charged state and after that, a discharge phase until the target SoC of 40 % follows in the two measurements of the figure. It becomes clear that the SoC difference before cycling is almost similar, with 7.7 % at the first measurement and 8.5 % at the second measurement before cycling. After cycling, it differs by approximately 5 %. With the knowledge of hysteresis, it seems likely that ending the cycling process form another direction leads to other equilibrium voltages. In case of cycling in a positive direction, there is a discharge of 20 % of SoC at the end, whereas in case of cycling in a negative direction, the cycling ends with a charge phase of 20 %. A simulation of the hysteresis using the Preisach model confirmed this theory. On the right axis is the voltage difference caused by hysteresis $\Delta U_{hysteresis}$ calculated with the Preisach model:

$$\Delta U_{hysteresis} = U_{hysteresis,cell\ 1} - U_{hysteresis,cell\ 2} \tag{6.1}$$

Negative ΔU_{Hyst} values at the end of the relaxation processes at 96, 119, and 131 h show invariable SoC differences. At the end of relaxation after the second cycling at 143 h, $\Delta U_{hysteresis}$ is near 0 V. This results in no SoC difference at the end of the relaxation process, which explains the unequal SoC spread at the end of the two measurements.
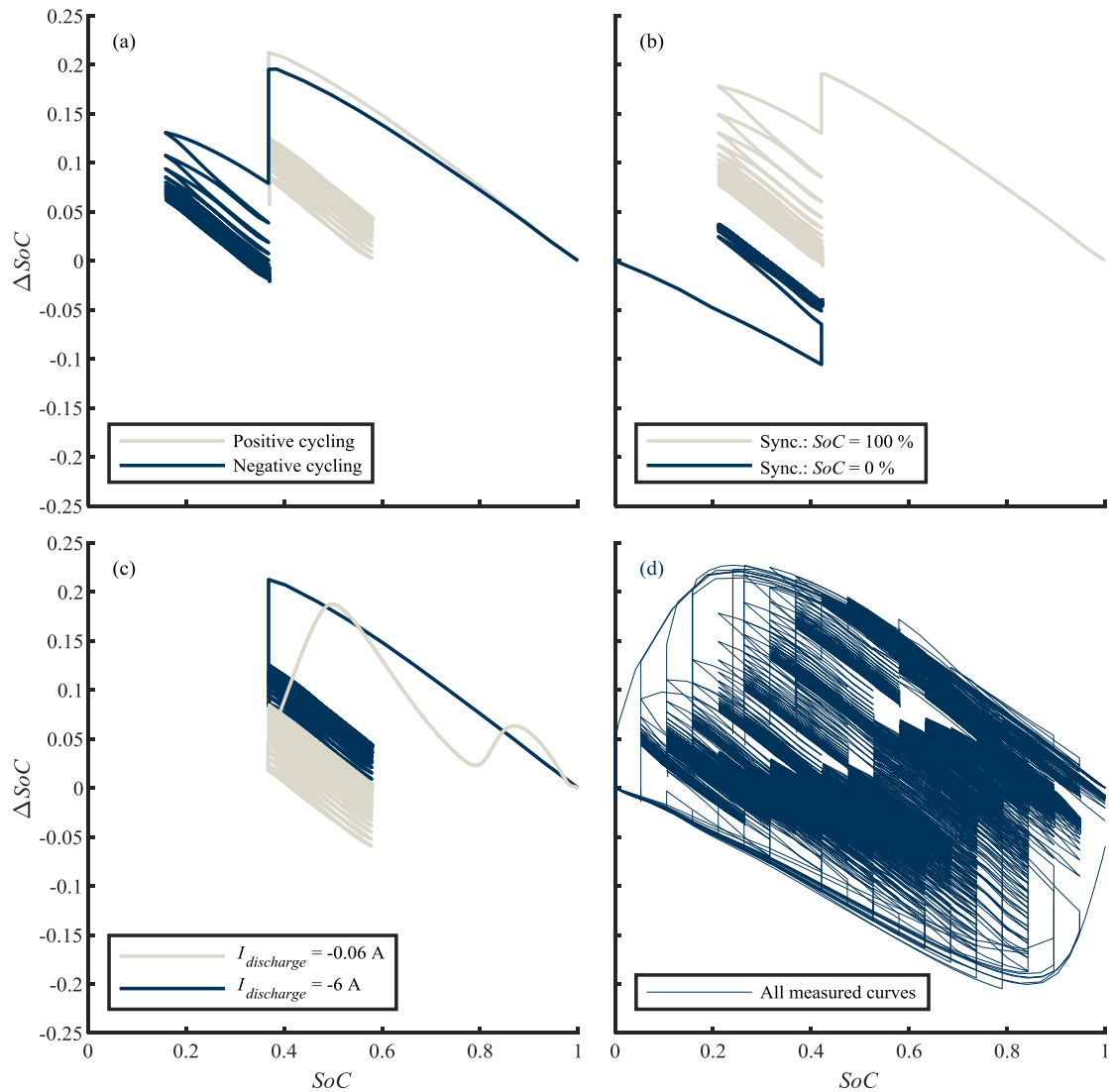
Figure 6.4: *SoC spread of Sony_FT cells in a 2p connection. Diagram (a) shows the effect of different cycling direction; diagram (b) shows the effect of different synchronisation and therefore starting points; diagram (c) shows the effect of different currents in the CC phase; and diagram (d) shows all measurements.*

Diagram (b) in Figure 6.4 analyses two measurements that have the same target SoC of 42 % but are synchronised with different SoCs: 0 and 100 %. Charging from 0 to 42 % of the SoC creates a negative SoC difference, whereas discharging from 100 to 42 % creates a positive SoC difference. Both measurements relax towards $\Delta SoC = 0$ during the first relaxation phase. At the end of the second relaxation phase, the SoC difference is reduced further. This is because the direction of the last charging process is in the opposite direction to the measurement synchronised at 100 % of SoC. The existing SoC spread at the end of the measurements is presumably the result of the long-time hysteresis history from the CC phase, but this is not fully certified.

In Figure 6.4 diagram (c), the synchronisation point, target SoC, and cycling direction are similar. The two measurements differ in the c-rate of the discharge current in the CC phase. Figure

6.6 shows the cell SoCs of measurements at a low current between 0 and 68 h and the cell SoCs of measurements at a high current from 68 to 92 h. The diagram only indicates the cells' SoCs. From 1 to 31 h, a low c-rate and from 69 to 70 h a high c-rate discharge the cells to the target SoC of 40 %. The influence of the c-rate on the CC current is also analysed in Figure 5.25 in Subsection 5.4.2. In most cases, a higher c-rate leads to a larger SoC difference. Furthermore, the SoC difference is influenced by the nonlinearity of the OCV at low c-rates. This influence also becomes clear in Figure 6.4 and in the cells' SoCs in the discharge phase at low c-rates from 1 to 31 h in Figure 6.6.
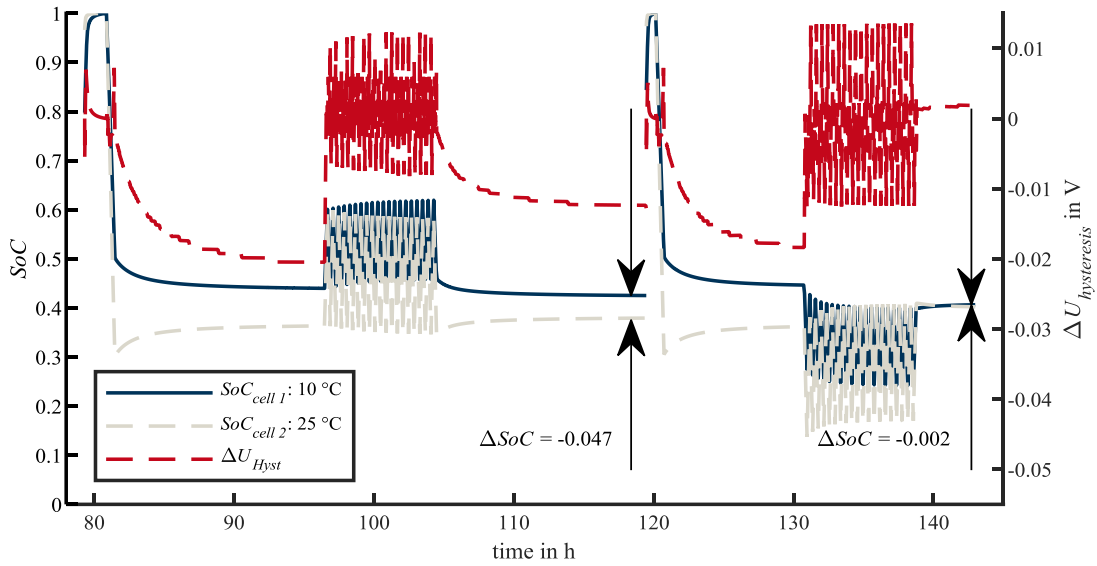
Figure 6.5: *Cell SoCs of a warm and a cold Sony_FT cell in 2p connection over time. Positive or negative cycling influences the SoC difference after the second relaxation phase due to coming from a different direction at the end of cycling.*
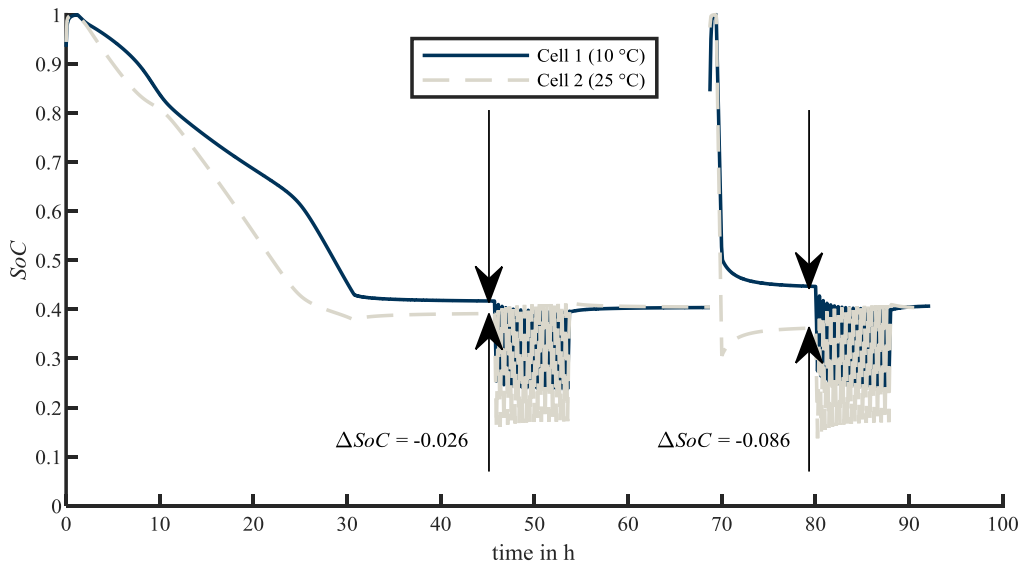
Figure 6.6: *Cell SoCs of a warm and a cold Sony_FT cell in a 2p connection over time. The c-rate of the CC phase influences the SoC difference after the first relaxation phase.*

The CC phase of the two measurements ends at different ΔSoC. In the case of a low c-rate, there are low overvoltages that lead to low equalisation currents between the cells. Therefore, the hysteresis value stays constant. At a high c-rate, the equalisation current leads to hysteresis differences and the ΔSoC remains at a higher level. After the cycling at ± 1 C in both measurements, no difference in ΔSoC remains.

Diagram (d) in Figure 6.4 illustrates all measurements of this type in one plot. Detailed analyses are not possible here. Nevertheless, in all measurements that were synchronised at 100 % of the SoC, the SoC difference grew while the CC discharged until approximately 23 % of the total SoC. At this point, the warm cell reached 12 % of the SoC, whereas the OCV of LFP cells dropped at further discharge. In measurements that were synchronised at 0 % of the SoC, the OCV of the warm cell rises strongly at high SoCs. From that point, the SoC difference decreases. The absolute SoC difference grew until the warm cell reached the SoC where the slope of the OCV strongly grew. This is the case at approximately 84 % of the total SoC. After these maxima, the total ΔSoC decreased at further charge and discharge.

Because of its steep SoC, the ΔSoC at NMC and NCA cells at the end of the CC phase were lower than those of LFP cells. Figure 6.7 presents the SoC spreads of Sony_FT cells in the diagram (a) and Sam_25R cells in diagram (b). ΔSoC values at the end of the CC phase that are larger than zero were synchronised at 100 % of the SoC and had a CC discharge phase. Negative ΔSoC values indicated measurements where the synchronisation took place at 0 % of the SoC. Those measurements have a CC charge phase. In the figure, it also becomes clear that hysteresis is far more crucial in flat OCVs. When the relaxation phase before cycling begins, the SoC difference vanishes almost completely in the Sam_25R cells. This is not the case in the Sony_FT cells. ΔSoC of up to 20 % were possible in total SoCs of 45 to 60 % where the OCV had its lowest slope (compare Figure 3.12 on page 45). The cycling phase generally reduced the SoC difference. Furthermore, most of the measurements exhibited a lower ΔSoC after cycling than they did before.

In this case, the SoC difference of Sam_25R cells was clearly lower and did not exceed 10 %. Moreover, the three other cells LG_HB2, Pan_PF, and LG_MJ1 did not exhibit an SoC spread as the LFP cells did. Therefore, these cells are not the focus of this chapter.

In terms of ageing, short-time SoC differences in NMC and NCA cells are not supposed to have relevant effects; however, this can differ in LFP cells. Keil et al. demonstrated an SoC dependence of calendric ageing [93]. Using Keil's results, a simple estimation of inhomogeneous ageing is possible. In a worst-case scenario, a 2p connection of LFP cells discharges to 74 % of SoC, such as the experiment in the present work, and is stored for a period of 9 months at 40 °C. In this scenario, Figure 6.7 shows an ΔSoC after the first relaxation phase, and therefore before cycling of 7 %. This means that one cell is at 70.5 and the other is at 77.5 %. Keil's results indicated that this would lead to a capacity decrease of 8 % and 9.5 %, respectively. One cell degrades 19 % faster than the other in this scenario. With the knowledge that the SoC difference becomes larger with a higher c-rate, this could also become worse.
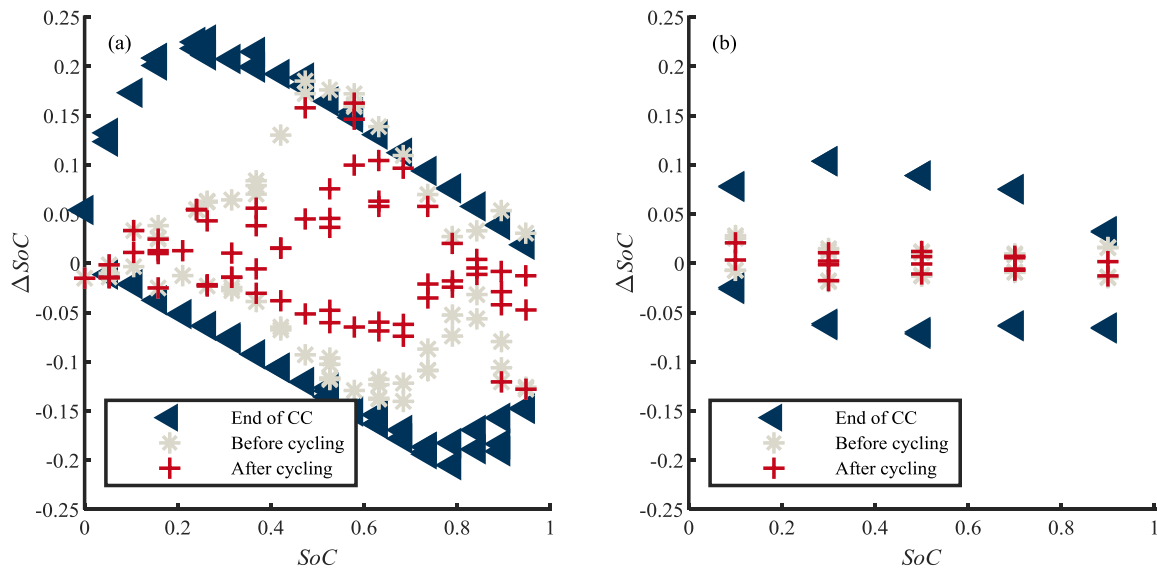
Figure 6.7: *SoC differences of 2p cells (10 °C and 25 °C) at the end of the CC phase, before and after cycling of Sony_FT cells in the diagram (a) and Sam_25R cells in diagram (b).*

6.1.3 Charge throughput

Charge throughput is a major ageing factor. In some degradation simulations, the cycle depth relativises this ageing parameter. This means that a low cycle depth causes less degradation [228, 229].

Figure 6.8 analyses the charge throughput distribution in the 2p connection with a temperature difference of 15 °C. The graphs in the two left-side diagrams show measurements where the cells were synchronised in a totally discharged state and then charged to 50 % of the SoC. Diagram (a) shows the results $|Q|$ of the cold cell in the CC, relaxation 1, cycling, and relaxation 2 phases on a logarithmic scale. This makes it clear that the charge throughput of the equivalation current during the relaxation phases is not crucial for the total values. The fact that the equalisation charge is lowest in the Sony_FT cells fits the observation that SoC differences are only partially equalised because of flat OCV characteristics and hysteresis.

Diagram (b) normalises the charge throughput of the cold cell $|Q|$ with the total charge of the certain phase $|Q_{phase,tot}|$. Bars of the values in the relaxation phases are not reasonable because all values are constantly 0.5. The charge that comes from one cell is the same that goes into the other cell. In the cycling phase, the LG_HB2 cells exhibit the most asymmetric current distribution. All cell types exhibit lower values of the charge throughput in the cold cell during cycling compared with in the CC phase. Hence, the absence of a relaxation phase that would lead to equivalation leads to more asymmetry in charge throughput.
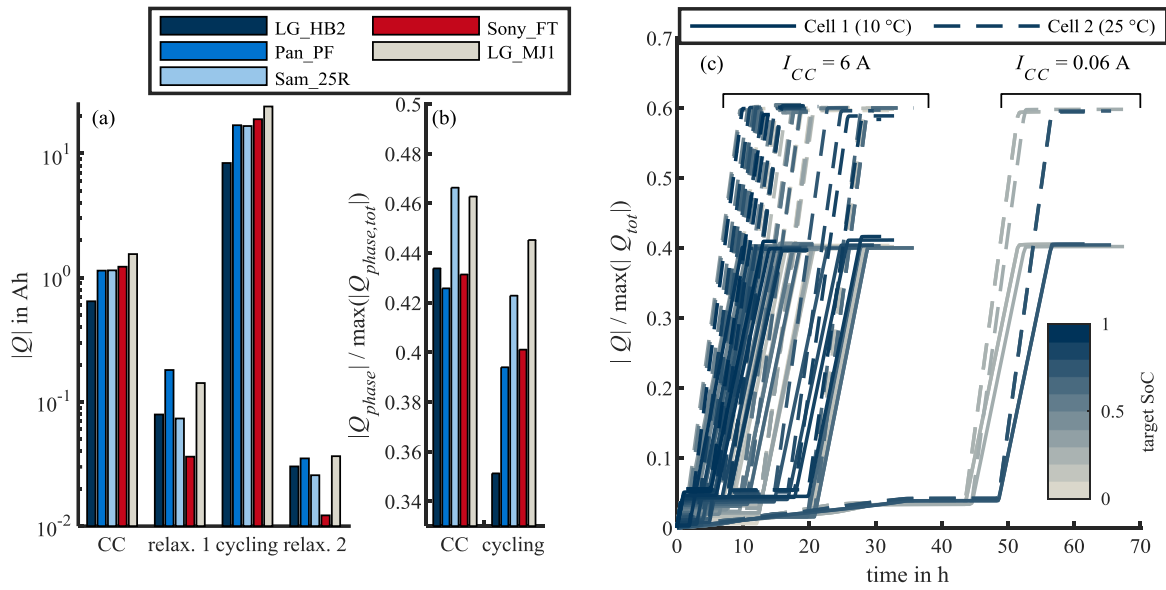
Figure 6.8:   *Comparison of the charge throughput of different cell types in a 2p connection. Diagram (a) shows the total charge throughput of the cold cell in different phases of the load profile on a logarithmic scale. Diagram (b) normalises that values of the total throughput in the CC and cycling phase.*

In these measurements, the current difference is created by an impedance difference triggered by a temperature difference. Furthermore, the temperature dependence of the cells is revealed in the results. The order of asymmetry in the cycling phase in diagram (b) is the same order as the temperature dependence of the impedance in Table 5.3 on page 83.

Diagram (c) shows all measurements of Sony_FT cells. There are results of different target SoCs, synchronisation SoCs at 0 and 100 %, cycling in positive and negative directions, and two different c-rates in the CC phase. The total charge throughput of the cells $|Q|$ is normalised by the total charge throughput of the two cells $|Q_{tot}|$. It becomes clear that the total normalised charge throughput is almost independent of the variation factors: synchronisation SoC, cycling direction, CC current, and target SoC. In all cases, a charge distribution of 3/2 between the warm and cold cell was found.

In addition, the total charge throughput of the cells was higher than in the case of a symmetric current distribution. This is because of the equalisation currents during the relaxation phases. These currents would not stress the cells in a totally even system. The charge throughput during the relaxation phases is less than 1 % of the total charge. This changes when the measurements are confined to only the CC and first relaxation phase. In this case, the equalisation after 50 % DoD is between 3 and 14 % of the charge throughput of these phases when examining the cold cell. Therefore, the relationship can become stronger for a load profile with more relaxation phases.

Ultimately, this increase in charge throughput in dynamic load has not been proven to lead to an increase of ageing in the same order. Thus, at this point, further research is necessary.

6.1.4 Power dissipation

High or low temperatures can harm battery cells [96]. A battery cell operating at ambient temperature will not become colder but warmer because of losses in the cells. This subsection concentrates on the irreversible heat because it causes the major part of the cell heating at current rates of 1 C [230]. In further analyses, it could be interesting to investigate also the reversible heat. Using the cell parameter and measured cell current for the experiment, the power dissipation can be calculated. Diagram (a) of Figure 6.9 shows the energy loss E_{loss} that comes from the integrated power dissipation over the time in each phase of the measurement. In diagram (b), the energy loss is divided by the total energy exchange of phase $E_{phase,tot}$.

$$E_{loss} = \int_{t_{start,phase}}^{t_{end,phase}} R_S \cdot i_{R_S}{}^2 + \sum_{k=1}^{K} R_{p,k} \cdot i_{R_{p,k}}{}^2 \mathrm{d}t \qquad (6.2)$$

$$E_{phase,tot} = \int_{t_{start,phase}}^{t_{end,phase}} U_n \cdot i_n \mathrm{d}t \qquad (6.3)$$

Both diagrams refer to the measurements that were synchronised at 0 and charged to 50 % of the SoC. The cycling phase started in a negative direction, and other measurements did not show significant changes in results.
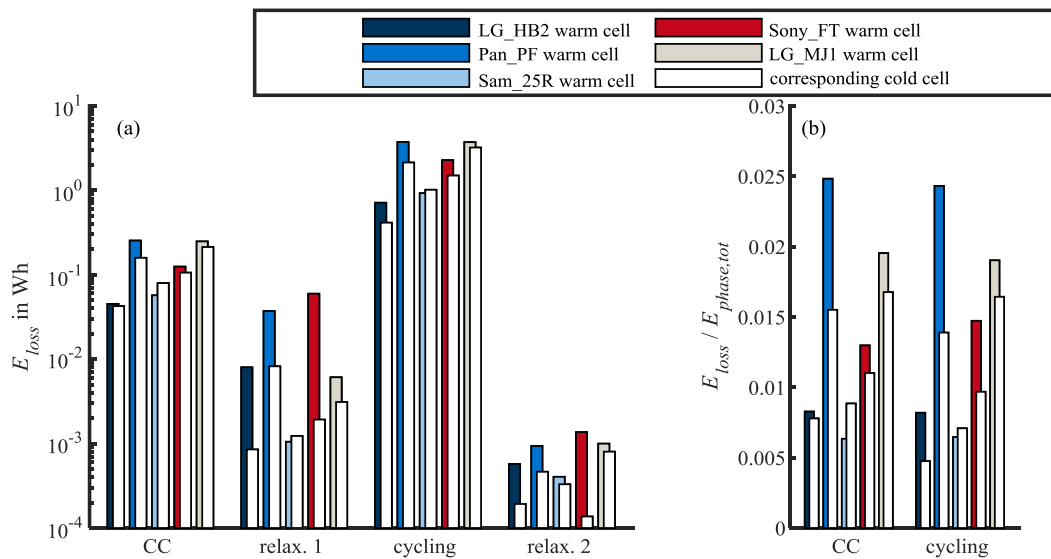
Figure 6.9: *Comparison of energy losses of different cell types in a 2p connection (only irreversible heat). Diagram (a) shows the total losses in different phases of the load profile on a logarithmic scale; diagram (b) normalises values of the energy of the CC and cycling phases.*

In almost all cases, the warmer cell generated more losses. This is because of the higher current and charge throughput despite lower impedance compared with the colder cell. The Sam_25R cell was the only exception. As mentioned previously, losses heat the cells. Assuming the ambient temperature was equivalent to the temperature of the cells at the beginning of the experiment, this means that the temperature of the warm cell rose more than that of the cold cell. Hence, the temperature difference became larger. Under the assumption of linear impedance

growth over temperature and linear heat emission, this would lead to positive feedback because the current distribution became more asymmetric through an increased impedance difference.

Furthermore, the asymmetric warming of cells is relevant to calendric ageing and safety. Keil et al. and Ecker et al. identified temperature as one of the major drivers of calendric ageing [21, 102]. Brand et al. observed the risk of a thermal runaway at temperatures above 104 °C [231].

The differences in relaxation phases between the cold and warm cells are caused by the inner relaxation processes in the cells, which depend on temperature. The fitting of these long-time constants is challenging, and therefore the parameters are supposed to have strong uncertainties. Because the losses during the relaxation phases are magnitudes below those in the CC and cycling phases, this phenomenon is not analysed further. Especially with the low currents during the relaxation phases, the reversible heat could have a significant and non-negligible influence which should be analysed in further investigations.

6.1.5 Nonlinear OCV

The nonlinearity of the OCV can lead to pronounced asymmetries in the current distribution. Simulation and measurement results in Subsection 5.4.2 also prove that this appears for instance at the SoCs of the graphite steps. Thus, the peaks of an asymmetric current can be identified quite simply. However, in Subsection 5.4.2 it became clear that graphite steps with a height in the range of 40 mV [155] only have a significant impact at low currents. When the overvoltage becomes larger than the step height, the effect on current distribution decreases. This is the case in cells with flat OCV curves such as the Sony_FT and with steep OCV curves such as LG_HB2 cells. Figure 6.10 compares the effects of those cells.
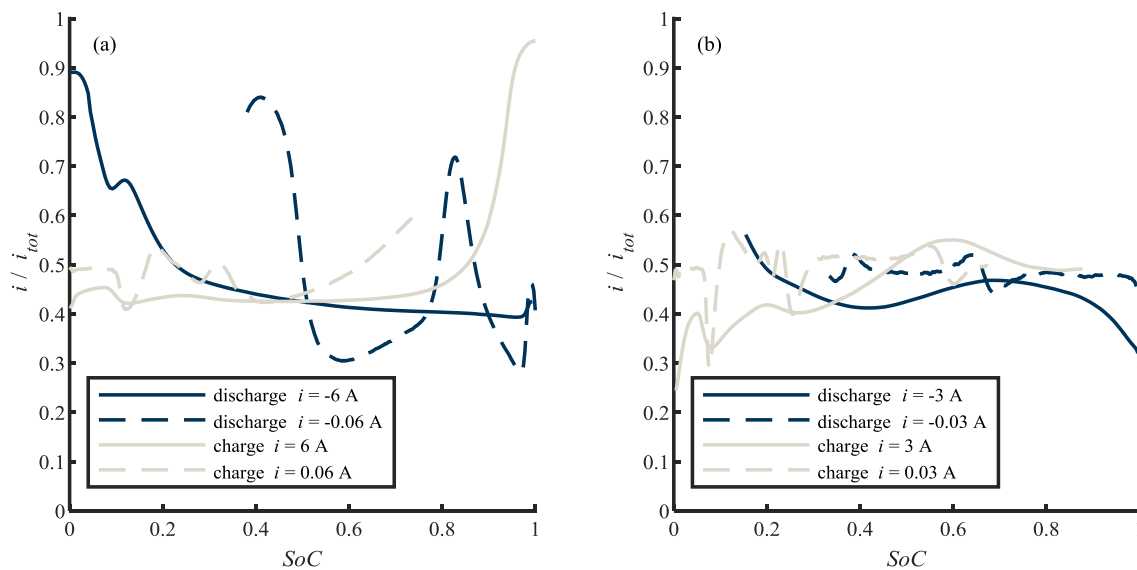
Figure 6.10: *Normalised measured current (i/i_{tot}) of a cold cell connected in parallel with a warm cell at different charge or discharge currents. Diagram (a) shows Sony_FT cells and diagram (b) shows LG_HB2 cells.*

At extremely low c-rates such as 0.01 C, the cold cell takes up to 84 % of the current. This does not appear at 1 C at this SoC. However, Figure 6.10 also shows that in case of 1 C the distribution becomes strongly asymmetric at the end of the charge or discharge process. This is where the OCV becomes nonlinear at the edges of the useable range of the electrode material. This is a critical situation, especially in the charge direction.

The ageing mechanism of plating is supposed to be triggered at anode potentials below 0 V [100, 221]. This is most critical at high SoCs because the OCV of the anode is lower than at low SoCs. The anode potential is also driven by overvoltages. At low temperatures, the impedance of the cells increases, and therefore the overvoltages increase. Because the overvoltages depend on the current, high currents also lead to increased overvoltage. Therefore, three supporting factors—high SoCs, low temperatures, and high currents—can increase the risk of plating when charging a parallel connection of two cells with a temperature difference.

6.2 Ageing

In critical operations, the risk of lithium plating at the end of a charging process is supposed to be the most important effect. This study performed an ageing experiment to prove this impact. First, 12 Sony_FT cells were cycled separately (1p). A cell with LPF cathode material showed strong nonlinearity at SoCs above 98 %, but also in Sam_25R and LG_MJ1 cells the OCVs had a positive curvature at high SoCs. For the ageing experiment, Sony_FT cells are used. The specific load profiles of the four groups of cells were from measurements in 2p connections and a temperature difference of 15 °C. All details of the analyses were explained in Section 4.3. The experiment included four groups, each with three cells; see Table 4.1 on page 64. The cells in group 1 and 2 were cycled with an CCCV reference load profile. The cells of group 3 and 4 were loaded with a profile measured in a parallel connection with a temperature difference (10 and 25 °C).

Figure 6.11 analyses the ageing in terms of capacity loss (a) and impedance growth (b). The ageing of the cold cells is more rapid than that of the warm cells. Furthermore, the three cold cells cycled with the load profile show an accelerated degradation at approximately 1500 equivalent full cycles (EFCs). The cells cycled in cold conditions using a CCCV profile as a reference lived for significantly longer.

Lithium plating leads to a loss of active anode material, and therefore to power loss [26]. The strong increase in impedance in Figure 6.11 (b) supports this theory. To verify the appearance of lithium plating, two cells were opened in a discharged condition. The first cell was from group 4. It was cycled in warm conditions with the load profile of a warm cell. It was not supposed to show lithium plating. The second cell was from group 3 and was cycled under cold conditions with the load profile of a cold cell. It showed the strongest degradation. Figure 6.12 and Figure 6.13 illustrate in each case one photo of the cathode and three photos of the anode at different areas. The cathodes do not show any significant inhomogeneity.
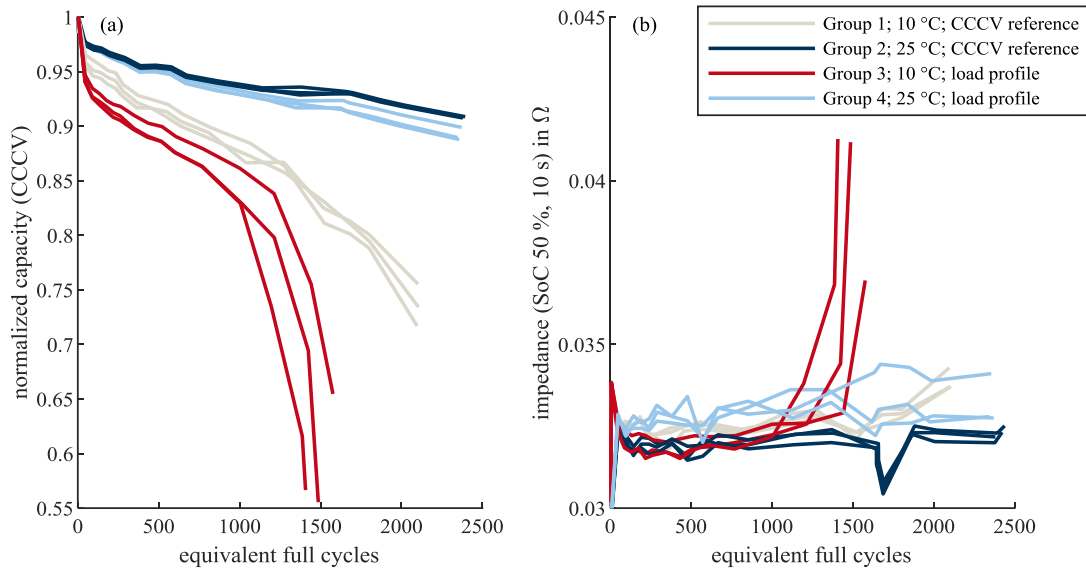
Figure 6.11:   Ageing behaviour of Sony_FT cells at different temperatures and different load profiles in terms of capacity loss (a) and impedance growth (b)
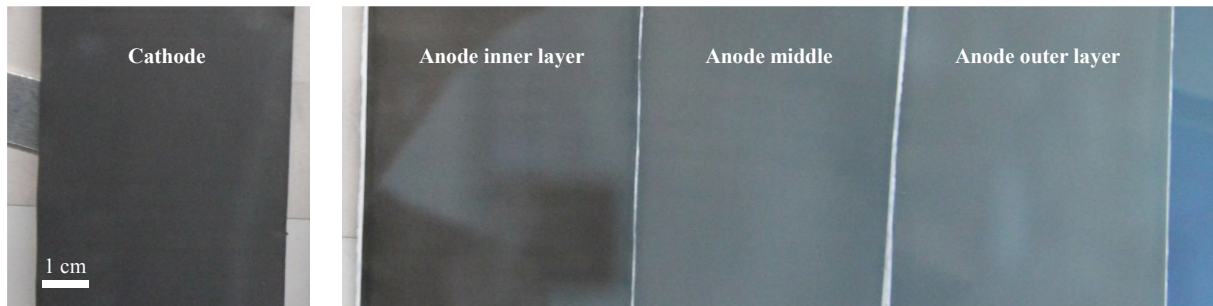
Figure 6.12:   Sony_FT cathode and anode at inner, middle, and outer positions cycled in warm conditions. No indication of lithium plating is visible in any area.
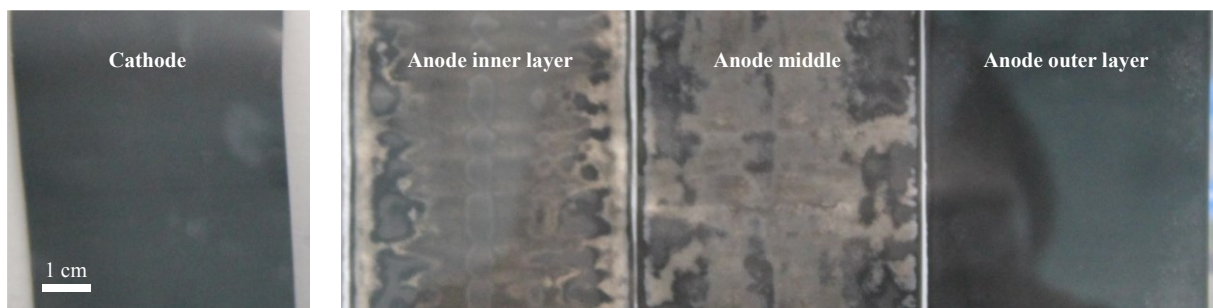
Figure 6.13:   Sony_FT cathode and anode at inner, middle, and outer positions cycled in cold conditions. The inner and middle areas of the anode show a strong indication of lithium plating.

Comparing the anodes, there was a significant difference at the inner and middle area of the electrode. The parts of the cold cycled cell exhibited a metallic layer on the electrode. This is a clear sign of lithium plating [151, 232]. The inner layer was affected the most. This can be explained by the position of the tabs inside the cell. The inner layer was near the tab and an

inhomogeneous current distribution inside the cell led to an excessive current near the tab [150, 154].

6.3 Summary and influences on system design and operation strategies

In this chapter, the effects of asymmetric current distribution in parallel-connected lithium-ion cells were analysed. Measurements on a parallel connection of two cells with different temperature (10 and 25 °C) and a load profile represented typical battery usage. This means a CV charging and discharging phase, respectively, a CC phase until a target SoC, a first relaxation phase, and a cycling phase of ± 20 % of SoC followed by a second relaxation phase. In this scenario, the cell types, synchronised SoC (0 or 100 %), CC current, target SoC and cycling direction were varied.

The evaluation of the SoC difference revealed that at the end of the first relaxation phase, SoC differences of up to 17 % appeared. These high values occurred in the Sony_FT cell with an LFP electrode material with a flat OCV. Cells with steeper slopes only showed SoC differences below 5 % after relaxation. Sections 5.2 and 5.3 illustrated the effect of hysteresis and entropy and how these phenomena can lead to significant SoC differences in cells with flat OCVs. The experiments with different c-rates in the CC phase and different cycling directions supported the assumption of the effects of hysteresis and entropy. Because calendric ageing [93] depends on the SoC, the differences can influence ageing in long storage phases. Furthermore, the difference in charge level could influence the operation of the system, especially when the SoC is brought to a steep area of the OCV.

The current in an electrochemical system is a factor of ageing and safety [21, 231]. Scaling up the maximum cell current from the datasheet using the number of parallel-connected cells would lead to overload in some cells because of asymmetric current distribution. Chapter 5 analysed the influencing factors of current distribution. The experiment of two parallel-connected cells helped to find situations where the overload of one cell was highest. Nonlinearities of the OCV—graphite steps for instance—led to a strong asymmetric current distribution at a small total c-rate. When the overvoltage at the internal impedance was higher than the height of the graphite step, this effect vanished [155]. Because low current does not lead to overload, the nonlinearity caused by graphite steps does not cause accelerated ageing. Other nonlinearities such as those at the end of charge or discharge can lead to an asymmetry that overloads one cell. Furthermore, short-term overload emerged from situations where the current changed.

In ageing experiments and simulations, the charge throughput is normally one of the most important drivers of ageing. When the current distribution is not symmetrically distributed, equalisation currents appear at relaxation phases where no external load is applied. This increases the total charge throughput of the cells. The measurements showed that this equalisation after 50 % DoD was between 3 and 14 % of the total charge throughput of the cold cell. In the warm cell, this was less because the total charge throughput was less. This would also change with the ratio between charge and relaxation phases. At present and to the author's

best knowledge, no studies have analysed the influence of short-term low equalisation currents on ageing. Thus, no proven statements on the influence of safety and ageing are possible.

A simulation of the power dissipation in different phases of the experiment showed that the major part of the dissipation occurred in the warmer cell. Consequently, the warmer cell became even warmer when the ambient temperature was cell temperature, thereby generating some kind of positive feedback. Only the Sam_25R cell represented an exception. In the 2p connection of two Sam_25R cells, the colder cell generated slightly more heat than did the warm cell. In this case, the temperature difference decreased.

The most obvious harmful operation is the charging of parallel-connected cells with temperature differences and LFP cathode material until the end of charge. In this constellation, the cold cell takes the major part of the current at the end of the charging procedure. This is a critical case because lithium plating increases at low temperatures, high SoCs, and high currents. All these factors are given in this scenario. An ageing experiment demonstrated accelerated ageing of cold cells under such conditions. Moreover, lithium plating was proven by opening the cells.

To prevent a harmful situation in the design of a storage system, the reasons for asymmetric current distribution must be eliminated—this starts with the cells. Even if the variation in cell parameters of new cells is low compared with other influencing factors, this will also make the current distribution asymmetric. Depending on the system, the temperature dependence of the cell's impedance is critical. Either the system design must have a homogeneous temperature distribution, or the temperature dependence of the cell's impedance should be as low as possible. These two factors create asymmetry because of temperature inhomogeneity. When temperature gradients cannot be prevented, they should go along a series connection and not along a parallel connection, because all cells of a series connection carry the same current independent of different cell impedances.

The impedances of cables were not part of the present study; nevertheless, they create additional ohmic resistance, and therefore they have the same effect as a parameter variation of R_s. Rumpf et al. showed the effects of an asymmetric connection of cells and the influence on current distribution in detail [144].

Furthermore, the analysis of Baumhöfer et al. showed that the variation of cell parameters increases with ageing [22]. In this paper, the cells aged individually and not in a parallel connection. Several other studies have investigated the change of cell parameters during ageing in a parallel connection [140, 146, 168, 169, 171, 188, 189]. For example, Pastor-Fernandez et al. came to the conclusion that in a parallel connection, the cell parameters converge during the degradation process [146]. Other authors such as Baumann et al. could not prove this theory [189]. The present study supports the results of Baumann et al. Plenty of reasons exist for current distribution and ageing. The experiments in this work confirmed that cell parameters do not occur in all cases. Hence, the parameters possibly converge during ageing, but this does not occur in every case. The constraints of convergence or divergence represent an interesting field of research for future studies.

In terms of operation strategies, especially the strong nonlinear areas of the OCV near 0 and 100 % of the SoC are important. They can influence the current distribution and cells that were charged or discharged less to take over the major current. Particularly in the case of charging, this can lead to lithium plating when the cold cell carries most of the load. An operation strategy could be to prevent this effect by stopping the charging process earlier or reducing the load current.

7 Conclusion and outlook

Parallel connections of battery cells are necessary to fulfil the energy and power requirements for large battery systems. With this, it is crucial to understand the current distribution in parallel-connected lithium-ion cells, especially because overcurrent increases the ageing of batteries and can cause safety issues. The results of this study structured and compared the factors that influence the current distribution in parallel-connected lithium-ion cells. Chapter 3 presented a flexible state-space simulation approach that was based on an EEC model. Validation measurements proved the accuracy of single-cell voltage simulations as well as the simulation of current distribution in the parallel connection.

Chapter 4 discussed the measurement of the current distribution at the cell and system levels. Shunt-based current sensing of the developed test setup was presented. Each cell was in a tempered copper shell, which allowed the cell temperature to be kept constant. A scaled comparison between cell and system level demonstrated that the effects at the cell level could be transferred to the system level. Because of that finding, it was possible to perform all further measurements at the cell level. Finally, an ageing experiment was described, which showed the effect of asymmetric current distribution on the cyclic degradation of battery cells. Chapters 5 and 6 focused on the main research questions of this thesis, which are restated as follows:

Research question 1: What are the influencing factors of current distribution in parallel-connected lithium-ion battery cells?

From the EEC of parallel-connected cells, it became clear that the OCV, internal impedances of the battery cells, and the external connection impedances influence the current distribution. This study focused on the cells' internal reasons. Figure 5.1 on page 67 structured the most relevant connections in the internal impedance and OCV, and showed how they lead to an asymmetric current distribution. It became clear that many back-couplings exist that make it difficult to analyse the single influence of the parameters, as shown in Figure 7.1:

Figure 7.1:   *Example of back-couplings in the causal loop of the current distribution*

Some influencing factors could not be controlled in measurements. In such cases, the simulation model helped to investigate their effects. The ΔSoC comparison of different influencing factors indicated that parameter variations in new cells are only relevant at very low frequencies. The ageing of cells can lead to significant impedance differences that impact the current

distribution. This study compared the effects on five different types of cells with different cathode materials.

In flat OCV curves such as that of an LFP | graphite cell, the influence increased with impedance differences caused by parameter variation, SoH, SoC, and temperature. Simulations with hysteresis calculations resulted in up to 8 % ΔSoC after 50 % DoD at a c-rate of 1 C, a temperature difference of 15 °C and LFP | graphite cells. Other cells with a steeper OCV only indicated an ΔSoC of approximately 2 % under the same conditions. Entropy could cause up to 5.5 % ΔSoC in LFP | graphite cells and up to 0.8 % ΔSoC in NMC | graphite cells when two parallel-connected cells had a temperature difference of 15 °C.

When there is a difference in cell capacity, the long-term relationship of the cell current with the total current is similar to that of the cell capacity and total capacity [25]. The OCV influenced the current distribution predominantly in its nonlinear areas. In the analysed cells, these were either proportionally small steps in the middle of the SoC or strong nonlinearities at low SoCs at high and low SoCs, respectively, using LFP | graphite cells. These small steps could have a strong influence but only at low currents. When the overvoltage at the internal impedance was much larger than the step height, then the step hardly had any influence on the distribution.

Research question 2: What are the impacts of asymmetric current distribution and how do they lead to unsafe situations or accelerated ageing?

Asymmetric current distribution can lead to overcurrent, SoC differences, asymmetric charge throughput, and power dissipation. Measurements with a load profile that represents a realistic usage of a battery system were used to analyse the appearance of critical and harmful situations. The tempering of the 2p connection for these experiments was constant at 10 and 25 °C. Short-term current peaks of up to 90 % of the total current appeared at the beginning of a current pulse. In the cycling phase when the current switched between - 1 and + 1 C, the peaks were higher than at the beginning of the CC phase where the current started at 0 A. Cells with a high temperature dependence of the impedance exhibited the highest maxima. At the end of the long CC phases, the cold cell took the major current because of the nonlinearity of the OCV. This effect was strongest in the LFP | graphite cells. The cold cell took up to 80 % of the total current at the end of a long CC discharge phase.

During long-term CC phases at high currents, the SoCs of the cells diverged until the OCV became strongly nonlinear at the limits of the usable SoC area. At low currents, the ΔSoC was lower and slight nonlinearities of the OCV from graphite steps led to nonmonotonic progress of the ΔSoC. During relaxation phases, an equalisation current lowered the ΔSoC but a gap remained because of hysteresis and entropy phenomena. This gap was below 2 % of SoC in cells with NMC or NCA cathode materials, but up to 20 % in cells with flat OCVs such as LFP cathode material.

The charge throughput of the cells increased because of equalisation currents. At a CC discharge of 50 % of DoD, the charge throughput increased from 3 to 14 % depending on the cell

type compared with a symmetric distribution. The cold cell took 35–44 % of the total charge throughput. Cells for which the impedance was highly dependent on temperature had a more asymmetric distribution.

In terms of power dissipation, the warm cell generated more heat than the cold one because of the higher current. Only one HP cell type with an NCA cathode resulted in slightly more heat generation in the cold cell. This means that in most cases the temperature difference worsened if the ambient temperature was assumed to be similar to the cell temperature at the beginning of the experiment.

Small OCV nonlinearities did not lead to critical states because of overcurrent because they were only relevant at low c-rates. Strong nonlinearities at the boundaries of the SoC could lead to a transfer of the major current from the warm cell to the cold cell even at high currents. This could lead to critical situations. For example, at the end of a charging process, the cold cell fulfilled the three most important criteria of lithium plating: a high SoC, a low temperature, and a high current. An ageing experiment on LFP | graphite cells confirmed that in this case, the cold cells exhibited accelerated ageing. This effect could also explain the plating of pouch cells at its edges, which was shown by Spingler et al. [233].

Research question 3: Which countermeasures can prevent these effects?

To prevent asymmetric current distribution, activities on different stages are possible. First, the choice of the cells. The production caused variation lead to parameter variations which are one reason for asymmetric current distribution. Less variation means more symmetric current distribution. Further, a homogenous change of the cells impedance parameters while the ageing helps. An asymmetric distribution comes from OCV and impedance dependences like temperature and SoC but also from the phenomena of voltage hysteresis and entropy. That means, cells that show less variation over temperature or SoC respectively have less hysteresis and entropy effects, provide more homogeneity in parallel connections. Especially the temperature dependence of the internal impedance is an important parameter for cells that are used in parallel connections and inhomogeneous temperature distribution. Therefore, a simple countermeasure is to keep system and cell parameter as homogenous as possible. In term of the OCV, a flat OCV is more influenced by asymmetric current than a steep one. The increase of the ohmic part of the cell's impedance leads to asymmetric current distribution. At the system level, the wiring impedances and the connection conductivity also makes the ohmic resistance of a branch grow and therefore it is supposed that they influence the current distribution in the same way than R_S. The results of Rumpf et al. confirm this conjecture [144]. Hence, also the system design should be as homogenous as possible. Also, the cooling should arrange similar temperatures of the parallel-connected cells. In terms of current distribution, a temperature gradient should better spread along series and not parallel connections.

In the ageing experiment of this study, the cells suffer at the end of the charging process were the cold cell takes the major part of the total current. With the knowledge of current distribution, this can be prevented by the adoption of the load profile. A reduction of the total current

at the end of the charge phase would solve the problem. The harmfulness of short-time over-current is not totally understood in science. If there is a deterioration through these peaks, they can be prevented by a reduction of the current rise rate. Further, the analysis of this study confirms that OCV nonlinearities have an influence on current distribution but only the strong nonlinearities at the edges of the SoC can lead to harmful overcurrent.

Outlook

One of the next steps in research could be to bring together current distribution within the cells and current distribution in parallel-connected systems. To utilize the maximum power of lithium-ion battery cells, two information are necessary. First, how is the current height at every point in the cell and in the system? Second, detailed knowledge of the influence of current on the ageing of cells is indispensable. Not only the effect of long-term CC cycling like in many ageing experiments is important but also the effect of short-term current peaks. In datasheets of battery cells often only one maximum charge current and one maximum discharge current are given. That is not enough to utilize the limits of the cells best. More dependencies in terms of SoC, temperature, current length and maybe others are necessary.

This can help to solve the problems of fast charging. Researchers like von Lüders proposed fast charge strategies that prevent lithium plating [232]. This and other similar approaches have two problems. They only work properly, when the cell parameters stay constant which is not the case while the ageing of the cells and when the current distribution is not totally homogeneous. Optimised fast charging is only possible with a detailed knowledge of current distribution within the cell and within the system, these strategies can be improved. Otherwise, areas violate the criteria of lithium plating and age.

With new electrode material in mind, the effects of the OCV on the current distribution should be considered. Especially lithium sulphur cells have an OCV that is not even monotonic. This means parallel-connected cells or areas of the electrodes can have an SoC difference and there is no force that equalises this state.

References

The references are grouped into "Scientific literature" starting on page 127, "Datasheets" on page 143, and "Web pages" on page 144.

Scientific literature

[2] A. Senyshyn, M. J. Mühlbauer, O. Dolotko, M. Hofmann, and H. Ehrenberg, "Homogeneity of lithium distribution in cylinder-type Li-ion batteries," (eng), *Scientific Reports*, vol. 5, p. 18380, 2015.

[3] D. Linden and T. B. Reddy, Eds., *Handbook of batteries,* 3rd ed. New York, NY: McGraw-Hill, 2002.

[4] G. P. Hammond and P. J.G. Pearson, "Challenges of the transition to a low carbon, more electric future: From here to 2050," *Energy Policy*, vol. 52, pp. 1–9, 2013.

[5] H.-W. Sinn, "Buffering volatility: A study on the limits of Germany's energy revolution," *European Economic Review*, vol. 99, pp. 130–150, 2017.

[6] J. G. Hayes and G. A. Goodarzi, *Electric powertrain: Energy systems, power electronics & drives for hybrid, electric & fuel cell vehicles*. Hoboken, NJ: John Wiley & Sons, 2018.

[7] M. Müller, *Stationary Lithium-Ion Battery Energy Storage Systems A Multi-Purpose Technology*. Dissertation. München, 2018.

[13] T. Hettesheimer *et al.,* "Entwicklungsperspektiven für Zellformate von Lithium-Ionen-Batterien in der Elektromobilität," http://publica.fraunhofer.de/documents/N-477577.html, 2017.

[15] T. Kimoto, "Material science and device physics in SiC technology for high-voltage power devices," *Japanese Journal of Applied Physics*, vol. 54, no. 4, p. 40103, 2015.

[16] S. Kasap and P. Capper, *Springer Handbook of Electronic and Photonic Materials*. Cham: Springer International Publishing, 2017.

[17] C. Speltino, A. Stefanopoulou, and G. Fiengo, "Cell equalization in battery stacks through State Of Charge estimation polling," in *American Control Conference (ACC)*, Baltimore, Maryland, USA, 2010, pp. 5050–5055.

[19] T. Bruen and J. Marco, "Modelling and experimental evaluation of parallel connected lithium ion cells for an electric vehicle battery system," *Journal of Power Sources*, vol. 310, pp. 91–101, 2016.

[20] K. Rumpf, M. Naumann, and A. Jossen, "Experimental investigation of parametric cell-to-cell variation and correlation based on 1100 commercial lithium-ion cells," *Journal of Energy Storage*, vol. 14, pp. 224–243, 2017.

[21] P. Keil, *Aging of Lithium-Ion Batteries in Electric Vehicles*. Dissertation. München, 2017.

[22] T. Baumhöfer, M. Brühl, S. Rothgang, and D. U. Sauer, "Production caused variation in capacity aging trend and correlation to initial cell performance," *Journal of Power Sources*, vol. 247, pp. 332–338, 2014.

[23] A. Nikolian *et al.*, "Complete cell-level lithium-ion electrical ECM model for different chemistries (NMC, LFP, LTO) and temperatures (−5 °C to 45 °C) – Optimized modelling techniques," *International Journal of Electrical Power & Energy Systems*, vol. 98, pp. 133–146, 2018.

[24] W. Dreyer *et al.*, "The thermodynamic origin of hysteresis in insertion batteries," (eng), *Nature materials*, vol. 9, no. 5, pp. 448–453, 2010.

[25] M. J. Brand, M. H. Hofmann, M. Steinhardt, S. F. Schuster, and A. Jossen, "Current distribution within parallel-connected battery cells," *Journal of Power Sources*, vol. 334, pp. 202–212, 2016.

[26] C. R. Birkl, M. R. Roberts, E. McTurk, P. G. Bruce, and D. A. Howey, "Degradation diagnostics for lithium ion cells," *Journal of Power Sources*, vol. 341, pp. 373–386, 2017.

[27] V. Ruiz *et al.*, "A review of international abuse testing standards and regulations for lithium ion batteries in electric and hybrid electric vehicles," *Renewable and Sustainable Energy Reviews*, vol. 81, pp. 1427–1452, 2018.

[28] M. H. Hofmann *et al.*, "Dynamics of current distribution within battery cells connected in parallel," *Journal of Energy Storage*, vol. 20, pp. 120–133, 2018.

[29] J. B. Goodenough and K.-S. Park, "The Li-ion rechargeable battery: a perspective," (eng), *Journal of the American Chemical Society*, vol. 135, no. 4, pp. 1167–1176, 2013.

[30] B. Rieger, *Methodik zur Simulation des mechanischen Verhaltens von Lithium-Ionen-Zellen*. Dissertation. München, 2017.

[31] D. Lin, Y. Liu, and Y. Cui, "Reviving the lithium metal anode for high-energy batteries," (eng), *Nature nanotechnology*, vol. 12, no. 3, pp. 194–206, 2017.

[32] M. Wohlfahrt-Mehrens, "Energiespeicher für die Elektromobilität: Stand der Technik und Perspektiven," DPG Frühjahrstagung: Arbeitskreis Energie, Dresden, Germany, Mar. 14 2001.

[33] A. Jossen and W. Weydanz, *Moderne Akkumulatoren richtig einsetzen,* 1st ed. Untermeitingen: Reichardt, 2006.

[34] A. H. Whitehead and M. Schreiber, "Current Collectors for Positive Electrodes of Lithium-Based Batteries," *J. Electrochem. Soc.*, vol. 152, no. 11, A2105, 2005.

[35] X. Huang, "Separator technologies for lithium-ion batteries," *J Solid State Electrochem*, vol. 15, no. 4, pp. 649–662, 2011.

[36] V. Deimede and C. Elmasides, "Separators for Lithium-Ion Batteries: A Review on the Production Processes and Recent Developments," *Energy Technology*, vol. 3, no. 5, pp. 453–468, 2015.

[37] M. Brand, *Lithium-ion battery cells and systems under dynamic electric loads*. Dissertation. München: Utz, Herbert, 2018.

[38] I. COMSOL. Burlington, MA: COMSOL Multiphysics, 2018.

[39] M. Moshkovich, M. Cojocaru, H.E. Gottlieb, and D. Aurbach, "The study of the anodic stability of alkyl carbonate solutions by in situ FTIR spectroscopy, EQCM, NMR and MS," *Journal of Electroanalytical Chemistry*, vol. 497, no. 1-2, pp. 84–96, 2001.

[40] K. Kanamura, "Anodic oxidation of nonaqueous electrolytes on cathode materials and current collectors for rechargeable lithium batteries," *Journal of Power Sources*, vol. 81-82, pp. 123–129, 1999.

[41] K. Xu, "High Anodic Stability of a New Electrolyte Solvent: Unsymmetric Noncyclic Aliphatic Sulfone," *J. Electrochem. Soc.*, vol. 145, no. 4, L70, 1998.

[42] *Secondary lithium-ion cells for the propulsion of electric road vehicles*, IEC 62660-1:2018 RLV, 2018.

[43] R. Jamal and R. Heinze, Eds., *Virtuelle Instrumente in der Praxis 2014: Mess-, Steuer-, Regel- und Embedded-Systeme ; Begleitband zum 19. VIP-Kongress*. Berlin, Offenbach: VDE-Verl., 2014.

[44] S. Buller, *Impedance-based simulation models for energy storage devices in advanced automotive power systems*. Dissertation. Aachen: Shaker Verlag GmbH, 2003.

[45] Y. Merla, B. Wu, V. Yufit, R. F. Martinez-Botas, and G. J. Offer, "An easy-to-parameterise physics-informed battery model and its application towards lithium-ion battery cell design, diagnosis, and degradation," *Journal of Power Sources*, vol. 384, pp. 66–79, 2018.

[46] A. Jossen, "Fundamentals of battery dynamics," *Journal of Power Sources*, vol. 154, no. 2, pp. 530–538, 2006.

[47] B. O. Ciocirlan and H. Herrmann, "Switching Contact Bounce Reduction," in *Proceedings of the 55th IEEE Holm Conference on Electrical Contacts*, Vancouver, British Columbia, Canada, 2009, pp. 56–64.

[48] S. B. Peterson, J. Apt, and J. F. Whitacre, "Lithium-ion battery cell degradation resulting from realistic vehicle and vehicle-to-grid utilization," *Journal of Power Sources*, vol. 195, no. 8, pp. 2385–2392, 2010.

[49] B. Y. Liaw and M. Dubarry, "From driving cycle analysis to understanding battery performance in real-life electric hybrid vehicle operation," *Journal of Power Sources*, vol. 174, no. 1, pp. 76–88, 2007.

[50] J. V. Paatero and P. D. Lund, "A model for generating household electricity load profiles," *Int. J. Energy Res.*, vol. 30, no. 5, pp. 273–290, 2006.

[52] American Automatic Control Council, Ed., *American Control Conference (ACC)*. Piscataway, NJ: IEEE, 2010.

[53] F. Baronti, G. Fantechi, R. Roncella, and R. Saletti, "High-Efficiency Digitally Controlled Charge Equalizer for Series-Connected Cells Based on Switching Converter and Super-Capacitor," *IEEE Trans. Ind. Inf.*, vol. 9, no. 2, pp. 1139–1147, 2013.

[54] A. C. Baughman and M. Ferdowsi, "Double-Tiered Switched-Capacitor Battery Charge Equalization Technique," *IEEE Trans. Ind. Electron.*, vol. 55, no. 6, pp. 2277–2285, 2008.

[55] C. Bonfiglio and W. Roessler, "A cost optimized battery management system with active cell balancing for lithium ion battery stacks," in *IEEE Vehicle Power and Propulsion Conference*, Dearborn, Michigan, USA, 2009, pp. 304–309.

[56] J. Gallardo-Lozano, E. Romero-Cadaval, M. I. Milanes-Montero, and M. A. Guerrero-Martinez, "Battery equalization active methods," *Journal of Power Sources*, vol. 246, pp. 934–949, 2014.

[57] W. Ren, J. Jin, Y. Fu, and C. Chang, "A novel test rig for in situ and real time measurement of welding force and impact force of contacts within electromagnetic relay," in *60th Holm Conference on Electrical Contacts*, New Orleans, LA, USA, 2014, pp. 1–7.

[58] L. Kumar and S. Jain, "Electric propulsion system for electric vehicular technology: A review," *Renewable and Sustainable Energy Reviews*, vol. 29, pp. 924–940, 2014.

[59] W. Eberle and F. Musavi, "Overview of wireless power transfer technologies for electric vehicle battery charging," *IET Power Electronics*, vol. 7, no. 1, pp. 60–66, 2014.

[60] B. Koushki, A. Safaee, P. Jain, and A. Bakhshai, "Review and comparison of bi-directional AC-DC converters with V2G capability for on-board EV and HEV," in *IEEE Transportation Electrification Conference and Expo*, Dearborn, MI, USA, 2014, pp. 1–6.

[61] D. Gerling, *Electrical machines: Mathematical fundamentals of machine topologies*. Berlin: Springer, 2015.

[62] K. A. Kalwar, M. Aamir, and S. Mekhilef, "Inductively coupled power transfer (ICPT) for electric vehicle charging – A review," *Renewable and Sustainable Energy Reviews*, vol. 47, pp. 462–475, 2015.

[63] P. Keil and A. Jossen, "Impact of Dynamic Driving Loads and Regenerative Braking on the Aging of Lithium-Ion Batteries in Electric Vehicles," *J. Electrochem. Soc.*, vol. 164, no. 13, A3081-A3092, 2017.

[64] F. Kindermann, *Implications of Current Density Distribution in Lithium-Ion Battery Graphite Anodes on SEI Formation*. Dissertation. München, 2017.

[65] P. B. Balbuena and Y. Wang, Eds., *Lithium-ion batteries: Solid-electrolyte interphase*. London: Imperial College Press, 2007.

[66] H. Helmholtz, "Studien über electrische Grenzschichten," *Ann. Phys. Chem.*, vol. 243, no. 7, pp. 337–382, 1879.

[67] M. Gouy, "Sur la constitution de la charge électrique à la surface d'un électrolyte," *J. Phys. Theor. Appl.*, vol. 9, no. 1, pp. 457–468, 1910.

[68] O. Stern, "Zur Theorie der elektrochemischen Doppelschicht," *Zeitschrift für Elektrochemie und angewandte physikalische Chemie*, vol. 30, no. 21-22, pp. 508–516, 1924.

[69] A. Fick, "Ueber Diffusion," *Ann. Phys. Chem.*, vol. 170, no. 1, pp. 59–86, 1855.

[70] A. Fick, "V. On liquid diffusion," *The London, Edinburgh, and Dublin Philosophical Magazine and Journal of Science*, vol. 10, no. 63, pp. 30–39, 1855.

[71] A. N. Gorban, H. P. Sargsyan, and H. A. Wahab, "Quasichemical Models of Multicomponent Nonlinear Diffusion," *Math. Model. Nat. Phenom.*, vol. 6, no. 5, pp. 184–262, 2011.

[72] E. Prada *et al.*, "Simplified Electrochemical and Thermal Model of LiFePO 4 -Graphite Li-Ion Batteries for Fast Charge Applications," *J. Electrochem. Soc.*, vol. 159, no. 9, A1508-A1519, 2012.

[73] J. P. Schmidt, A. Weber, and E. Ivers-Tiffée, "A novel and fast method of characterizing the self-discharge behavior of lithium-ion cells using a pulse-measurement technique," *Journal of Power Sources*, vol. 274, pp. 1231–1238, 2015.

[74] E. Redondo-Iglesias, P. Venet, and S. Pelissier, "Global Model for Self-Discharge and Capacity Fade in Lithium-Ion Batteries Based on the Generalized Eyring Relationship," *IEEE Trans. Veh. Technol.*, vol. 67, no. 1, pp. 104–113, 2018.

[75] M. Shen and Q. Gao, "A review on battery management system from the modeling efforts to its multiapplication and integration," *Int. J. Energy Res.*, vol. 43, no. 10, pp. 5042–5075, 2019.

[76] S. Nejad, D. T. Gladwin, and D. A. Stone, "A systematic review of lumped-parameter equivalent circuit models for real-time estimation of lithium-ion battery states," *Journal of Power Sources*, vol. 316, pp. 183–196, 2016.

[77] E. Barsoukov and J. R. Macdonald, Eds., *Impedance spectroscopy: Theory, experiment, and applications,* 2nd ed. Hoboken (New Jersey): Wiley-Interscience, 2005.

[78] J. R. Macdonald and G. B. Cook, "Analysis of impedance data for single crystal na β-alumina at low temperatures," *Journal of Electroanalytical Chemistry and Interfacial Electrochemistry*, vol. 168, no. 1-2, pp. 335–354, 1984.

[79] P. L. Moss, G. Au, E. J. Plichta, and J. P. Zheng, "An Electrical Circuit for Modeling the Dynamic Response of Li-Ion Polymer Batteries," *J. Electrochem. Soc.*, vol. 155, no. 12, A986, 2008.

[80] H. J. Bergveld, *Battery management systems: Design by modelling*. Dissertation. Dordrecht: Springer, 2002.

[81] M.-T. von Srbik, M. Marinescu, R. F. Martinez-Botas, and G. J. Offer, "A physically meaningful equivalent circuit network model of a lithium-ion battery accounting for local electrochemical and thermal behaviour, variable double layer capacitance and degradation," *Journal of Power Sources*, vol. 325, pp. 171–184, 2016.

[82] S. Raël and M. Hinaje, "Using electrical analogy to describe mass and charge transport in lithium-ion batteries," *Journal of Power Sources*, vol. 222, pp. 112–122, 2013.

[83] M. J. Brand *et al.,* "Electrical resistances of soldered battery cell connections," *Journal of Energy Storage*, vol. 12, pp. 45–54, 2017.

[84] M. J. Brand, P. A. Schmidt, M. F. Zaeh, and A. Jossen, "Welding techniques for battery cells and resulting electrical contact resistances," *Journal of Energy Storage*, vol. 1, pp. 7–14, 2015.

[85] M. J. Brand *et al.,* "Detachable electrical connection of battery cells by press contacts," *Journal of Energy Storage*, vol. 8, pp. 69–77, 2016.

[86] E. Sarasketa-Zabala *et al.,* "Validation of the methodology for lithium-ion batteries lifetime prognosis," in *27th World Electric Vehicle Symposium and Exhibition*, Barcelona, Spain, 2013, pp. 1–12.

[87] J. Vetter *et al.,* "Ageing mechanisms in lithium-ion batteries," *Journal of Power Sources*, vol. 147, no. 1-2, pp. 269–281, 2005.

[88] I. Bloom *et al.,* "Differential voltage analyses of high-power, lithium-ion cells," *Journal of Power Sources*, vol. 139, no. 1-2, pp. 295–303, 2005.

[89] A. J. Smith, J. C. Burns, and J. R. Dahn, "High-Precision Differential Capacity Analysis of LiMn2O4/graphite Cells," *Electrochem. Solid-State Lett.*, vol. 14, no. 4, A39, 2011.

[90] A. J. Smith, H. M. Dahn, J. C. Burns, and J. R. Dahn, "Long-Term Low-Rate Cycling of LiCoO 2 /Graphite Li-Ion Cells at 55°C," *J. Electrochem. Soc.*, vol. 159, no. 6, A705-A710, 2012.

[91] A. J. Smith and J. R. Dahn, "Delta Differential Capacity Analysis," *J. Electrochem. Soc.*, vol. 159, no. 3, A290-A293, 2012.

[92] H. M. Dahn, A. J. Smith, J. C. Burns, D. A. Stevens, and J. R. Dahn, "User-Friendly Differential Voltage Analysis Freeware for the Analysis of Degradation Mechanisms in Li-Ion Batteries," *J. Electrochem. Soc.*, vol. 159, no. 9, A1405-A1409, 2012.

[93] P. Keil and A. Jossen, "Calendar Aging of NCA Lithium-Ion Batteries Investigated by Differential Voltage Analysis and Coulomb Tracking," *J. Electrochem. Soc.*, vol. 164, no. 1, A6066-A6074, 2017.

[94] P. Keil and A. Jossen, "Charging protocols for lithium-ion batteries and their impact on cycle life—An experimental study with different 18650 high-power cells," *Journal of Energy Storage*, vol. 6, pp. 125–141, 2016.

[95] M. Lewerenz, A. Marongiu, A. Warnecke, and D. U. Sauer, "Differential voltage analysis as a tool for analyzing inhomogeneous aging: A case study for LiFePO4|Graphite cylindrical cells," *Journal of Power Sources*, vol. 368, pp. 57–67, 2017.

[96] T. Waldmann, M. Wilka, M. Kasper, M. Fleischhammer, and M. Wohlfahrt-Mehrens, "Temperature dependent ageing mechanisms in Lithium-ion batteries – A Post-Mortem study," *Journal of Power Sources*, vol. 262, pp. 129–135, 2014.

[97] V. Zinth *et al.*, "Lithium plating in lithium-ion batteries at sub-ambient temperatures investigated by in situ neutron diffraction," *Journal of Power Sources*, vol. 271, pp. 152–159, 2014.

[98] V. Zinth *et al.*, "Inhomogeneity and relaxation phenomena in the graphite anode of a lithium-ion battery probed by in situ neutron diffraction," *Journal of Power Sources*, vol. 361, pp. 54–60, 2017.

[99] C. von Lüders *et al.*, "Lithium plating in lithium-ion batteries investigated by voltage relaxation and in situ neutron diffraction," *Journal of Power Sources*, vol. 342, pp. 17–23, 2017.

[100] N. Legrand, B. Knosp, P. Desprez, F. Lapicque, and S. Raël, "Physical characterization of the charging process of a Li-ion battery and prediction of Li plating by electrochemical modelling," *Journal of Power Sources*, vol. 245, pp. 208–216, 2014.

[101]   M. Ecker *et al.*, "Development of a lifetime prediction model for lithium-ion batteries based on extended accelerated aging test data," *Journal of Power Sources*, vol. 215, pp. 248–257, 2012.

[102]   M. Ecker *et al.*, "Calendar and cycle life study of Li(NiMnCo)O2-based 18650 lithium-ion batteries," *Journal of Power Sources*, vol. 248, pp. 839–851, 2014.

[103]   M. Ecker, P. Shafiei Sabet, and D. U. Sauer, "Influence of operational condition on lithium plating for commercial lithium-ion batteries – Electrochemical experiments and post-mortem-analysis," *Applied Energy*, vol. 206, pp. 934–946, 2017.

[104]   M. Ecker, *Lithium plating in lithium-ion batteries*. Dissertation. Düren: Shaker Verlag GmbH, 2016.

[105]   P. Keil *et al.*, "Calendar Aging of Lithium-Ion Batteries," *J. Electrochem. Soc.*, vol. 163, no. 9, A1872-A1880, 2016.

[106]   J. P. Schmidt, A. Weber, and E. Ivers-Tiffée, "A novel and precise measuring method for the entropy of lithium-ion cells: ΔS via electrothermal impedance spectroscopy," *Electrochimica Acta*, vol. 137, pp. 311–319, 2014.

[107]   N. Damay, C. Forgez, M.-P. Bichat, and G. Friedrich, "A method for the fast estimation of a battery entropy-variation high-resolution curve – Application on a commercial LiFePO4/graphite cell," *Journal of Power Sources*, vol. 332, pp. 149–153, 2016.

[108]   W. Dreyer, C. Guhlke, and R. Huth, "The behavior of a many-particle electrode in a lithium-ion battery," *Physica D: Nonlinear Phenomena*, vol. 240, no. 12, pp. 1008–1019, 2011.

[109]   L. Zhu, Z. Sun, H. Dai, and X. Wei, "A novel modeling methodology of open circuit voltage hysteresis for LiFePO4 batteries based on an adaptive discrete Preisach model," *Applied Energy*, vol. 155, pp. 91–109, 2015.

[110]   F. Baronti, N. Femia, R. Saletti, C. Visone, and W. Zamboni, "Preisach modelling of lithium-iron-phosphate battery hysteresis," *Journal of Energy Storage*, vol. 4, pp. 51–61, 2015.

[112]   S. F. Schuster, M. J. Brand, P. Berg, M. Gleissenberger, and A. Jossen, "Lithium-ion cell-to-cell variation during battery electric vehicle operation," *Journal of Power Sources*, vol. 297, pp. 242–251, 2015.

[113]   S. F. Schuster, M. J. Brand, C. Campestrini, M. Gleissenberger, and A. Jossen, "Correlation between capacity and impedance of lithium-ion cells during calendar and cycle life," *Journal of Power Sources*, vol. 305, pp. 191–199, 2016.

[114]   J. Euler and L. Horn, "Stromverteilung in akkumulatorenplatten aus rohrförmigen elementen," *Electrochimica Acta*, vol. 10, no. 11, pp. 1057–1066, 1965.

[115] P. Maire, A. Evans, H. Kaiser, W. Scheifele, and P. Novák, "Colorimetric Determination of Lithium Content in Electrodes of Lithium-Ion Batteries," *J. Electrochem. Soc.*, vol. 155, no. 11, A862, 2008.

[116] G. Zhang, C. E. Shaffer, C.-Y. Wang, and C. D. Rahn, "In-Situ Measurement of Current Distribution in a Li-Ion Cell," *J. Electrochem. Soc.*, vol. 160, no. 4, A610-A615, 2013.

[117] G. Zhang, C. E. Shaffer, C.-Y. Wang, and C. D. Rahn, "Effects of Non-Uniform Current Distribution on Energy Density of Li-Ion Cells," *J. Electrochem. Soc.*, vol. 160, no. 11, A2299-A2305, 2013.

[118] J. Wilhelm *et al.*, "In Situ Neutron Diffraction Study of Lithiation Gradients in Graphite Anodes during Discharge and Relaxation," *J. Electrochem. Soc.*, vol. 165, no. 9, A1846-A1856, 2018.

[119] P. J. Osswald *et al.*, "Current density distribution in cylindrical Li-Ion cells during impedance measurements," *Journal of Power Sources*, vol. 314, pp. 93–101, 2016.

[120] W. A. Paxton, Z. Zhong, and T. Tsakalakos, "Tracking inhomogeneity in high-capacity lithium iron phosphate batteries," *Journal of Power Sources*, vol. 275, pp. 429–434, 2015.

[121] J. Liu, M. Kunz, K. Chen, N. Tamura, and T. J. Richardson, "Visualization of Charge Distribution in a Lithium Battery Electrode," *J. Phys. Chem. Lett.*, vol. 1, no. 14, pp. 2120–2123, 2010.

[122] S. V. Erhard *et al.*, "Simulation and Measurement of the Current Density Distribution in Lithium-Ion Batteries by a Multi-Tab Cell Approach," *J. Electrochem. Soc.*, vol. 164, no. 1, A6324-A6333, 2017.

[123] R. Jamal and R. Heinze, Eds., *Virtuelle Instrumente in der Praxis 2016: Mess-, Steuer-, Regel- und Embedded-Systeme : Begleitband zum 21. VIP-Kongress*. Berlin, Offenbach: VDE Verlag GmbH, 2016.

[124] M. Fleckenstein, O. Bohlen, M. A. Roscher, and B. Bäker, "Current density and state of charge inhomogeneities in Li-ion battery cells with LiFePO4 as cathode material due to temperature gradients," *Journal of Power Sources*, vol. 196, no. 10, pp. 4769–4778, 2011.

[125] J. Euler and W. Nonnenmacher, "Stromverteilung in porösen elektroden," *Electrochimica Acta*, vol. 2, no. 4, pp. 268–286, 1960.

[126] E. Meissner, "Calculation of potential distribution and voltage drop at electrodes on high-rate discharge: literature survey and computer-aided approach," *Journal of Power Sources*, vol. 42, no. 1-2, pp. 103–118, 1993.

[127] G.-H. Kim, K. Smith, K.-J. Lee, S. Santhanagopalan, and A. Pesaran, "Multi-Domain Modeling of Lithium-Ion Batteries Encompassing Multi-Physics in Varied Length Scales," *J. Electrochem. Soc.*, vol. 158, no. 8, A955, 2011.

[128] M. Xu, Z. Zhang, X. Wang, L. Jia, and L. Yang, "A pseudo three-dimensional electro-chemical–thermal model of a prismatic LiFePO 4 battery during discharge process," *Energy*, vol. 80, pp. 303–317, 2015.

[129] P. J. Osswald *et al.*, "Temperature dependency of state of charge inhomogeneities and their equalization in cylindrical lithium-ion cells," *Journal of Power Sources*, vol. 329, pp. 546–552, 2016.

[130] W. Song *et al.*, "Non-uniform effect on the thermal/aging performance of Lithium-ion pouch battery," *Applied Thermal Engineering*, vol. 128, pp. 1165–1174, 2018.

[131] C. E. Holland, J. W. Weidner, R. A. Dougal, and R. E. White, "Experimental character-ization of hybrid power systems under pulse current loads," *Journal of Power Sources*, vol. 109, no. 1, pp. 32–37, 2002.

[132] S. M. Lukic, S. G. Wirasingha, F. Rodriguez, J. Cao, and A. Emadi, "Power Manage-ment of an Ultracapacitor/Battery Hybrid Energy Storage System in an HEV," in *IEEE Vehicle Power and Propulsion Conference*, Windsor, UK, 2006, pp. 1–6.

[133] P. Bentley, D. A. Stone, and N. Schofield, "The parallel combination of a VRLA cell and supercapacitor for use as a hybrid vehicle peak power buffer," *Journal of Power Sources*, vol. 147, no. 1-2, pp. 288–294, 2005.

[134] V. Bolborici, F. P. Dawson, and K. K. Lian, "Hybrid Energy Storage Systems: Connect-ing Batteries in Parallel with Ultracapacitors for Higher Power Density," *IEEE Ind. Appl. Mag.*, vol. 20, no. 4, pp. 31–40, 2014.

[135] D. Cericola, P. W. Ruch, R. Kötz, P. Novák, and A. Wokaun, "Simulation of a superca-pacitor/Li-ion battery hybrid for pulsed applications," *Journal of Power Sources*, vol. 195, no. 9, pp. 2731–2736, 2010.

[136] N. Omar *et al.*, "Effectiveness evaluation of a Supercapacitor-battery parallel combina-tion for Hybrid Heavy Lift Trucks," in *24th International Battery Hybrid and Fuel Cell Elec-tric Vehicle Symposium and Exhibition*, Stavanger, Norway, 2009, pp. 2584–2594.

[137] D. Shin, Y. Kim, Y. Wang, N. Chang, and M. Pedram, "Constant-current regulator-based battery-supercapacitor hybrid architecture for high-rate pulsed load applica-tions," *Journal of Power Sources*, vol. 205, pp. 516–524, 2012.

[138] A. U. Schmid, L. Eringer, I. Lambidis, and K. P. Birke, "Electrochemical balancing of lithium-ion cells by nickel-based cells," *Journal of Power Sources*, vol. 367, pp. 49–56, 2017.

[139] F. An *et al.*, "Cell sorting for parallel lithium-ion battery systems: Evaluation based on an electric circuit model," *Journal of Energy Storage*, vol. 6, pp. 195–203, 2016.

[140] R. Gogoana, M. B. Pinson, M. Z. Bazant, and S. E. Sarma, "Internal resistance matching for parallel-connected lithium-ion cells and impacts on battery pack cycle life," *Journal of Power Sources*, vol. 252, pp. 8–13, 2014.

[141] T. Bruen, J. Marco, and M. Gama, "Current Variation in Parallelized Energy Storage Systems," in *IEEE Vehicle Power and Propulsion Conference*, Coimbra, Portugal, 2014, pp. 1–6.

[142] N. Yang, X. Zhang, B. Shang, and G. Li, "Unbalanced discharging and aging due to temperature differences among the cells in a lithium-ion battery pack with parallel combination," *Journal of Power Sources*, vol. 306, pp. 733–741, 2016.

[143] S. Kamalisiahroudi, J. Huang, Z. Li, and J. Zhang, "Study of temperature difference and current distribution in parallel-connected cells at low temperature," *International Journal of Mechanical and Mechatronics Engineering*, vol. 8, pp. 1596–1599, 2014.

[144] K. Rumpf *et al.*, "Influence of Cell-to-Cell Variations on the Inhomogeneity of Lithium-Ion Battery Modules," *J. Electrochem. Soc.*, vol. 165, no. 11, A2587-A2607, 2018.

[145] M. P. Klein and J. W. Park, "Current Distribution Measurements in Parallel-Connected Lithium-Ion Cylindrical Cells under Non-Uniform Temperature Conditions," *J. Electrochem. Soc.*, vol. 164, no. 9, A1893-A1906, 2017.

[146] C. Pastor-Fernández, T. Bruen, W. D. Widanage, M. A. Gama-Valdez, and J. Marco, "A Study of Cell-to-Cell Interactions and Degradation in Parallel Strings: Implications for the Battery Management System," *Journal of Power Sources*, vol. 329, pp. 574–585, 2016.

[147] M. W. Verbrugge, "Three-dimensionai temperature and current distribution in a battery module," *AIChE J.*, vol. 41, no. 6, pp. 1550–1562, 1995.

[148] R. E. Gerver and J. P. Meyers, "Three-Dimensional Modeling of Electrochemical Performance and Heat Generation of Lithium-Ion Batteries in Tabbed Planar Configurations," *J. Electrochem. Soc.*, vol. 158, no. 7, A835, 2011.

[149] M. Guo and R. E. White, "A distributed thermal model for a Li-ion electrode plate pair," *Journal of Power Sources*, vol. 221, pp. 334–344, 2013.

[150] B. Wu, Z. Li, and J. Zhang, "Thermal Design for the Pouch-Type Large-Format Lithium-Ion Batteries," *J. Electrochem. Soc.*, vol. 162, no. 1, A181-A191, 2015.

[151] J. Cannarella and C. B. Arnold, "The Effects of Defects on Localized Plating in Lithium-Ion Batteries," *J. Electrochem. Soc.*, vol. 162, no. 7, A1365-A1373, 2015.

[152]   Z. An, L. Jia, L. Wei, C. Dang, and Q. Peng, "Investigation on lithium-ion battery electrochemical and thermal characteristic based on electrochemical-thermal coupled model," *Applied Thermal Engineering*, vol. 137, pp. 792–807, 2018.

[153]   M. M. Forouzan, B. A. Mazzeo, and D. R. Wheeler, "Modeling the Effects of Electrode Microstructural Heterogeneities on Li-Ion Battery Performance and Lifetime," *J. Electrochem. Soc.*, vol. 165, no. 10, A2127-A2144, 2018.

[154]   N. Lin, F. Röder, and U. Krewer, "Multiphysics Modeling for Detailed Analysis of Multi-Layer Lithium-Ion Pouch Cells," *Energies*, vol. 11, no. 11, p. 2998, 2018.

[155]   F. E. Hust, *Physico-Chemically Motivated Parameterization and Modelling of Real-Time Capable Lithium-Ion Battery Models - a Case Study on the Tesla Model S Battery*. Dissertation. Aachen: AACHENER BEITRÄGE DES ISEA, 2018.

[156]   I. Hunt *et al.*, "The Effect of Current Inhomogeneity on the Performance and Degradation of Li-S Batteries," *J. Electrochem. Soc.*, vol. 165, no. 1, A6073-A6080, 2018.

[157]   R. Spurrett, C. Thwaite, A. Holland, D. Lizius, and G. J. Dudley, "Modeling of highly-parallel lithium-ion batteries," in *Space Power, Proceedings of the Sixth European Conference*, Porto, Portugal, 2002, p. 685.

[158]   V. M. Byrne and P. K. Ng, "Behaviour of Systems Mixing Parallel Strings of Lithium-Ion and Lead-Acid Batteries for Telecommunications Applications," in *27th International Telecommunication Energy Conference*, Berlin, Germany, 2005, pp. 211–216.

[159]   M.-S. Wu, C.-Y. Lin, Y.-Y. Wang, C.-C. Wan, and C. R. Yang, "Numerical simulation for the discharge behaviors of batteries in series and/or parallel-connected battery pack," *Electrochimica Acta*, vol. 52, no. 3, pp. 1349–1357, 2006.

[160]   G. L. Plett and M. J. Klein, "Simulating battery packs comprising parallel cell modules and series cell modules," in *24th International Battery Hybrid and Fuel Cell Electric Vehicle Symposium and Exhibition*, Stavanger, Norway, 2009, pp. 1–17.

[161]   M. Guo and R. E. White, "Thermal Model for Lithium Ion Battery Pack with Mixed Parallel and Series Configuration," *J. Electrochem. Soc.*, vol. 158, no. 10, A1166, 2011.

[162]   J. Zhang, S. Ci, H. Sharif, and M. Alahmad, "Modeling Discharge Behavior of Multi-cell Battery," *IEEE Trans. Energy Convers.*, vol. 25, no. 4, pp. 1133–1141, 2010.

[163]   G. J. Offer, V. Yufit, D. A. Howey, B. Wu, and N. P. Brandon, "Module design and fault diagnosis in electric vehicle batteries," *Journal of Power Sources*, vol. 206, pp. 383–392, 2012.

[164]   S. Miyatake, Y. Susuki, T. Hikihara, S. Itoh, and K. Tanaka, "Discharge characteristics of multicell lithium-ion battery with nonuniform cells," *Journal of Power Sources*, vol. 241, pp. 736–743, 2013.

[165] B. Wu *et al.*, "Coupled thermal–electrochemical modelling of uneven heat generation in lithium-ion battery packs," *Journal of Power Sources*, vol. 243, pp. 544–554, 2013.

[166] J. Jiang *et al.*, "An analysis of optimized series and parallel method for traction lithium-ion batteries," in *The 1st International Conference on Intelligent Green Building and Smart Grid*, Taipei, Taiwan, 2014, pp. 1–7.

[167] X. Gong, R. Xiong, and C. C. Mi, "Study of the characteristics of battery packs in electric vehicles with parallel-connected lithium-ion battery cells," *IEEE Trans. on Ind. Applicat.*, vol. 51, no. 2, pp. 1872–1879, 2015.

[168] A. Cordoba-Arenas, S. Onori, and G. Rizzoni, "A control-oriented lithium-ion battery pack model for plug-in hybrid electric vehicle cycle-life studies and system design with consideration of health management," *Journal of Power Sources*, vol. 279, pp. 791–808, 2015.

[169] L. Wang, Y. Cheng, and X. Zhao, "Influence of connecting plate resistance upon LiFePO4 battery performance," *Applied Energy*, vol. 147, pp. 353–360, 2015.

[170] N. Kakimoto and K. Goto, "Capacity-Fading Model of Lithium-Ion Battery Applicable to Multicell Storage Systems," *IEEE Trans. Sustain. Energy*, vol. 7, no. 1, pp. 108–117, 2016.

[171] N. Ganesan *et al.*, "Physics based modeling of a series parallel battery pack for asymmetry analysis, predictive control and life extension," *Journal of Power Sources*, vol. 322, pp. 57–67, 2016.

[172] Y. Merla *et al.*, "Extending battery life: A low-cost practical diagnostic technique for lithium-ion batteries," *Journal of Power Sources*, vol. 331, pp. 224–231, 2016.

[173] L. Wang, X. Zhao, L. Liu, and R. Wang, "Battery pack topology structure on state-of-charge estimation accuracy in electric vehicles," *Electrochimica Acta*, vol. 219, pp. 711–720, 2016.

[174] Y. Zhang, R. Zhao, J. Dubie, T. Jahns, and L. Juang, "Investigation of current sharing and heat dissipation in parallel-connected lithium-ion battery packs," in *Energy Conversion Congress & Expo*, Milwaukee, WI, USA, 2016, pp. 1–8.

[175] T. Zimmermann, M. H. Hofmann, M. Steinhardt, G. Rahn-Koltermann, and A. Jossen, "Intelligente Steuerungs- und Verschaltungskonzepte für modulare Elektrofahrzeug-Batteriesysteme zur Steigerung der Effizienz und Sicherheit sowie zur Senkung der Systemkosten: DriveBattery2015 Phase 2," *Katalog der Technischen Informationsbibliothek Hannover*, 2017.

[176] Y. Zhang *et al.*, "Nonuniform current distribution within parallel-connected batteries," *Int. J. Energy Res.*, vol. 42, no. 8, pp. 2835–2844, 2018.

[177]   T. Grün, K. Stella, and O. Wollersheim, "Influence of circuit design on load distribution and performance of parallel-connected Lithium ion cells for photovoltaic home storage systems," *Journal of Energy Storage*, vol. 17, pp. 367–382, 2018.

[178]   T. Grün, K. Stella, and O. Wollersheim, "Impacts on load distribution and ageing in Lithium-ion home storage systems," *Energy Procedia*, vol. 135, pp. 236–248, 2017.

[179]   M. Dubarry, A. Devie, and B. Y. Liaw, "Cell-balancing currents in parallel strings of a battery system," *Journal of Power Sources*, vol. 321, pp. 36–46, 2016.

[180]   C. Pastor-Fernández, K. Uddin, G. H. Chouchelamane, W. D. Widanage, and J. Marco, "A Comparison between Electrochemical Impedance Spectroscopy and Incremental Capacity-Differential Voltage as Li-ion Diagnostic Techniques to Identify and Quantify the Effects of Degradation Modes within Battery Management Systems," *Journal of Power Sources*, vol. 360, pp. 301–318, 2017.

[181]   N. Damay, C. Forgez, G. Friedrich, and M.-P. Bichat, "Heterogeneous behavior modeling of a LiFePO 4 -graphite cell using an equivalent electrical circuit," *Journal of Energy Storage*, vol. 12, pp. 167–177, 2017.

[182]   F. Chang, F. Roemer, M. Baumann, and M. Lienkamp, "Modelling and Evaluation of Battery Packs with Different Numbers of Paralleled Cells," *World Electric Vehicle Journal*, vol. 9, no. 1, p. 8, 2018.

[183]   S. Neupert and J. Kowal, "Inhomogeneities in Battery Packs," *World Electric Vehicle Journal*, vol. 9, no. 2, p. 20, 2018.

[184]   S. Koch, A. Fill, K. Kelesiadou, and K. Birke, "Discharge by Short Circuit Currents of Parallel-Connected Lithium-Ion Cells in Thermal Propagation," *Batteries*, vol. 5, no. 1, p. 18, 2019.

[185]   A. Samba *et al.*, "Impact of Tab Location on Large Format Lithium-Ion Pouch Cell Based on Fully Coupled Tree-Dimensional Electrochemical-Thermal Modeling," *Electrochimica Acta*, vol. 147, pp. 319–329, 2014.

[186]   B. Rieger *et al.*, "Multi-Dimensional Modeling of the Influence of Cell Design on Temperature, Displacement and Stress Inhomogeneity in Large-Format Lithium-Ion Cells," *J. Electrochem. Soc.*, vol. 163, no. 14, A3099-A3110, 2016.

[187]   A. J. Fairweather, D. A. Stone, and M. P. Foster, "Evaluation of UltraBattery™ performance in comparison with a battery-supercapacitor parallel network," *Journal of Power Sources*, vol. 226, pp. 191–201, 2013.

[188]   W. Shi *et al.*, "Effects of imbalanced currents on large-format LiFePO 4 /graphite batteries systems connected in parallel," *Journal of Power Sources*, vol. 313, pp. 198–204, 2016.

[189]   M. Baumann, L. Wildfeuer, S. Rohr, and M. Lienkamp, "Parameter variations within Li-Ion battery packs – Theoretical investigations and experimental quantification," *Journal of Energy Storage*, vol. 18, pp. 295–307, 2018.

[190]   J. Sturm *et al.*, "Modeling and simulation of inhomogeneities in a 18650 nickel-rich, silicon-graphite lithium-ion cell during fast charging," *Journal of Power Sources*, vol. 412, pp. 204–223, 2019.

[191]   J. Kim and B. H. Cho, "Screening process-based modeling of the multi-cell battery string in series and parallel connections for high accuracy state-of-charge estimation," *Energy*, vol. 57, pp. 581–599, 2013.

[192]   T. Zimmermann *et al.*, "Review of system topologies for hybrid electrical energy storage systems," *Journal of Energy Storage*, vol. 8, pp. 78–90, 2016.

[193]   M. Wohlfahrt-Mehrens, C. Vogler, and J. Garche, "Aging mechanisms of lithium cathode materials," *Journal of Power Sources*, vol. 127, no. 1-2, pp. 58–64, 2004.

[194]   A. Barré *et al.*, "A review on lithium-ion battery ageing mechanisms and estimations for automotive applications," *Journal of Power Sources*, vol. 241, pp. 680–689, 2013.

[195]   F. M. Kindermann, A. Noel, S. V. Erhard, and A. Jossen, "Long-term equalization effects in Li-ion batteries due to local state of charge inhomogeneities and their impact on impedance measurements," *Electrochimica Acta*, vol. 185, pp. 107–116, 2015.

[208]   V. V. Viswanathan *et al.*, "Effect of entropy change of lithium intercalation in cathodes and anodes on Li-ion battery thermal management," *Journal of Power Sources*, vol. 195, no. 11, pp. 3720–3729, 2010.

[209]   J. Schiffer *et al.*, "Model prediction for ranking lead-acid batteries according to expected lifetime in renewable energy systems and autonomous power-supply systems," *Journal of Power Sources*, vol. 168, no. 1, pp. 66–78, 2007.

[210]   S. Adam, *MATLAB und Mathematik kompetent einsetzen: Eine Einführung für Ingenieure und Naturwissenschaftler,* 2nd ed. Weinheim: Wiley-VCH Verlag GmbH & Co. KGaA, 2017.

[211]   W. Waag, S. Käbitz, and D. U. Saue, "Experimental investigation of the lithium-ion battery impedance characteristic at various conditions and aging states and its influence on the application," *Applied Energy*, vol. 102, pp. 885–897, 2013.

[212]   C. Campestrini *et al.*, "Validation and benchmark methods for battery management system functionalities: State of charge estimation algorithms," *Journal of Energy Storage*, vol. 7, pp. 38–51, 2016.

[214]   A. Barai, W. D. Widanage, J. Marco, A. McGordon, and P. Jennings, "A study of the open circuit voltage characterization technique and hysteresis assessment of lithium-ion cells," *Journal of Power Sources*, vol. 295, pp. 99–107, 2015.

[215]   A. Marongiu, F. G. W. Nußbaum, W. Waag, M. Garmendia, and D. U. Sauer, "Comprehensive study of the influence of aging on the hysteresis behavior of a lithium iron phosphate cathode-based lithium ion battery – An experimental investigation of the hysteresis," *Applied Energy*, vol. 171, pp. 629–645, 2016.

[216]   A. Eddahech, O. Briat, and J.-M. Vinassa, "Thermal characterization of a high-power lithium-ion battery: Potentiometric and calorimetric measurement of entropy changes," *Energy*, vol. 61, pp. 432–439, 2013.

[217]   J. Li *et al.*, "An electrochemical–thermal model based on dynamic responses for lithium iron phosphate battery," *Journal of Power Sources*, vol. 255, pp. 130–143, 2014.

[218]   M. Guo, G. Sikha, and R. E. White, "Single-Particle Model for a Lithium-Ion Cell: Thermal Behavior," *J. Electrochem. Soc.*, vol. 158, no. 2, A122, 2011.

[219]   S. Ziegler, R. C. Woodward, H. H.-C. Iu, and L. J. Borle, "Current Sensing Techniques: A Review," *IEEE Sensors J.*, vol. 9, no. 4, pp. 354–376, 2009.

[220]   W. Pettigrew, "Curent Sensing - Selecting the Most Effective Current Sensing Technology," *Power Electronics Europe*, vol. 8, pp. 27–31, 2007.

[221]   C. von Lüders, J. Keil, M. Webersberger, and A. Jossen, "Modeling of lithium plating and lithium stripping in lithium-ion batteries," *Journal of Power Sources*, vol. 414, pp. 41–47, 2019.

[222]   S. F. Schuster, *Reuse of Automotive Lithium-Ion Batteries: An Assessment from the Cell Aging Perspective*. Dissertation. München, 2016.

[223]   T. Utsunomiya, O. Hatozaki, N. Yoshimoto, M. Egashira, and M. Morita, "Self-discharge behavior and its temperature dependence of carbon electrodes in lithium-ion batteries," *Journal of Power Sources*, vol. 196, no. 20, pp. 8598–8603, 2011.

[224]   T. F. Fuller, "Simulation and Optimization of the Dual Lithium Ion Insertion Cell," *J. Electrochem. Soc.*, vol. 141, no. 1, p. 1, 1994.

[225]   M. Doyle, "Comparison of Modeling Predictions with Experimental Data from Plastic Lithium Ion Cells," *J. Electrochem. Soc.*, vol. 143, no. 6, p. 1890, 1996.

[226]   M. Hess, *Kinetics and stage transitions of graphite for lithium-ion batteries*. Dissertation. Zürich: ETH Zurich, 2013.

[227]   M. Winter and J. O. Besenhard, "Lithiated Carbons," in *Handbook of battery materials*, C. Daniel and J. O. Besenhard, Eds., 2nd ed., Weinheim: Wiley-VCH Verlag, 2011, pp. 433–478.

[228]   M. Naumann, *Techno-economic evaluation of stationary battery energy storage systems with special consideration of aging*. Dissertation. München, 2018.

[229]   C. Guenther, B. Schott, W. Hennings, P. Waldowski, and M. A. Danzer, "Model-based investigation of electric vehicle battery aging by means of vehicle-to-grid scenario simulations," *Journal of Power Sources*, vol. 239, pp. 604–610, 2013.

[230]   T. M. Bandhauer, S. Garimella, and T. F. Fuller, "A Critical Review of Thermal Issues in Lithium-Ion Batteries," *J. Electrochem. Soc.*, vol. 158, no. 3, R1, 2011.

[231]   M. Brand *et al.*, "Electrical safety of commercial Li-ion cells based on NMC and NCA technology compared to LFP technology," *World Electric Vehicle Journal*, vol. 6, no. 3, pp. 572–580, 2013.

[232]   C. von Lüders, *Experimentelle und simulative Untersuchung von Lithium-Plating und Lithium-Stripping in Lithium-Ionen-Zellen*. Dissertation. München, 2019.

[233]   F. B. Spingler, W. Wittmann, J. Sturm, B. Rieger, and A. Jossen, "Optimum fast charging of lithium-ion pouch cells based on local volume expansion criteria," *Journal of Power Sources*, vol. 393, pp. 152–160, 2018.

Datasheets

[196]   A123Systems, "A123Systems High Power Model: APR18650M1A: datasheet," 2009.

[197]   E-One Moli Engergy Corp., "E-One Moli Engergy Model: IHR18650A: datasheet," 2008.

[198]   LG Chem, "LG Chem Model: LG ICR18650HB2: datasheet," 2011.

[199]   LG Chem, "LG Chem Model: INR18650 MJ1: datasheet," 2016.

[200]   Panasonic Corporation, "Panasonic Model: NCR18650PF: datasheet," 2012.

[201]   Shenzhen O'CELL Technology Co., Ltd., "O'CELL Model: IFR18650E: datasheet," 2011.

[202]   L. Samsung SDI Co., "Samsung Model: INR18650-25R: datasheet," 2014.

[203]   L. OptimumNano Energy Co., "OptimumNano Model: OPT-26650F: datasheet," 2015.

[204]   Sony Energy Devices Corporation, "SONY Model: US26650FTC1: datasheet," 2010.

[205]   Panasonic Corporation, "Panasonic Model: NCR18650B: datasheet," 2014.

[206]   Guangzhou Great Power Energy & Technology Co., Ltd., "Great Power Model: 26650/3400mAh 3.2 V: datasheet," 2017.

[207]   A123Systems, "A123Systems High Power Model: ANR26650M1: datasheet," 2007.

Web pages

[1]   Sony Global, *Sony History Chapter13 Recognized as an International Standard.* [Online] Available: https://www.sony.net/SonyInfo/CorporateInfo/History/SonyHistory/2-13.html. Accessed on: Jul. 24 2018.

[8]   D. B. Gray, *Tesla Switches on World's Biggest Lithium Ion Battery.* [Online] Available: https://www.scientificamerican.com/article/tesla-switches-on-world-rsquo-s-biggest-lithium-ion-battery/. Accessed on: Jul. 25 2018.

[9]   J. Griffin, *100 Years of Innovation: History of the Electric Drill.* [Online] Available: https://www.ecmag.com/section/your-business/100-years-innovation-history-electric-drill. Accessed on: Sep. 19 2019.

[10] G. Hawley, *Understanding Tesla's lithium ion batteries.* [Online] Available: https://evan-nex.com/blogs/news/understanding-teslas-lithium-ion-batteries. Accessed on: Sep. 19 2019.

[11] M. Burger, *Alles über den E-Bike Akku.* [Online] Available: https://www.radfahren.de/ser-vice/e-bike-akku/. Accessed on: Nov. 03 2019.

[12] M. Eberhard, *A Bit About Batteries.* [Online] Available: https://www.tesla.com/blog/bit-about-batteries. Accessed on: Nov. 03 2019.

[14] ecomento UG, *Tesla: 2170-Batteriezelle vorerst exklusiv für Model 3 - ecomento.de.* [Online] Available: https://ecomento.de/2017/06/23/tesla-2170-batteriezelle-vorerst-exklusiv-fuer-model-3/. Accessed on: Oct. 10 2019.

[18] *The new 2017 BMW i3 (94 Ah): More range paired to high-level dynamic performance.* [Online] Available: https://www.press.bmwgroup.com/usa/article/detail/T0259560EN_US/the-new-2017-bmw-i3-94-ah-:-more-range-paired-to-high-level-dynamic-performance?lan-guage=en_US. Accessed on: Jul. 31 2018.

[51] Federal Ministry for the Environment, Nature Conversation, Building and Nuclear Safety, *Effizienzhaus Plus – Project report.* [Online] Available: http://www.forschungsiniti-ative.de/effizienzhaus-plus/. Accessed on: Jun. 24 2018.

[111] jhart12, *Preisach Model MATLAB.* [Online] Available: https://github.com/jhart12/Preisach_Model_MATLAB. Accessed on: Jun. 17 2019.

[213] I. The MathWorks, *MATLAB fmincon: Find minimum of constrained nonlinear multivariable function.* [Online] Available: https://www.mathworks.com/help/optim/ug/fmincon.html. Accessed on: Mar. 20 2019.

References

146

List of Figures

List of Figures

List of Tables

Appendix

Analysis of a hybrid battery system

A usage of asymmetric current distribution in a way of a combination of HP and HE cells seems not wise in most cases. Figure A 1 analyses a simple constellation using the analytical calculation from chapter 3.1. A 1 C discharge current is applied to a 2p connection of an HP and a HE cell. There are six combinations beginning with a strong HP and HE cell design which means the resistance coefficient of the HP is $\lambda = 1.5$ Ah $\cdot$ 0.010 $\Omega = 0.015$ AhΩ and the one of the HE cell is by $\lambda = 3.5$ Ah $\cdot$ 0.040 $\Omega = 0.140$ AhΩ and ending with $\lambda = 0.067$ AhΩ for the HP and $\lambda = 0.086$ AhΩ for the HE cell. The capacities of the cells change equivalent. The discharging starts at 100 % of SoC and the OCV is assumed linear with a slope of 0.01 V/%.
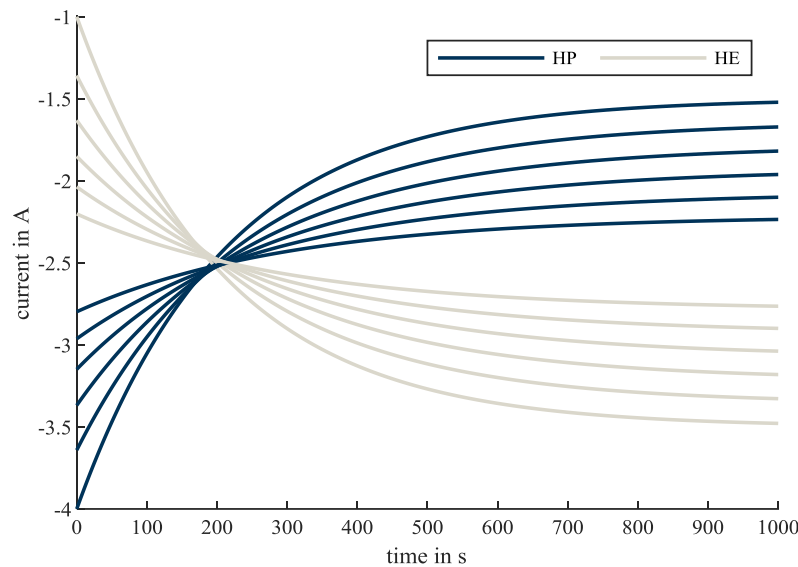
Figure A 1:   *Current distribution of a system design consisting of an HP and a HE cell connected in parallel and discharged from a fully charged state with and CC current of 1 C calculated with the simple analytic model from chapter 3.1 (model type: $OCV_{lin}(SoC) + \underline{Z}_R$).*

In the beginning, the HP cell takes the major part of the current in all cases. Due to the rising SoC and therefore OCV, the HE takes more and more of the current until an intersection point at about 200 s. The time of the intersection point is independent of the current height. After this intersection, the HE cell carries most of the load. This is against the idea of preventing the HE cell from high current. Only in the first 200 s the HP cell relieves the HE cell. Hence, within this time, a change of the current direction is necessary to further stress the HP cell more than the HE cell. For all applications that do not use this window, this kind of hybrid cell combination does not bring advantages and it is needful to know that in this calculation, the effects of nonlinear OCV, hysteresis, temperature influence and nonohmic impedances are not considered.